From MALDI-TOF Mass Spectrometry to Soft-Landing for Electronics

Dissertation

zur Erlangung des Grades
„Doktor der Naturwissenschaften“
im Promotionsfach Chemie

am Fachbereich Chemie, Pharmazie und Geowissenschaften
der Johannes Gutenberg-Universität Mainz

Anna Maria Cristadoro
geboren in Enna, Italien

Mainz 2008

Tag der mündlichen Prüfung: 17.12.2008

To my family

Il piú nobile dei piaceri é la gioia di capire”

“The noblest pleasure is the joy of understanding”

Leonardo da Vinci

TABLE OF CONTENTS

1 Introduction

1.1 Mass spectrometry: New bridges between past and future

The history of mass spectrometry begins in 1886 with Eugen Goldstein and his investigation of the electric discharge, obtained when a large voltage is applied across a pair of electrodes in a vessel containing a gas at low pressure. He found that if a channel or canal was cut through the cathode, a beam of light appeared on the side remote from the anode. He called the beam *Kanalstrahlen*, canal rays [1].

In 1898 W. Wien (Berlin, Nobel prize 1911) [2] managed for the first time to establish the masses of the canal ray analytes through deflection measurements. Based on his study J. J. Thomson [3-4] (Cambridge, Nobel prize 1906 for the discovery of the electrons) in 1920 developed the "Parabola spectrometer" (**Figure 1**). His instrument geometry consisted of an electrical and a magnetical field parallel to each others, which discriminated the ions with respect to their different mass to charge ratios.

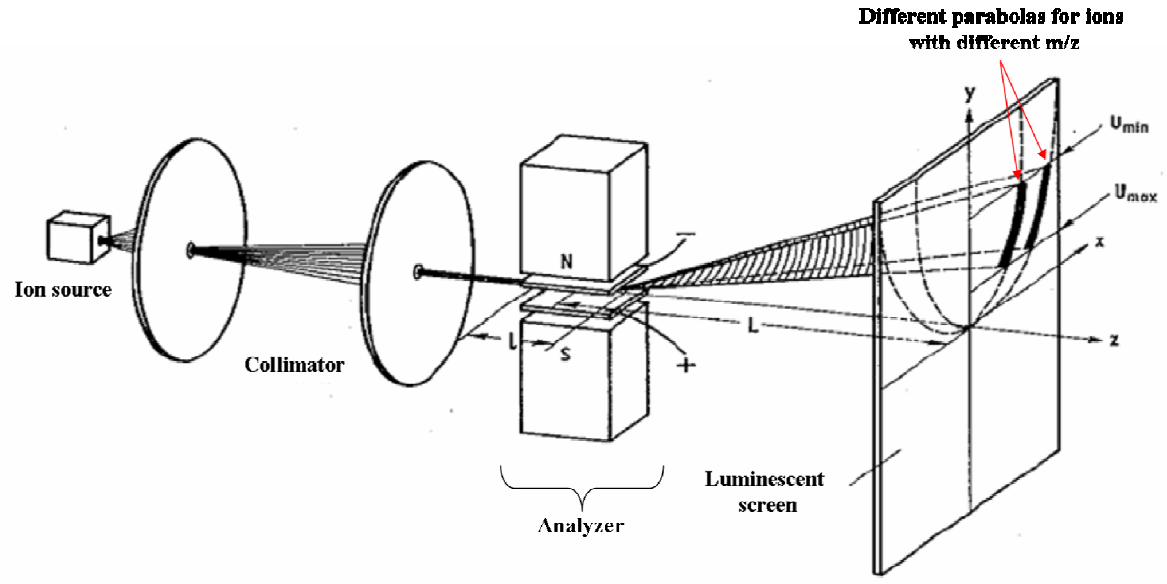

Figure 1. Sketch of Thomsos´s parabola spectrometer.

Pro mass the parabola spectrometer described a parabola on a luminescent screen and by using this apparatus for studying Neon rays; Thomson observed different parabolas, due to the different natural isotopes of the element Neon (^{20}Ne, ^{21}Ne, ^{22}Ne, **Figure 2**). Thus, he discovered the isotopes.

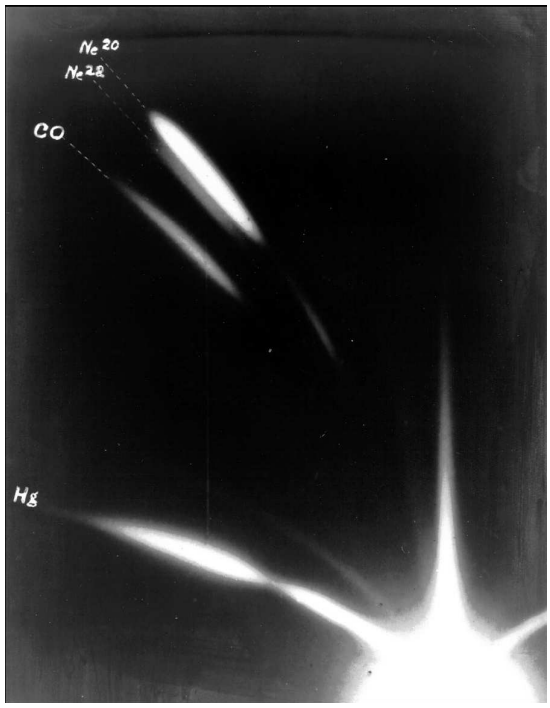

Figure 2. Positive ray parabolas of neon obtained by Thomson in 1912.

The history of mass spectroscopy is therefore strictly related to the progress of nuclear physics, as the mass spectrometric results confirmed definitively the hypothesis of the atomic constitution of matter. Thomson's construction, which is still today used as ion source, can thus be considered as the ancestor of the today's mass spectrometer.

With the time, mass spectrometers have been used by almost all chemists and many researchers from neighboring disciplines such as physics, medicine, or biology as a powerful analytical tool [5]. Within the last few years, due to the contribution of John B. Fenn and Koichi Tanaka (Nobel prizes in Chemistry, 2002), mass spectrometry has expanded its application field to the mass characterization of thermally unstable and low volatile molecules. Through the development of soft-ionization techniques, such as electrospray ionization (ESI) and matrix assisted laser desorption/ionization time-of flight mass spectrometry (MALDI-TOF MS), the mass characterization of large biomolecules and synthetic polymers became possible [6-7].

Nowadays the mass spectrometry principles, mainly ionization and ion separation, have found even novel fields of application. Mass spectrometers have been used to obtain films of giant and non-volatile molecules, inaccessible for traditional film forming techniques, such as vapor deposition or solution processing [8-9]. By means of ESI and MALDI intractable analytes have been ionized, separated depending on their different mass to charge ratios and collected on a surface with retention of their structures, in a process now known as "soft-landing". Using mass analyzers possessing high mass

resolution even allowed growing thin films of molecules possessing isotopic purity. In this sense, these investigations step back to the origin of mass spectrometry, which arose with the discovery of the isotope and ends up as a novel tool for collecting isotopically pure analytes.

1.2 Ionization techniques

A first important step in mass spectrometry is the generation of ions from the sample of interest. Depending on the type of sample different ionization techniques are used.
In general, ions or excited species are formed by removal or addition of an electron giving a radical cation $A^{+\cdot}$ or anion $A^{-\cdot}$ (1.1 and 1.2), respectively, or by addition of other charged species (1.4)[10]:

$$A + e^- \rightarrow A^{+\cdot} + 2e^- \qquad (1.1)$$

or with lower probability

$$A + e^- \rightarrow A^{-\cdot} \qquad (1.2)$$

or

$$A + e^- \rightarrow A^* + e^- \qquad (1.3)$$

Where A denotes the molecular species to be ionized, e^- an electron; the * (1.3) indicates an excited states.

Depending on the analyte structure, the thermal energy prior to ionization, the energy gained during ionization, and the environment of the ion, determining whether it collides or not with other species, further fragmentation can happen, leading to other ions (I^+), radical cations ($R^{+\cdot}$) and neutrals N:

$$A^{\cdot +} \rightarrow I^+ + N^\cdot \text{ or } R^{+\cdot} + N \qquad (1.4)$$

For non-volatile macromolecules, such as biomolecules and synthetic polymers, the conditions of the traditional ionization methods lead to considerable fragmentation, which causes complications in the mass spectrum and does not allow the visualization of the intact mass of the analyte. Thus, a direct ionization from the condensed state, offered by

field desorption (FD), fast atom bombardment (FAB), ESI and MALDI would be of great advantage. Among all the so-called "soft-ionization" techniques, the attention will be pointed in the next section on the MALDI process.

1.3 MALDI-TOF-MS

The key feature of the MALDI technique, pioneered by Hillenkamp [11] and Karas [12], is the Nitrogen laser irradiation of the sample dispersed in an ultraviolet absorbing matrix. MALDI is a "soft" ionization technique in which the energy from the laser is spent in volatilizing the matrix rather than in degrading the analytes [13].
The mechanism related to the desorption and ionization of the analyte molecules in MALDI is strictly related to the analyte nature.

The most plausible process, valid for non absorbing analytes at the nitrogen laser wavelength (λ = 337 nm), dates back to the roots of MALDI [14]. This mechanism, known as excited-state proton transfer (ESPT) is characterized by the following steps:

1. The matrix molecules M absorb the laser light and form an excited species (1.5):

$$M + h\nu \rightarrow M^* \qquad (1.5)$$

2. The excited matrix transfers a proton to the analyte (primary ions) as following (1.6):

$$M^* + A \rightarrow (M\text{-}H) + AH^+ \qquad (1.6)$$

Further ionization can happen in the gas phase. In fact, the primary ions are created in a moderately hot bath of neutral molecules and clusters. Thus, they can undergo collisions and consequently secondary ion-molecules reactions leading to protonated or cationized analyte species.

If the analyte itself absorbs the laser light, the most straightforward explanation for laser generated ions would be multiphoton ionization (MPI; absorption of n photons $h\nu$) leading to an analyte radical cation (1.7):

$$A \rightarrow A^{\cdot +} + e^{-} \qquad (1.7)$$

This process, which is known as photoionization, is the most probable ionization mechanism for analytes possessing high absorption coefficients at the laser wavelength.

The generation of ions in MALDI is a complex and still not completely understood phenomenon. Ion signals depend in fact not only on the amount of the analyte present in a mixture, but also on its chemical composition, and may suffer from suppression by other components present in the sample. [15-16-17-18-19] Thus, the extraction of quantitative information from MALDI spectra is not a straightforward procedure [6]. A strategy for overcoming this drawback will be proposed in this study.

1.3.1 Matrices and sample preparation techniques for MALDI analyses

Preparation of an appropriate analyte/matrix mixture is one of the most important steps of a MALDI analysis. The choice of the proper matrix is in fact crucial for the visualization of the analyte. Generally, if there is an idea of the acidity or basicity of the analyte, a matrix with an appropriate proton affinity or basicity should be selected. If cationized analytes are to be expected, a matrix should be chosen, which does not compete for the cation with the analyte. In general, matrix and sample preparation should serve three aims:

a) Co-crystallization with the analyte in a large molar excess to prevent cluster formation of analyte molecules;

b) Strong absorption of the exciting laser light in the matrix with subsequent transfer to the analyte;

c) Achieving ionization of the analyte.

The most widespread sample preparation procedure is the so-called dry droplet method, which is schematized in **Figure 3 a**. Appropriate amounts of matrix and analyte are dissolved in compatible, preferentially identical solvents and mixed to achieve a molar ratio of analyte to matrix between 1:100 and 1:1000. 1-1.5 µl of this solution is spotted

onto a stainless steel target, allowed to dry and then introduced into the ion source of the spectrometer.

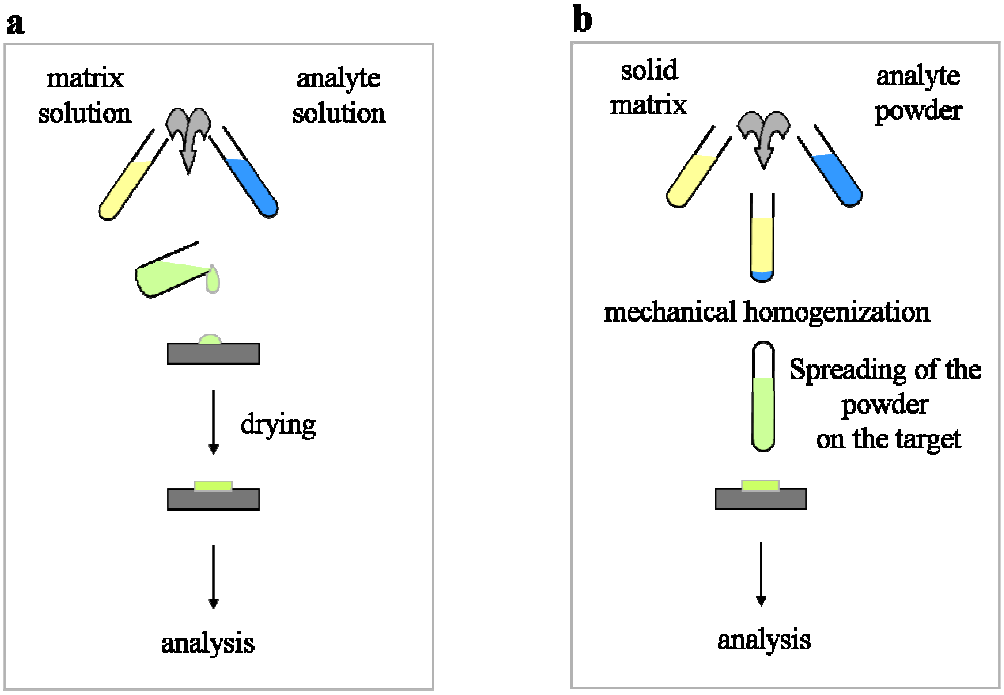

Figure 3. Sample preparations for MALDI MS: a) dried droplet procedure, b) solvent-free sample preparation.

A totally different preparation procedure, known as "solvent-free sample preparation", was described by Przybilla et. al. [20]. In this case, the analyte is mechanically mixed with a suitable matrix as reported in **Figure 3 b**. Then, the mixture is spread with the help of a flat spatula on the target and is ready for the exposition to the Nitrogen irradiation in the ionization source of the MALDI apparatus. This procedure is of great advantage for molecules, which suffer from lack of solubility and it will mainly used in this investigation for the qualitative and quantitative mass characterization of giant molecules bearing a large aromatic π-system.

1.3.2 Solvent-free technique and characterization of giant polycyclic aromatic hydrocarbons

The discovery of a preparation procedure, which did not require the use of solvents, allowed the mass analyses of slightly soluble or insoluble samples, which previously could not be characterized via traditional analytical methods. Within the past five years, intensive

investigations have shown that this procedure can be used complementary to the solvent-based sample preparation for the analysis of polymers and uniquely for the characterization of slightly soluble or insoluble polycyclic aromatic hydrocarbons (PAHs) and other intractable systems [21-22].

PAHs are chemical compounds that consist of fused aromatic rings and do not contain heteroatoms or carry substituents [23]. PAHs occur in oil, coal, and tar deposits, and are produced as byproducts of fuel burning (whether fossil fuel or biomass). They are also found in the interstellar medium, in comets, and in meteorites [24-25].

In graphene the PAH motif is extended to large 2D sheets and it can be considered as the largest member of the PAH family.

Successful attempts to synthesize graphene-like structures have produced large PAHs (more than six fused rings), which have attracted notable attention as semiconducting materials. The synthetic strategies proposed by Müllen et al. [26-27] have allowed designing molecules with defined size and geometry, such as disc-like or triangle-like flat aromatic systems, with the interesting characteristic to self-assemble into stable two dimensional superstructures due to the overlap of their large aromatic π-systems.

Due to the strong intermolecular interactions non-substituted nanographene molecules suffers from the lack of solubility in common organic solvent. Thus, over the years, the introduction of linear or branched alkyl chains has been thought as a strategy to increase solubility and allow processability of this family of molecules [28].

1.3.2.1 HBC molecules carrying aliphatic alkyl chains

Attaching long aliphatic chains to the large aromatic core of the PAHs leads to molecules possessing a liquid crystalline nature. This phase of matter has properties between those of a conventional liquid, and those of a solid crystal, and can be divided into two categories: thermotropic and lyotroic liquid crystals (LC) [29]. Thermotropic LCs exhibit a phase transition into the LC phase as temperature is changed, whereas lyotropic LCs exhibit phase transitions as a function of concentration of the mesogen in a solvent as well as temperature. Thermotropic LCs manifest different phases depending on the temperature at which they are observed:

1) Nematic: the molecules have no positional order, but they have long-range orientational order;

2) Smectic: the molecules are positional ordered along one direction;

3) Cholesteric: this phase exhibits a twisting of the molecules and is observable only for chiral molecules;

4) Disc-shaped mesogens, such as substituted PAHs, can orient themselves in a layer-like fashion known as the discotic nematic phase. If the disks pack into stacks, the phase is called discotic columnar. The columns themselves may be organized into rectangular or hexagonal arrays.

The different phases are schematized in **Figure 4**.

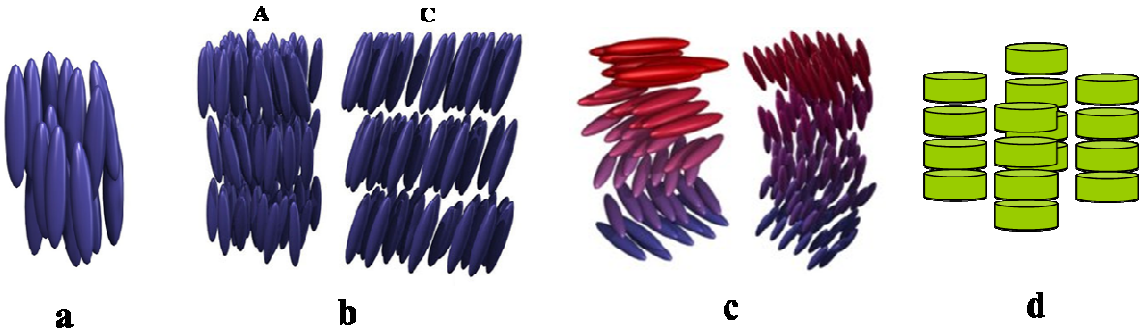

Figure 4. Thermotropic liquid crystalline phases: a) nematic, b) smectic A and C, c) cholesteric, (a-c: also known as calamitic LC), d) discotic columnar.

The alkyl chains anchored to the aromatic core of PAHs permits processing of the molecules from solution in order to obtain suitable films for device applications.

Over the last few years, the semiconducting characteristics of PAHs have been successfully used for building organic field effect transistors (OFET) and solar cells as an alternative to all inorganic devices [30-31]. Sketches of the different devices are reported in **Figure 5 a** and **b**.

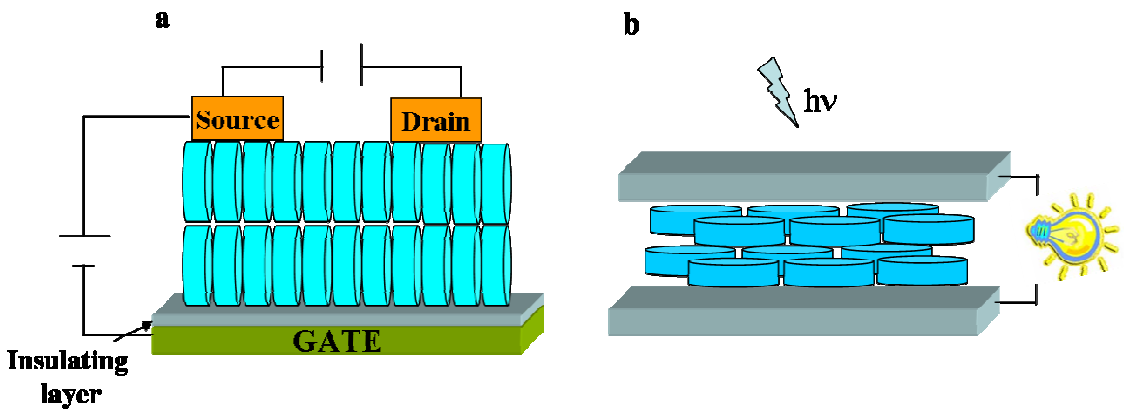

Figure 5. Schematic representation of an organic field effect transistor (OFET) (a) and a solar cell (b) based on PAHs.

An OFET is a type of transistor that relies on an electric field to control the shape and hence the conductivity of a 'channel' in an organic semiconductor material (**Figure 5 a**). A solar cell or photovoltaic cell is a device that converts solar energy into electricity by the photovoltaic effect (**Figure 5 b**). Nowadays, photovoltaic arrays are objects of intensive investigations as they generate a form of renewable electricity, particularly useful in situations where electrical power from the grid is unavailable such as in remote area power systems, Earth-orbiting satellites and space probes, remote radiotelephones and water pumping applications.

In order to make such devices working efficiently with PAH films as semiconducting layers, the arrangements of the large aromatic systems need to be controlled. The packing of PAHs can in fact vary from lying with their aromatic plane flat on top of the deposition surface, defined as face-on, to standing on their edge perpendicularly to the substrate (edge-on). The edge-on geometry is preferred for OFET (**Figure 5 a**), whereas the face-on fashion is desirable for solar cell (**Figure 5 b**).

This can be understood considering the different working mechanisms of the two devices. In an OFET, the application of a voltage between the source electrode and the gate generates a conducting channel in the semiconducting film of PAH molecules. For PAH molecules in “edge-on” arrangement, charge carriers drift through the columns from the source electrode to the drain electrode under controlled gate voltage. In contrast, the large monodomain "face-on" arrangement of the discs leads to a homeotropic phase, which allows faster charge transport between the top and bottom electrodes and favors the photovoltaic performance (**Figure 5 b**) [31]. Thus, great efforts have been spent in developing strategies to control the packing and the orientation of the molecules on the

surface, as it has been discovered to be the key for reaching improved device performances [32].

1.4 Innovative use of the mass spectrometry principles

1.4.1 Soft-landing

Parallel to the development of novel ionization techniques, such as MALDI and ESI, for the mass characterization of giant analytes, the mass spectrometry principles have found application in other fields. A wide variety of gas phase ions with kinetic energies from 1–10^7 eV are being used for the growth and modification of state-of-the-art material interfaces. Ions can be deposited for growing thin films; they can be used to expose fresh interfaces by sputtering; modify the phases of interfaces; dope trace elements into interface regions; impart specific chemical functionalities to a surface; toughen materials; and create micron- and nanometer-scale interface structures.

Based on the collision energy, ion-surface collision studies can be categorized into four energy regimes: (1) the thermal range with ions having kinetic energies below 1 eV, (2) the hyperthermal range involving ions having energies 1-100 eV, (3) the low-energy range from 0.1 to 10 keV, and (4) the high-energy range covering ion energies into the MeV regime.

Hyperthermal and low energy ions deposit their kinetic energy solely into the surface without affecting the bulk region. When the landed species retain their structure, getting in contact with the deposition surface, the deposition process is defined as “soft-landing”.

The soft-landing of molecular ions onto surfaces, first proposed in 1977[33], was later demonstrated [8] with low–kinetic energy (typically 5 to 10 eV) mass-selected ion beams at polyfluorinated self-assembled monolayer (SAM) surfaces.

Via employing the mass spectrometer as a novel deposition apparatus, Cooks et al. profited also of using mass spectrometry as a separation method [8]. The mass spectrometer analyzer in fact discriminates among components having different mass to charge ratios, which can be separated and individually soft-landed. Within their experiments, dedicated to the separation of complex protein mixtures, Cooks et al. coupled an electrospray ion source to a quadrupole mass analyzer. This allowed collecting the proteins with retention of their biologic activity and producing arrays of proteins on the soft-landing deposition substrate.

1.4.2 MALDI-soft-landing

The deposition of large molecules possessing large aromatic π-systems represents a big challenge as large molecules commonly imply lower processability due to either their low solubility in liquid media or the occurrence of thermal cracking during vacuum sublimation. A way to overcome this drawback was developed by Räder et al. [34-8]. In that study, the MALDI was used in a soft-landing apparatus as ionization source. Moreover, to allow the deposition of intractable analytes, the solvent-free method was employed for the sample preparation. A schematic representation of the soft-landing principle is reported in **Figure 6**.

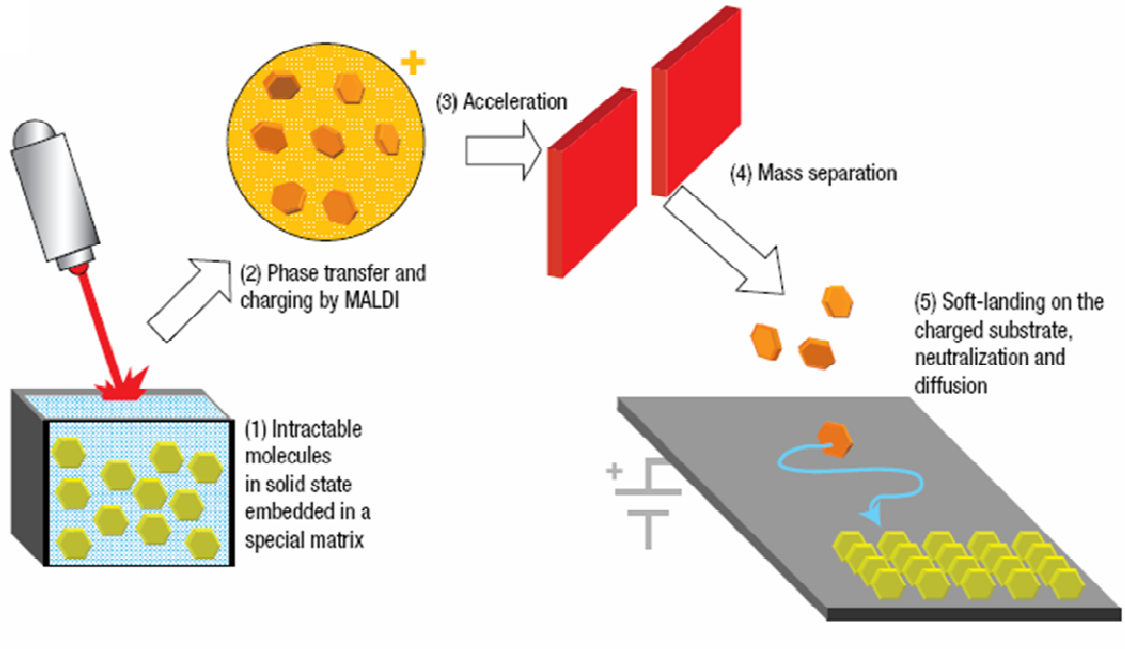

Figure 6. Schematic diagram of the MALDI- soft-landing set-up.

As shown in **Figure 6** ions from the desired analyte are generated via MALDI. The soft-ionization, ensured by the presence of a matrix, allows the desorption ionization of intact species, which are discriminated due their different mass to charge ratio via a mass analyzer. Potentials are then used to decelerate and focus the ion beam, which is finally collected on a deposition surface.

Through this procedure, extraordinarily large and insoluble molecules, such as synthetic nanographenes, were processed at the highly oriented pyrolitic graphite (HOPG) surface into ultrapure crystalline architectures. Their molecular structures are presented in **Figure 7**.

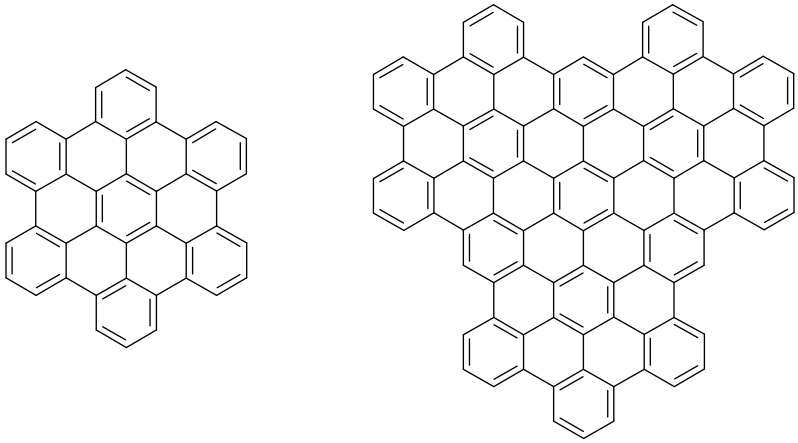

Molecular Weight =522,612
C42H18

Molecular Weight =1183,310
C96 H30

Figure 7. Molecular structures of the soft-landed analytes: $C_{42}H_{18}$ (Hexa-peri-hexabenzocoronene, HBC) and $C_{96}H_{30}$ (super-phenalene).

Scanning force microscopy (AFM) and scanning tunneling microscopy (STM) made it possible to gain direct insight into the self-organization of the molecules on the surfaces on the micro and nanoscale, respectively. The hexa-peri-hexabenzocoronene (HBC) molecules deposited on the surface via soft-landing were found to assemble into an edge-on arrangement. The self-organization observed in soft-landed films was remarkably different from that usually found for dry $C_{42}H_{18}$ films prepared on HOPG either from vacuum sublimation [35] or solution processing [36-37]. In both of these cases, the $C_{42}H_{18}$ discs adsorb 'face-on' on the basal plane of the HOPG forming hexagonally packed layers, as observed by STM, SFM and angle-resolved ultraviolet photoelectron spectroscopy (ARUPS). This behavior has been attributed to the strong affinity between graphite and the nanographene [38]. The different packing of $C_{42}H_{18}$ on HOPG in the films prepared by soft-landing provides evidence of a modest affinity between the two materials. A justification for this unusual self-assembly tendency was hypothesized to be the charged character of the $C_{42}H_{18}$ during soft-landing or the decelerating potential applied to the collecting surface. Experimental proofs for this theory were however not reported in that study.

1.5 References

[1] E. Goldstein, *Berlin Ber.*, **1886**, 39, 691.

[2] W. Wien, Kanalstrahlen, 1927, Handb. D. Exper. Phys. XIV.

[3] J. J. Thomson, *Philos. Mag.*, **1907**, 13, 561.

[4] J. J. Thomson, Royal Institution, Weekly Meeting, January 17, 1913.

[5] C. A. Schalley, *Modern Mass Spectrometry*, 2003, Springer-Verlag Berlin Heidelberg.

[6] H. Pasch, W. Schrepp, MALDI-TOF Mass Spectrometry of Synthetic Polymers, 2003, Springer-Verlag Berlin Heidelberg.

[7] R. M. Caprioli, *Continuous- Flow Fast Atom Bombardment Mass spectrometry*, 1990, Wiley ans Sons, Chichester West Sussex, England.

[8] H. Luo, S. A. Miller, R. G. Cooks, S. J. Pachuta, *Int. J. Mass Spectrom. Ion Processes* **1998**, 174, 193.

[9] H. J. Räder, K. Müllen, *Nachrichten aus der Chemie*, **2006**, 54, 746.

[10] F. W. Mclafferty, F. Turecek, *Interpretation of Mass Spectra*, University science books, fourth edition, Sausalito, California.

[11] F. Hillenkamp, R. Kaufmann, R. Nitsche, E. Unsold, *Appl. Phys.* **1975**, 8, 341.

[12] M. Karas, U. Bahr, *NATO ASI Series, Series C: Mathematical and Physical Sciences* **1997**, 504, 33.

[13] R. P. Lattimer, G. Montaudo, Mass spectrometry of polymers, 2001, CRC press, Roca Raton, USA.

[14] M. Karas. D. Bachmann, U. Bahr, F. Hillenkamp, **1987**, *Int. J. Mass Spectrom. Ion. Proc*, 78, 53.

[15] S. L. Cohen, B. T. Chait, *Anal. Chem.* **1996**, 68, 31.

[16] M. Kussmann, E. Nordhoff, H. Rahbek-Nielsen, S. Haebel, M. Rossel-Larsen, L. Jakobsen, J. Gobom, E. Mirgorodskaya, A. Krol-lKristensen, L. Palm, P. Roepstorff, *J. Mass Spectrom.* **1997**, 32, 593.

[17] A. Vertes, G. Irinyi, R Gijbels, *Anal.Chem*. **1993**, 65, 2398.

[18] R. E. Johnson, *Int. J. Mass Spectrom Ion proc*, **1999**, 139, 25.

[19] H. Ehring, M. Karas, F. Hillenkamp, *Organic Mass Spectrometry* **1992**, 27, 472.

[20] L. Przybilla, J-D. Brand, K. Yoshimura, H. J. Räder, K. Müllen, *Analytical Chemistry* **2000**, 72, 4591.

[21] S. Trimpin, A. C. Grimsdale, H. J. Räder, K. Müllen, *Analytical Chemistry* **2002**, 74, 3777.

[22] K. Yoshimura, L. Przybilla, S. Ito, J. D. Brand, M. Wehmeir, H. J. Räder, K. Müllen, *Macromolecular Chemistry and Physics* **2001**, 202, 215.

[23] J. C. Fetzer, *The Chemistry and Analysis of the Large Polycyclic Aromatic Hydrocarbons*, 2000, Wiley, New York.

[24] L. J. Alamandola, A. G. G. M. Tielens, J. R. Barker, *Astrophys. J.* **1985**, 290, L25.

[25] F. C. Gillett, W. J. Forrest, K. M. Merrill, *Astrophys. J.* **1973**, 183, 87.

[26] J. Wu, K. Müllen, *Carbon-Rich Compounds*, **2006**, 90.

[27] C. D. Simpson, J. Wu, M. D. Watson, K. Müllen, *Journal of Materials Chemistry*, **2004**, 14, 494.

[28] A. Fechtenkötter, K. Müllen, Abstracts of Papers, 220th ACS National Meeting, Washington, DC, United States, August 20-24, **2000**.

[29] P. J. Collings, M. Hird, *Introduction to liquid crystals*, 1997, Taylor & Francis.

[30] J. Li, M. Kastler, W. Pisula, J. W. F. Robertson, D. Wasserfallen, A. C. Grimsdale, J. Wu, K. Müllen, *Advanced Functional Materials*, **2007**, 17, 2528.

[31] J. Wu, W. Pisula K. Müllen, *Chem. Rev.* **2007**, 107, 718.

[32] W. Pisula, M. Kastler, D. Wasserfallen, M. Mondeshki, J. Piris, I. Schnell, K. Müllen. *Chemistry of Materials* **2006**, 18, 3634.

[33] V. Franchetti, B. H. Solka, W. E. Baitinger, J. W. Amy, R. G. Cooks, *Int. J. Mass Spectrom. Ion Phys.* **1977**, 23, 29.

[34] H. J. Räder, A. Rouhanipour, A. M. Talarico, V. Palermo, P. Samori, K. Müllen, *Nature Materials*, **2006**, 5, 276.

[35] R. Staub, M. Toerker, T. Fritz, T. Schmitz-Hubsch, F. Sellam, K. Leo, *Surface Science* **2000**, 445, 368.

[36] P. Samori, N. Severin, C. D. Simpson, K. Müllen, J. P. Rabe, *J. Am. Chem. Soc.* **2002**, 124, 9454.

[37] P. Samori, M. Keil, R. Friedlein, J. Birgerson, M. Watson, K. Müllen, W. R. Salaneck, J. P. Rabe, *J. Phys. Chem. B*, **2001**, 105, 11114.

[38] R. Friedlein, X. Crispin, C. D. Simpson, M. D. Watson, F. Jackel, W. Osikowicz, S. Marciniak, M. P. de Jong, P. Samori, S. K. M. Jonsson, M. Fahlman, K. Müllen, J. P. Rabe, W. R. Salaneck, *Phys. Rev. B*, **2003**, 68, 195414.

2 Objectives

1. **Quantification of natural and synthetic PAH mixtures via MALDI-MS**: This study investigates the desorption/ionization characteristics of soluble and insoluble large PAHs by using the solvent-free technique for the sample preparation with the aim to propose a strategy for a reliable quantification by MALDI of intractable PAH mixtures, which cannot be characterized via traditional analytical techniques.

    - The investigation of the desorption/ionization of PAHs is at first carried out on model mixtures of synthetic PAHs. HBC carrying alkyl chains of different length are synthesized and blended together for studying the role of the intermolecular interactions on their desorption and ionization efficiencies.
    - Then, the desorption/ionization behavior of molecules possessing different aromatic structures, such as HBC and its dendritic precursor in the cyclodehydrogenation reaction, are investigated.
    - A strategy is finally proposed for the quantitative characterization of synthetic PAH mixtures.
    - Moreover, extending the information acquired via studying model mixtures made of synthetic PAHs, solvent-free quantitative MALDI analyses are applied even to more complex carbon-rich systems, such as mesophasic pitch samples, which are produced by the thermal polymerization of an aromatic oil feedstock and can serve as precursors for advanced carbon materials.

2. **Soft-landing mass spectrometry**: The unique purification conditions offered by soft-landing MS are used for depositing mass-defined polyethylenoxide (PEO) chains on a gold surface. The morphology of PEO chains in the soft-landed films is analyzed by means of AFM. Moreover, the processes involved in a soft-landing deposition are studied via performing soft-landing experiments on rod-like, polar molecules. In particular, this study investigates the influence of the strong electrical field (~ 8 kV/cm), required in a soft-landing deposition for the collection of intact molecules, on the final packing of the molecules in a soft-landed film.

3. **Electrical field orientation**: the electrical field influence on the packing of molecules, bearing a large π-system, is investigated via soft-landing-independent experiments:

    - The packing of symmetrically and not symmetrically substituted HBCs in drop-cast films, prepared in presence of an electrical field, is studied by means of morphology (AFM, STM), optical and diffraction (electron and X-ray) analyses.
    - Alignment experiments are then performed on rod-like polymers and small molecules, which are suitable candidates for novel electronics. The electronic performances of OFET made thereof are measured and compared to the ones of reference films prepared in absence of an electrical field.

In summary, this study has the aim to gain deeper insight and to clarify the basic principles, which regulate the desorption/ionization of giant macromolecules and their "soft-deposition" on a surface moving from MALDI-TOF mass spectrometry to soft-landing for electronics.

3 Desorption / ionization characteristics of polycyclic aromatic hydrocarbons in MALDI-TOF and laser desorption mass spectrometry

3.1 Introduction

Matrix assisted laser desorption ionization mass spectrometry (MALDI-MS) is a powerful tool for the qualitative characterization of giant molecules, biopolymers and synthetic polymers [39-40-41]. However, quantitative investigations, requiring the evaluation of signal intensities of mixture components, are still not applicable in most cases due to the complex mechanism, on which the technique is based. In fact, a great number of parameters, such as the instrumental settings, different desorption and ionization probabilities of the analytes, matrix influence, cluster formation and intermolecular interactions in the solid state play a role in the desorption/ionization process [42]. Furthermore, the success of the MALDI analysis is strongly affected by the sample preparation.

Currently, two general sample preparation techniques are used: the solvent-based and the solvent-free method [43-20]. In the traditional solvent-based sample preparation, the solvent has the role of homogenizing the matrix and analyte in order to allow the desorption/ionization of intact giant molecules. On the contrary, the solvent-free sample preparation represents the only opportunity to assess the structures and purity of slightly soluble or insoluble samples. In the solvent-free preparation method, the three-component system sample-matrix-solvent is reduced to a two-component system, with the advantage of macroscopically homogeneous analyte mixtures with high shot-to-shot reproducibility.

The absence of a solvent avoids homogenization problems during solvent evaporation, caused by crystallization effects. Furthermore, this sample preparation is faster and less operator-dependent [44]. The high shot-to-shot reproducibility of this technique, resulting in equal signal intensities of all mixture components independent of the sample position, is a prerequisite for a deeper understanding of the basic principles of the matrix assisted desorption/ionization process. In this work, the solvent-free method was thus employed for analyzing the desorption/ionization characteristics of polycyclic aromatic hydrocarbons (PAHs). This class of molecules is characterized by the presence of extended aromatic π systems, which confer those promising electronic properties for novel organic electronic devices [45-46]. Due to their structures, PAHs absorb strongly at 337 nm, the wavelength of the nitrogen laser, and possess a different ionization mechanism in comparison to molecules, which do not

absorb the laser light. Non-absorbing molecules at 337 nm are commonly ionized by cation attachment with alkaline cations or hydrogen. Their desorption/ionization process is therefore complicated by additional parameters such as nature and concentration of the added cationizing salt and the different cation affinities of all mixture components. On the other hand, PAHs are photoionized after absorption of laser light and desorb as radical cations [47]. Thus, they show single signals in the MALDI spectra related to the radical cations of PAHs ($PAHs^{\cdot+}$). Because of their structure, they represent suitable models for complex natural systems such as asphaltenes, pitch and heavy oil [48-49-50]. It is therefore interesting to clarify the mechanism regulating their desorption/photoionization process.

In this work, we studied the influence of the intermolecular interactions between PAHs on their desorption efficiency via analyses of equimolar mixtures of hexabenzocoronenes (HBCs), composed of the parent HBC [51] and three alkylated ones with increasing side chain lengths: hexamethyl-hexabenzocoronene (HBC-C_1), hexapropyl-hexabenzocoronene (HBC-C_3) and hexakis(dodecyl)hexabenzocoronene (HBC-C_{12}) (mixture 1, **Figure 8**). The mixture components were chosen such that they possess not only the same ionization mechanism, but also virtually the same ionization efficiency. Since the relative signal intensity of a mixture component in a mass spectrum is composed of the ionization and the desorption efficiency, our model system, consisting of molecules with comparable ionization efficiencies simplifies the interpretation. Thus, differences in signal intensities of our model mixture can be directly correlated to differences in the desorption efficiency. For the sake of simplicity, the correlation between the physico-chemical properties of PAHs and their desorption behavior was studied via analyses of three representative equimolar binary mixtures: HBC/HBC-C_1 (mixture 2), HBC/HBC-C_8 (mixture 3) and HBC/HBC-C_{12} (mixture 4).

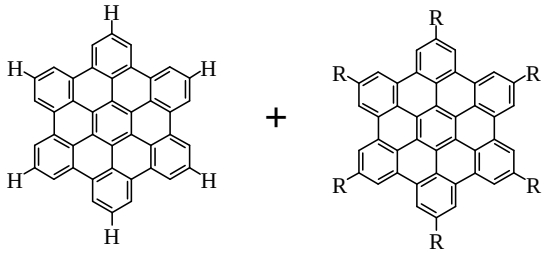

HBC HBC-Cn

mixture 1: quaternary mixture
HBC (R_1= H) + HBC-C_1 (R_2 = CH_3) + HBC-C_3 (R_3 = C_3H_7) + HBC-C_{12} (R_4 = $C_{12}H_{25}$)

mixture 2: binary mixture
HBC (R_1 = H) + HBC-C_1 (R_2 = CH_3)

mixture 3: binary mixture
HBC (R_3 = H) + HBC-C_8 (R_2 = C_8H_{17})

mixture 4: binary mixture
HBC (R_4 = H) + HBC-C_{12} (R_2 = $C_{12}H_{25}$)

Figure 8. Structures of the analytes composing the bends 1, 2, 3, 4.

To study the matrix influence on the desorption-photionization behavior of HBC, the analyses were conducted by using two different matrices, 7,7,8,8-tetracyanoquinodimethane and trans-2-[3-(4-tert-butylphenyl)-2-methyl-2-propenylidene]malononitrile (TCNQ and DCTB, structure in **Figure 9**) [20] and also by laser desorption.

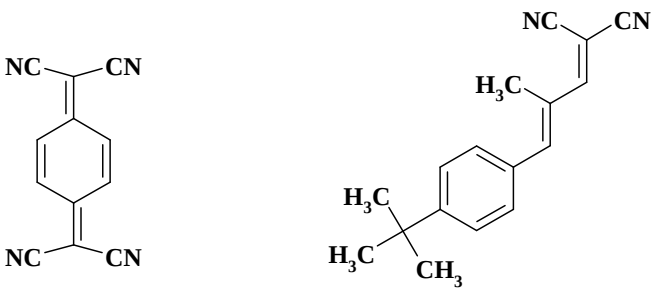

TCNQ **DCTB**

Figure 9. Structure of TCNQ and DCTB.

Moreover, in order to define the influence of the aromatic structure of PAHs on the MALDI response, an equimolar mixture of HBC-C_{12}/

hexakis(dodecyl)hexaphenylbenzene [52] (mixture 5) as well as a bigger PAH containing 222 carbon atoms ($C_{222}H_{42}$) and its dendritic precursor ($C_{222}H_{150}$)[53] (mixture 6) were studied (**Figure 10**).

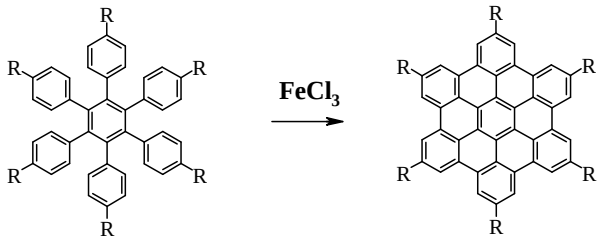

HPB-C_{12} HBC-C_{12}

mixture 5: binary mixture
HPB-C_{12} (R = $C_{12}H_{25}$) + HBC-C_{12} (R-$C_{12}H_{25}$)

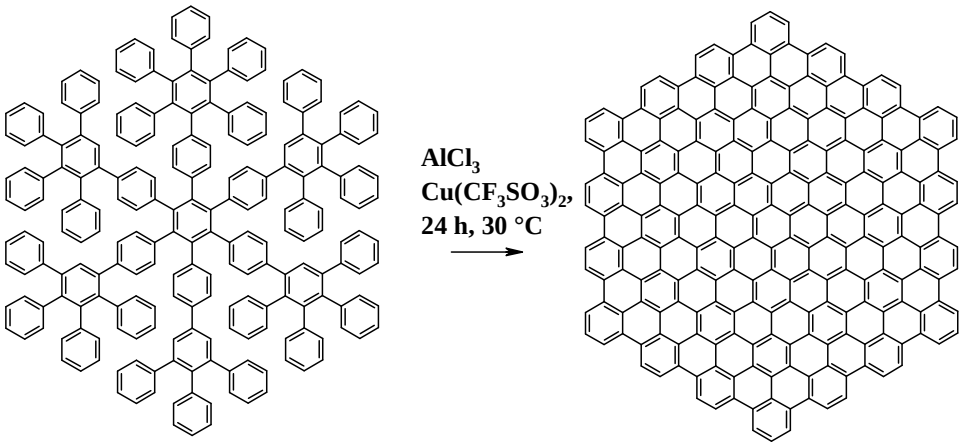

$C_{222}H_{150}$ $C_{222}H_{42}$

mixture 6: binary mixture
$C_{222}H_{150}$ + $C_{222}H_{42}$

Figure 10. Structures of the analytes composing the bends 5 and 6.

3.2 Desorption/photoionization behavior of PAHs

3.2.1 Multicomponent HBC mixtures

The MALDI spectrum of an equimolar multicomponent mixture made of HBCs with linear alkyl chains of different length (HBC-C_1, HBC-C_3, HBC-C_{12}) and the non substituted HBC (mixture 1, **Figure 8**) in TCNQ as matrix is presented in **Figure 11 a** (**set 1**). For the series of alkylated HBCs (ions at m/z 606.5 (B), 775.2

(C), 1532.6 (D)), the signal intensity decreases with increasing alkyl chain length, whereas the ion at m/z 521.9 (A) for the non-alkylated HBC is of anomalously low intensity. We assume that this phenomenon is related to the different strength of the intermolecular interactions between the aromatic cores of the HBC molecules. Molecules with stronger intermolecular interactions should require more energy to be transferred into the gas phase. When the same laser intensity is employed to photoionize and desorb the analytes, weakly aggregated molecules should reach easier the gas-phase. Thus, their signal in the resulting MALDI spectrum should possess higher intensity than that of other species.

It is known that the disc shaped HBC molecules have a strong tendency to aggregate and to form columnar structures with a close face-to-face arrangement. The interaction among unsubstituted HBC molecules, however, is stronger than the interaction among the alkyl substituted HBCs, because of the increased steric hindrance caused by the alkyl chains. In fact, as shown by previous X-ray investigations [15-54], the intermolecular distance between unsubstituted HBC discs is 0.342 nm whereas the distance for HBC-C_{12} is 0.350 nm. This causes the weakening of the π–π interactions among the molecules, which translates in the MALDI spectrum of **Figure 11 a** in a preferential desorption of alkylated HBCs with respect to the unsubstituted ones. Since the intermolecular distance among the aromatic cores is mainly influenced by the steric hindrance of the first alkyl chain segment attached directly to the aromatic core, there is only a minor steric influence of the alkyl chain length. This indeed explains qualitatively the big intensity jump between substituted and unsubstituted HBCs; however, it does not yet explain the relatively high intensity drop in the row of HBCs with increasing chain length, not expected for such narrow distributions. Hence, we attribute the decrease in signal intensity of substituted HBC molecules with increasing alkyl chain length to the sum of two factors: i) intensity loss with increasing mass and ii) the increase in solid state interaction energy of the alkyl chains with increasing chain length. This theory is supported by diffraction patterns of alkylated HBCs showing a halo for the amorphous packing of the alkyl chains at the disc periphery [52]. The combination of both factors requires additional energy for the desorption of the alkyl substituted molecules with increasing chain length, which results in an anomalous high reduction of relative signal intensities with increasing molecular weight.

As the desorption/photoionization behavior of HBCs could also be affected by the nature of the MALDI matrix, the analyses of the same analyte mixture was also carried out by using DCTB as the matrix (**set 2**, **Figure 11 b**).

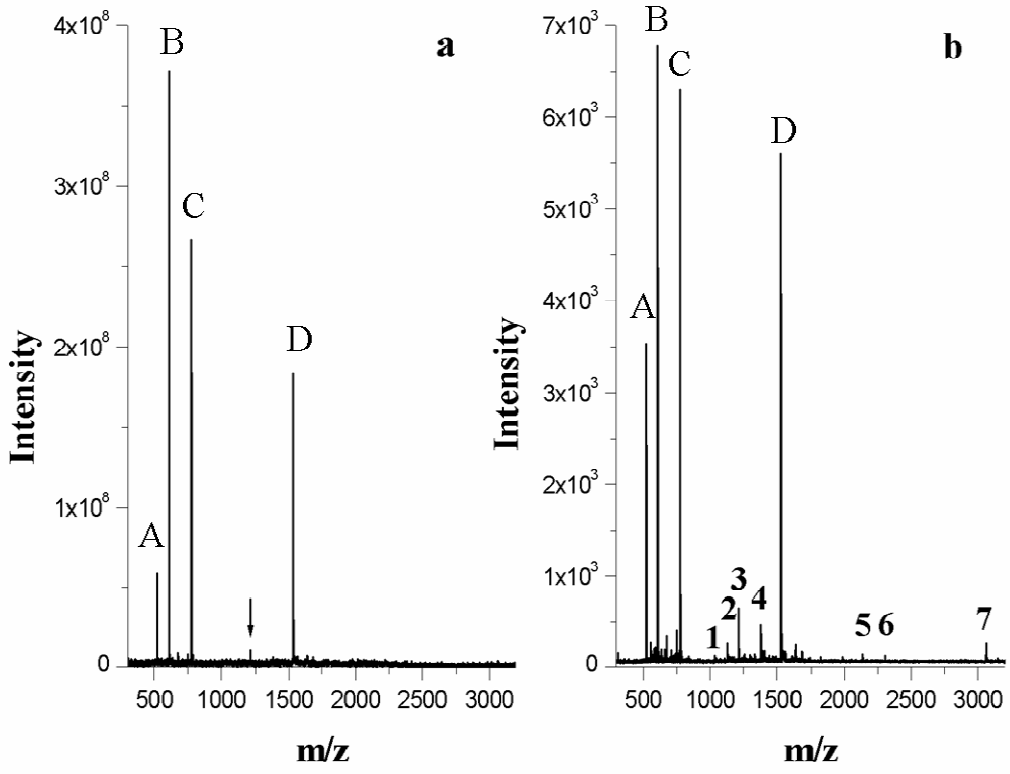

Figure 11. **a) MALDI spectrum of an equimolar mixture of HBC, HBC-C_1, HBC-C_3, HBC-C_{12} molecules in TCNQ matrix (set 1). b) MALDI spectrum of equimolar mixture of HBCs in DCTB matrix (set 2).**

As **Figure 11 b** displays, the HBCs qualitatively maintained the same desorption/photoionization tendency in the DCTB matrix. The unsubstituted HBC molecules show again the lowest signal intensity compared to the alkylated ones; however, the differences are less pronounced. We suggest that the variation in relative signal intensities of the HBC molecules going from TCNQ to DCTB (molecular structures in **Figure 9**) could be influenced by the following factors: i) appearance of additional signals in the MALDI spectrum of **Figure 11 b**; ii) the non-planar structure of the DCTB matrix molecules.

i) The additional signals appearing in **Figure 11 b** could be assigned to stable HBC clusters with the compositions presented in **Table 1**.

Table 1. Composition of the clusters formed by HBC molecules.

Cluster	Ion detected (m/z)	Composition
1	1044.4	$(HBC)_2^{\cdot+}$ low signal intensity
2	1128.2	$(HBC/HBC\text{-}C_1)^{\cdot+}$
3	1213.2	$(HBC\text{-}C_1)_2^{\cdot+}$
4	1381.7	$(HBC\text{-}C_1/HBC\text{-}C_3)^{\cdot+}$
5	2138.3	$(HBC\text{-}C_1/HBC\text{-}C_{12})^{\cdot+}$ low signal intensity
6	2307.1	$(HBC\text{-}C_3/HBC\text{-}C_{12})^{\cdot+}$ low signal intensity
7	3064.2	$(HBC\text{-}C_{12})_2^{\cdot+}$ low signal intensity

Whereas in TCNQ matrix only dimeric HBC-C_1 species (peak indicated by the black arrow in **Figure 11 a**) were observed, mixed aggregates involving HBC-C_1 and other HBC molecules were found with DCTB as matrix. The high clustering tendency of HBC-C_1 molecules in DCTB relates qualitatively to the reduction in signal intensity of their peak at m/z 606.5.

The notable cluster presence in the gas phase is explainable by two phenomena: i) cluster formation during the first step of the desorption/photoionization process, ii) mixed parent/alkyl-HBC aggregates already present in the solid state. The contact between different HBCs in the solid state happens very likely during solvent-free sample preparation and could favour the mixed cluster formation.

The apparent differences in relative signal intensities between the different matrices may come from the different matrix affinities with respect to the analyte molecules.

Contrary to TCNQ molecules, the DCTB molecules possess a non-planar structure (**Figure 9**), which have a different influence on the strong intermolecular aggregations among HBC molecules. It was observed that the use of TCNQ as matrix often leads to a darkening of the HBC-TCNQ powder after the milling procedure for solvent-free preparation. This phenomenon could be related to the formation of charge-transfer complexes consisting of the electron donor HBC and the strong electron acceptor TCNQ, which is not observable by employing DCTB as the matrix.

The different interactions between HBC discs and the non-planar DCTB molecules could justify the matrix effect on the desorption/photoionization behaviour of the HBC series.

3.2.2 7,7,8,8-tetracyanoquinodimethane (TCNQ) -HBC interactions

For a deeper understanding of the nature of the interactions between TCNQ and HBC molecules, the influence of TCNQ on the self-assembly of HBC-C_{12} was studied. For the sake of simplicity and to permit the characterization of the resulting blends via diffraction, morphological and absorption analyses, HBC-C_{12} and TCNQ molecules were dissolved in THF in equimolar amount. Thus, the HBC-C_{12}/TCNQ interactions were analyzed by studying dry films prepared via drop-casting the solution of the analyte on glass surfaces and slow evaporation in an atmosphere saturated with vapour of solvent.

It is worth noting that the mixing of two molecules that self-assemble into superstructures is complex, since additional interactions between the different components complicate the description of the system [55-56]. As illustrated in **Figure 12**, several different supramolecular assemblies can be formed in the mixture, which range from a heterogeneous phase to micro- and even nanoseparation.

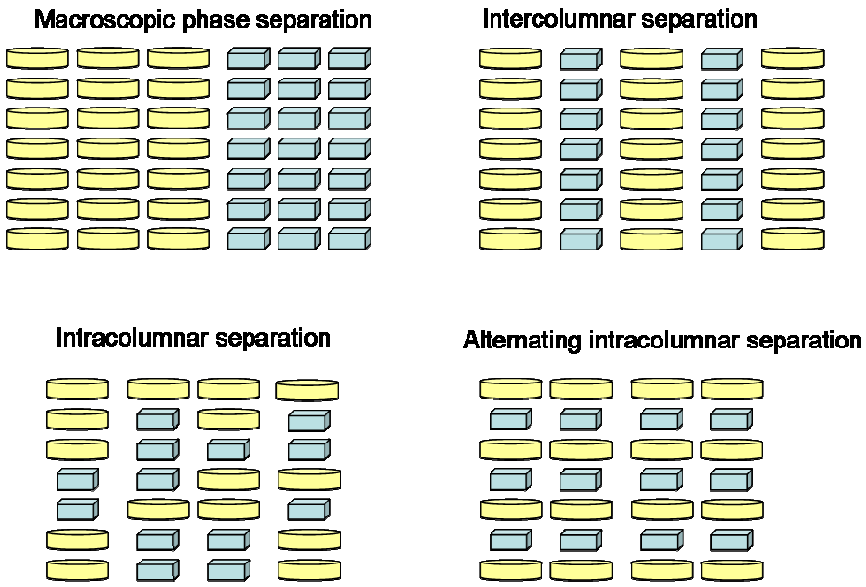

Figure 12. Different possible supramolecular organizations in a mixture of two compounds with different molecular architectures.

Previous investigations have shown that when TCNQ is blended with electron-rich molecules, such as coronene, alternating stacks of the acceptor and donor molecules are formed, leading to an enhanced columnar stability [57]. The coronene molecule is sandwiched between two TCNQ molecules and the structure is stabilized by the formation of a charge transfer complex. To verify if this is the most favorable packing for HBC-C_{12}/TCNQ blends too, electron and X-ray diffraction analyses were performed. Additionally, the film morphology was investigated via transmission electron microscopy. Furthermore, the properties of the electron-donor acceptor mixture in solution were studied via UV-vis spectroscopy.

3.2.2.1 Transmission electron microscopy

The transmission electron micrographs in **Figure 13** show the surface of films obtained by blending HBC-C_{12} and TCNQ molecules in equimolar ratio. It can be observed that the HBC-C_{12} donor and TCNQ acceptor molecules do not form a continuous film, but create supramolecular fibers, which possess an internal helical structure, as it can be recognized by a closer analysis of the TEM micrograph of **Figure 13**. The helices have an average width of 200 nm and are several µm in length.

HBC-C_{12} molecules are known to self-assemble into supermolecular fibre-like structures [58], however the formation of helical architectures has never been observed.

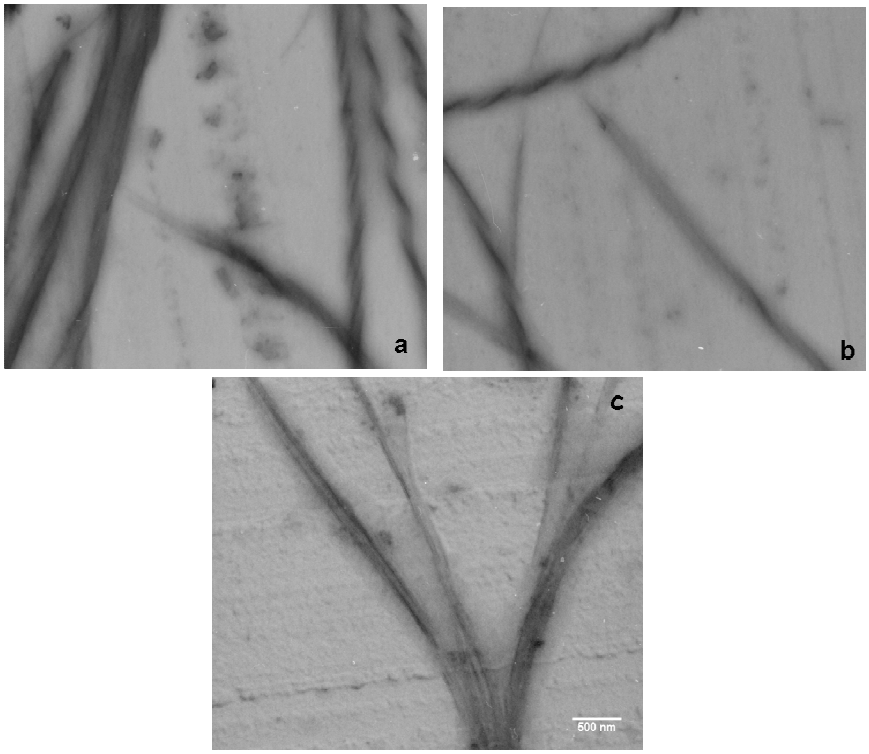

Figure 13. Elastic TEM micrographs of the surface of a film prepared by drop-casting a solution of HBC-C_{12}/TCNQ mixture in a 1/1 molar ratio.

In literature, the self-assembly into helix superstructures has been reported for a variety of different molecules such as helicates [59], phthalocyanine derivatives [60] and recently for discotic molecules [61]. In all these cases, this phenomenon seems to be driven by different noncovalent interactions such as hydrogen bonds and aromatic π interactions between low molecular weight species. In this work, the driving force for building a helix structure might be found in the strong donor-acceptor interactions among HBC-C_{12} and TCNQ molecules. To support this hypothesis, the molecular packing of the molecules creating the helix structures was studied via electron diffraction analyses.

Figure 14 b displays the electron diffraction micrograph of a HBC-C_{12}/TCNQ mixture with a molar ratio of 1-1. For comparison an electron diffraction micrograph of pure TCNQ molecules is reported in **Figure 14 a** as well.

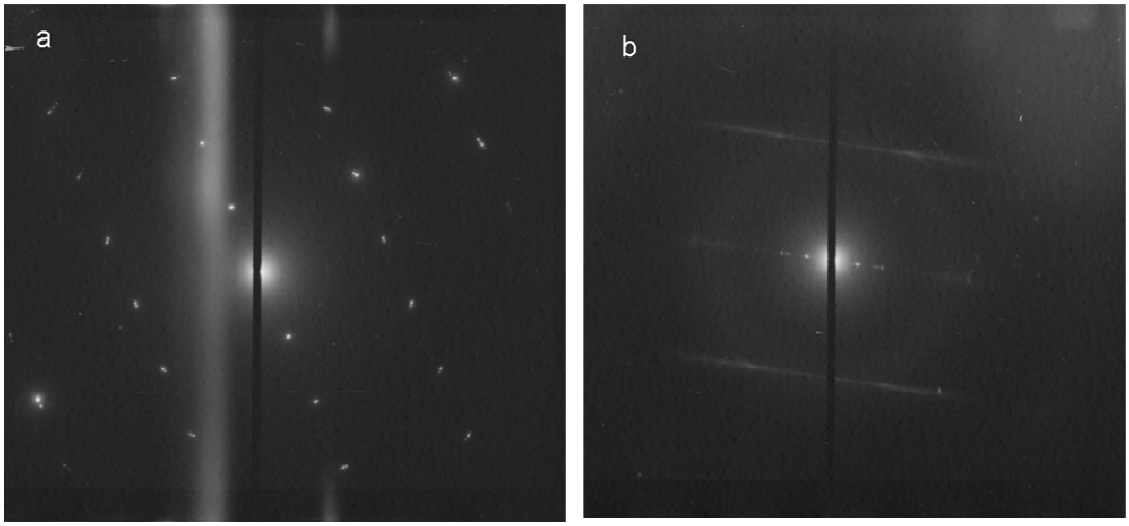

Figure 14. a) Electron diffraction micrograph of a crystalline TCNQ film b) electron diffraction micrograph of HBC-C12/TCNQ mixture in a 1/1 molar ratio.

Figure 14 b shows a fiber-like diffractogram, in which two sets of reflections can be recognized. At the equator a sequence of reflections at positions 1, √3, 2 and √7 are observed, which are characteristic for the hexagonal columnar packing [62]. The meridian reflections, which are related to the intermolecular distance within a column, correspond to a d-value of 0.478 nm. As already observed for the zone-cast HBC-C_{12} films [63], this might be justified by molecules tilted with respect to the column axis. However, considering a π–π distance between the HBC-C_{12} cores molecules of 0.350 nm [62], the tilt-angle can be calculated to be 43 °, which slightly differs from the value reported in literature (45°). Additionally, the meridional reflections in **Figure 14 b**, do not form arcs, but appear as straight lines. This phenomenon is caused by molecular stacks, which are axially shifted (not in register, see **Figure 15 b**), and is probably due to the influence of TCNQ molecules on the HBC-C_{12} packing.

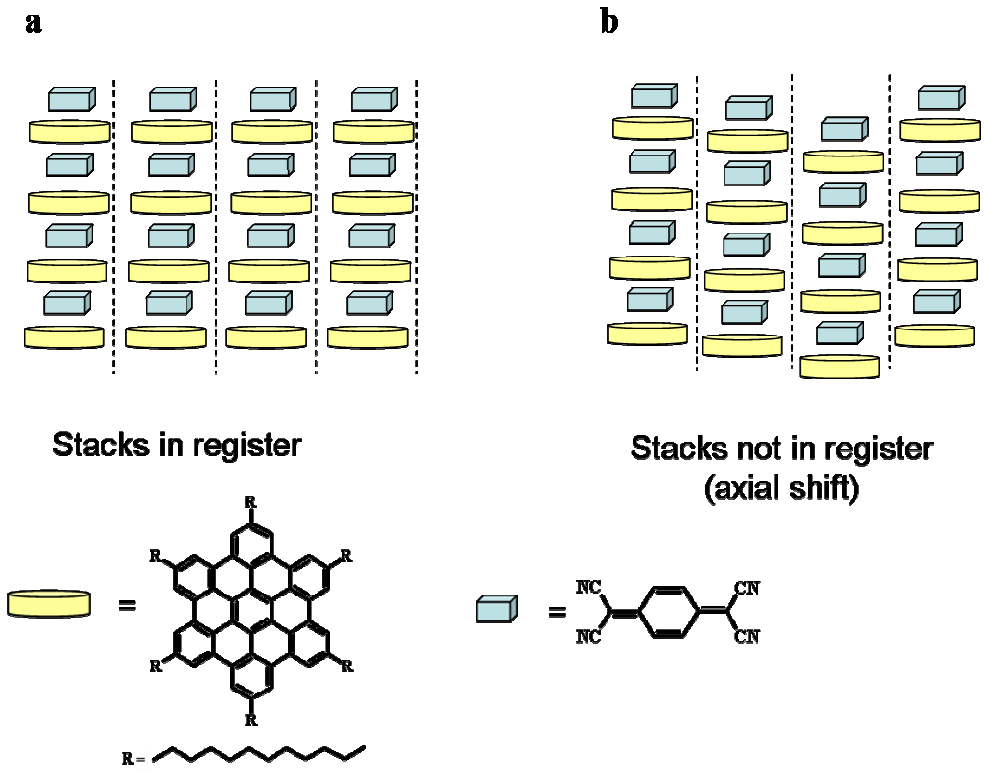

Figure 15. Proposed arrangements of the stacks and molecular structures of the analytes.

The diffractogram presented in **Figure 14 b** can be explained by considering columnar structures made of HBC-C_{12} intercalated by TCNQ molecules similar to the charge transfer complexes reported in literature for coronene/TCNQ blends [57] (alternating intracolumnar separation, see **Figure 12**). In that work the π–π distance between TCNQ and coronene was observed to be 0.30 nm on average. Considering the same π–π stacking for HBC-C_{12}/TCNQ blend, it is possible to calculate a tilt angle of the molecules with respect to the columnar axis of 46°. A non-regular intracolumnar separation has however to be considered as well. In fact, the non-regular intercalation of TCNQ molecules between the HBC-C_{12} cores would not give reflections. Thus, it cannot be observed, but it cannot be ruled out either.

On the drop-cast films of HBC-C_{12}/TCNQ aggregates, no sites were found with reflections coming from either crystals of HBC-C_{12} columns or isolated TCNQ crystals. Therefore, macroscopic phase segregation phenomena of TCNQ and HBC-C_{12} molecules can be excluded.

These observations suggest the intracolumnar separation, schematized in **Figure 12**, as the most plausible structure for HBC-C_{12}/TCNQ complexes.

3.2.2.2 UV-vis spectroscopy study

To fully clarify the nature of the complex obtained by blending HBC-C_{12} and TCNQ molecules in molar ratio 1-1, their THF solutions were studied via UV-vis spectroscopy. In **Figure 16** the solutions of TCNQ, HBC-C_{12} and the 1-1 HBC-C_{12}/TCNQ molar mixture in THF, respectively, are shown. The darkening of the solution, obtained by blending HBC-C_{12} and TCNQ molecules can be related to the formation of charge transfer complexes.

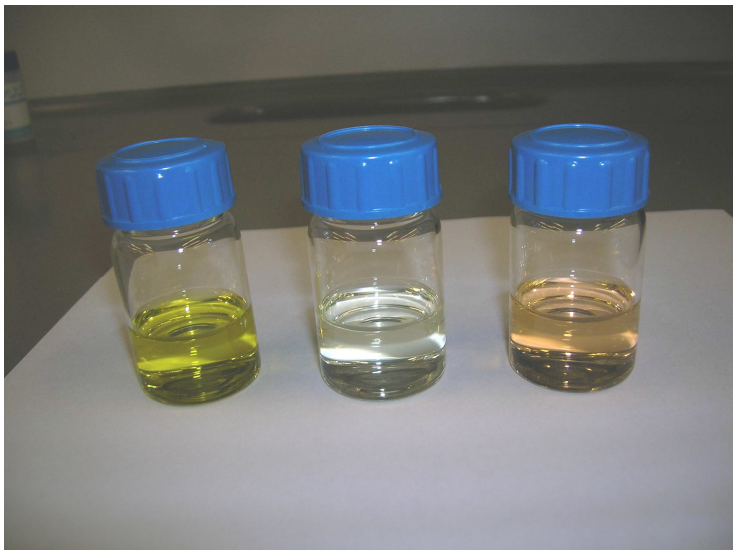

Figure 16. Solutions of TCNQ (left), HBC-C_{12} (center) and the 1-1 HBC-C_{12}/TCNQ mixture (right) in THF.

Figure 17 reports the absorption spectra of HBC-C_{12} molecules in THF (green trace), of TCNQ molecules (black trace) and of the equimolar mixture HBC-C_{12}/TCNQ (red trace).

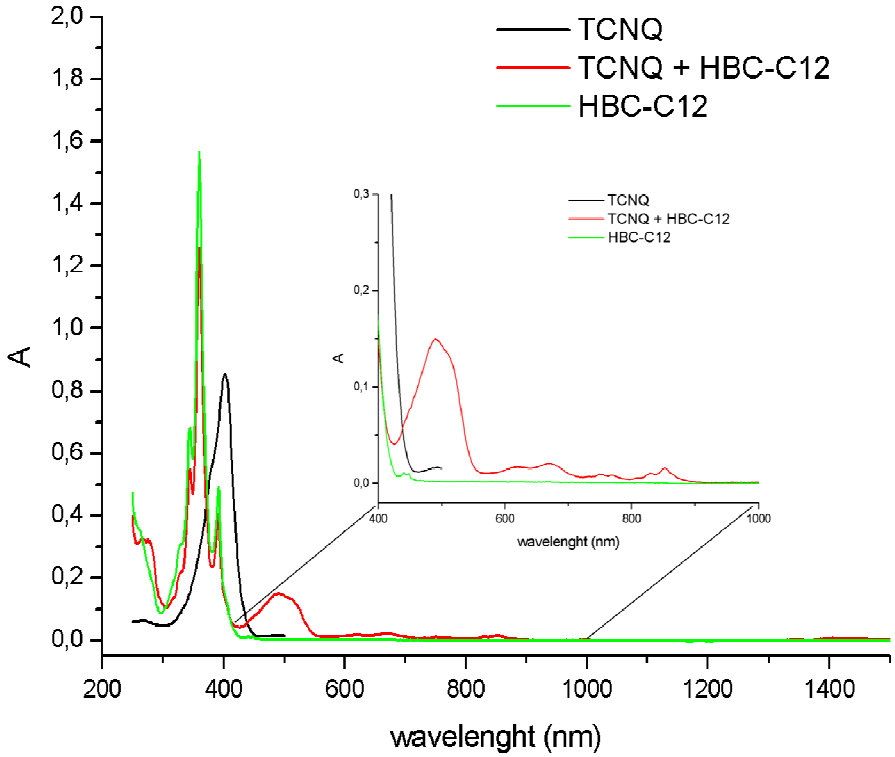

Figure 17. UV-vis absorption spectrum of a solution of TCNQ molecules in THF (black trace), HBC-C_{12} molecules (green trace) and TCNQ/HBC-C_{12} molecules in 1-1 ratio (red trace).

In the UV-vis spectrum of the mixture TCNQ-HBC-C_{12}, the absorption peak of the TCNQ molecules is not present; on the contrary, together with the absorption bands of HBC-C_{12} molecules new absorption bands appear. These additional bands, which are better visualized in the zoom-in inset of **Figure 17**, are due to presence of $TCNQ^-$ species in solution [64]. This suggests that charge transfer complexes between HBC-C_{12} and TCNQ molecules are formed in solution and likely are trapped in place during solvent evaporation with the formation of supramolecular helix architectures as a result.

3.2.2.3 Formation of charge transfer complexes during solvent free-sample preparation

An attempt of transferring the information obtained by the previous study to the interactions between HBC-C_{12} and TCNQ molecules during sample preparation for MALDI analyses is complicated by two factors:

1) The high matrix to analyte ratio, necessary for a soft desorption/photoionization of the analyte;

2) The preparation procedure, which does not require the use of a solvent and is based on the mechanical mixing of the analyte with a matrix.

The analyses conducted on the model system are however helpful to understand why TCNQ matrix promotes the formation of radical cations and how it interacts with the HBC electron-rich analyte molecules. It is interesting to point out that even in TCNQ/HBC-C_{12} blends with a molar ratio of 1-1, obtained from solution, the charge transfer complexes among the components are of the type ABABA. The intercalation of TCNQ molecules between the HBC-C_{12} cores can therefore justify the reduced cluster tendency of the HBC molecules in a MALDI analysis performed with TCNQ as a matrix when compared to that with DCTB. However, even for equimolar TCNQ/HBC blends, prepared by drop-casting, the formation of stacks with non regular intracolumnar separation cannot be ruled out. The formation of structures of this type is even more likely when blends are produced by mechanical mixing of the analyte, such as during the solvent-free preparation procedure for MALDI analyses. The absence of a solvent, in fact, does not allow blending of analyte and matrix at a molecular level. Nevertheless, the formation of charge transfer complex occurs, as the darkening of the powder after the mechanical mixing indicates.

Since the mixtures obtained via solvent free-sample preparation are not homogeneous at a molecular level, the presence of relatively large columnar stacks of HBC-C_{12} molecules intercalated by TCNQ molecules cannot be excluded. Thus, the intermolecular interactions between the flat aromatic cores of the HBC-C_{12} molecules, which are responsible for their spontaneous assembly into columnar superstructures, should influence the desorption/photoionization behavior of the discotic molecules. In order to valorize this hypothesis the desorption-photoionization of binary mixture of substituted and unsubstitued HBC molecules was investigated. The choice to restrict the attention to binary HBC blends was taken to minimize the mutual influence of the different substituted HBCs on their desoption/photoionization behavior, previously observed in **Figure 11**.

3.2.3 Analyses of binary HBC mixtures

Figure 18 a, **b** and **c** show MALDI spectra of the binary mixtures 2, 3 and 4, respectively, prepared by the solvent-free sample preparation method.

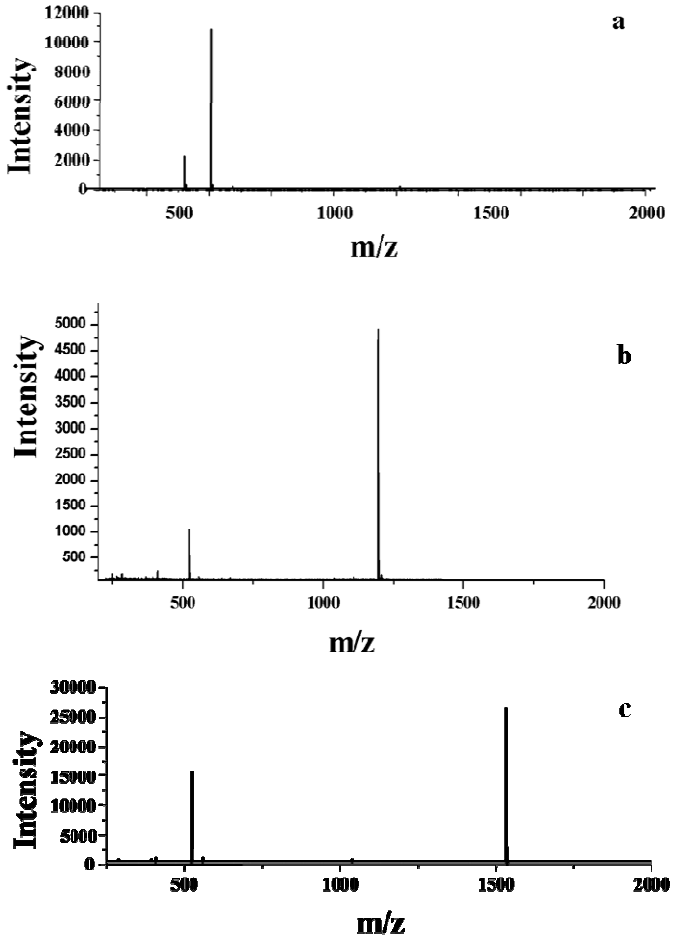

Figure 18. a) MALDI spectrum of HBC and HBC-C_1 molecules in an equimolar mixture b) MALDI spectrum of HBC and HBC-C_8 molecules in an equimolar mixture c) MALDI spectrum of HBC and HBC-C_{12} molecules in an equimolar mixture.

The spectra show only peaks corresponding to the radical cations of the HBCs in **Figure 18 a** (ions at m/z 522.1 for HBC and 606.8 for HBC-C_1), in **Figure 18 b** (ions at m/z 522.3 for HBC and 1195.6 for HBC-C_8) and in **Figure 18 c** (ions at m/z 522.2 for HBC and 1532.3 for HBC-C_{12}). No traces of adducts with protons or alkal cations were visible. A notable difference in signal intensity between the peaks of the substituted and the non substituted species is evident in all three spectra, again with the unusual behavior that the respective high mass component is overestimated.

Comparable trend was additionally observed for other HBC/substituted HBC mixtures (HBC/HBC-C_6, HBC/HBC-C_{14}), too. As the photoionization efficiency is related to the absorption of the analyte molecules at 337 nm [65], we can assume that the unsubstituted as well as the alkylated HBC molecules have comparable ionization efficiencies. They possess the same aromatic core and absorb at the laser wavelength with virtually the same adsorption coefficient (**Figure 19**).

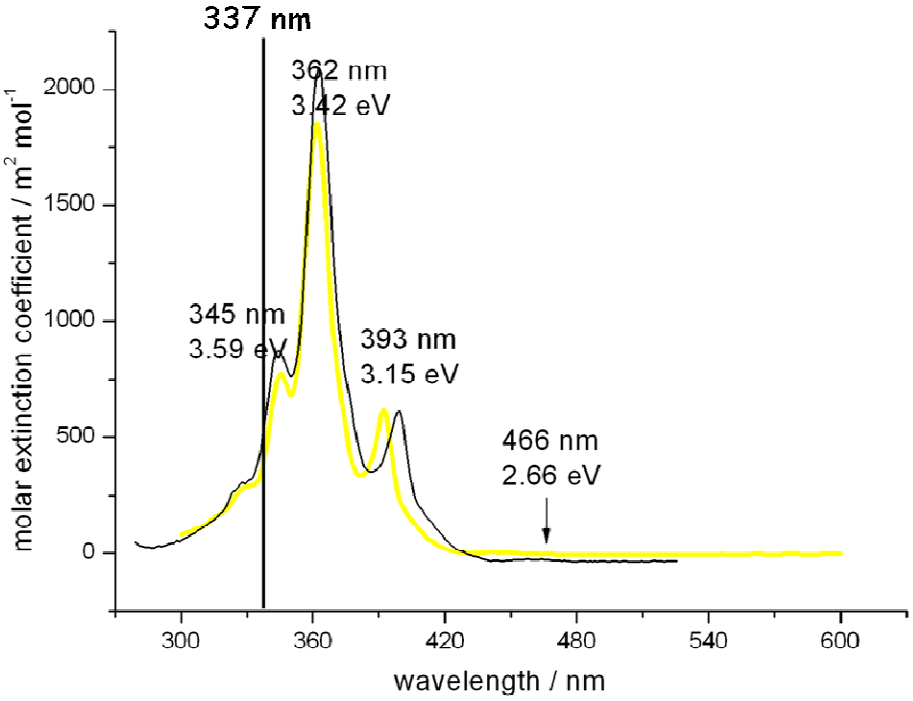

Figure 19. UV-vis spectra of HBC (yellow trace) and HBC-C_{12} (black trace) in 1,2,4 trichlorobenzene

However, as shown by Friedlein et al. [66], the ionization potential of HBC molecules (6.0 eV) can be slightly reduced by the presence of alkyl chains at the HBC periphery (5.5 eV for HBC-$C_{8,2}$). This phenomenon, which facilitates the formation of radical cations for substituted HBCs, probably contributes also to the higher signal intensity of alkylated HBCs in **Figure 18**. Furthermore, as already mentioned, the different strength of the π–π interactions between unsubstituted and alkylated HBCs should also be responsible for the change in the desorption efficiency. From NMR measurements of HBCs in solution, it is known that their association constants drop off with increasing size of the substituents attached to the aromatic core [15, 67-68-69].

Assigning this to the solid state, it can be argued that the more weakly associated alkyl-HBC molecules desorb more easily than the more strongly associated HBC molecules under the same experimental conditions.

3.2.4 Laser desorption of HBCs

To analyze the desorption/photoionization characteristics of HBCs without the matrix support, laser desorption analyses were also performed. **Figure 20 a** shows a laser desorption spectrum of the unsubstituted HBC molecules.

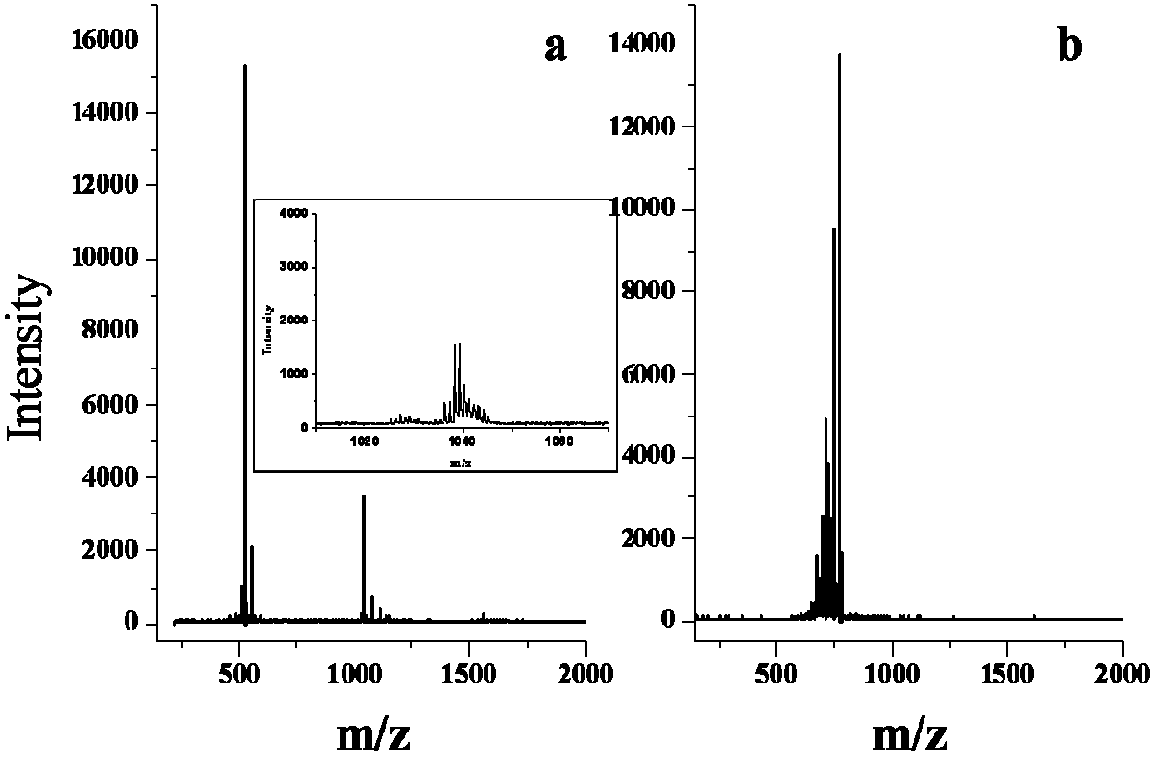

Figure 20. a) Laser desoprtion spectrum of unsubstituted HBC molecules with magnified region between m/z 1000-1100. b) Laser desorption spectrum of HBC-C_3 molecules.

As opposed to MALDI, the direct absorption of laser light causes laser-induced fragments and reactions between the analyte molecules. For HBC, four different reaction products can be observed, which are rationalized by the structures shown in **Figure 21 a-f**.

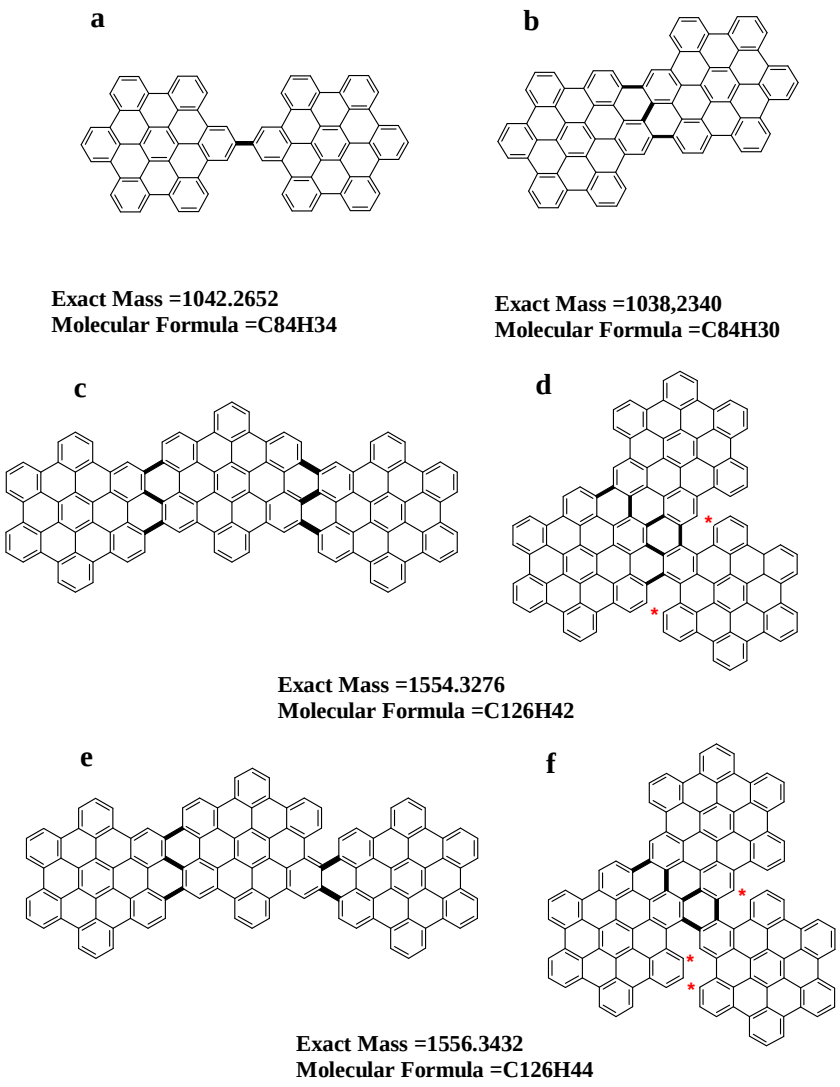

Figure 21. Proposed structures of laser-induced reaction products from HBC molecules. The new covalent C-C bonds are pointed out in bold.

If three C-H bonds were broken and new C-C bonds were formed in each HBC molecule, dimers (two HBCs minus six hydrogen atoms) with a molar mass of m/z 1039.1 were formed. On the other hand, the loss of two H atoms leads to the formation of dimers at m/z 1043.5. Furthermore, by reaction among three HBCs, two different trimers were produced with masses m/z 1555.5 and m/z 1557.7, respectively. Among all the reported structures for the trimers (see **Figure 21 c-d** and **e-f**), the linear ones are the most plausible. Non-linear structures should in fact further proceed dehydrogenating (the red asterisks in **Figure 21** indicate the reactive centres) and form products at lower masses, which are not present in the LD spectrum of **Figure 20**.

The change in laser desorption behavior of substituted HBC molecules was studied via analysis of HBC-C_3 molecules, representatively. The corresponding LD spectrum (**Figure 20 b**), recorded with the same experimental conditions as used in **Figure 20 a**, shows no reactions among the HBC-C_3 molecules. However, intense fragmentation of the side chains can be induced at higher laser power. Only after almost complete fragmentation of the side chains, oligomerization is observed too. For alkylated HBC, it is likely that the fragmentation reactions required less energy than the polymerization ones, which took place only when the more reactive species caused by fragmentation started reacting.

The laser desorption characteristic of HBCs leads to the conclusion that reliable qualitative and quantitative investigations of PAHs were not feasible by this method, due to the risk of laser induced reactions. The corresponding MALDI measurements, however, avoid fragmentation and laser induced reactions among the analyte molecules completely due to the much softer desorption mechanism in presence of the matrix.

3.2.5 Influence of the UV absorption efficiency on signal intensity

To demonstrate the influence of the aromatic structure of analyte molecules on their desorption/ionization, an equimolar binary mixture of hexakis(dodecyl)hexabenzocoronene (HBC-C_{12}) and its dendritic precursor hexakis(dodecyl)hexaphenylbenzene (HPB-C_{12}) was investigated.

The respective MALDI spectrum is presented in **Figure 22 a**. The peak at m/z 1532.5, corresponding to HBC-C_{12}, is much more intense than that of HPB-C_{12} at m/z 1544.9. This finding is consistent with the large difference of the molar extinction coefficients at 337 nm between the molecules (**Figure 22 b**) [65]. In fact, the more extended aromatic π system of HBC-C_{12} allows significantly higher absorption at the laser light wavelength than HPB-C_{12} with a huge influence on their photoionization efficiency. Therefore, the higher photoionization efficiency of HBC-C_{12} molecules translates into a higher ionization probability. Consequently, the HPB-C_{12} signal at m/z 1544.9 is dwarfed by the HBC-C_{12} signal, even though HPB-C_{12} molecules cannot form columnar aggregates and should hence desorb relatively easily.

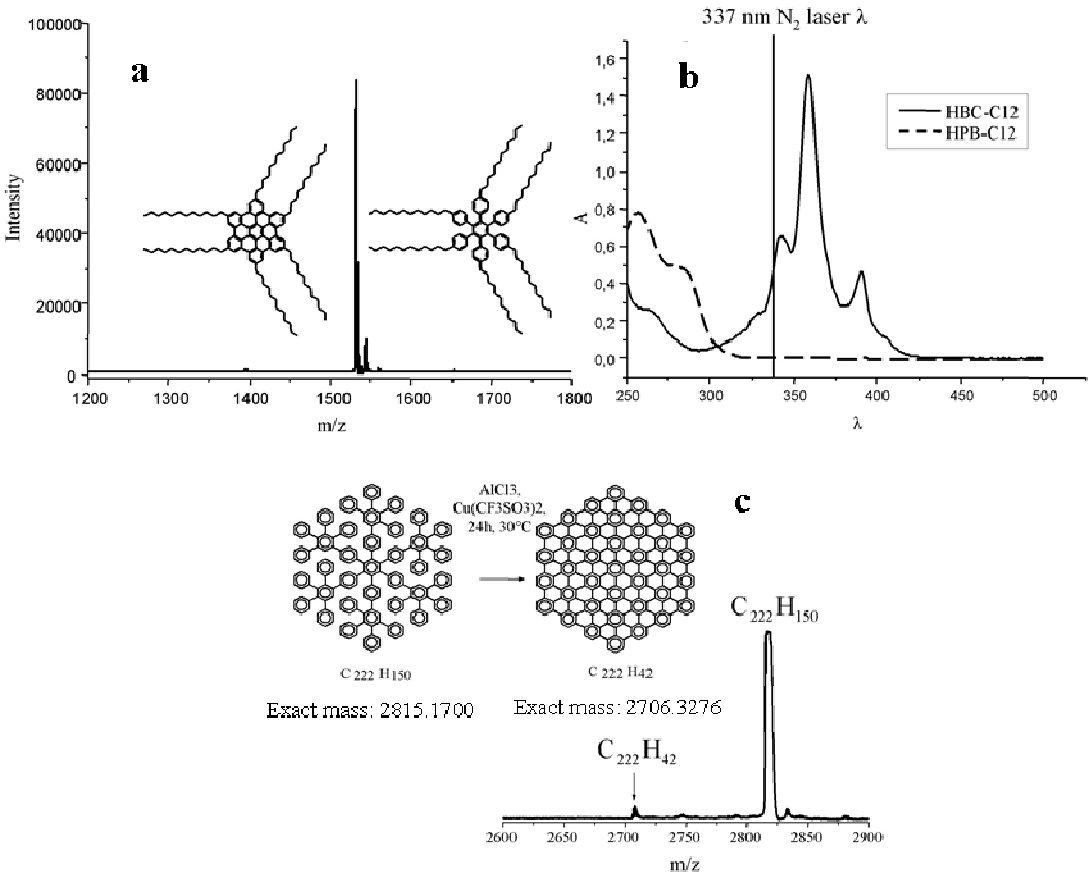

Figure 22. a) MALDI spectrum of an equimolar mixture of HBC-C_{12} and its dehdritic precursor HPB-C_{12} in TCNQ matrix. b) UV-vis spectra of HBC-C_{12} and HPB-C_{12}. c) MALDI spectrum of an equimolar mixture of $C_{222}H_{42}$ and its cyclodehydrogenation precursor $C_{222}H_{150}$, recorded by using TCNQ as matrix.

When both components of a mixture of molecules with different π systems absorb significantly (but not necessarily equally), the issue of the intermolecular interactions again becomes dominant. **Figure 22 c** shows a MALDI spectrum of an equimolar mixture of $C_{222}H_{42}$ and its precursor in the cyclodehydrogenation reaction $C_{222}H_{150}$. Even though the extended π system of $C_{222}H_{42}$ has a high absorption at 337 nm, its signal in the MALDI spectrum is dwarfed by that of the more weakly absorbing $C_{222}H_{150}$. In this case, the signal intensity seems to be dominated by the strong intermolecular interactions of the large planar π systems of $C_{222}H_{42}$. The much weaker interactions in $C_{222}H_{150}$ combined with a significant adsorption at 337 nm [65] and their lower ionization potential due to the extended aromatic system [66] in comparison to HPB-C_{12}, appears to increase the desorption probability.

3.3 Conclusions

Within this investigation we explored the complex desorption/ionization characteristics of PAHs with well defined aromatic hydrocarbon mixtures. The different desorption/ionization probabilities of PAHs in MALDI could be described by two general properties: 1. aggregation tendency, 2. adsorption at 337 nm. A high aggregation tendency leads to a decreased desorption probability. Alkyl chain substiutents at the aromatic core reduce the aggregation tendency nearly independently of chain length. A strong UV absorption at 337 nm yields a high ionization probability. Therefore, both factors have to be considered for the correct evaluation of the MALDI spectra of multicomponent mixtures. The principles of the desorption and ionization behavior of alkylated PAHs should be of interest for other systems, such as heavy oil, pitch or asphaltenes in the analysis either by MALDI or by LD. One must be careful with quantitative information as shown for our model systems. Especially LD measurements can be suspected to be unsuitable for qualitative as well as for quantitative measurements of natural PAH mixtures, since they produced not only fragments, but also numerous reaction products with higher molecular weight, which are often wrongly attributed either to gas phase clusters or to already existing mixture components. A better understanding of PAH chemistry and physics in MALDI and LD mass spectrometry, therefore, should pave the way for more reliable qualitative as well as quantitative measurements.

3.4 References

[39] K. Tanaka, H. Waki, Y. Ido, S. Akita, Y. Yoshida, T. Yoshida, *Rapid. Commun. Mass Spectrom.* **1988**, 2, 151.

[40] D. C. Schriemer, L. Li, *Anal. Chem.* **1996**, 68, 2721.

[41] P. M. Peacock, C. N. McEwen, *Anal. Chem*, **2006**, 78, 3957.

[42] M. Karas, R. Krüger, *Chem. Rev.* **2003**, 103, 427.

[43] S. Trimpin, A. Rouhanipour, R. Az, H. J. Räder, K. Müllen, *Rapid Commun. Mass Spectrom*. **2001**, 15, 1364.

[44] S. Trimpin, S. Keune, H.J. Raeder, K. Müllen, *J. Am. Soc. Mass Spectrom.* **2006**, 17, 661.

[45] L. Schmidt-Mende, A. Fechtenkötter, K. Müllen, E. Moons, R. H. Friend, J.D. MacKenzie, *Science* **2001**, 293, 1119.

[46] W. Pisula, A. Menon, M. Stepputat, I. Lieberwirth, U. Kolb, A. Tracz, H. Sirringhaus, T. Pakula, K. Müllen, *Adv. Mat.* **2005**, 17, 684.

[47] H. J. Räder, J. Spickermann, M. Kreyenschmidt, K. Müllen, *Macromol. Chem. Phys.* **1996**, 197, 3285.

[48] W. F. Edwards, M. C. Thies, *Energy & Fuels* **2005**, 19, 984.

[49] W. F. Edwards, L. Jin, M. C. Thies, *Carbon* **2003**, 41, 2761.

[50] A. R. Hortal, B. Martinez-Haya, M. D. Lobato, J. M. Pedrosa, S. Lago, *J. Mass Spectrom.* **2006**, 41, 960.

[51] M. D. Watson, A. Fechtenkötter, K. Müllen, *Chem. Rev.* **2001**, 101, 1267.

[52] A. Fechtenkötter, K. Saalwächter, M. A. Harbison, K. Müllen, H. W. Spiess, *Angew. Chem*. **1999**, 38, 3039.

[53] C. D. Simpson, J. D. Brand, A. J. Berresheim, L. Przybilla, H. J. Räder, K. Müllen, *Chem.*s *Eur. J.* **2002**, 8, 1424.

[54] R. Goddard, M. W. Haenel, W. C. Herndon, C. Krüger, M. Zander, *J. Am. Chem. Soc.* **1995**, 117, 30.

[55] D. T. Bong, T. D. Clark, J. R. Granja, M. R. Ghadiri, *Angew. Chem., Int. Ed.* **2001**, 40, 988.

[56] V. Percec, C. H. Ahn, G. Ungar, D. J. P. Yeardley, M. Moller, S. S. Sheiko, *Nature* **1998**, 391, 161.

[57] X. Chi, C. Besnard, V. K. Thorsmølle, V. Y. Butko, A. J. Taylor, T. Siegrist, A. P. Ramirez, *Chem. Mater.* **2004,** 16, 5751.

[58] A. Tracz, D. Wostek, I. Kucinska, J. K. Jeszka, M. Watson, K. Mullen, T. Pakula, NATO Science Series, II: Mathematics, Physics and Chemistry, **2002**, 59 (Molecular Low Dimensional and Nanostructured Materials for Advanced Applications), 315.

[59] C. Nuckolls, T. J. Katz, J. Castellanos, *J. Am. Chem. Soc.* **1996**, 118, 3767.

[60] H. Engelkamp, S. Middelbeek, R. J. M. Nolte, *Science* **1999**, *284*, 785.

[61] W. Pisula, Z. Tomovic, M. D. Watson, K. Müllen, J. Kussmann, C. Ochsenfeld, T. Metzroth, J. Gauss, Jo*urnal of Physical Chemistry B* , **2007**, 111, 7481.

[62] S. Ito, M. Wehemeier, D. J. Brand, C. Kübel, R. Epsch, J. P. Rabe, K. Müllen, *Chem. Eur. J.* **2000**, 6, 23, 4327.

[63] J. Piris, W. Pisula, A. Tracz, T. Pakula, K. Müllen, J. M. Warman, Liquid Crystals, 31, 993.

[64] H. T. Jonkman, J. Kommandeur, *Chemical Phisics Letters*, **1972**, 15, 496.

[65] M. Remmers, B. Müller, K. Martin, H. J. Räder, K. Werner, *Macromol.* **1999**, 32, 1073.

[66] R. Friedlein, X. Crispin, W. Osikowicz, S. Braun, M. P. de Jong, C. D. Simpson, M. D. Watson, F. von Kieseritzky, P. Samori, S. K. M. Jönsson, M. Fahlman, F. Jäckel, J. P. Rabe, J. Hellberg, K. Müllen, W. R. Salaneck, *Synth. Met.* **2004**, 147, 79.

[67] R. B. Martin, *Chem. Re*v. **1996**, 96, 3043.

[68] J. Wu, A. Fechtenkötter, J. Gauss, M. D. Watson, M. Kastler, C. Fechtenkötter, M. Wagner, K. Müllen, *J. Am. Chem. Soc.* **2004**, 126, 11311.

[69] M. Kastler, W. Pisula, D. Wasserfallen, T. Pakula, K. Müllen, *J. Am. Chem. Soc.* **2005**, 127, 4286.

4 Quantitative analyses of fullerene and polycyclic aromatic hydrocarbon mixtures via solvent-free MALDI-MS.

4.1 Introduction

Quantitative and reliable information via matrix assisted laser desorption mass spectrometry (MALDI) represents a big challenge. The qualitative characterization of polymers and macromolecules is straightforward, as the MALDI approach is sensitive, fast and flexible.

Despite these potential benefits, quantitative determinations by MALDI are still complicated. As previously observed for PAHs, the MALDI response is strongly influenced by the different photoionization efficiencies and desorption probabilities of the analytes composing a mixture. Therefore, caution has to be used in extracting quantitative information from a MALDI spectrum of a multicomponent blend.

Here the benefits of an internal standard as a means of overcoming these difficulties are examined. It has been reported that the use of standards labeled with stable isotopes, such as ^{2}H, ^{13}C, ^{15}N, ^{18}O delivers good results in terms of quantification accuracy [70-71]. Additionally, the use of structurally modified compounds as internal standard has been successfully employed for the relative quantification of low molecular weight compounds [72]. To date, however, standard molecules with properties resembling those of the analyte have been used to quantify a single component in a mixture. The method proposed here also has the aim of allowing quantification of both components of a binary mixture by using one of them as an internal standard. This is of special value for an intractable component not obtainable as a pure sample.

Most quantitative MALDI-based investigations have used the traditional solvent-based technique for sample preparation. However, this approach often leads to the so-called hot-spot formation due to severe inhomogeneities caused by crystallization due to solvent evaporation, which implies a large variation in relative signal intensities. As already discussed in the previous chapter, improved homogeneity can be achieved by employing the solvent-free sample preparation [43]. This technique not only overcomes the most encountered problems of solubility, miscibility, and segregation effects during crystallization resulting from unfavorable analyte and matrix polarities, but also allows the characterization of insoluble samples. The many benefits of this preparation technique and the introduction of a standard molecule could offer the possibility for more reliable quantitative characterizations by MALDI-TOF-MS for either soluble or insoluble samples.

As the quantitative MALDI characterization is also affected by interferences caused by the type and the concentration of additional cationizing salts for the ionization of the analytes, this work is centered on the MALDI-based quantitative analyses of polycyclic aromatic hydrocarbons (PAHs) and fullerenes, representative for samples, which undergo photoionizazion during MALDI and desorb as radical cations ($M^{+\cdot}$).

For this investigation we have chosen hexabenzocoronene (HBC) among the PAH family, as it possesses promising electronic properties for novel organic electronic devices [45-73-74-75]. The most important issue for improved electronic properties is the absence of impurities and solvent-free MALDI-MS has already been used to detect traces of byproducts or starting materials, which come from incomplete reactions during synthesis [6]. Here, we explore the possibility of obtaining not only qualitative, but also quantitative information for a model system composed of the HBC-C_{12} molecule and its precursor (hexakis(dodecyl)hexaphenylbenzene HPB-C_{12}) in the cyclodehydrogenation reaction (HPB-C_{12} → HBC-C_{12}) (**Figure 23**) [52]. HPB-C_{12} molecules (the starting material) are here used as internal standard while applying the standard addition method [76] to the MALDI analyses, in order to develop a general procedure for measuring the yield of reactions from binary mixtures when only one of the two components involved is available as a pure sample.

Furthermore, the feasability of quantitative MALDI analyses by employing the traditional solvent-based sample preparation method for the MALDI analyses is tested, in order to compare results from the two different preparation techniques.

Additionally, quantitative MALDI-based analyses of fullerene mixtures are performed (**Figure 23**), as they can be characterized by independent methods to evaluate the reliability of the MALDI-based approach.

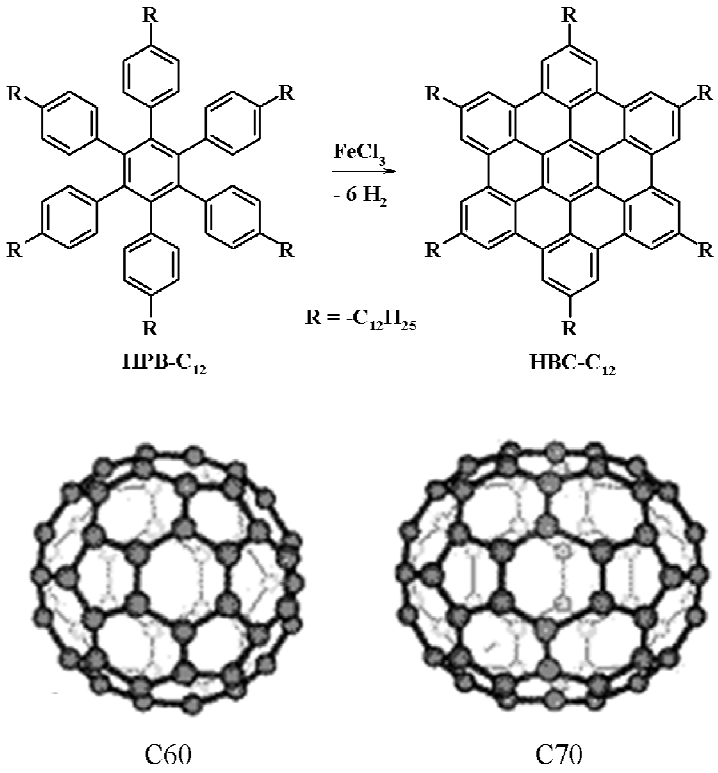

Figure 23. Structures of the analytes.

4.2 The standard addition method

Our approach to the quantification rests upon applying the standard addition method in MALDI analyses with the aim to quantitatively characterize binary mixtures of unknown compositions. This work proceeds through the following steps:

1. A model system composed of a binary mixture is analyzed by MALDI;
2. One of the two analytes (analyte 1) is subsequently added to the initial mixture and for each new mixture a MALDI spectrum is recorded;
3. The amount of analyte 1 in the initial binary mixture is determined by evaluation of the calibration curve;
4. The amount of the second analyte (analyte 2) is calculated from the weight of the initial mixture.

4.3 MALDI quantification of HBCs

For the quantitative characterization of a cyclodehydrogention reaction, we have chosen HBC-C_{12} and its precursor molecule HPB-C_{12} as a model system. An HPB-C_{12}/HBC-C_{12} mixture (1/1 in mass ratio), which simulates the components of an incomplete cyclodehydrogention reaction, was prepared. Then, a MALDI analysis was carried out by employing the solvent-free sample preparation. The corresponding spectrum is reported in **Figure 24 a**. Subsequently, defined amounts of HPB-C_{12} molecules were added stepwise to the initial mixture (**Table 7**, experimental part), while recording the resulting MALDI spectra (**Figure 24 b-g**).

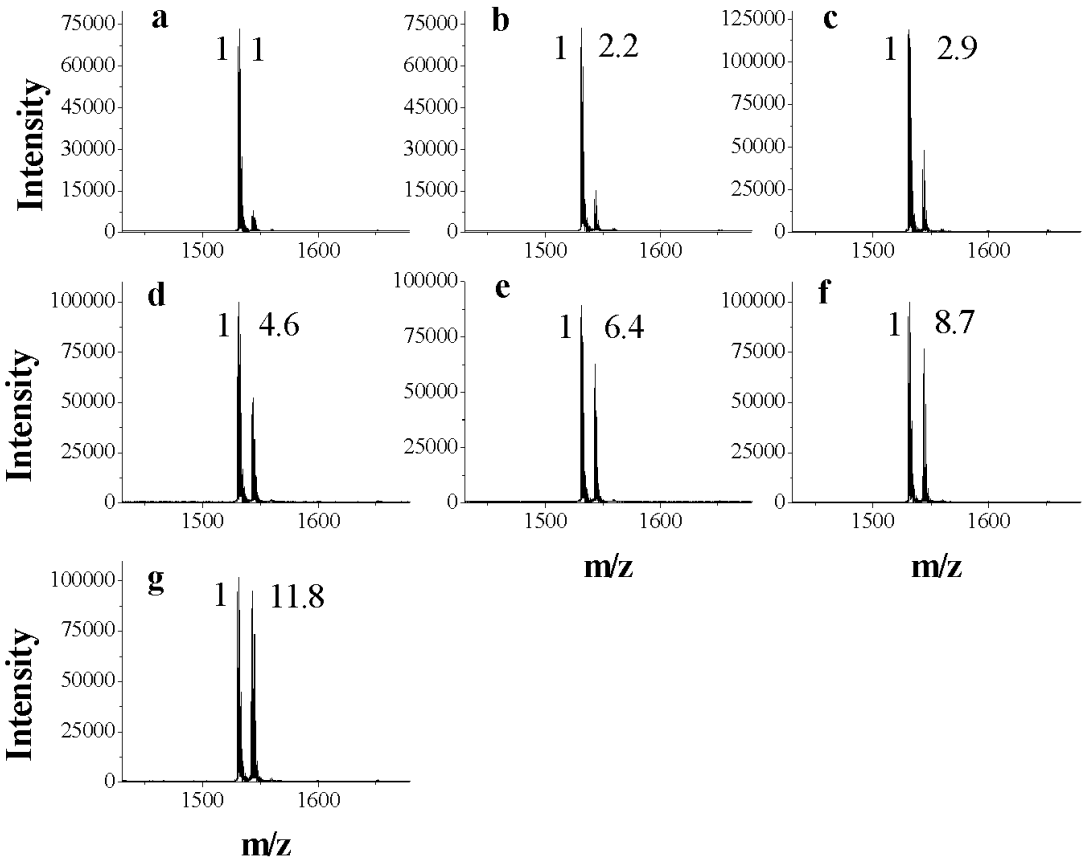

Figure 24. a) MALDI spectrum of an HPB-C_{12}/HBC-C_{12} mixture 1/1 in mass ratio. b) - g) MALDI spectra of HPB-C_{12}/HBC-C_{12} mixtures with a fixed amount of HBC-C_{12} molecules and increasing amounts of HPB-C_{12}, prepared by solvent-free sample preparation.

Only two abundant ions are present in the spectra for HBC-C_{12} at m/z 1532.3 and for HPB-C_{12} at m/z 1544.0. No adducts due to protonation or cationization of the analytes are detected. Thus, any potential interference to the quantitative MALDI

analyses, caused by the presence of a cationizing agent, can be ruled out. The spectrum of the HPB-C_{12}/HBC-C_{12} mixture of mass ratio 1/1 displays strong underestimation of the precursor species, caused by the different desorption/photoionization of the analytes [77] as already observed in Chapter 3.

Quantification was achieved by calculating the intensity ratios from the MALDI spectra, expressed as Int.(HPB-C_{12})/Int.(HBC-C_{12}), which are listed in **Table 8** (experimental part).

The intensity ratio, obtained for the initial HPB-C_{12}/HBC-C_{12} mixture (mixture 1), was fixed at the y intercept of the Cartesian axes, as reported in **Figure 25**. The Int.(HPB-C_{12})/Int.(HBC-C_{12}) values obtained for the other mixtures (mixture 2 to mixture 7) were then plotted versus the added weight of HPB-C_{12} standard molecules.

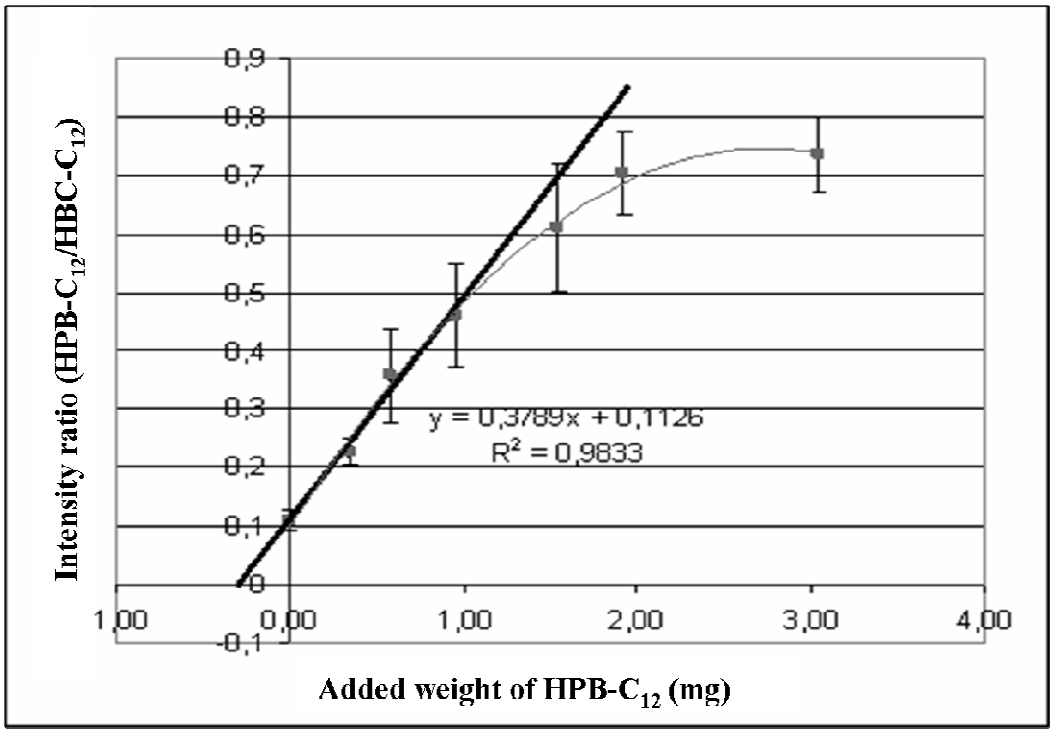

Figure 25. Plot of the intensity ratios HPB-C_{12}/HBC-C_{12} versus added amount of HPB-C_{12}.

The obtained plot in **Figure 25** clearly displays two regimes. For small amounts of added standard molecules, the MALDI response increases linearly. On the contrary, for HPB-C_{12}/HBC-C_{12} mass ratios larger than 4.6, the signal intensity deviates significantly from linearity. The experimental data points belonging to the

linear regime can be interpolated by a straight line of equation (y = 0.3789 x + 0.1126) with correlation coefficient R^2 of 0.9833. According to the standard addition method, the absolute value of the x-intercept is the concentration of HPB-C_{12} in the initial mixture (mixture 1). Therefore, through extrapolation of the calibration line (y = 0.383x + 0.1069) to y = 0, the amount (mg.) of HPB-C_{12} in the mixture 1 is calculated to be 0.28 g. This mass value differs from the true one by less than 4%.

The deviation from the linearity of the calibration curve for HPB-C_{12}/HBC-C_{12} mass ratios larger than 4.6 can be explained considering the total analyte to matrix (A/M) ratio, which increases significantly during the addition of the HPB-C_{12} standard molecules. This strongly affects the MALDI response for sample-matrix molar ratios lower than 1:850. The matrix presumably plays the role of disturbing the strong interactions between HBC molecules and it works optimally only when a certain sample-matrix threshold has been surpassed. Furthermore, low A/M ratios may favour suppression phenomena, which are emphasized for the system HPB-C_{12}/HBC-C_{12} by the different desorption/photoionization efficiencies of the analytes.

As discussed in Chapter 3, HBC-C_{12} molecules create radical cations much easier than their HPB-C_{12} precursors [77]. For low A/M ratios, the higher contact probability between the analytes may enhance charge transfer phenomena between HPB-C_{12} and HBC-C_{12} molecules with an increased formation of HBC-$C_{12}^{\cdot +}$ species. The importance of matrix dilution during the desorption/photoionization process, has already been proven for similar systems [77]. Within this work it was recognized that not only a suitable matrix has to be employed to avoid fragmentation and laser-induced reactions among the analyte molecules [78], but also that the matrix amount has to exceed a threshold to avoid strong deviation from the linearity. Further experiments have also shown that the deviation form the linearity can however be corrected by increasing the matrix dilution up to the threshold value of 1:850 (A/M).

Comparative quantitative analyses for the system HPB-C_{12}/HBC-C_{12} were performed by using the solvent-based sample preparation. An equimolar mixture of HBC-C_{12} and HPB-C_{12} was prepared and analyzed via solvent-based MALDI (**Figure 26**).

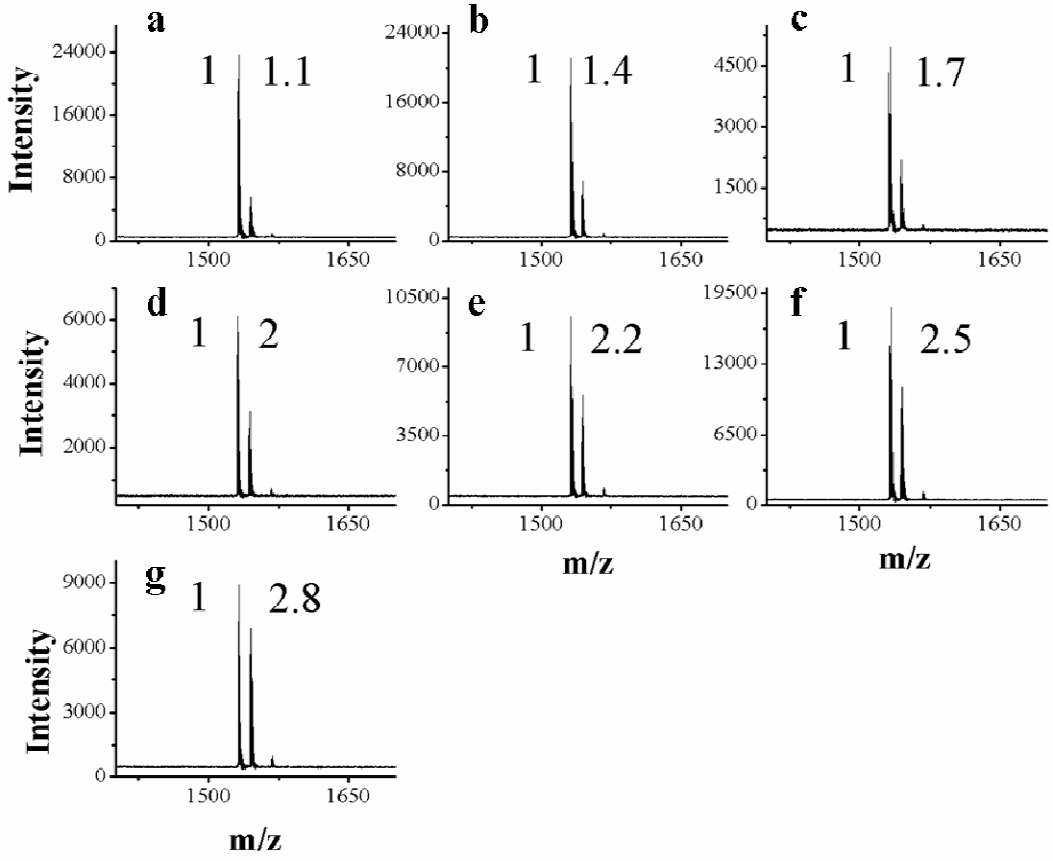

Figure 26. a) MALDI spectra of HBC-C_{12}/HPB-C_{12} mixtures with varying molar ratios, obtained via solvent-based sample preparation.

Defined volumes of the HPB-C_{12} solution in THF were subsequently added (**Table 9**, experimental part). The MALDI spectra of HPB-C_{12} and HBC-C_{12} mixtures with varying molar ratios are reported in **Figure 26 a-g**. As opposed to the solvent-free sample preparation, two abundant ions and a weak one are visible. The ones at m/z 1532.3 and 1544.5 are related to the radical cations of HBC-C_{12} and HPB-C_{12} molecules, respectively, whereas the peak at m/z 1567.6 is due to the sodiated HPB-C_{12} (HPB-C_{12} + Na^+). It is interesting to point out that, by employing the solvent-based sample preparation, HPB-C_{12} molecules undergo photoionization and formation of radical cations and supplementary cation attachment to some extent. This suggests the presence of additional species, which could represent an obstacle for a reliable quantitative investigation. The presence of sodiated adducts was not recorded at all by employing the solvent-free preparation procedure. Analogous to the quantitative work, carried out via solvent-free MALDI-MS, the standard addition method was

applied in solvent-based MALDI analyses, by plotting the responses (expressed in **Table 10** as intensity ratios HPB-C_{12}/HBC-C_{12}, experimental part) against the increasing amount of HPB-C_{12} expressed in µl of added solution (**Figure 27**). The sodiated HPB-C_{12} species were neglected.

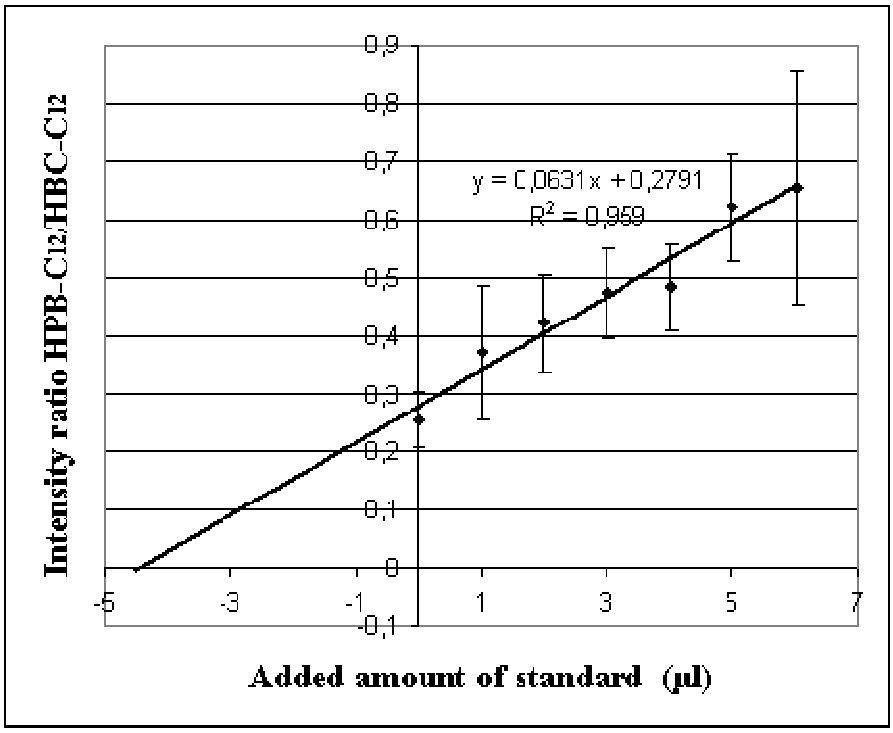

Figure 27. Intensity ratios HPB-C_{12}/HBC-C_{12} versus added µl of HPB-C_{12}.

The data points obtained via the solvent-based sample preparation could be interpolated by a straight line. Contrary to the solvent-free sample preparation, no strong deviations from linearity were observed increasing the analyte to matrix concentration (**Figure 27**). This phenomenon could be related to use of the solvent during the sample preparation procedure, which weakens the intermolecular π–π interactions among the HBC cores. From the evaluation of the data points and extrapolation of the straight line in **Figure 27**, the volume of HPB-C_{12} solution (µl) present in the mixture 1 (**Table 9**, experimental part) was calculated to be 4.3 µl. This value differs from the true amount of 4.0 µl by 7.5 %. However, it has to be pointed out that quantitative solvent-based MALDI analyses could be carried out only after overcoming the problems related to the presence of hot-spots. In fact, via performing solvent-based MALDI analyses, cocrystallization and segregation phenomena, which

caused large variations in signal intensities, were encountered. As a result, the data points, reported in **Figure 27**, possess a large error-bar. The interferences due to the presence of hot-spots could be overcome by increasing the number of measurements for each sample mixture via dropping solutions with the same concentration of analytes in three different places on the sample holder and summing for each place 500 single shots to give an average spectrum. Such homogeneity problems were indeed not encountered during solvent-free MALDI analysis, which required many fewer measurements and which was therefore recognized to be the most favorable preparation procedure for quantitative analysis.

4.4 Quantitative analysis of fullerenes

Quantitative MALDI analyses of fullerenes were conducted as a further proof for the method with the additional opportunity to compare the mass spectrometric results with an independent quantitative procedure such as HPLC. C60 and C70 buckyballs undergo photoionization with formation of radical cations, but due to their spherical shape, should not lead to complications due to strong aggregation. Thus, they were chosen as another model system for this study. Mixtures of C60 and C70 fullerenes were prepared as described in the experimental part (**Table 11**) and MALDI spectra were recorded analogous to the previous measurements (**Figure 28 a**).

Two abundant ions at m/z 720.3 and 840.6 are present corresponding to the C60 and C70 radical cations, respectively. A small amount of impurities, due to higher-mass fullerenes, is also present. In contrast to the previous system (HPB-C_{12}/HBC-C_{12}), C60 and C70 molecules possess comparable photoionization/desorption efficiencies. This minimizes the problems related to suppression phenomena, which have been encountered in the characterization of disc-shaped molecules and thus simplifies the quantitative characterization. As shown in **Figure 28 a**, the MALDI measurement responds linearly to the increase of one analyte (C70) and the data points expressed as Int.C70/Int.C60 versus the molar ratio of the C70/C60 mixtures (**Table 12**, experimental part) can be interpolated by a straight line (**Figure 28 b**). It is interesting to point out that for this system, no strong deviations from linearity were observed by increasing the analyte/matrix concentration. Probably, spherical-shaped

C60 and C70 fullerenes aggregate less strongly than large and planar aromatic systems, which can assemble into columnar structures. Consequently, their desorption is less influenced by a variation in the dilution of the analytes with the matrix.

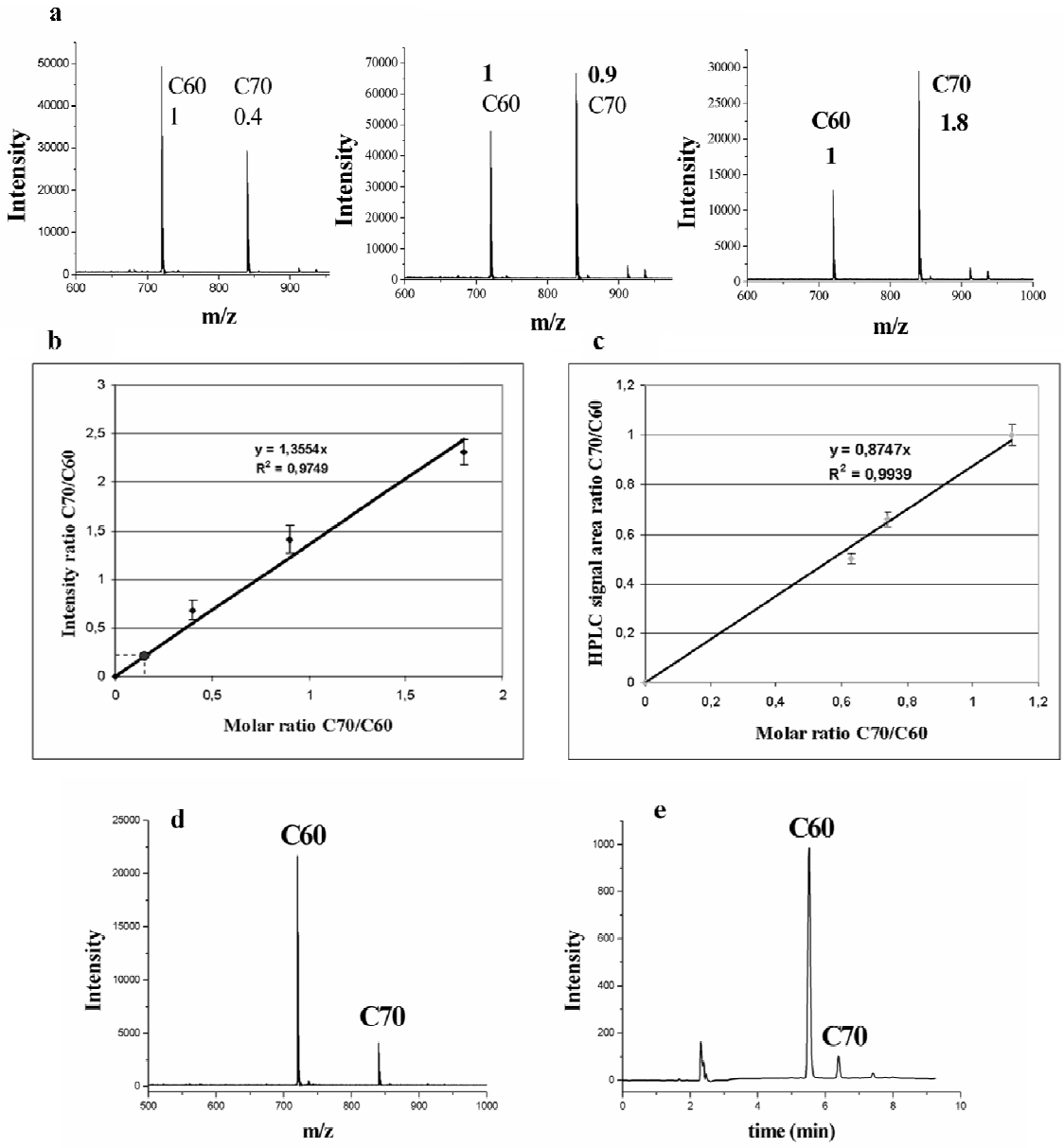

Figure 28. a) MALDI spectra of the mixtures C70/C60 with different molar ratios. b) MALDI calibration curve for the system C70/C60. c) HPLC calibration curve for the system C70/C60. d) MALDI spectrum of commercial fullerite mixture. e) HPLC diagram of commercial fullerite mixture.

The measured calibration curve of equation (y = 1.3554x) has a satisfactory correlation coefficient R^2 of 0.9749. Therefore, it was used for the measurement of the

C70/C60 amount in a commercially available mixture of fullerenes (fullerite). The MALDI spectrum for the fullerite mixture of unknown molar ratio is reported in **Figure 28 d**. From the MALDI spectrum the intensity ratio C70/C60 is calculated to be 0.203 ± 0.010, which corresponds to a molar ratio of 0.150 ± 0.060, calculated by using the calibration curve of **Figure 28 b**.

To check the accuracy of the quantitative MALDI analyses by an independent method, the fullerite mixture was also characterized via HPLC. A calibration curve for the HPLC analyses is obtained by mixing fullerenes C60 and C70 in known ratios (**Table 13**, experimental part). The corresponding plot is reported in **Figure 28 c**. A straight line of equation y = 0.8747x and correlation coefficient of 0.9939 (R^2) interpolates the data points (**Table 14**, experimental part). The HPLC response for the fullerite mixture is plotted in the calibration curve and the molar ratio C70/C60 is estimated to be 0.170 ± 0.041. Within the experimental error, the two values are consistent. This result strengthens therefore the feasability of quantitative analysis via MALDI-TOF-MS.

4.5 Conclusions

This work explores the feasibality of reliable quantitative MALDI analyses via solvent-free-sample-preparation, as this procedure comprises the unique convenience to be applicable for insoluble samples as well. As quantitative MALDI measurements are even more complicated for species ionized by cation-attachment, we investigated model systems, such as PAHs and fullerenes, which undergo photoionization and do not require additional cationizing salts. The standard-addition-method is applied in MALDI for quantitative characterization of binary mixtures. Two different systems are tested. Set-1 is composed of hexakis(dodecyl)hexabenzocoronene and hexakis(dodecyl)hexaphenylbenzene, which represent product and precursor of a cyclodehydrogenation reaction. Set-2 is a mixture of C60 and C70 fullerenes. In terms of Set-1, severe anomalies could be detected due to a strong influence of the matrix/analyte ratio on the correlation between signal intensity and analyte amount. This evidence can be related to the strong intermolecular interactions among the HBC aromatic cores hampering the desorption step and to intermolecular charge transfer, which influences the ionization probability. Minor interferences with the quantitative

MALDI characterization are encountered in the analysis of C60 and C70 fullerenes. The spherical shape of C60 and C70 buckyballs avoids strong aggregation and their similar absorption coefficients at the laser wavelength are responsible for similar photoionization probabilities. Thus, no molecule-dependent anomalies in their desorption-photoionization behaviour are recognized.

4.6 References

[70] A. I. Gusev, W. R. Wilkinson, A. Proctor, D. M. Hercules *Fresenius' J. of Anal. Chem.* **1996**, 354, 455.

[71] F. Zappacosta, R. S. Annan *Anal. Chem.* **2004**; 76, 6618.

[72] D. Bungert, S. Bastian, D. M. Heckmann-Pohl, F.Giffhorn, E. Heinzle, A. Tholey *Biotechnology Letters* **2004**, 26, 1025.

[73] W. Pisula, A. Menon, M. Stepputat, I. Lieberwirth, U. Kolb, A. Tracz, H. Sirringhaus, T. Pakula, K. Müllen *Adv. Mat.*, **2005**, 17, 684.

[74] A. Cristadoro, G. Lieser, H. J. Räder, K. Müllen *ChemPhysChem*, **2007**, 8, 585.

[75] A. Cristadoro, M. Ai, H. J. Räder, J. Rabe, K. Müllen *J. Phys. Chem. C*, **2008**, 112, 5563.

[76] D. A. Skoog, J. L. Leary, *Principles of Instrumental Analysis*, IV ed.; Saunders College Publishing: Orlando; 1992.

[77] A. Cristadoro, H. J. Räder, K. Müllen, *Rapid Commun. Mass Spectrom.* **2007**, 21, 2621.

[78] A. R. Hortal, P. Hurtado, B. Martınez-Haya, O. C. Mullins *Energy & Fuels* **2007**, 21, 2863.

5 MALDI quantitative characterization of natural mesophase pitch samples via solvent-free sample preparation.

5.1 Introduction

Petroleum pitches are a class of carbonaceous oligomers, which can serve as precursors for advanced carbon materials including high thermal conductivity carbon fibres [79-80].

The insolubility of high molecular weight (MW) carbonaceous pitches (e.g. mesophases) in even aggressive solvents has always been a significant obstacle to their MW characterization. So far, characterization of various carbonaceous species like coal and petroleum derived materials has been well established up to the molecular weights of ~ 450 Da using various characterization methods like gas chromatography (GC) and GC coupled with mass spectrometry (GC-MS); whereas, analysis of higher molecular weight species was limited by their volatility [81]. Similarly, characterization using Gel Permeation Chromatography (GPC) and several Mass Spectrometry (MS) techniques was hampered by low solubility of these compounds [82-83]. Indeed, MALDI-TOF mass spectrometry can be used as a tool to obtain highly resolved mass spectra for insoluble pitches, when the solvent-free technique for sample preparation is employed [49].

The interpretation of the MALDI spectra of a mesophase pitch sample and the extraction of reliable qualitative and quantitative information is nevertheless complicated by the presence of numerous carbonaceous species of unknown molecular structure, which possess different ionization and desorption efficiencies.

Within this work, MALDI analyses supported by UV-vis, IR and NMR absorption investigations give us the unique capabilities for identifying the specific molecular structures, which exist in a special petroleum pitch sample, technically known as Pitch M-50. This investigation aims for a better understanding of the desorption/ionization characteristics of carbonaceous pitches by employing an optimized methodology formerly worked out in Chapter 3 with model mixtures composed of synthetic PAHs [77]. Understanding the desorption/ionization behaviorof the pitch components is in fact a requirement for extracting qualitative and quantitative information from the MALDI spectra.

For the quantification of pitch M-50, dense gas extraction [84], a novel separation method developed for the component isolation of the pitch sample M-50, was coupled to the MALDI analyses for fractionation and characterization of the oligomeric pitch

M-50. 1) Fractionation of the oligomeric pitch allows isolating its components and recording their MALDI spectra. 2) Mixing them in known ratios allows building a calibration curve, which can be used for quantification of the different oligomeric units present in the original pitch mixture.

5.2 Pitch M-50: Where does it come from?

Petroleum pitches are produced by the thermal polymerization of an aromatic oil feedstock; thus, they are oligomeric in nature and consist of a molecular weight distribution (MWD) of polycyclic aromatic hydrocarbons.

The MALDI mass spectrum of M-50, a commercially available pitch from Marathon Petroleum Company is shown in **Figure 29**. As the high molecular weight fractions of the pitch M-50 sample suffer from lack of solubility, the solvent-free sample preparation was employed for the mass characterization, which does not discriminate for the insoluble component. TCNQ was selected as a matrix for these experiments as it has been previously demonstrated that it is a suitable choice for highly reproducible mass analyses of synthetic PAHs [77-85].

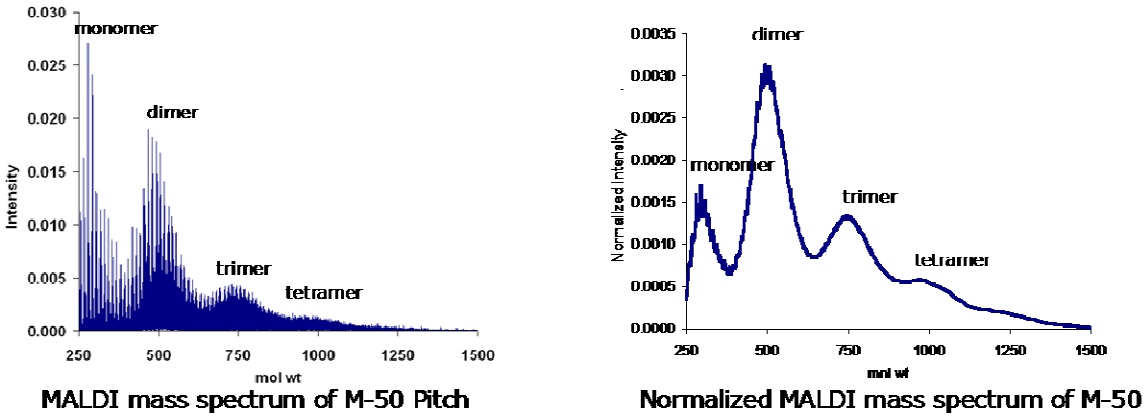

Figure 29. MALDI spectrum of pitch M-50, not normalized (left), normalized (right), TCNQ is employed as the matrix.

As shown in **Figure 29**, the oligomeric nature of the pitch is obvious. Of course, the oligomers themselves are not pure, as the starting "monomer" for the pitch (i.e., the aromatic decant oil), is itself a polydisperse material. What we have labeled "monomer" has a m/z range of 210-388, roughly centered around a maximum of m/z

280; “dimer” m/z 388-645, centered at m/z 470; trimer m/z of 645-890, centered around m/z 730; and tetramer m/z at 890-1120, centered at m/z 990. In the MALDI spectrum, reported in **Figure 29** (right), the area under the peaks have been normalized to sum to 1.0.

5.3 Dense gas extraction

To produce pitches for a given application, it is logical to control the mol wt distribution (MWD) of the starting pitch, similar to what is done for manufacturing goods from polymers. According to literature, dense-gas extraction (DGE) is a multistage separation technique, which can be used for the fractionation of carbonaceous pitches [84]. The extractive solvent is a dense gas in the vicinity of its critical temperature, with the pressure being high enough so that the solvent has significantly more extractive power than an ideal gas (the pressure and temperature do not have to be supercritical, thus the more general term ‘‘dense gas’’ in lieu of the more specific form ‘‘supercritical fluid’’). As the goal is to obtain narrow molecular weight fractions of pitch, the dense gas and the solute are contacted in a packed column with a separation power equivalent to a number of equilibrium stages, and liquid reflux back down the column is used to further enhance product purity. In essence, then, DGE is a countercurrent, multistage supercritical extraction technique with reflux. A schematic representation of the DGE apparatus for continuous and semi-batch extraction of pitches is reported in **Figure 30 a** and **b**, respectively.

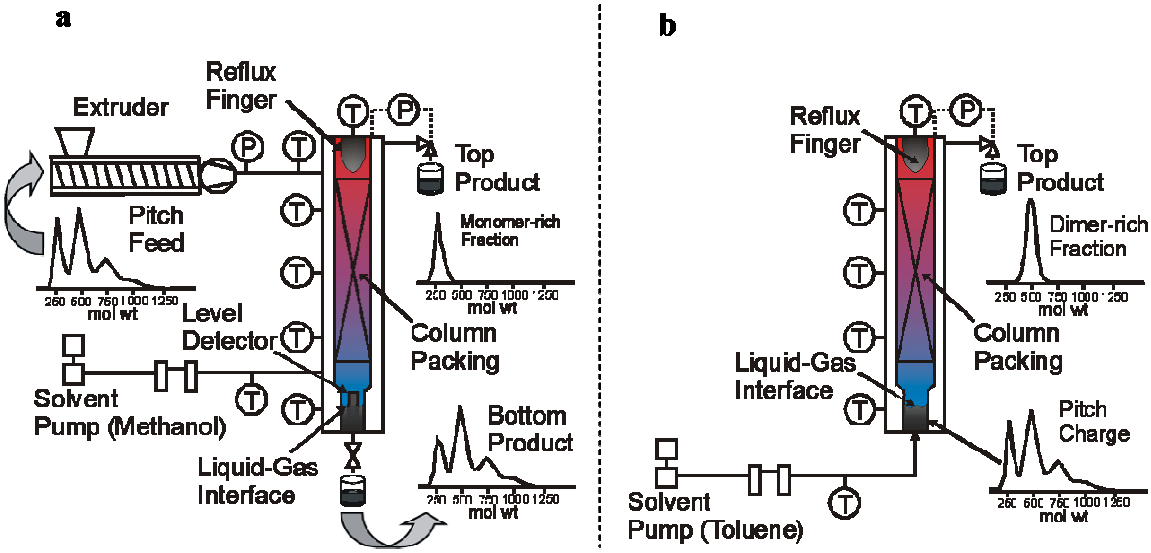

Figure 30. Dense-gas extraction apparatus for continuous fractionation of pitches (a), for semi-batch fractionation of pitches (b).

Within this work, the pitch sample M-50 was delivered to the top of the column in the molten state (300 °C) and toluene and methanol were used as the extractive solvents. According to the schematic representation reported in **Figure 30**, a solvent-rich phase containing extracted pitch species was taken off as top-product and a pitch-rich liquid phase, containing the unextracted pitch species was taken off as bottom-product [86]. The continuous DGE process could deliver two monomer-rich fractions with purity of 98% and 79%. The semi-batch run was instead used to extract dimer-rich fractions with 97% and 89% purity. The MALDI spectra of the two monomeric and dimeric fractions are reported in **Figure 31 a-b** and **31 c-d**, respectively.

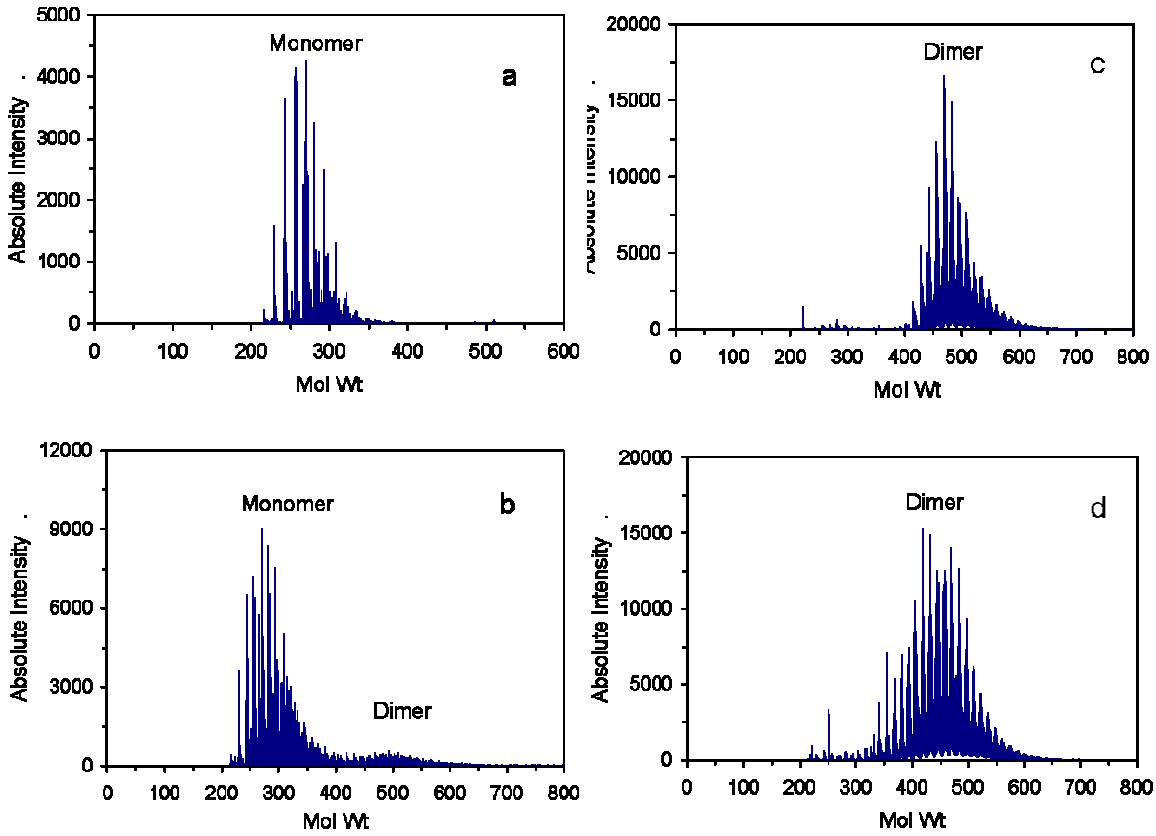

Figure 31. MALDI mass spectra of (a) 98% monomer and (b) 79% monomer (c) 97% dimer and (d) 89% dimer fractions isolated from M-50 pitch.

In particular, 98% monomer and 97% dimer fractions isolated by DGE were also analyzed using MALDI-post source decay (PSD), and FD mass spectrometry (MS); and by ^{1}H-NMR, UV-Vis, and FT-IR spectroscopy to propose suitable molecular structures for the pitch components.

5.4 Analytical and structural characterization of the monomer-rich fractions

5.4.1 UV-Visible spectroscopy

All PAH structures proposed in this investigation for the monomer-rich fraction of M-50 pitch were selected among other possible isomers by considering their UV-Vis absorption spectra and comparing them with the absorption spectra for the 79 and 98% monomer pitch fractions.

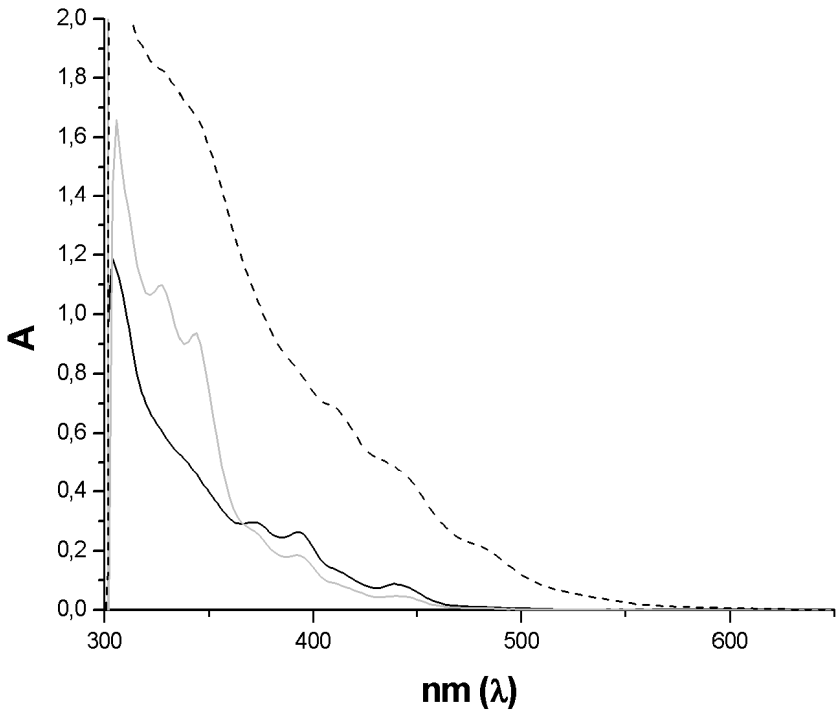

Figure 32. UV-Vis spectra for the 79% (black) and 98% (gray) monomer fractions, and for the 97% dimer fraction (dotted line) of M-50 pitch.

As shown in **Figure 32**, species belonging to 98% absorb strongly between 300 and 360 nm and weakly at higher wavelengths. For example, benzo[b]fluorene possesses a comparable absorption at these wavelengths [87]; thus, it is likely that it is a significant constituent in the 98% pure monomer. On the other hand, the PAH molecule benzo[a]pyrene absorbs strongly from 350 to 410 nm [89], and thus would not be expected to be a major constituent in the 98% fraction. The monomer fraction of 79% purity absorbs light at higher wavelengths (red shift) in comparison to the 98% monomer fraction. This is probably due to the presence of species with a larger polycyclic π-system, evidence that is consistent with the broader signal distribution of this monomer fraction in the FD mass spectrum (see below). Additional information on the use of UV-Vis to assist in the selection of the most likely PAH structures is given in the subsequent discussions below.

5.4.2 Proton NMR spectroscopy

^{1}H-NMR analyses of the 98% monomer fraction is given in **Figure 33**.

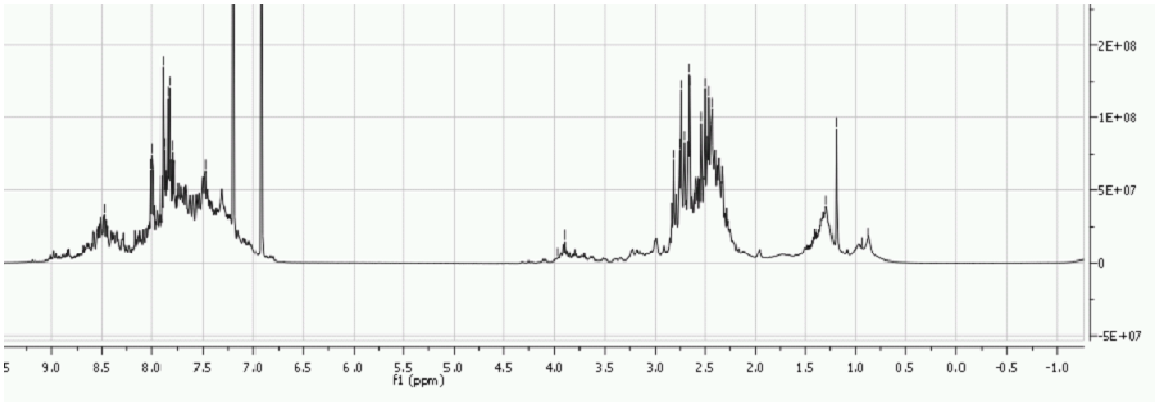

Figure 33. ^{1}H-NMR of the 98% monomer fraction.

The chemical shifts between 2.76 and 2.43 ppm are related to the presence of -CH_2- groups attached to the aromatic rings, whereas the chemical shifts between 8.85 and 7.30 ppm are characteristic for the protons of the condensed aromatic rings. The ratio between aliphatic hydrogens in the α position with respect to the aromatic rings vs. the aromatic protons was evaluated via integration of the corresponding signals and found to be 1/1.33. The strong signals at 7.20 and 6.94 arise from the o-dichlorobenzene solvent and at 1.20 ppm from trace amounts of water, respectively. The presence of alkyl substituents with ethyl or longer chains is recognized by the peaks between 0.94 and 0.88 ppm, which are related to aliphatic protons in the ß position with respect to an aliphatic -CH_2- group, and by the signals between 1.26 and 1.40 ppm, which are related to aliphatic protons in the ß position with respect to a phenyl group. They are, however, relatively rare when compared to the number of methyl groups directly connected to the aromatic core (related to the signal between 2.76 and 2.43 ppm). From the NMR spectrum, the ratio CH_3-CH_2-/-CH_2-Ph is calculated to be 1/15. The peak at 3.96 ppm is related to the presence of sp^3 hybridization that bridges two aromatic rings, evidence of the presence of a methylene bridge between two aromatic rings.

5.4.3 FT-IR spectroscopy

The FT-IR absorption spectrum for the 98% monomer fraction is shown in **Figure 34**.

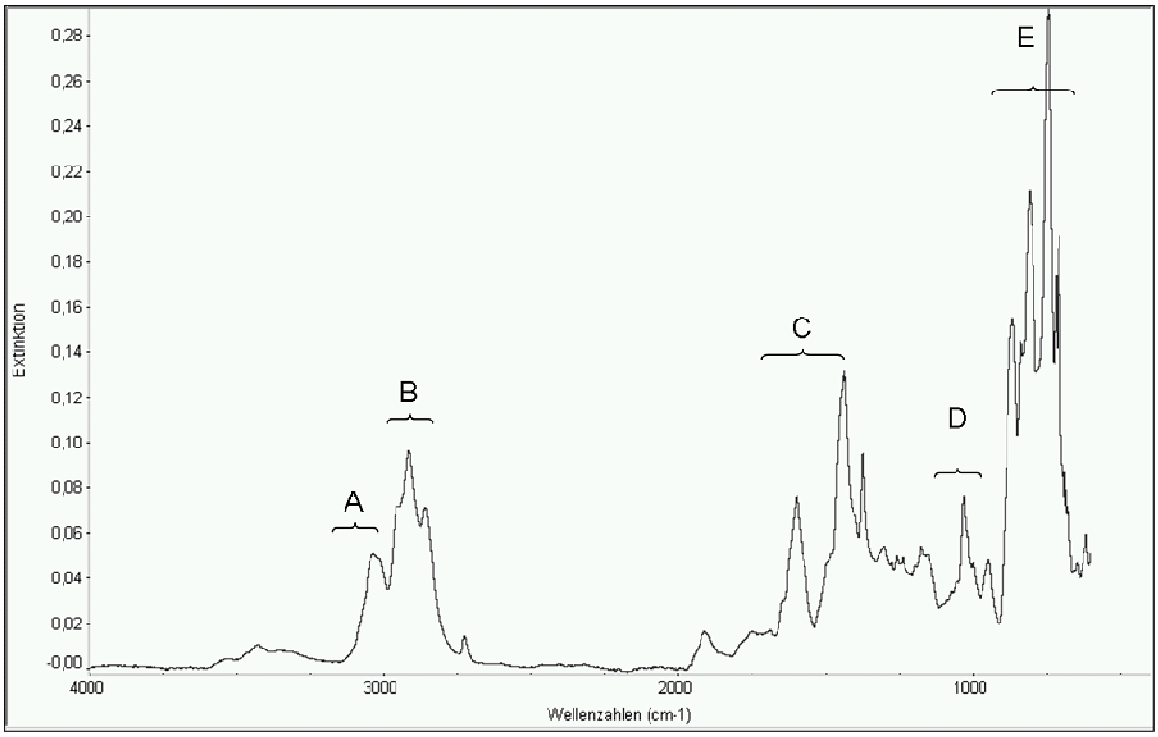

Figure 34. FT-IR spectrum for the 98% monomer fraction. The spectrum for the 79% monomer fraction is very similar to that shown above.

The band **A** at 3046-3014 cm^{-1} of weak intensity is related to aromatic C-H stretching. The bands at 2961, 2915, and 2856 cm^{-1} of the group **B** can be related to stretching of the C-H methylic and provide evidence of the presence of sp^3 carbon atoms. The group **C** bands at 1598 and 1438 cm^{-1} are caused by stretching of the C=C atoms of the aromatic ring, the group **D** bands are related to the C-H in-plane bending, and the group **E** bands are related to out-of-plane bending of =C-H in the aromatic ring.

The group **E** consists of three bands. For PAHs, these bands can be related to the number of neighboring hydrogen atoms present on aromatic rings [88]. Taking methyl-substituted naphthalene as a model system, the FT-IR spectrum will show three absorption bands for ß-substituted naphthalene (one for the isolated hydrogen, one for the two neighboring H atoms on one ring, and one for the four hydrogen

atoms on the other ring), but only two for α-substituted naphthalene. Thus, the presence of three absorption bands provides evidence that alkylation of the PAH aromatic backbone in the monomer-rich fraction occurs preferentially at the ß position (see **Figure 35**).

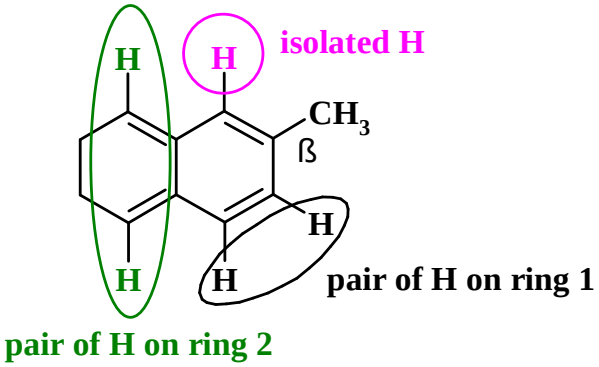

Figure 35. Molecular structure of ß-substituted naphthalene.

5.4.4 Field Desorption, MALDI, and MALDI-Post Source Decay mass spectrometry

FD-MS spectra for the 98% and 79% monomer fractions are shown in **Figure 36 a** and **b**.

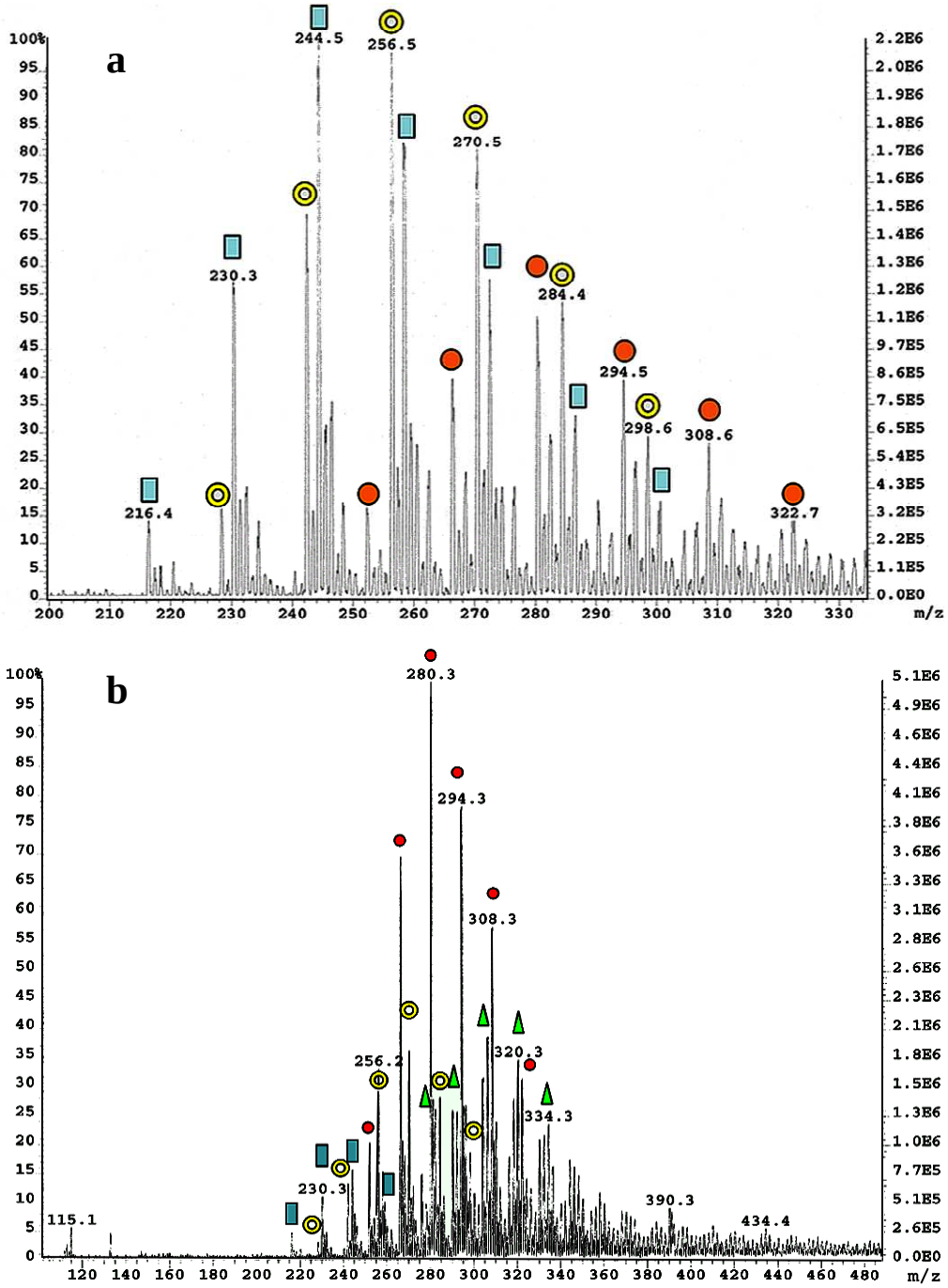

Figure 36. FD mass spectra of pitch fractions with purities of (a) 98 and (b) 79% monomer.

FD-MS was used in addition to MALDI, as matrix (i.e., TCNQ) signals could have interfered with the signals for low molecular weigth pitch species. However, this did not turn out to be the case, as spectra obtained by the two different MS techniques were found to be essentially identical. Our analysis of the monomer-rich fractions, based on information obtained from FD, MALDI, and MALDI-Post Source decay (PSD) mass spectrometry, is summarized in **Table 2**.

Table 2. Molecular weights and degree of alkylation of species present in the monomer-rich fraction of M-50 pitch as determined by FD-MS and MALDI-PSD-MS.

	Blue rectangles	Yellow rings	Orange dots	Green triangles [a]	Alkyl substituents
m/z	216.4	228.3	252.3	278.3	0
m/z	230.3	242.4	266.5	292.2	CH_3
m/z	244.5 [b]	256.5 [b]	280.5 [b]	306.3 [b]	2 x CH_3
m/z	258.4	270.5	294.5	320.3	3 x CH_3
m/z	272.6 [c]	284.4	308.6	334.5	4 x CH_3 or (CH_2CH_3 + 2 x CH_3)
m/z	286.7 [c]	298.6	322.7		5 x CH_3 or different combinations of methyl, ethyl groups.
m/z	300.8 [c]				6 x CH_3 or different combinations of methyl, ethyl groups.

[a] This PAH series was not observed in appreciable amount in the 98% monomer fraction.
[b] The most prevalent species in each PAH distribution. (all contained two methyl substituents)
[c] These signals were not prevalent in the 79% monomer fraction.

The lowest-mass signal present in the FD spectrum (**Figure 36 a** and **b**, blue rectangle) of the monomer isolated from the M-50 Pitch at m/z 216.4 is due to the presence of the PAH benzofluorene (mol wt = 216.3) and its isomers, such as benzo[b]fluorene (see **Figure 37 a**). The NMR spectra in **Figure 33** indicates that benzo[c]fluorene is also equally probable, but not benzo[a]fluorene. In benzo[a]fluorene, in fact, the signals related to the sp^3 Hs, which bridge two aromatic rings should appear at higher ppm. For benzo[b]fluorene and benzo[c]fluorene instead their signal appears at 3.96 ppm, as observed in the H-NMR spectrum reported in **Figure 33**. Rectangular blue marks delineate a signal distribution that starts at 216.4, has a repeating unit of 14 Da, and extends to 300.8 Da. This distribution provides

strong evidence of the presence of alkyl groups anchored to the base aromatic structure of benzofluorene (see **Table 2** and **Figure 37 b**).

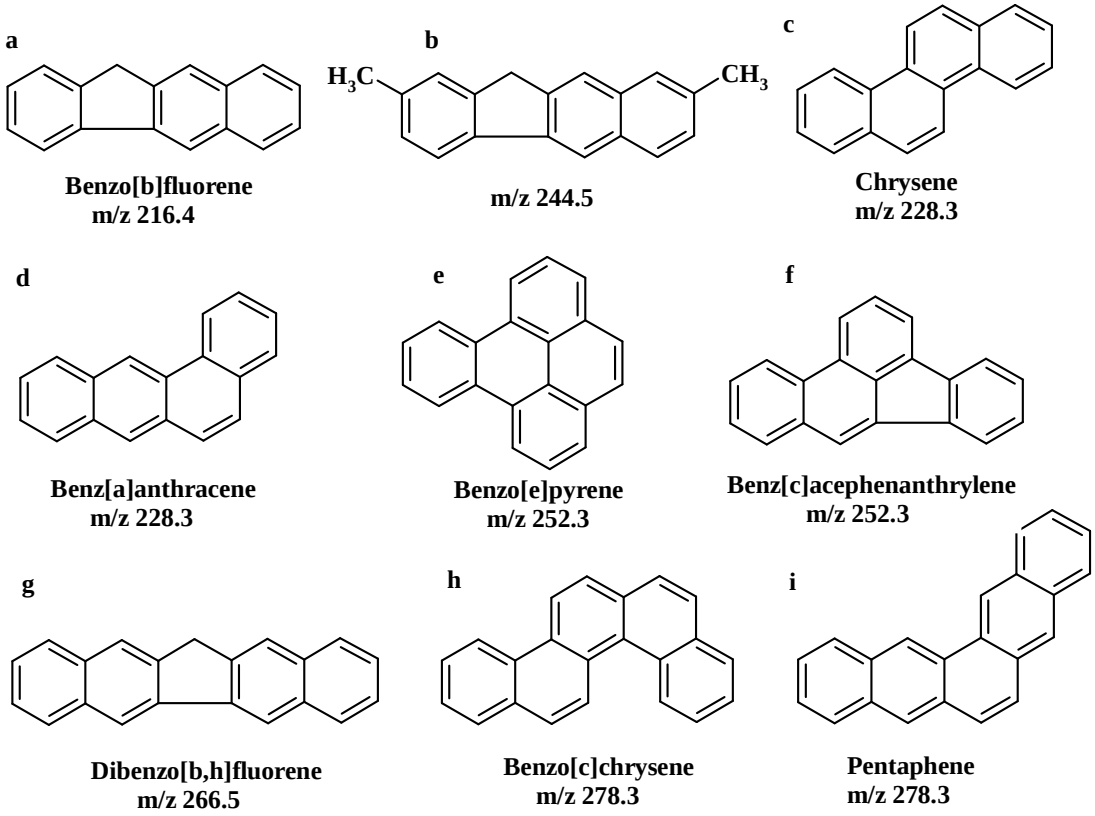

Figure 37. PAH structures present in the 98% monomer fraction: (a) Benzo[b]fluorene (m/z = 216.4) and (b) its most common alkylated homolog (m/z = 244.5). PAH structures for the m/z = 228.3 series include (c) chrysene, (d) benz[a]anthracene, and their alkylated h

The fragmentation behavior by MALDI-PSD of the "blue rectangle" signal distribution, described above, is given in **Figure 38**. In this experiment, the ion of interest was isolated using a selecting device (in this study an ion gate) so that all fragment ions may be associated with their correct precursor.

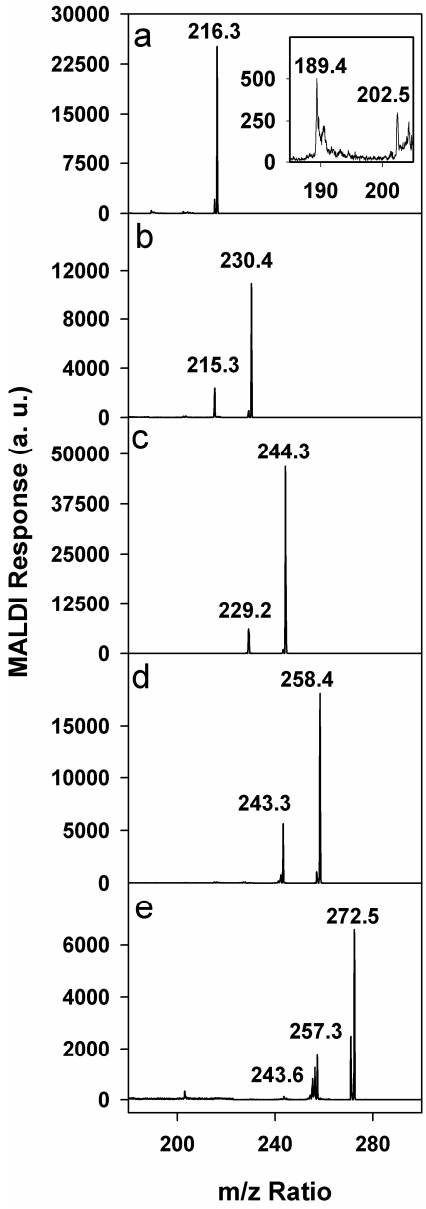

Figure 38. PSD results for the series of PAHs beginning at benzofluorene (m/z = 216.3): (a) base aromatic structure; (b-d) one to three methyl substituents, respectively; (e) limited ethyl substituents are also likely to be present.

The spectrum at m/z = 216.3 (**Figure 38 a**) is consistent with the benzofluorene structure in two ways: (1) No significant fragments are observed, which are consistent with mass spectra for the fluorenes [13], and (2) the low-intensity peak at 202.5 m/z is consistent with the loss of the methylene group from benzofluorene. In **Figure 38 b-e** fragmentation patterns for the "blue rectangle" signal distribution are shown, with m/z = 230.4, 244.3, 258.4, and 272.5. In every

case, a de-methylated ion (i.e., ~15 Da less than the parent peak) of appreciable magnitude is present. Furthermore, the stability of the de-methylated benzofluorene ion is consistent with the mass spectrum for the methylfluorenes, which also have a highly stable de-methylated ion [89]. For the species at 272.5 (**Figure 38 e**), a de-ethylated ion at 243.6 is observed at less than one-tenth the intensity of the de-methylated ion at 257.3. This difference in intensity can be explained considering the fragmentation mechanism of ethylated benzene rings suggested by Silverstein et. al. [88] and reported in **Scheme 1** .

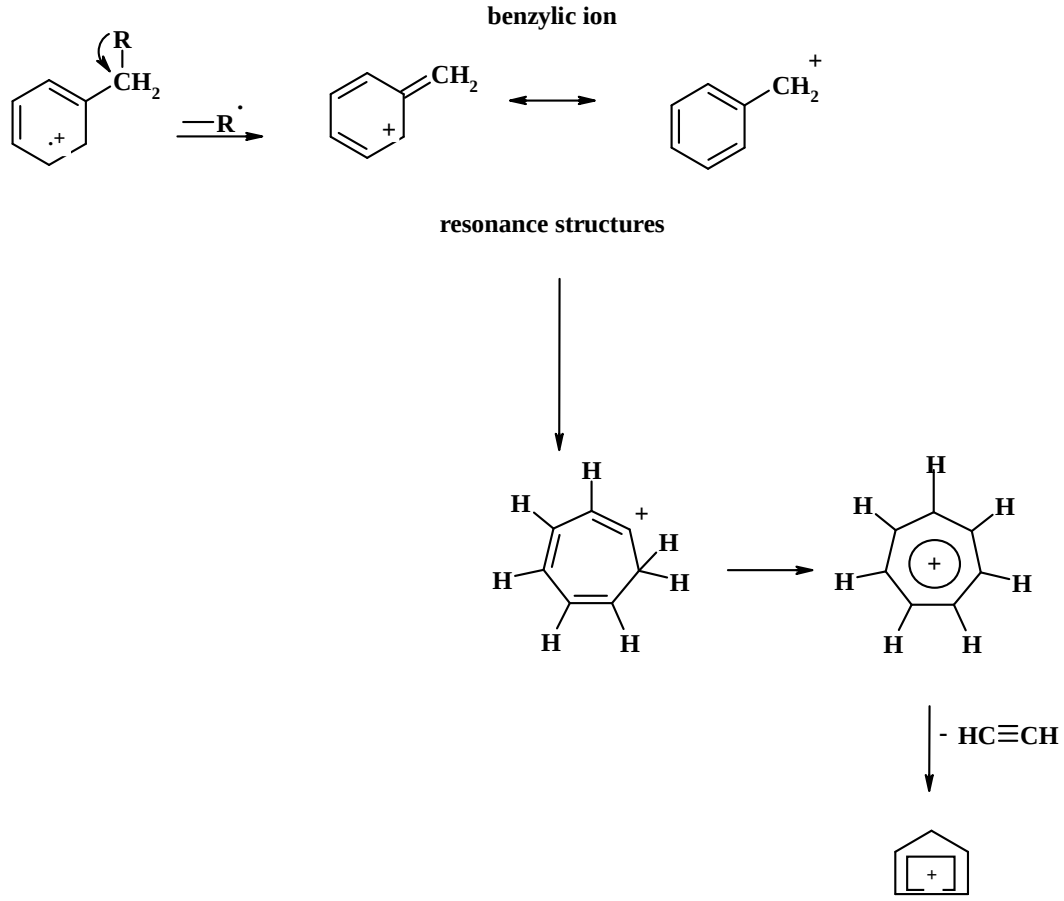

Scheme 1. Fragmentation mechanism of alkylated benzene.

By elimination of a methylic radical, the highly stable benzylic ion is formed. This can further rearrange to form a seven-member ring and eliminate an actylene molecule. On the contrary, the elimination of an ethylic radical is less probable as an unstable benzene ion is generated.

Moreover, loss of a methylic radical can also be related to the presence of two methylic groups anchored to the same aromatic ring. In this case, the fragmentation

route, reported in **Scheme 2**, begins with a rearrangement of the benzene ring to form a methylated seven-member radical cation before loosing a methylic radical. Then, the benzylic cation can eliminate an acetylene molecule.

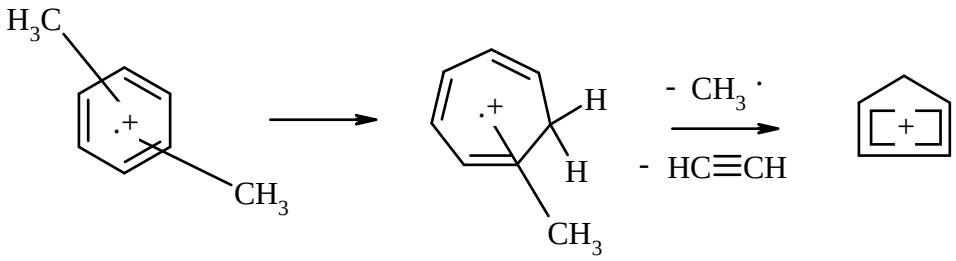

Scheme 2. Fragmentation route of dimethyl benzene.

PSD could not be applied to the higher molecular weight in the benzofluorene series because of the difficulty in isolating the species of interest from nearby signals of comparable intensity.

In **Figure 36**, another PAH and its alkylated homologs are shown by signal distribution labeled with yellow rings, and begin with an m/z of 228.3, with this signal being due to the presence of chrysene and related isomers (**Figure 37 c-d**). Analysis of the UV-Vis spectrum of the monomer fraction eliminates the linear naphthacene as a significant species at 228.3. Analogous to benzofluorene, the distribution has a repeat unit of 14 Da, indicating the addition of alkyl groups up to an m/z of 298.6 (see **Table 2**). Once again, the most prevalent structure has the equivalent of two methyl groups (m/z = 256.5).

PSD was not carried out on the species at 228.3, 242.4, or 284.4 Da because of the difficulty in isolating these signals from those nearby. Fragmentation spectra for the species at 256.2 and 270.2 m/z (see **Figure 39 a-b**) show the loss of methyl groups, which can be due either to the loss of a methyl subsistent anchored directly to the aromatic core or to the loss of a $–CH_3$ group from an ethyl subsistent [90]. As for the benzofluorene series, a signal for de-ethylated ions is observed only for the higher molecular weight species, here for m/z = 298.5, see **Figure 39 c**. A signal (albeit a very small one) for loss of yet another methyl group is also observed at 254.7.

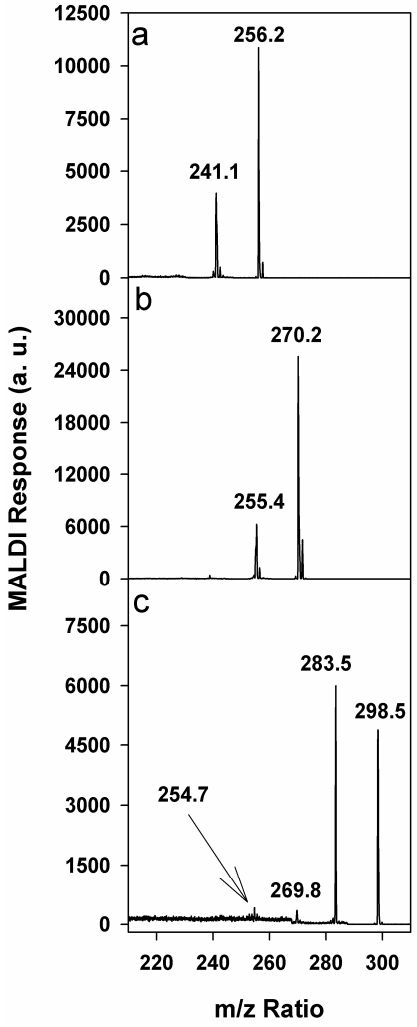

Figure 39. PSD results for the series of PAHs beginning with chrysene and benz[a]anthracene (m/z = 228.3): (a-b) two and three methyl substituents, respectively; (c) limited ethyl substituents are also likely to be present.

The next series of PAHs begins with the signal at 252.4 (**Figure 36**, orange dots) and includes 5-ringed compounds, such as the isomers of benzofluoranthene and also benzo[e]pyrene (see **Figure 37 e-f**), with the presence of the above compounds being consistent with their UV-Vis spectra. As with the previous two series of PAH compounds, a distribution of signals differing from one another by multiples of 14 is observed. PSD results for m/z = 266.5 (see **Figure 40 b**) show no de-methylation peaks, but this is not surprising, as mass spectra for alkylated fluoranthene and pyrene show essentially no tendency for loss of a single methyl group [91,10]. On the other hand, for all species above 266.5, including 280.5, 294.3, and 308.5 (**Figure 40 c-e**, respectively), the loss of methyl groups was observed, and for 308.5, a signal for a de-

ethylated ion is also present. Another PAH series that cannot be ruled out would be isomers of dibenzofluorene, with the base aromatic system having an m/z of 266.5 (see **Figure 37 g**).

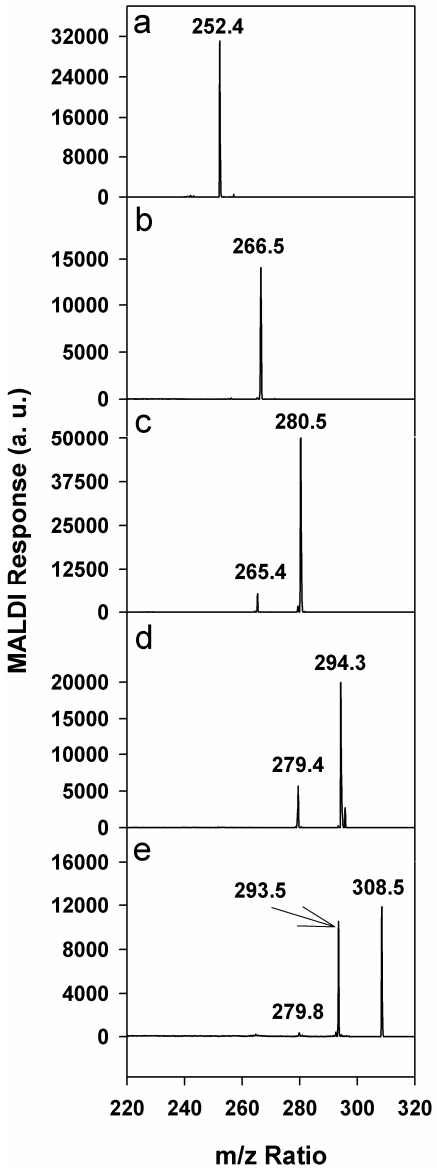

Figure 40. PSD results for the series of PAHs beginning with isomers of benzofluoranthene and with benzo[e]pyrene (m/z = 252.4): (a) base aromatic structure; (b-d) one to three methyl substituents, respectively; (e) limited ethyl substituents may also be present.

All PAH series discussed up to now were prominent in both the 79% and 98% monomer fractions. However, the series beginning at m/z = 278.3 (green triangles, **Figure 36 b**) is essentially absent in the purer fraction, demonstrating how DGE operating conditions can be used to control the composition of pitch fractions.

Typical 5-ring PAHs that would be expected in the 278.3 series are given as **Figure 37 h**, **i**. As shown in **Table 2**, the alkylated homologs of the 278.3 series extend up to 334.5 Da, equivalent to 4 alkyl groups. Signal intensities for species in the 278.3 series were not strong enough to carry out PSD, so we were not able to confirm that all multiples of 14 in the series are, in fact, the result of alkylation. Nevertheless, this was the case for the other three PAH series that were studied, so one would expect the trend to continue.

5.4.5 Analytical and structural characterization of the dimer-rich fractions

The MALDI mass spectrum for the 97% dimer fraction is given in **Figure 41**. FD-MS was also applied to the dimer fraction, and the resulting spectrum was found to be very similar to that obtained via MALDI.

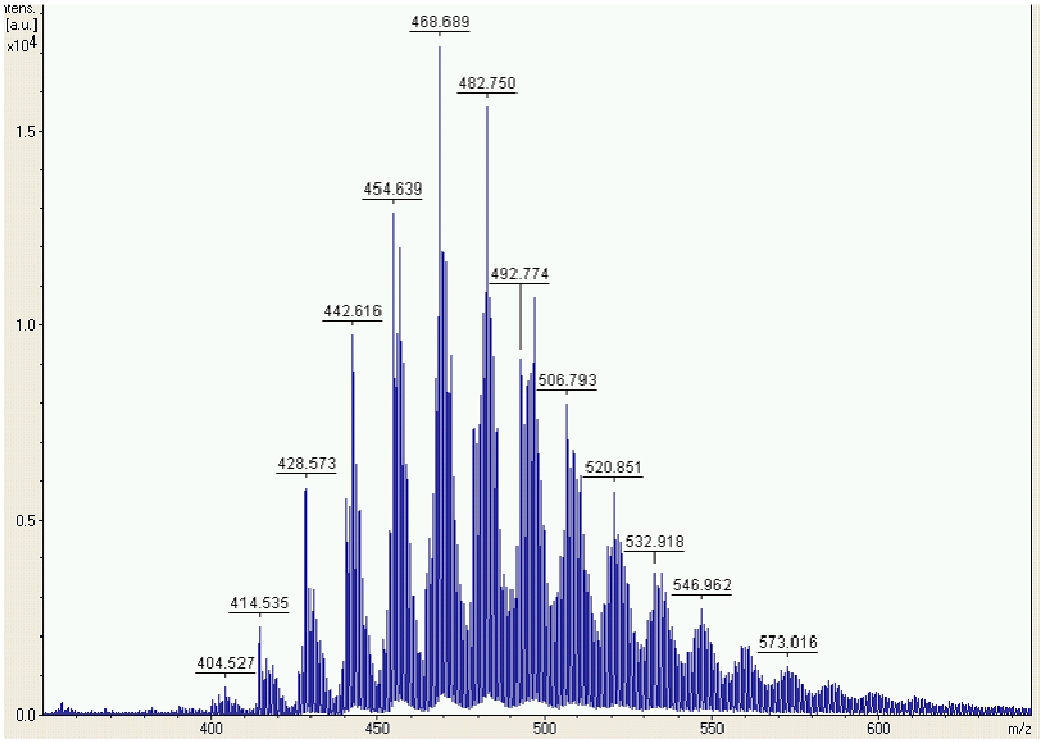

Figure 41. MALDI mass spectrum for the 97% dimer pitch fraction.

The molecular structures of the most prevalent dimer species in the 97% dimer fraction were predicted by assuming dehydrogenation reactions between the most prevalent monomer species in the 98% monomer fraction (see **Figure 37**). Results of

possible combinations are given in **Table 3**, with examples of the resultant dimer structures given in **Figure 42**.

Table 3. Prominent peaks observed in MALDI mass spectrum for 97% dimer (Fig. 15) can be explained by condensation of prominent peaks in MALDI of 98% monomer fraction (Fig. 10).

Monomer Reactant 1 (m/z)	Monomer Reactant 2 (m/z)	Hydrogen Atom Loss	Dimer Product (m/z)
216.4	216.4	4	428.6
216.4	230.3	4	442.6
216.4	244.5	6	454.6
228.3	230.3	4	454.6
216.4	244.5	4	456.7
230.3	244.5	6	468.7
228.3	242.4	2	468.7
244.5	244.5	6	482.8
230.3	256.5	4	482.8
216.4	280.5	4	492.8
244.5	256.5	4	496.8
256.5	256.5	6	506.8
244.5	280.5	4	520.9

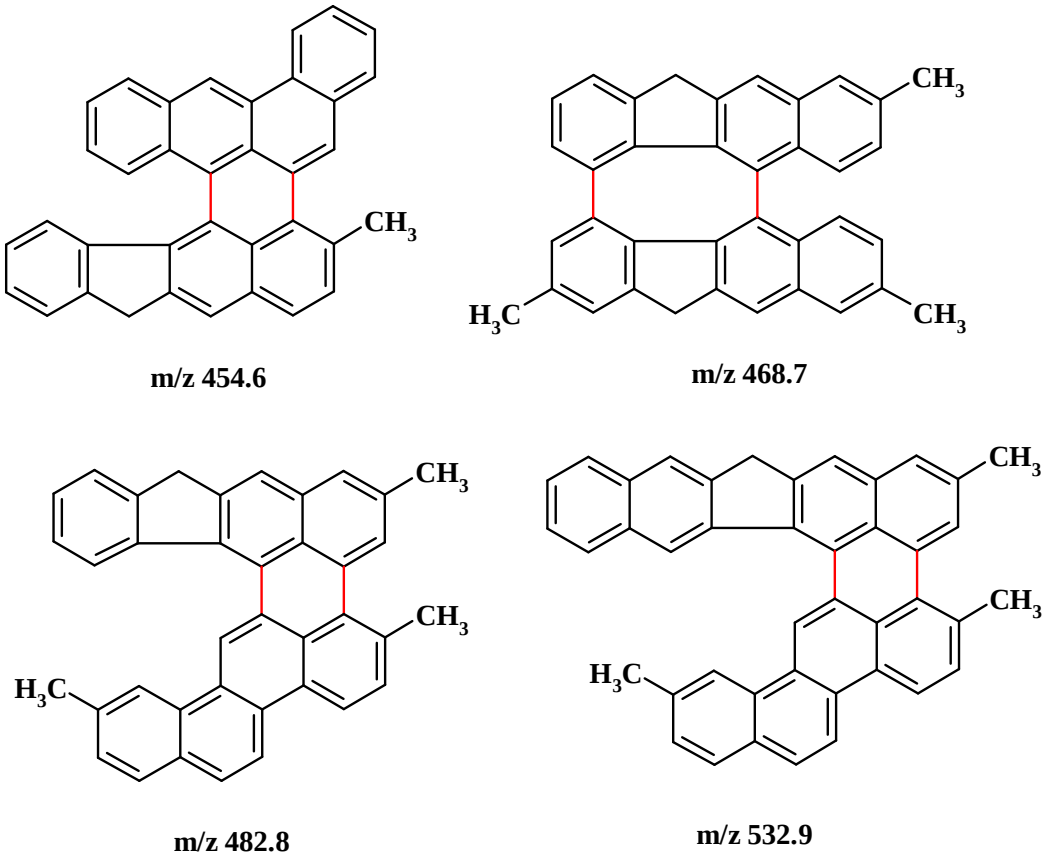

Figure 42. Proposed PAH structures for the major constituents in the 97% dimer fraction, see Table 3.

Comparison of the data reported in **Table 3** with the dimer spectrum in **Figure 41** reveals several interesting points: (1) Condensation reactions, with the elimination of 4-6 hydrogen atoms, were successful in predicting the origin of the most prevalent dimer species. (2) The geometry of the monomer "reactants" is such that the formation of dimers from the loss of larger amounts of hydrogen (e.g., 8-10 atoms) would be unlikely. Consistent with this observation is the fact that assuming the loss of larger amounts of hydrogen from condensation of the most prevalent monomer species did not produce the major dimer species observed in the spectrum. (3) The benzofluorene (m/z = 216.3) monomer seems to have participated in the formation of dimer more than can be explained by its concentration in **Figure 36 a**. This can be explained by the loss of methyl group(s) from the alkylated homologs of benzofluorene, with this loss being the initiation step for the condensation reaction. Another possible explanation is that the distribution of monomeric species in the pitch is no longer similar to its amount in the pitch precursor because of the different

reactivities of the various monomeric species; thus, the benzofluorene may have been more prevalent in the original monomeric starting material. (4) Referring to the structures in **Figure 42**, the most prevalent dimer species formed are not highly condensed. There should be a greater loss of H atoms than what is observed. In addition, with most methyl groups being β-substituted, reactions at these sites would also tend to produce a not fully condensed PAH backbone structure.

UV-Vis spectra of the 97% dimer fraction (**Figure 32**) also supports the existence of not fully condensed PAH structures. A massive presence of extended aromatic structures in the dimer-rich vs. the monomer-rich fractions would drastically shift the absorption of visible light to higher wavelengths [92]. However, the "red shift", although observable, is relatively small.

5.5 Mass analysis of high molecular weight components of M-50 pitch

According to Montaudo et al. [93-94], MALDI-TOF-MS can be used for the characterization of the molecular weight distribution of synthetic polymers with narrow polydispersity (D < 1.3). On the other hand, MALDI fails in reporting reliable information on the weight distribution of polymer with higher polydisperisty. Due to detector saturation phenomena and other discrimination effects, described in Chapter 3, the analytes with higher molecular weight are not detected or severely underestimated in the resulting MALDI spectrum. To check the presence of higher molecular weight components, polymer fractionation or suppression of the lowest molecular species is therefore required.

Within this investigation the low mass oligomers from a sample of pitch M-50, already deprived from its monomer content, were suppressed via detector gating to check the presence of pitch oligomers at higher masses.

In **Figure 43** different MALDI spectra of the same pitch sample are shown. The spectra differ from each other by the application of different detector gating setting: at m/z of 0 (red trace), at m/z of 700 (black trace) and at m/z of 1600 (green trace), respectively.

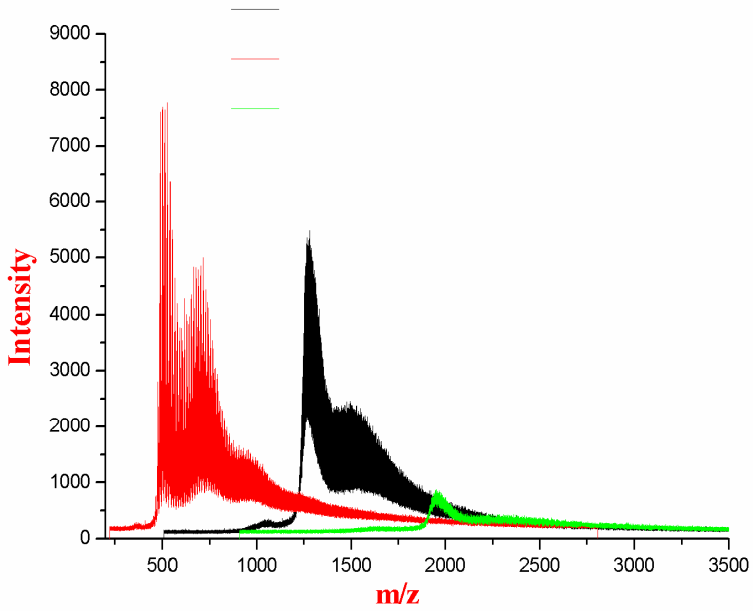

Figure 43. Detection of high mass oligomers present in the pitch sample by using detector gating (red trace: dimers, trimers and tetramers, black trace: pentamers, hexamers and heptamers, green trace: heptamers and octamers).

It is worth noting that the detection of completely underestimated species up to octamers is detectable.

5.6 Quantification of pitch M-50 via MALDI-TOF-MS

Quantification of the content of monomer, dimer, trimer and tetramer belonging to the pitch M-50 sample was achieved via coupling dense gas extraction to MALDI-TOF-MS to fractionate and characterize the pitch sample.

Continuous DGE was used to deliver three separated pitch fractions enriched in monomer, dimer and in trimer, respectively. Supercritical toluene (P_C: 41.1 bar, T_C: 318.6 ^{0}C) was used as extraction solvent for all the DGE experiments.

According to a previous study [77] to simplify the quantification procedure, this investigation was restricted to the study of binary mixtures obtained by mixing the monomer-rich with the dimer-rich fractions (Set 1) and the dimer-rich with the trimer-rich fractions (Set 2) in defined amount.

Normalized MALDI spectra for these three fractions are shown in **Figure 44**.

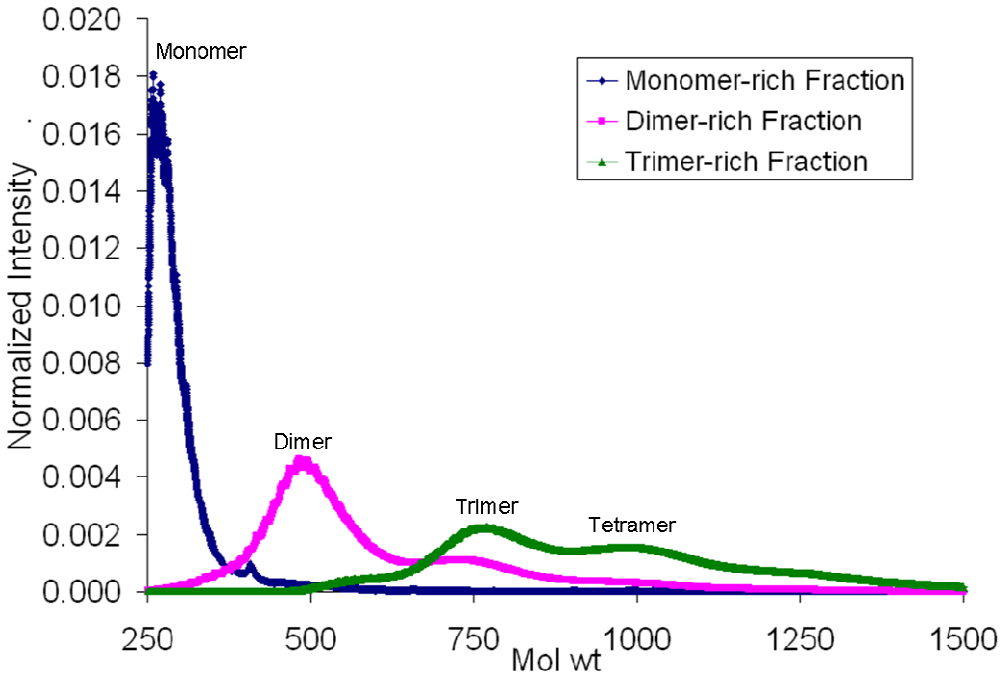

Figure 44. Normalized MALDI spectra for Monomer-rich, Dimer-rich, and Trimer-rich fractions.

5.6.1 Analysis of monomer-rich/dimer-rich mixtures (Set 1)

Monomer-rich and dimer-rich fractions were blended together to obtain mixtures of known compositions. To overcome the homogenization problems in preparing the blends, caused by the sticky nature of the monomer-rich fraction, the monomer itself and the blends were cooled in liquid Nitrogen to guaranty the effective milling of the components with the MALDI matrix. Six different blends were prepared and for each blend MALDI analyses were performed. **Figure 45** displays the corresponding MALDI spectra.

The corresponding monomer/dimer area ratios were evaluated from the spectra and reported in a graph vs. the related monomer/dimer molar ratios (see **Figure 45 b**).

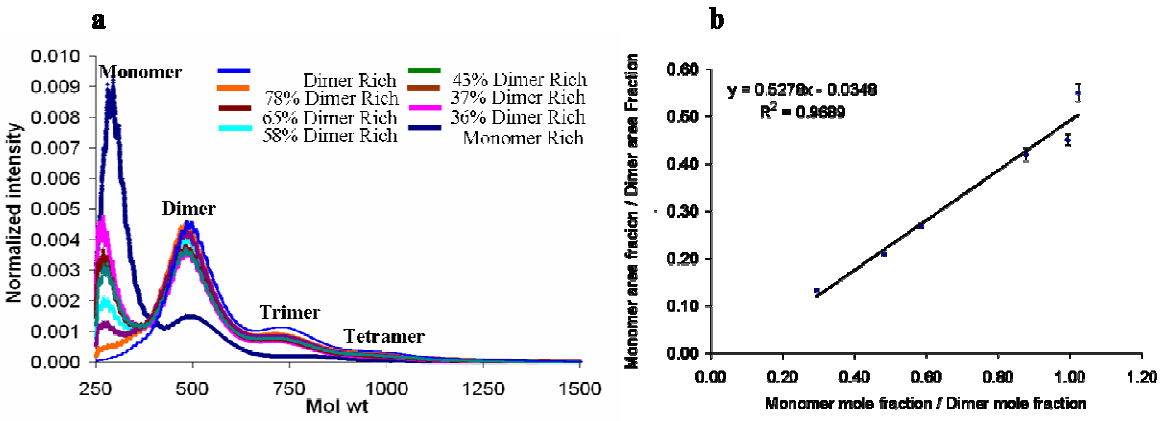

Figure 45. a) Normalized MALDI spectra of monomer-rich/dimer-rich mixtures with different molar ratios. b) Calibration curve for the monomer/dimer mixtures.

The data points of **Figure 45 b** can be interpolated by a straight line with correlation coefficient R^2 of 0.9689 and equation y= 0.5278x-0.0348.

The slope, lower than 1.0 of the straigth line in **Figure 45 b**, indicates the tendency of the MALDI process to overestimate the dimer-species. This phenomenon can be justified considering the different absorption behavior of monomer-rich and dimer-rich fractions of the laser light, as shown in **Figure 32**. The weaker absorption of the monomer at 337 nm comports a lower photoionization efficiency, which justifies its underestimation according to the relationship in **Figure 45 b** [77, 65].

5.6.2 Analysis of dimer-rich/monomer-rich mixtures (Set 2)

Similarly to the procedure employed for Set 1, the isolated dimer-rich and trimer-rich fractions were mixed in different known amounts to build a suitable calibration curve for the pitch M-50 sample. For each of the eight mixtures a MALDI spectrum was recorded, as reported in **Figure 46 a**.

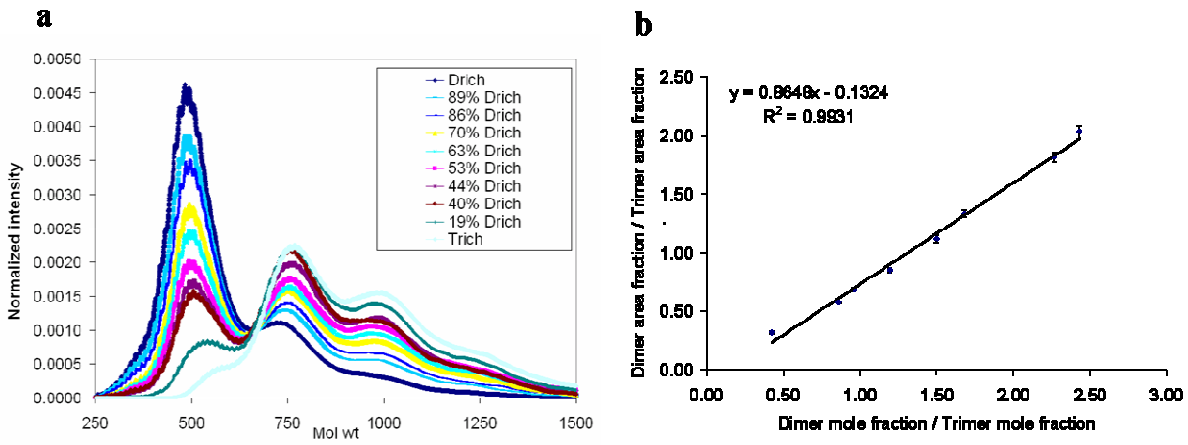

Figure 46. a) Normalized MALDI spectra of dimer-rich/trimer-rich mixtures with different molar ratios. b) Calibration curve for the dimer/trimer mixtures.

Then, the corresponding dimer/trimer area ratios were evaluated from the spectra and reported in a graph vs. the related dimer/trimer molar ratios (**Figure 46 b**). The data points could be interpolated by a straight line with a satisfactory correlation coefficient ($R^2 = 0.9931$) and equation y = 0.8648 x - 0.1324.

Similarly to the results obtained for Set 1, the slope of the straight line in **Figure 46 b** is lower than one. This indicates most probably the overestimation of trimer, due to an increased ionization probability.

Note that the two relationships for the binary mixtures, monomer/dimer and dimer/trimer, take the under/over estimations into consideration and provide quantitative information of monomer, dimer, and trimer present in the mixture even with unknown oligomeric composition.

From the experience with DGE of petroleum pitches, we know that monomer, dimer, and trimer, combined together, comprise of 80 to 85% of the M-50 petroleum pitch. Therefore, by getting information about the mole fractions of monomer, dimer, and trimer, we can achieve quantitative information for any pitch sample with an accuracy as high as 85%.

5.7 Conclusions

The characterization of petroleum pitches on a molecular level has long been a difficult task, but the separation of the pitch into its oligomeric fractions via dense-gas extraction (DGE), followed by the application of both new and conventional spectrometric and spectroscopic techniques to those fractions, has given us new capabilities for identifying the specific molecular structures in petroleum pitches. The monomer-rich fraction is approximately Gaussian with respect to molecular weight distribution and is dominated by species that are built upon a relatively small number of well defined, PAH backbone structures. Methyl and, to a very limited extent, ethyl groups decorate these backbones in an approximately Gaussian distribution, with 2 methyl groups/PAH molecule being the most common molecular makeup. The overall molecular weight distribution of the dimer fraction is also approximately Gaussian, and the most prevalent species are consistent with combination of the most common monomer species via condensation, with the accompanying loss of 4-6 hydrogens.

After defining the structures of the main pitch components, this study moved to the quantification of the amount of monomer, dimer, trimer and tetramer belonging to the pitch sample via solvent-free MALDI-MS. The chosen strategy consisted in coupling the DGE process with the MALDI analysis and proceeded through the following steps: 1) DGE was employed to fractionate the pitch sample, and 2) MALDI analyses of mixtures, prepared with known amounts of pitch components, were carried out to obtain calibration curves for the quantitative characterization of the pitch M-50 sample. The two obtained relationships take the under/over estimations into consideration and provide quantitative information on monomer, dimer, and trimer present in the mixture with unknown oligomeric composition. These relationships are linear in nature and can be used as calibration curves for the quantitative analysis of the petroleum pitch samples.

5.8 References

[79] Y. V. Basova, D. D. Edie, P. Y. Badheka, H.-C. Bellam *Carbon*, **2005**, 43, 1533.

[80] M. E. Beauharnois, D. D. Edie, M. C. Thies *Carbon*, **2001**, 39, 2101.

[81] A. A. Herod, K. D. Bartle, R. Kandiyoti *Energy and Fuels* **2007**, 21, 2176.

[82] F. M. Dauché, G. Bolanos, A. Blazic, M. C. Thies *Carbon* **1998**;, 36, 953.

[83] M. Zhuang, K. Gast, M. C.Thies *Ind Eng Chem Res* **2002**, 41,78.

[84] W. F. Edwards, M. C. Thies, *Carbon* **2005**, Volume Date 2006, 44, 243.

[85] A. Cristadoro, H. J. Räder, K. Müllen, *Rapid Comm. in Mass Spectrometry*, **2008**, in print.

[86] E. Cervo, M. C. Thies *Chem. Eng. Technol.* **2007**, 30, 742.

[87] Jinno Laboratory, School of Materials Science, Toyohashi University of Technology, Toyohashi, Japan. http://chrom.tutms.tut.ac.jp/JINNO/DATABASE/00alphabet.html (accessed June **2008**).

[88] R. M. Silverstein, F. X. Webster, D. Kiemie Spectrometric Identification of Organic Compounds, 7th Edition. John Wiley & Sons Ltd, Chichester, UK. 2002, p. 87.

[89] National Institute of Standards and Technology (NIST) Chemistry WebBook. http://webbook.nist.gov/chemistry/ (accessed June **2008**).

[90] R. M. Silverstein, F. X. Webster, D. Kiemie Spectrometric Identification of Organic Compounds, 7th Edition. John Wiley & Sons Ltd, Chichester, UK. 2002, p. 14 and 18.

[91] CAS SciFinder. http://www.cas.org/products/scifindr/index.html (accessed June **2008**)

[92] Y. Avlasevich, C. Kohl, K. Müllen, *J. Mater. Chem.* **2006**, 16, 1053.

[93] G. Montaudo, F. Samperi, M S. Montaudo *Progress in Polymer Science*, **2006**, 31, 277.

[94] G. Adamus, P. Rizzarelli, M. S. Montaudo, M. Kowalczuk, G. Montaudo, *Rapid Communications in Mass Spectrometry*, **2005**, Volume Date 2006, 20, 804.

6 Soft-landing Mass spectrometry

6.1 Introduction

Low-energy (1-100 eV) hyperthermal ion beams can be soft-landed on surfaces to modify their properties in a controlled fashion [95-96].

Collisions of low-energy ions with surfaces that result in ion soft-landing (SL) may be regarded as the capture of intact mass-selected polyatomic ions at solid or liquid surfaces [97-[98-33]. The term SL has been used to describe two distinct processes, one in which neutralization occurs during ion-surface collision and one in which the ion preserves its charge. The study, reported in this chapter, is concerned with the first phenomenon. The discharge process is determined by the nature of the deposition surface. Its physical and chemical properties play a crucial role in determining the outcome of ion-surface collisions. Neutralization is a dominant process in collisions of ions with clean metal surfaces. Thus, as mainly metallic surfaces were employed for the soft-landing studies reported here, one can assume that the ions lose their charge touching the surface and no retention of charges occurs.

In these experiments, mass spectrometry serves as a method of separation based on physical principles that are different from and complementary to those employed in more conventional separation methods. Soft-landing mass spectrometry allows in fact ionization of the analytes and their deposition on conducting surface after purification due to the mass/charge selection of an analyzer.

When a polymer is ionized, the analyzer can be used not only for removing possible impurities, but also for selecting single chains from the polymer distribution. On the other hand, when full-aromatic rod-like molecules are ionized, the analyzer allows not only elimination of by-products or starting materials, but also the isolation of single isotopes and their deposition as intact molecules on a conducting surface. Aim of this study is to investigate the conditions for the deposition of intact mass-defined polymer chains and the morphology of the soft-landed films obtained thereof. For these experiments poly(ethylenoxide) oligomers (PEO) were chosen as a model system and landed on a gold surface.

Moreover, dibenzo[b,b']thieno[2,3-f:5,4-f']carbazole (DBTC) molecules, as an example for rod-like and polar molecules, were also soft-landed to grow thin and crystalline films, which could be studied via diffraction and morphological analyses. The packing of the DBTC molecules in soft-landed film was then compared to that of

a reference film obtained via drop-casting. For all the experiments presented in this study, liquid secondary ion mass spectrometry (LSIMS) was selected for the ionization of the analytes.

6.1.1 The soft-landing apparatus

The success of a soft-landing deposition and the number of molecules, which are landed on a surface with retention of their structures, is determined by the correct selection of the apparatus geometry and by the convenient tuning of the landing parameters.

Within this work, the soft-landing apparatus was assembled as following:

1) Liquid secondary Ion Mass Spectrometry as ionization source;
2) A double focusing sector field analyzer for the ion selection;
3) A decelerating unit;
4) A deposition unit.

A schematic representation of the employed soft-landing apparatus is reported in **Figure 47**.

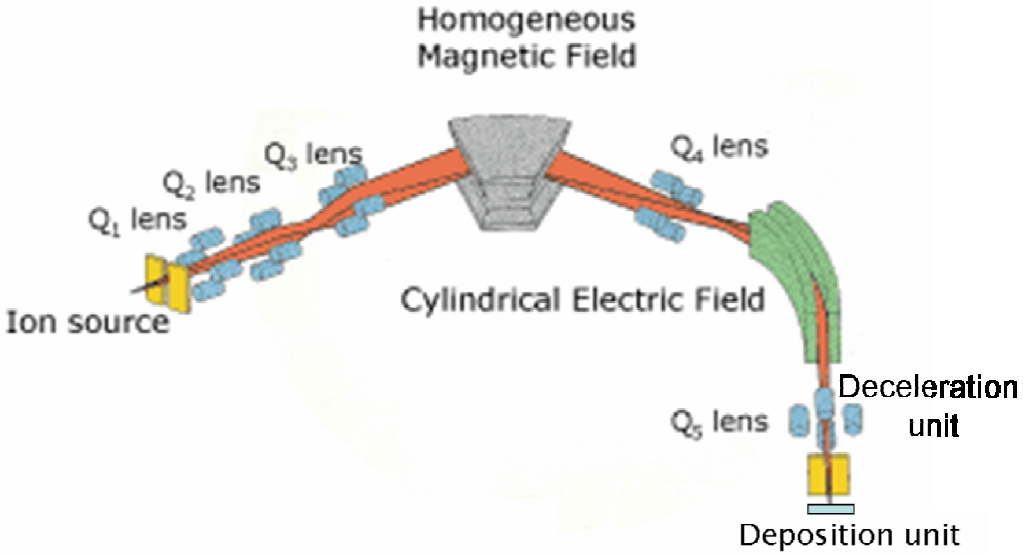

Figure 47. Schematic representation of the soft-landing apparatus.

1) Why LSIMS?

In LSIMS, secondary ions are formed by bombarding an analyte/matrix coated surface with high energy primary ions. Bombarding the liquid matrix/analyte mixture with primary ions (usually Cs^+ at 35 keV) results in the formation of matrix ions and leads to indirect sample ionization. The use of liquid matrix, such as 3-nitrobenzylalcohol (3-NBA), allows the desorption of intact ions with masses up to 10000 Da. Furthermore, the liquid mixture of matrix and analyte allows the use of a continuous flow source, which guarantees the continuous formation of ions for relatively long period of time. Coupling continuous flow LSIMS with SL should increase the number of soft-landed molecules collected on the deposition surface. This is a prerequisite for the soft-deposition of monolayers or multilayers of molecules. Consequently, LSIMS was used in this work for the soft-deposition experiments.

2) Why using a double focusing sector field analyzer?

The selection of the double focusing sector field as analyzer unit in this work is justified by the high signal resolution, which this geometry guarantees [99]. The double focusing sector field comprises a magnetical field analyzer followed by an electrical field analyzer.

The ions can be focused outside the first analyzer when the centrifugal force is equal to the magnetical force generated by a magnetical field B_1. As described by **Equation 1** only ions with mass to charge ratios equal to m_1/ze can reach the decelerating unit.

$$\frac{m_1 v_1^{\,2}}{r_1} = Bzev_1 \rightarrow \quad \text{centrifugal force = magnetical force} \qquad \textbf{Equation 1}$$

The ions, which pass through the first analyzer, are then additionally filtered by an electrical sector field unit. This is an energy analyzer, which discriminates the ions depending on their different kinetic energy. For a given electrical field E_1 only the ions possessing mass to charge ratios of m_1/ze can be directed in the focus point of the analyzer obeying to the following formalism (**Equation 2**):

$$\frac{m_1 v_1^{\,2}}{r_1} = E_1 ze \quad \rightarrow \quad \text{centrifugal force = electrostatic force} \qquad \textbf{Equation 2}$$

where v_1 is the ion speed and r_1 the radius of curvature of the ions under the influence of an electrical field E_1.
The benefit of the double focusing sector field analyzer is the extremely precise m/ze selection, which guarantees even isotopic resolution.

3) Decelerating potential for a soft-deposition

After the purification step, carried out via the analyzer, the ions can reach the deceleration unit. Here, deceleration potentials avoid their crash-landing on the desired surface. According to Cooks et al. [95], the range of energy, which allows landing of ions avoiding crash, is comprised between 10 and 100 eV. At higher and lower energies different processes take place [95], as shown in **Figure 48**.

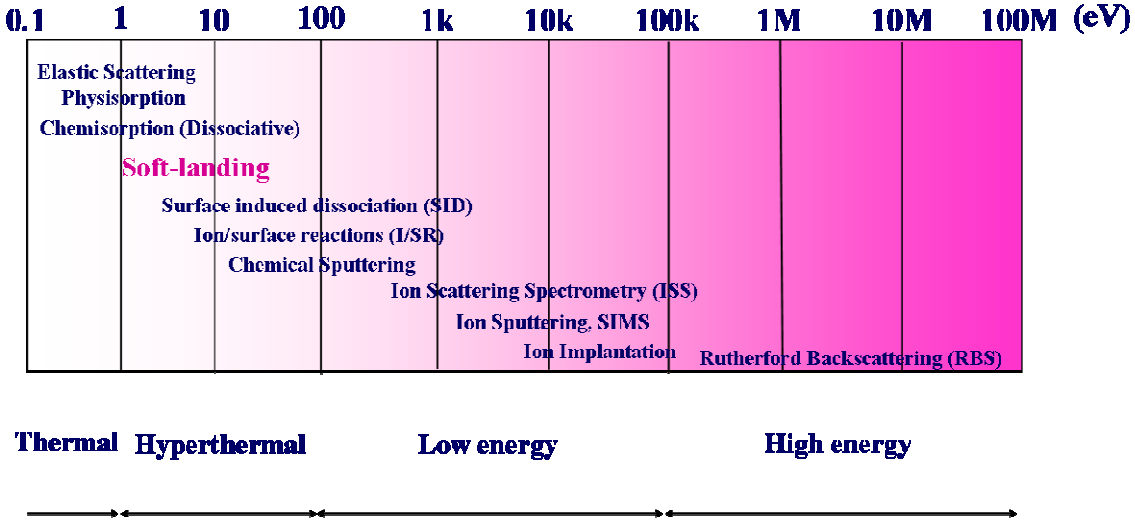

Figure 48. Encountered processes during deposition of ions with different landing energies.

However, according to the experiments conducted by Yang et al. [100], focused principally to the soft-deposition of polycyclic aromatic hydrocarbons and oligomers, SL can be performed up to a landing energy of 180 eV without production of fragments. Yang et al. recognized however a maximum in the amount of soft-landed molecules via using a landing energy comprised between 60 and 80 eV. For higher energy values, they reported a decrease in the amount of landed molecules, probably due to rebounding or sputtering processes, as no fragments of the ions were detected.

Thus, for this investigation landing energies of 70 eV on average were chosen.

4) Ion collection and deposition substrates

After deceleration of the ion beam by means of decelerating potentials, the ions, possessing a residual energy of 70 eV, can reach the deposition surface intact and are focused by means of focusing potentials into an area as large as 1 x 1 mm^2.

The choice of an appropriate landing surface is of huge importance as it determines the discharging process of the ion beam. By choosing an earthed metallic surface, the ions release their charge to the conducting substrate. Thus, pure and intact molecules are collected.

Within this study, different deposition surfaces were used: 1) A modified stainless steal surface, on which a thin layer of TCNQ molecules was deposited via thermal sublimation. 2) Gold and HOPG for the morphology studies of the soft-landed thin films. 3) Carbon-coated copper grid for performing electron diffraction analyses.

The deposition of analytes was at first carried out onto a TCNQ-coated metallic substrate (see **Figure 49)**. The dimensions of the target were designed such that it could fit in a modified sample holder for MALDI analyses. After each deposition, the procedure, schematized in **Figure 49**, was followed: 1) the target was taken out from the soft-landing apparatus and brought in the ionization source of a MALDI instrument. 2) Here, the entire deposition target was scanned by using a movable sample holder when performing MALDI analyses. 3) Once reached the focus point, the analyte signal was detected and a spectrum was recorded. The thin TCNQ layer, which covered the metallic target, allowed measuring MALDI spectra of the analyte without risk of damage and fragmentation of the landed molecules due to direct exposition to the nitrogen laser light (337 nm). 4) To mark the area, in which the analyte signal was detected, the intensity of the MALDI laser beam was increased so much that a part of the thin TCNQ/analyte film could be removed. For demonstration reasons, the laser beam was in **Figure 49** used to write the logo MPI on the metallic deposition target modified with TCNQ.

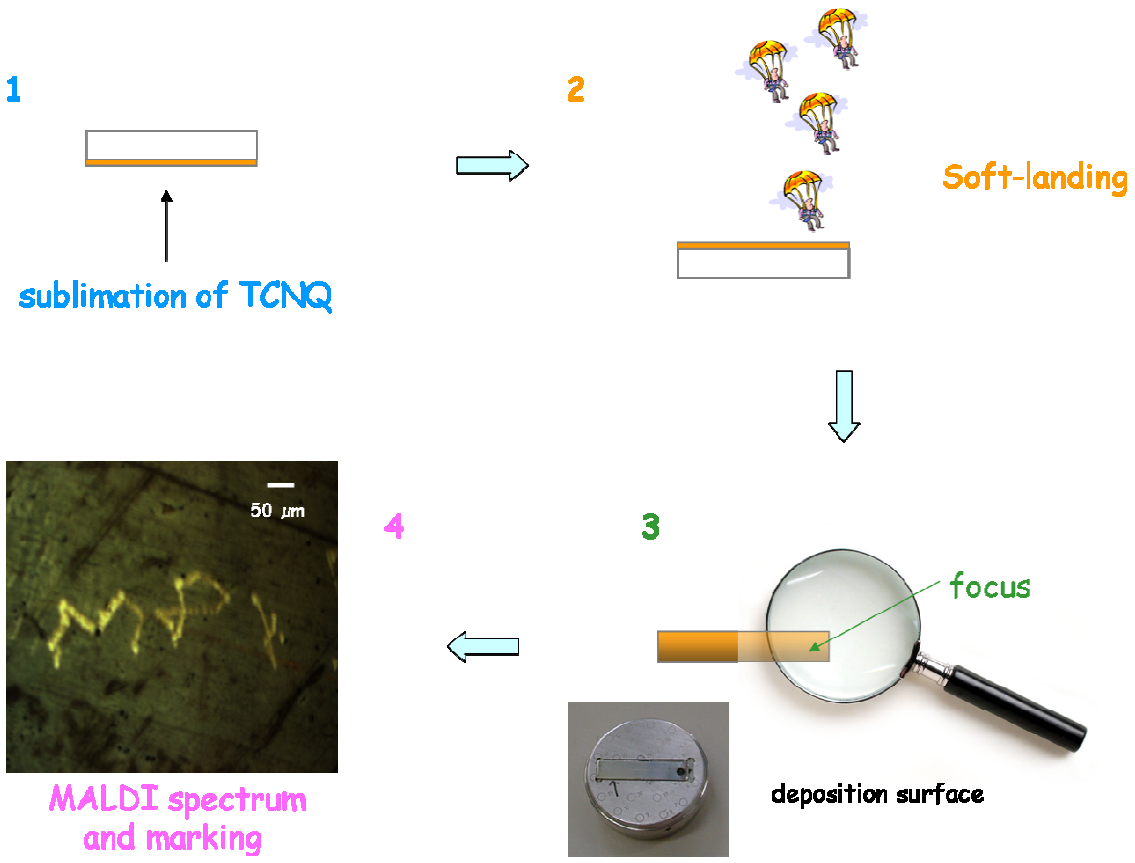

Figure 49. Schematic representation of the required procedure for the visualization of the analyte molecules, deposited via Soft-landing mass spectrometry.

Note that the optical identification of the focus point was a necessary requirement to study the morphology of the films of soft-landed molecules. The other deposition surfaces (gold, HOPG and carbon coated cupper) were in fact placed, before performing the deposition, onto the identified focus point of the collection target. Then, after soft-landing of the analye, they were differently analyzed.

6.2 Deposition of mass-defined polymer chains

6.2.1 Why PEO oligomers?

Using LSIMS as ionization source for the soft-landing experiments required the choice of polar polymers, which could be mixed with the 3-NBA matrix and

transferred into the gas phase. PEO oligomers fulfilled these conditions; consequently, they were selected as a model system in this investigation.

Before performing the soft-landing deposition, a MALDI spectrum of the selected PEO oligomer was recorded.

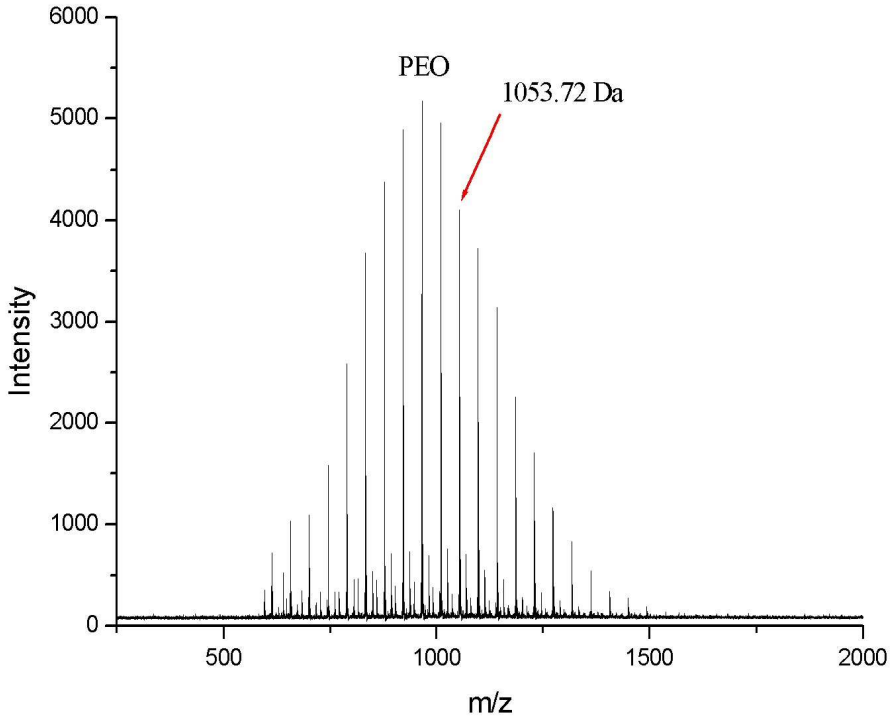

Figure 50. MALDI spectrum of PEO in TCNQ matrix before soft-landing.

As shown in **Figure 50**, the selected PEO oligomers have a narrow polymer distribution (polydispersity index = 1.14). This guaranteed the desorption/ionization of the highest number of polymer chains with comparable molar mass. Consequently, it allowed the soft-deposition of the highest number of polymer chains on the landing substrate.

In the mass spectrum reported in **Figure 50**, three polymer distributions with different intensity are present. PEO chains desorb via cation-attachment as adduct of the type $[PEO: Na]^+$ (higher signal intensity) and $[PEO: K]^+$ (weaker signal intensity). The difference in signal intensity is due to a higher Na^+ affinity of the PEO chains, which leads to the preferential desorption of sodiated PEO clusters.

To determine the nature of the terminal groups of the PEO chains, the mass of one PEO chain (e.g. m/z 1053.7, see **Figure 50**) was divided by the mass of the PEO repeating unit:

Repeating unit of PEO: 44.0 Da

1053.7 Da / 44.0 Da = 23.9

Consequently, 23 repeating units of PEO belong to the chains with molar mass 1053.7 Da. The difference between the calculated mass for 23 repeating units of PEO (23 x 44.0 Da = 1012.6) and the recorded one, corresponds to the mass of the PEO terminal group plus that of the cationizing salt.

1053.7 Da = 23 x **44.0** Da (**-CH_2CH_2O-**) + **23** Da (**Na**) + **18** Da (end group **HO**-$(CH_2CH_2O)_n$-**H**)

The calculation above let to conclude that the PEO oligomer chains at 1053.7 Da are –H, –OH terminated. Moreover, the MALDI reported in **Figure 50** reports the presence of a third distribution of low intensity, which can be assigned to the presence of cyclic polymer chains, which desorb as adduct with Na^+.

As the distribution of chains H-OH terminated is the most abundant in the MALDI spectrum of **Figure 50**, one of the oligomer chains of higher intensity (m/z 1053.7) was selected for performing soft-landing experiments.

Via tuning the analyzer parameters, only the mass-selected chains with m/z of 1053.7 were deposited on a TCNQ-modified metallic target. After a deposition time of 7 hours, the presence of the mass-selected PEO chains was verified by performing MALDI analysis.

The corresponding MALDI spectrum is reported in **Figure 51**.

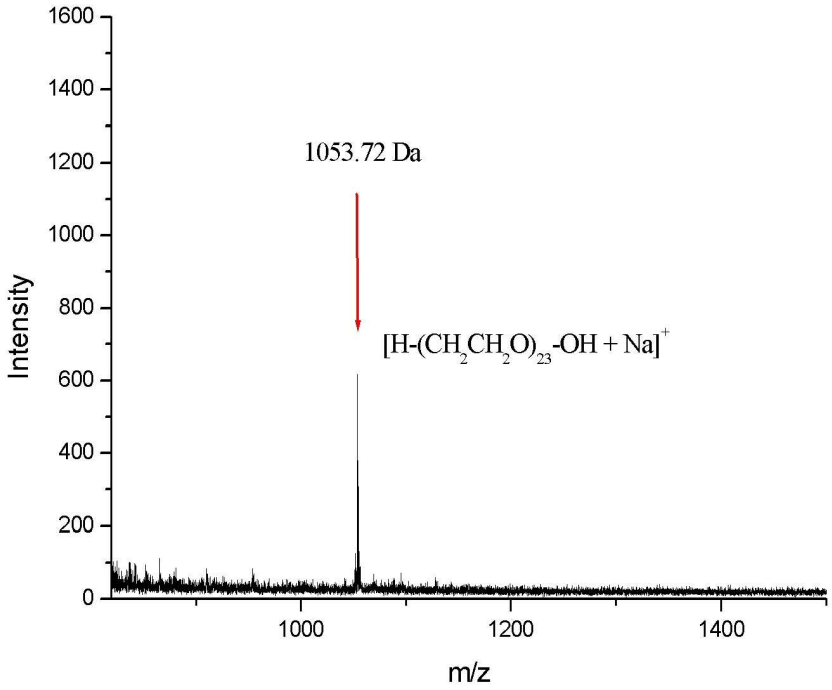

Figure 51. MALDI spectrum of mass-selected PEO chains in TCNQ matrix after soft-landing.

The presence of single chains of the desired mass (m/z 1053.7) shows the successful deposition of mass-defined polymer chains via soft-landing mass spectrometry.

6.2.2 Morphological analysis of soft-landed PEO films

To study the morphology of soft-landed PEO films, soft-landing deposition was performed for 7 hours on gold-coated mica surface. Then, atomic force microscopy analyses were performed. The corresponding AFM micrographs are shown in **Figure 52**.

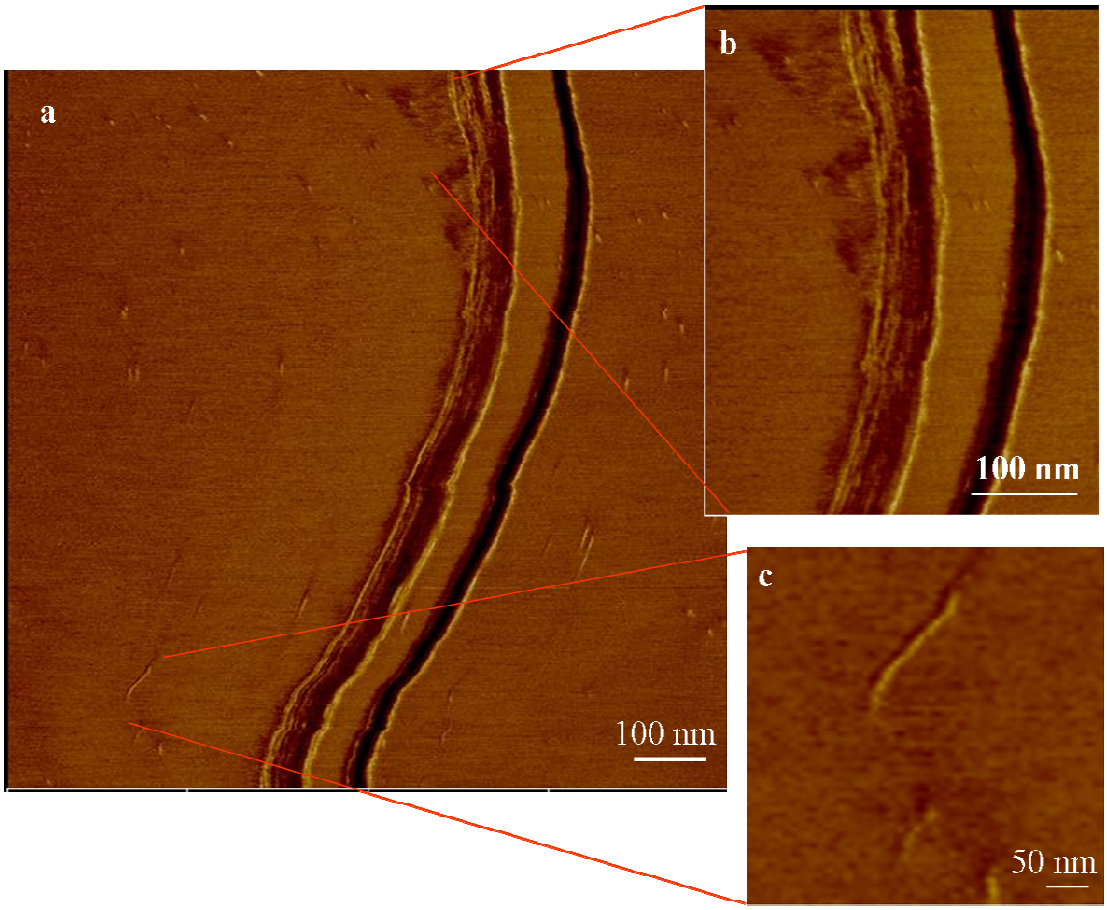

Figure 52. AFM phase micrograph of a soft-landed film of mass-defined polymer chains.

The AFM micrograph of **Figure 52** shows the presence of fibers which consist of thin fibrillae, having an average width of 8 nm. Assembly of PEO chains in fiber-like structures has been reported by Kakade et al. [101] in the characterization of PEO films prepared via electrospinning. In electrospinning experiments [102], the polymer solution is sprayed on top of a conducting surface by means of a syringe in presence of an electrical field (~ 1-3 kV/cm). In that study, the influence of the electrical field on the polymer chains was considered responsible for the formation of fiber-like structure.

The formation of PEO fibers in soft-landing experiments is likely related to the presence of electrical fields of comparable intensity to that used in electrospinning experiments, which are generated by the decelerating voltages, necessary to avoid fragmentation of the ions reaching the surface. The positively charged single polymer chains are repelled from the positive-charged collecting substrate. Thus, once landed on the deposition substrate, they still possess high mobility and freely migrate until they reach a small surface inhomogeneity. There, they start aggregating with other

polymer chains and generate fibers. Note in fact that the assembly of the PEO chains in fiber-like structure occurs close to a roughness inhomogeneity of the gold surface.
Moreover, it is interesting to point out that the fibrillae composing the fibers are of uniform width. This may be related to the identical length of the mass-selected PEO chains (9.36 nm in completely stretched conformation). It is plausible to assume that the polymer chains are assembled with their backbone almost perpendicular to the fibrilla axis, as the measured width of the fibrillae agrees well within the experimental error to the calculated length of the PEO chains.
It is worth noting that the purification conditions ensured by soft-landing are unique as the isolation of polymer chains of selected masses cannot be achieved by traditional separation techniques, such as GPC or dialysis. The study of the morphology of films composed of mass-selected polymer chains can therefore be performed only when the thin polymer films are prepared via soft-landing. Soft-landing deposition can thus be regarded as a completely novel tool to produce polymer films with extraordinary purity and unique morphology. In fact, the mass selection of the PEG chains combined with the presence of the strong electrical field, which decelerates the positively charged PEG ion beam, are in this work supposed responsible for the formation of fibrillae-like structures possessing a uniform width.
Moreover, the great advantage of the soft-landing technique is the vacuum deposition of molecules possessing a molecular weight, which is critical for thermal sublimation. The soft-ionization source, used in these experiments, allows in fact, the soft-ionization of the polymer chains without risk of fragmentation.

6.3 Deposition of ultra-thin films of rod-like molecules

6.3.1 Dibenzo[b,b']thieno[2,3-f:5,4-f']carbazole (DBCZ) molecules as a model system.

As already specified for the SL deposition of PEO chains, the use of LSIMS, as ionization source, restricts the choice of a suitable analyte to molecules which possess high polarity due, for example, to the presence of hetheroatoms in their structure. Analytes with high polarity can be in fact mixed with the NBA matrix, required for LSIMS, and can be ionized with high yield to ensure adequate coverage of the deposition surface. DBCZ molecules satisfied these requirements. Thus, they

were chosen as a representative system for rod-like molecules in this investigation. Their molecular structure is reported in **Figure 53**.

m/z = 463.7

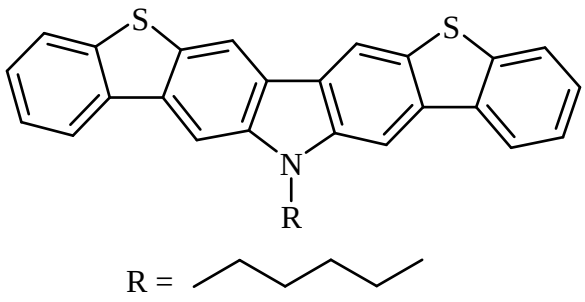

Figure 53. Molecular structure of Dibenzo[b,b']thieno[2,3-f:5,4-f']carbazole molecules

Moreover, DBCZ molecules are soluble in the most of the organic solvents due to the presence of alkyl chains ($-C_6H_{13}$). This allowed comparing the packing of the molecules in soft-landed polymer films to that of drop-cast reference samples. The choice of preparing a reference sample via solution processing techniques instead of using vacuum-based deposition (e.g. thermal evaporation) was made due to the possibility to grow from solution single crystals of the analyte for gaining information about the DBCZ molecular packing.

6.3.2 Soft-landing of DBCZ molecules

DBCZ molecules were first soft-landed on a stainless steal surface previously covered with a thin layer of TCNQ molecules, for a deposition time of two hours. Before performing the soft-landing deposition, a MALDI spectrum of the analyte was recorded (see **Figure 54 a)** and showed the natural isotopic distribution of the DBCZ molecules. The signal of the analyte appears at m/z of 463.6, which is the calculated mass value for a DBCZ molecule. This means that the analyte desorbs as radical cation and no cation attachment occurs. The most abundant isotope belonging to the analyte, possessing an m/z value of 463.7 (pointed by an arrow in **Figure 54 a**), was chosen for soft-landing deposition. Via tuning the sector field analyzer, the mass to charge value (m/z) of 463.6 was selected and the single isotopes were collected as intact molecule on the deposition surface.

A MALDI spectrum was recorded to verify the success of the deposition experiment and it is reported in **Figure 54 b**.

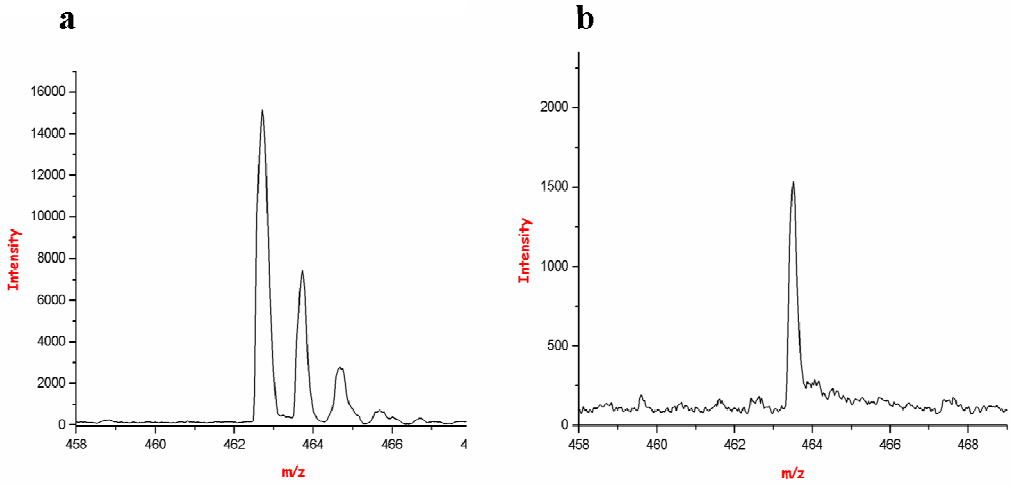

Figure 54. a) MALDI spectrum of DBCZ molecules before soft-landing. b) MALDI spectrum of DBCZ after soft-landing.

The two MALDI spectra of **Figure 54** differ for the number of displayed isotopes. In the spectrum recorded after soft-landing only the selected isotope is present. This demonstrates that the soft-landing deposition proceeded successfully and no sublimation took place. Soft-landing experiments require, in fact, high vacuum and under these conditions, sublimation of volatile species can occur. The sublimation process, however, should bring on the deposition surface molecules possessing their natural isotopic distribution. As demonstrated by the MALDI of **Figure 54 b**, sublimation can be ruled out.

6.3.3 Electron diffraction analyses of DBCZ films

In order to perform a comparative investigation on the packing of the DBCZ molecules deposited on a conducting surface via soft-landing with respect to the packing of the same molecules deposited via drop-casting, two sets of electron diffraction experiments were carried out.

1) At first, a drop of a solution in THF of (5 mg/mL) DBCZ molecules was cast on carbon-coated copper grid for TEM analyses and the self-assembling behavior of the

molecules was studied. 2) Then, the analyte was soft-landed on a modified deposition target and electron diffraction was carried out.

6.3.3.1 Self-assembly of DBCZ molecules in a drop-cast film

Figure 55 reports an electron diffraction micrograph of a drop-cast DBCZ film.

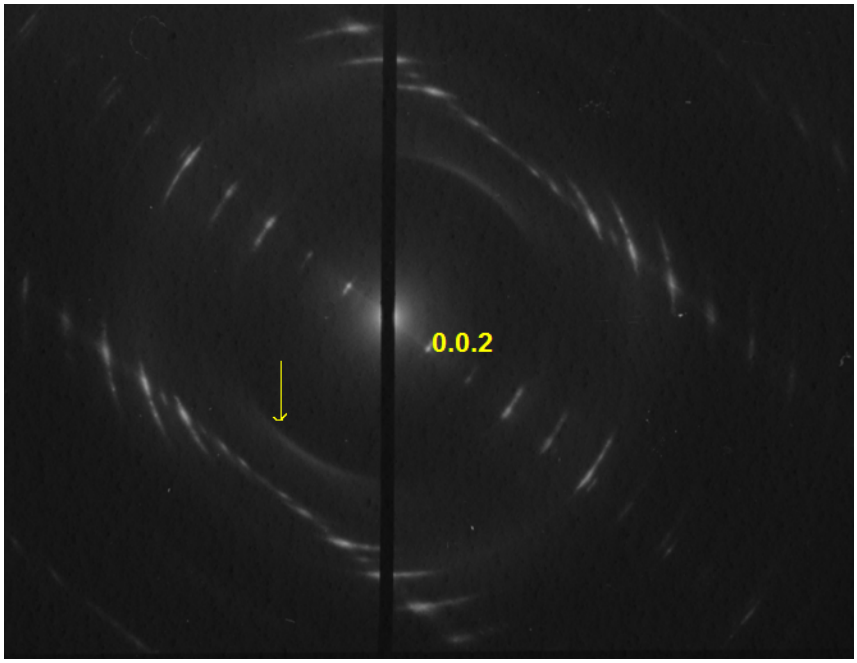

Figure 55. Electron diffraction micrograph of a drop-cast DBCZ film.

The electron diffractogram shows a multiplicity of reflections belonging to a zone of a single crystal diffraction pattern. The central row line (equator) is constituted by ten reflections of type 00ℓ, in which the ℓ value assumes always even values up to 0.0.20. The 002 reflection corresponds to a d value of 1.84 nm; therefore, the 001 reflection is calculated to be 3.69 nm and it is considered as the c-parameter of the unit cell of the DBCZ in the drop-cast film.

At a beam incidence perpendicular to the film surface, we find on the meridian a reflection, which is indicated as 100 and can be defined as “zone” {010}. By tilting the film round the central row line as axis, a sequence of zone patterns appears. The sequence of zone patterns allows the evaluation of the third dimension of the unit cell of the DBCZ crystal. From this set of analyses the values of the a- and b-axes of the

DBCZ unit cell could be determined to be 0.45 nm for a (reflection of type 100) and 1.82 nm for the b-parameter, respectively. Moreover, these data allowed to conclude that the molecules packed in an orthorhombic cell ($a \neq b \neq c$, $\alpha = \beta = \gamma = 90°$).

The density (ρ) of the unit cell was calculated from the following formalism (**Equation 3**):

$$\rho = (Z)\ M/N_A V \qquad \textbf{Equation 3}$$

where Z is the number of molecules in an unit cell, M is the dibenzo[b,b']thieno[2,3-f:5,4-f']carbazole molecular weight (463.6 Da); N_A is the Avogadro's number and V is the volume of the unit cell. For an orthorhombic cell the parameter V is calculated from the unit cell parameters as (a x b x c).

In order to have a reasonable value for the crystallographic density ($\rho > 1$), the crystalline cell created by the dibenzo[b,b']thieno[2,3-f:5,4-f']carbazole molecules has to be constituted from a number of molecular unit higher than 1. For an N value of 4 the density ρ assumes a value of 1.02 gcm^{-3}.

Additional reflections, which are belonging to a basic reflection in the {010} zone pattern with a d-value of 0.579 nm (pointed by the yellow arrow in **Figure 55**), do not belong to the crystal lattice defined previously. This evidence may be explained attributing to DBCZ molecules a polymorphic nature and thus the ability to crystallize into different crystalline lattices, both visualized in the electron diffraction micrograph of **Figure 55**.

The polymorphic nature of the DBCZ molecules was additionally revealed by means of X-ray diffraction analyses. According to the experimental results, related to the study of a DBCZ single crystal grown from THF, the molecules pack in a triclinic lattice with unit cell axes of a = 5.85 Å, b = 20.29 Å, c =21.92 Å, and angles alpha = 105.34°, beta = 97.41°, gamma = 91.18°, respectively. The position of the molecules in the mentioned triclinic cell is reported in **Figure 56**

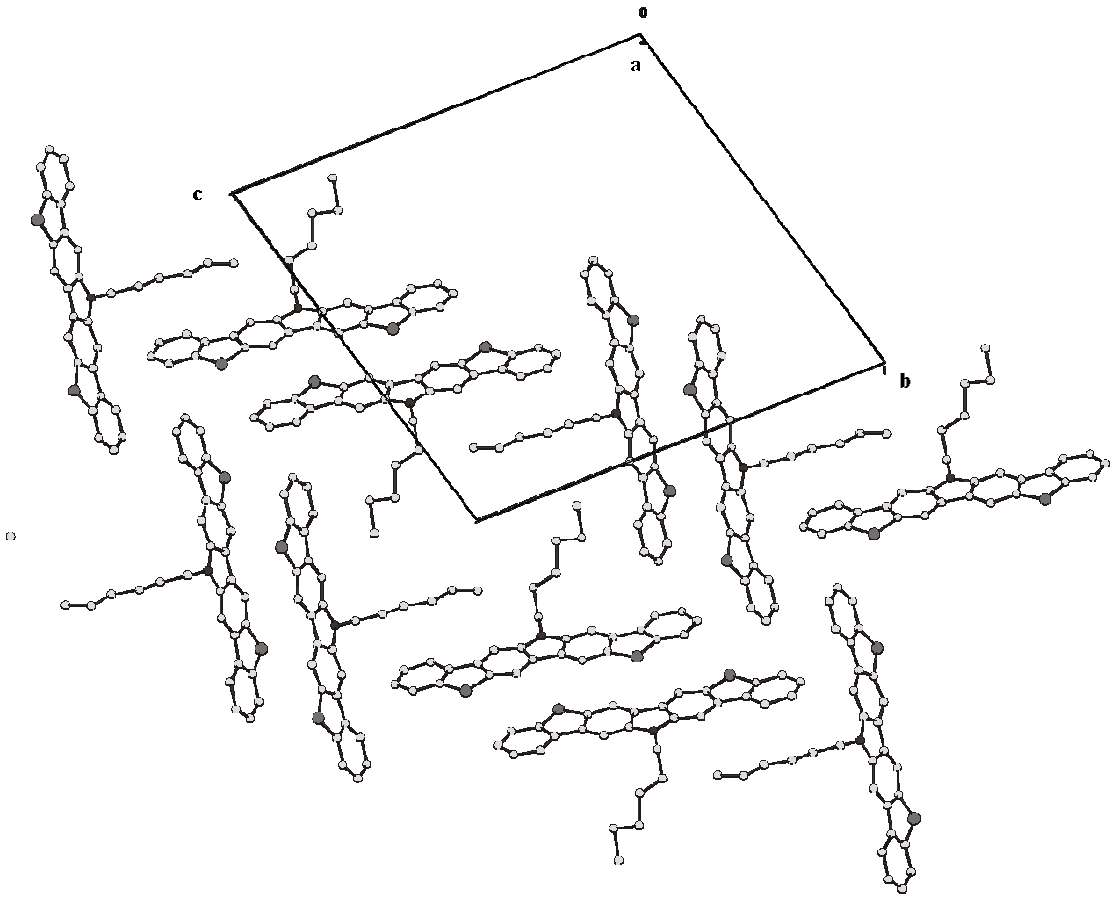

Figure 56. DBCZ molecules packed in a triclinic cell.

These d-values agree well with the X-ray diffraction analyses performed on drop-cast films from THF (5mg/mL) in reflection mode, which are reported in **Figure 57**.

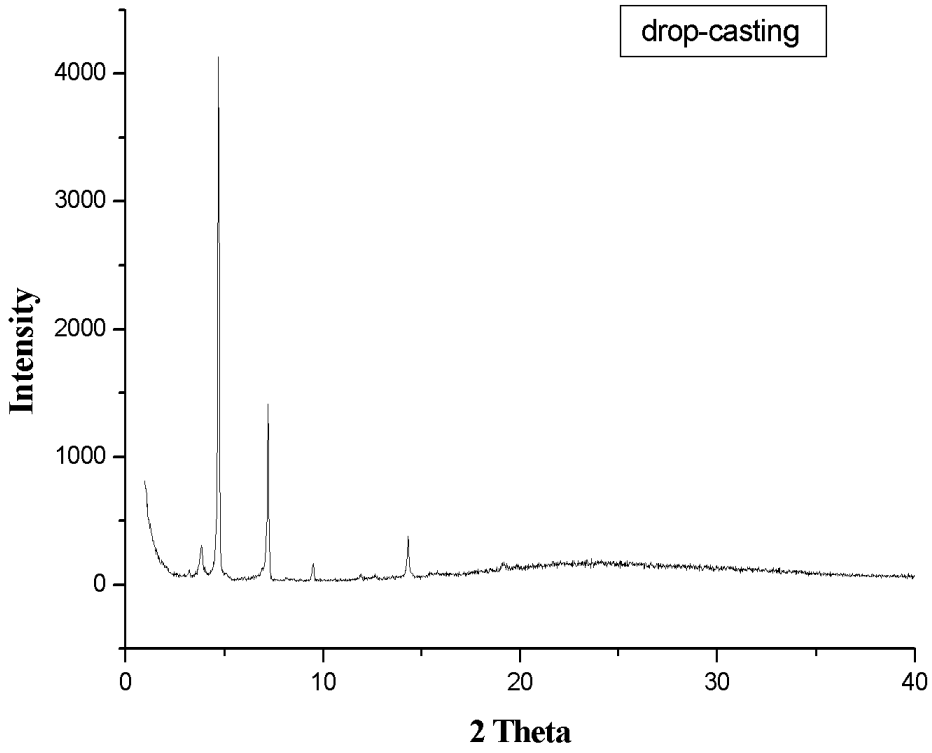

Figure 57. X-ray diffractogram of a drop-cast DBCZ film from a solution in THF, recorded with a powder diffractometer in reflection geometry.

The X-ray diffractogram shows a multiplicity of peaks superimposing a broad halo (2 θ = 25°), which is probably related to the disordered packing of the alkyl chains. The d-values related to the observed reflections are summarized in **Table 4**.

Table 4. D-value of the X-ray reflections of the drop-cast DBCZ film

2 θ [°]	d [Å]	Intensity [a.u]
3.2	27.7	very weak
3.9	22.8	weak
4.7	18.9	very strong
7.2	12.2	strong
9.6	9.2	weak
14.3	6.2	weak
19.2	4.6	very weak

The reflections, which could not be indexed in the electron diffractogram reported in **Figure 55**, possessing a d-value of 0.579 nm, very likely belong to the same crystalline structure revealed by the single-crystal X-ray analysis of DBCZ molecules. In this structure, the 0.579 nm reflection can be indexed as 100.

6.3.3.2 Assembly behaviour of soft-landed DBCZ molecules

To investigate the morphology of the soft-landed DBCZ molecules and their assembly behavior, the soft-landing deposition surface needed to be modified to allow further transmission electron microscopy and diffraction analyses.

A carbon-coated copper grid suitable for TEM analyses was positioned in the focus region of the aluminium soft-landing target and landing experiments were performed for a period of three days. Then, electron diffraction analyses were carried out. The corresponding electron micrograph is reported in **Figure 58**.

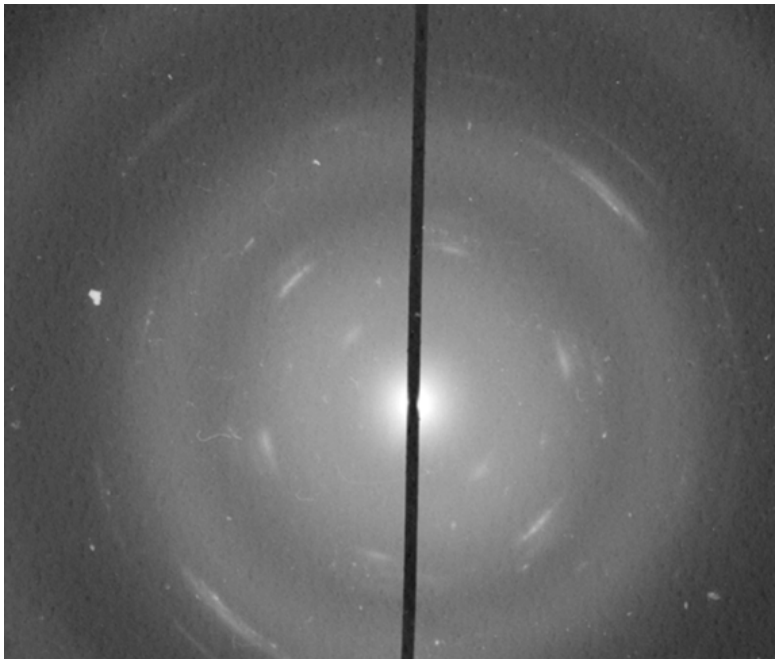

Figure 58. Electron diffraction pattern of a soft-landed DBCZ film.

Figure 58 looks like a single crystal diffraction pattern in which probably two zones are superimposed.

The innermost reflections correspond to a d-value of 0.57 nm, which agrees well with the 100 reflection observed in the diffraction micrograph of the drop-cast film (reflection pointed by a yellow arrow in **Figure 55**) and attributed to the triclinic structure observed for the single-crystal DBCZ growth from THF (a = 5.85 Å, b = 20.29 Å and 21.92 Å).

This suggestion is supported by the observation of the morphology of the soft-landed film that was investigated via transmission electron microscopy. The corresponding TEM micrograph is shown in **Figure 59**.

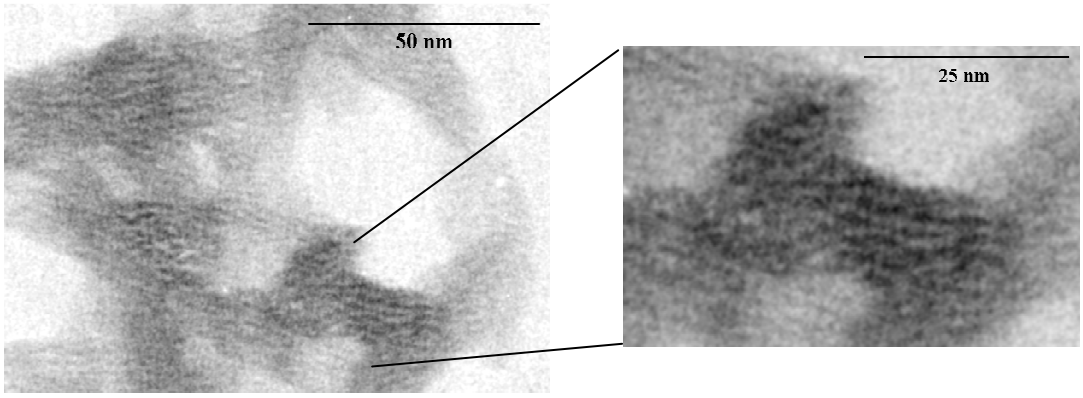

Figure 59. TEM micrograph of the soft-landed DBCZ film.

The TEM image presents regions with different contrast due to thickness dishomogeneity of the soft-landed film. The darkest regions show a periodicity of ~ 3.6 nm, which is only compatible with the triclinic structure.

Note that the same periodicity was additionally visualized by means of scanning tunnelling microscopy (STM) in DBCZ films soft-landed onto an HOPG surface. The corresponding STM images are reported in **Figure 60**.

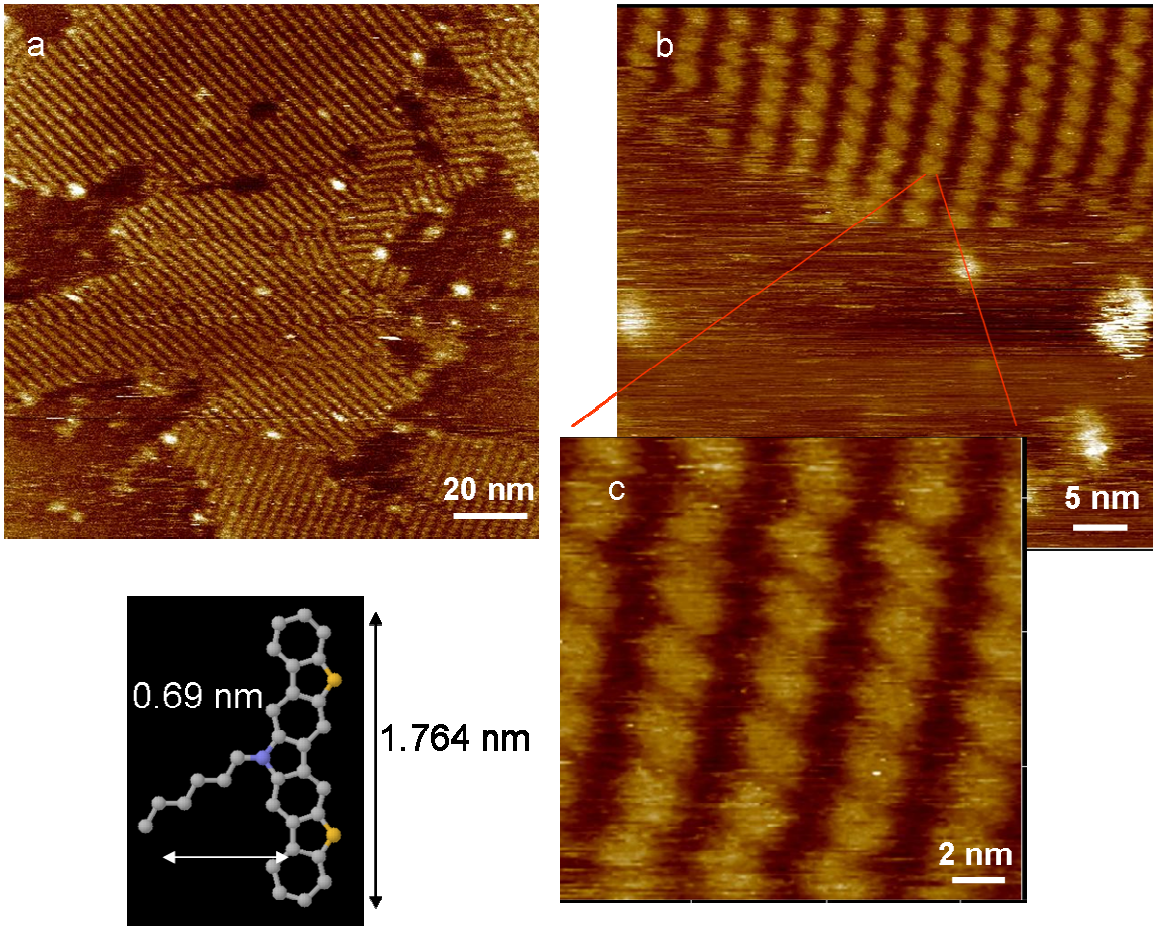

Figure 60. STM images of a DBCZ film prepared via Soft-landing MS.

In the STM current images the bright features (corresponding to high tunneling probability) can be attributed to π-conjugated aromatic structures. The aliphatic side chains, which are attributed to the dark parts of the images, could not be resolved. The distance between two rows has a value of 3.4 nm ± 0.3 nm and agrees well with the periodicity observed in the TEM micrograph of **Figure 59**. Moreover, considering the alkyl chains responsible for the formation of dark space, the presence of bright spots in the STM micrograph of **Figure 60** can be well explained by the assembly of the DBCZ molecules in the triclinic cell that has been depicted in **Figure 56**.

This additional evidence leads to conclude that soft-landing of DBCZ molecules allows growing films with a preferential triclinic structure, whereas two different DBCZ polymorphs (orthorhombic and triclinic) are grown via drop-casting.

6.4 Conclusions

Within this chapter, soft-landing has been used to grow thin films of PEO oligomers and DBCZ rod-like molecules on a conducting surface. The advantages, offered by this novel deposition technique can be summarized as following:

1) Soft-landing can profit from the soft-ionization conditions, ensured by the LSIMS ionization source, to deposit thermally instable molecules, such as PEO polymer chains, and to study the morphology of the vacuum-landed films, made thereof.
2) Soft-landing offers a unique purification procedure as it permits the deposition of mass-selected PEO chains and of single isotope DBCZ molecules. Note that these extraordinary conditions, which are offered by the use of a mass analyzer, cannot be reached by other purification or separation techniques, such as, for example, GPC fractionation for the PEO polymer chains or thermal evaporation for the rod-like DBCZ molecules.
3) Soft-landing allows growing films of the analytes possessing a novel molecular arrangement on the deposition surface. The use of an electrical field, as strong as 8 kV/cm, necessary for the deceleration of the ion beam, is recognized to have an influence on the landing of the molecules and on their final packing. In detail, the morphology studies of the soft-landed films of mass-defined polymer chains show that the PEO chains assemble preferentially into fibre structures, constituted by thin fibrillae of uniform width. The electrical field influence is as well recognized on the assembly of DBCZ molecules in soft-landed films. The packing of the rod-like molecules in soft-landed films differs substantially from that of drop-cast reference films. Films obtained via drop-casting shows in fact that DBCZ molecules could grow crystals possessing two different crystalline cells. Soft-landed films indeed allow growing exclusively one of the DBCZ polymorph. Experimental evidence of the electrical field influence on the packing of molecules

bearing large aromatic system will be further discussed in the following Chapter.

6.5 References

[95] V. Grill, J. Shen, C. Evans, R. G. Cooks *Re*V. *Sci. Instrum*. **2001**, 72, 3149.

[96] L. Hanley, S. B. Sinnott *Surf. Sci.* **2002**, 500, 500.

[97] B. Gologan, J. R. Green, J. Alvarez, J. Laskin, R. G. Cooks *Phys. Chem. Chem. Phys*. **2005**, *7*, 1490.

[98] R. G. Cooks, T. Ast, M. A. Mabud *International Journal of Mass Spectrometry and Ion Processes*, **1990**, 100, 209.

[99] H. Ewald, H. Hintrnberger, Methoden und Anwendungen der Massenspektoskopie, 1953, Verlag Chemi, GmbH., Winheim, Germany, p.82.

[100] X. Yang, H. J. Räder, A. Rouhanipour, K. Müllen, *Eur. J. Mass Spectrom.* **2005**, 11, 287.

[101] M. V. Kakade, S. Givens, K. Gardner, K.H. Lee, D. B. Chase, J. F. Rabolt, *J. Am. Chem. Soc.* **2007**,

[102] D. H. Reneker, I. Chun, *Nanotechnology*, **1996**, 7, 216.

7 Electrical field effect on the assembly of substituted HBC molecules

7.1 Introduction

Controlling the orientation of organic semiconducting molecules for organic field effect transistors (OFET) [103], sensors [104] and solar cells [45], is of key importance for obtaining improved device performance [105] and much effort has been spent to enhance the degree of order in organic thin-films [106,107,108,109,110].

Among various organic semiconductors, polycyclic aromatic hydrocarbons (PAH) have attracted particular interest. Substituted hexa-peri-hexabenzocoronene (HBC) is an example of disc-shaped PAH molecules forming columnar stacks in which overlapping π orbitals are oriented parallel to the columnar axis. In the stacking direction these columns have electronic properties resembling those of graphite; therefore, the application of substituted HBC molecules for novel and more efficient devices is related to the degree of unidirectional order in the resulting films.

Numerous investigations have reported different alignment techniques for substituted HBC molecules, such as zone-casting [111], Langmuir-Blodgett film preparation [112] and the use of alignment layers [113]. Recently, Shklyarevkiy et al.[114] have investigated the influence of strong magnetical fields in aligning substituted HBC molecules and reported an induced crystallization in fibril superstructures perpendicularly oriented to the magnetical field. The success of the alignment techniques depends upon the choice of experimental parameters such as the temperature gradient and optimal flow rate for zone casting, the presence of prepatterned teflon layers, and the amphiphilicity of the molecules for Langmuir-Blodgett deposition. A minor number of restrictions and easier settable experimental conditions could be obtained by the use of electrical fields for the alignment of organic semiconducting molecules. The application of electrical fields for inducing order in thin films of polymer liquid crystals [115-116] and block copolymers [117] has been the object of previous studies. So far these investigations were dedicated to the alignment of polymeric fibril superstructures in the direction of the external field. Here we explore the possibility to use electrical fields as a new tool for creating long-range oriented films of discotic, organic semiconducting molecules by using two kinds of HBCs as model systems: hexa(para-n-dodecylphenyl)hexabenzocoronene (HBC-PhC_{12}) as a model compound for non-polar discotic molecules and 2-cyano-

5,8,11,14,17-penta(3,7-dimethyloctanyl)-hexa-peri-hexabenzocoronene (HBC-CN) for discotic molecules bearing a strong dipole moment.

The assembly of theses HBCs under the influence of an external electrical field is investigated on different surfaces, such as glass, gold and highly oriented pyrolitic graphite (HOPG). The growth of HBC films with different packing is related in fact to the choice of the substrate [118]. Both glass and polycrystalline gold surfaces are amorphous and do not exercise epitaxial phenomena during the film formation process of HBC molecules. They however differ in their conductive nature. On the other hand, HOPG is a conducting and highly oriented substrate of graphitic nature which can induce epitaxial growth phenomena due to a surface recognition process between graphitic surface and graphene-like molecules [119-120]. Its employment, moreover, allows performing scanning tunneling microscopy analyses to study the packing of the HBC molecules in the first organic layers on the surface.

7.2 Electrical field orientation of non-polar HBC molecules

7.2.1 HBC-PhC_{12} molecules as a model system

The HBC-PhC_{12} molecule is a kind of nanographene, which contains an extended aromatic core and long alkyl chains symmetrically decorating the core periphery. The molecular structure of HBC-PhC_{12} is reported in **Figure 61**.

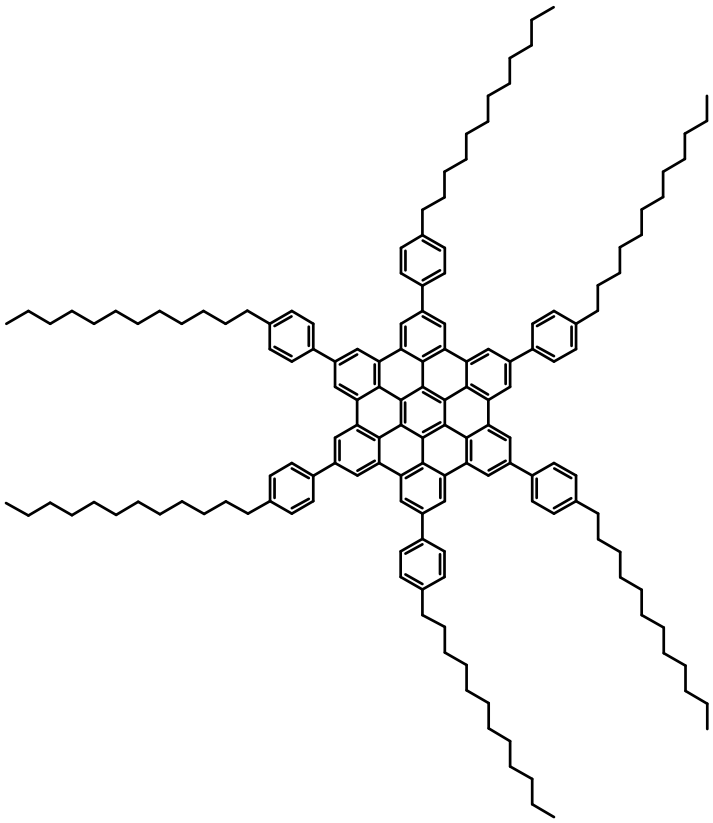

Figure 61. Molecular structure of HBC-PhC$_{12}$.

The dodecylphenyl substituents attached to the rigid aromatic core are responsible for the discotic liquid crystal nature of these molecules and lead additionally to a good solubility in the most common solvents. Differential scanning calorimetry (DSC) data have reported for HBC-PhC$_{12}$ molecules a clear mesophase transition at 80°C. However, HBC-PhC$_{12}$ possesses in the solid phase a second phase transition. This additional change in enthalpy at a temperature of 18° C can be related to the freezing of the 180°-flip motion of the phenyl rings of the side chains. According to a previous investigation [136], HBC-PhC$_{12}$ molecules aggregate into columnar stacks already in diluted solutions. The high tendency of HBC-PhC$_{12}$ molecules to form columnar structures is related to the strong π–π interactions between neighboring aromatic rings and to the microphase separation of the alkyl side chains from the aromatic core. The self-assembly of HBC-PhC$_{12}$ molecules on different substrates has been the object of previous studies [121-122]. This system has been thoroughly understood; therefore, it is a suitable model for electrical field alignment experiments.

7.3 Formation of HBC-PhC$_{12}$ columns induced from an external electrical field: the theory

The possibility to orient HBC-PhC$_{12}$ molecules by using an external electrical field can be related to the anisotropy of a liquid crystal medium. Electric alignment of anisotropic molecules originates from the anisotropy of their polarizability α, characterized by $\Delta\alpha = \alpha\| - \alpha\perp$, the difference in α between two orthogonal molecular axes. The polarizability value α_{ij} is related to the response (p_i = polarization) of a molecular dipole to an external electrical field (E) by the following equation:

$$p_i = \mu_i + \alpha_{ij} E_j \qquad \textbf{Equation 4}$$

where μ_i is the permanent dipole. In a homogeneous linear and isotropic dielectric medium, the polarization p_i is aligned with and proportional to the electric field E. In an anisotropic material, the polarization and the field are not necessarily in the same direction. Then, the i^{th} component of the polarization is related to the j^{th}, according to **Equation 4**.

This expression represents the relative tendency of a charge distribution, like the electron cloud of an atom or molecule, to be distorted from its normal shape by an external electric field.

In the case of HBC-PhC$_{12}$ molecules, which do not possess a permanent dipole, the value of p_i depends only on the polarizability α_{ij} of the molecule. Polarizability is a tensor of second order [123] and its value for HBC has not been reported in the literature. Therefore, we used the polarizability value for coronene molecules, in consideration that their planar and discotic structure can be considered representative for HBC molecules. According to Matsuzawa et al.[124], the average polarizability for coronene molecules is 33.7 x 10^{-24} cm^3, where the average polarizability can be written as:

$$\alpha = \sum_i \alpha_{ii} / 3 \qquad \textbf{Equation 5}$$

As the polarizablility of a disc-like molecule on the axis perpendicular to its aromatic core is circa zero, the polarizability value of a coronene molecule can be exclusively considered as the polarizability along its planar axis. Therefore we can write [(1)]:

$$\alpha_{plan} = 33.7 \times 10^{-24}\ cm^3 = 3.74 \times 10^{-39}\ C \cdot m^2/V \qquad \textbf{Equation 6}$$

The necessary energy (ΔW) for a coronene molecule to be oriented in the direction of an electrical external field E (5×10^5 V/m) is given by the following equation:

$$\Delta W = \alpha E^2/2 = 4.675 \times 10^{-28}\ J \qquad \textbf{Equation 7}$$

Considering that the aromatic structure of a HBC-PhC_{12} molecules is more extended than that of coronene molecules, the polarizability value of the HBC-PhC_{12} molecules will be larger than the here reported value.
However, the value of ΔW for a coronene molecule in presence of an electrical field of 5×10^5 V/m, which has been employed for the alignment experiments in this work, is considerably smaller than the thermal energy of the molecules at a temperature of 20 C°.

$$\Delta W_{temp} = k_B T = 4.0 \times 10^{-21}\ J \qquad \textbf{Equation 8}$$

where k_B is the Bolzman constant and T is the temperature.

The capability of HBC-PhC_{12} molecules to be oriented has, therefore, to be searched in its possibility to form liquid-crystals (LC). In a LC mesophase the difference in electric energy of *N* self-assembled molecules can become large enough to align the molecules (**Figure 62**, $N\alpha E^2/2 \sim k_B T$) [125].

[1] Remark: $\alpha_{SI} = 4\pi\varepsilon_0 \times 10^{-6}\ \alpha_{CGS}$

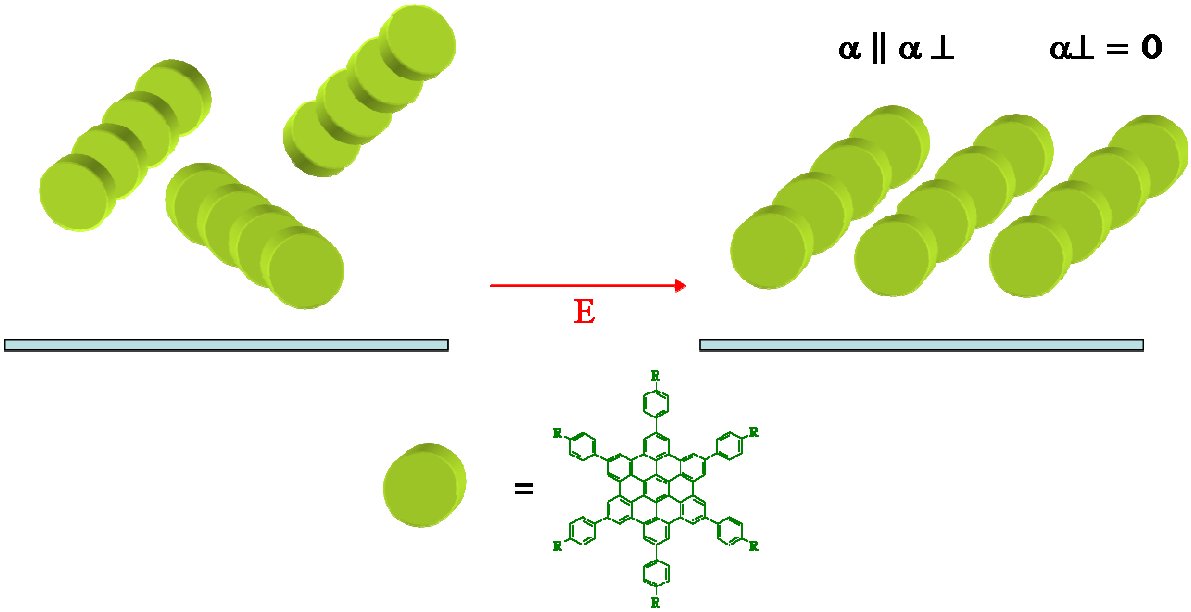

Figure 62. Schematic draw of the electrical field action on the HBC-PhC$_{12}$ molecules

In absence of an external electrical force, the HBC-PhC$_{12}$ molecules can form unoriented domains made of columnar aggregates, as schematized in **Figure 63 a**. The presence of an external field can indeed exert a torque on the domains until a parallel orientation of such induced dipoles along the field direction is established (**Figure 63 b**) [126].

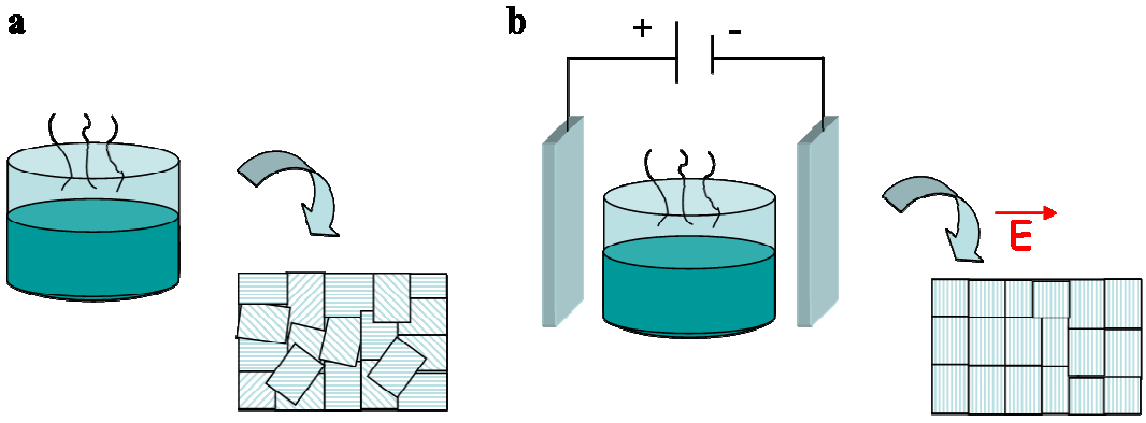

Figure 63. a) Schematic representation of unoriented microdomains, obtained via drop-casting, b) unidirectionally oriented domains obtained via drop-casting in presence of an external electrical field.

7.4 Alignment experiments and film characterization

7.4.1 Film preparation

The experiments to increase the degree of supramolecular order in films of HBC-PhC_{12} molecules were carried out in a home-built apparatus, which is schematically reported in **Figure 64**.

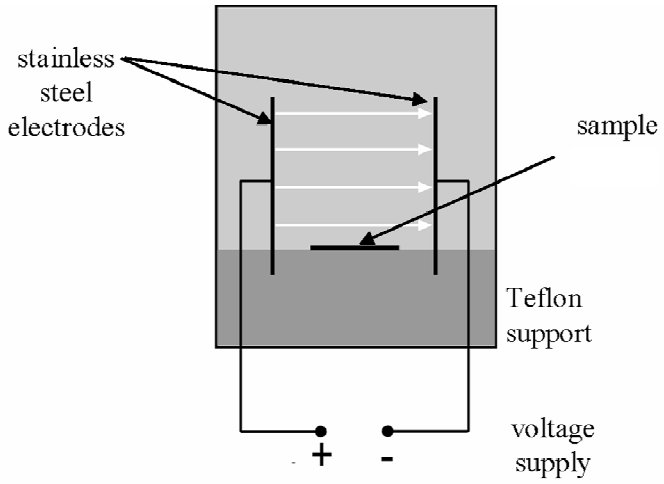

Figure 64. Schematic representation of the apparatus for alignment experiments by means of electrical fields.

The aligned films of HBC-PhC_{12} molecules were prepared from a concentrated solution in p-xylene (15 mg/ml). A drop of HBC-PhC_{12} solution was cast on a glass surface placed between the electrodes and then an electrical field with a strength of 4-5 kV/cm (DC) was applied parallel to the glass surface and maintained until the complete evaporation of the solvent (1 hour). Solvent evaporation in the presence of an electric field yielded dry layers of HBC-PhC_{12} molecules with an average film area of 1 cm^2 and an average film thickness of 300 nm. The HBC-PhC_{12} films, displaying a very high degree of supramolecular order, were characterized by polarizing microscopy, atomic force microscopy, scanning and transmission electron microscopy as well as X-ray and electron diffraction.

7.4.2 Optical microscopy

Detailed information about the supramolecular organization of the field-force oriented HBC-PhC_{12} films was revealed by polarizing microscopy. The features observed between crossed polarizers elucidate details of the supramolecular order of the specimens.

For field oriented HBC-PhC_{12} films, an alternation of black and bright stripes, oriented in the direction of the external applied electric field, was visualized in the polarizing microscope. The stripes, which were repeatedly observed in all the field-force oriented films prepared with identical experimental conditions, have a width of about 10 µm as shown by the optical micrograph of **Figure 65 a**.

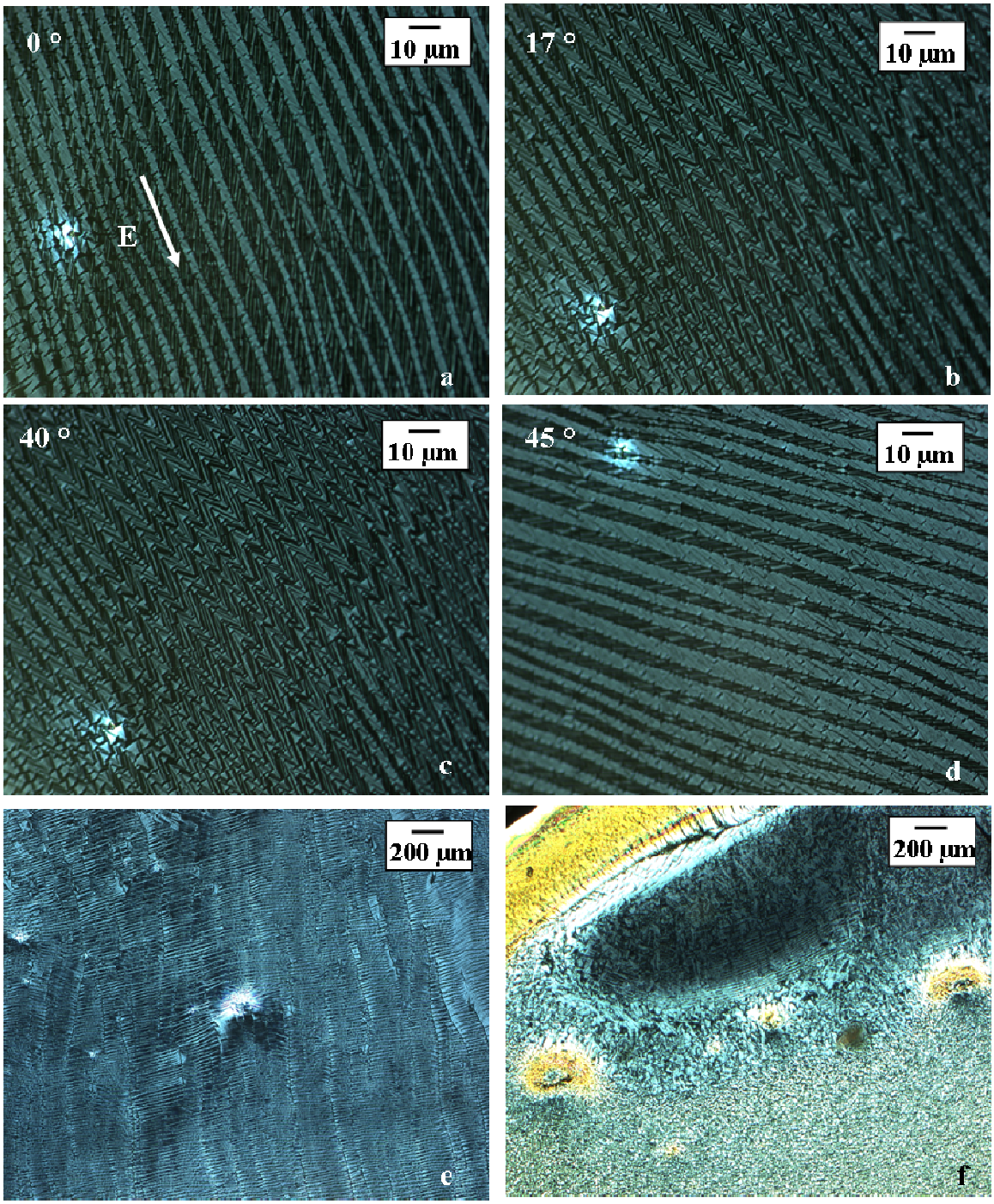

Figure 65. a) Optical micrograph displaying an alternation of bright and dark stripes under crossed polarizers. The white arrow indicates the direction of the previously applied electric field. b-d) Change in optical features of oriented HBC-PhC$_{12}$ molecules during rotation of the sample stage. e) Optical micrograph of a field-force oriented HBC-PhC$_{12}$ film at lower magnification. f) Optical micrograph of a reference HBC-PhC$_{12}$ drop-cast film under crossed polarizers.

Upon rotation of the stage between crossed polarizers (**Figure 65 b**, 17° and **4 c**, 40°), the optical feature consisting of alternating stripes (undulating feature)

develops into a herring-bone structure. At a rotation angle of 45°, the initially observed alternating black and bright stripes exchange their brightness (**Figure 65 d**).

For unidirectional oriented film, theory predicts [127] that, if the optical axis of the specimen is oriented along the axis of a crystal and lays parallel to the polarizer or to the analyzer, a totally dark field would appear through the eyepieces of a microscope under crossed-polarized illumination, as schematized in **Figure 66 a**. For each rotation of the sample stage of an angle α, light would pass through the analyzer and a bright micrograph would be observed with a maximum of brightness at an angle of 45°.

Undulating textures are indeed characteristic for oriented specimens of liquid crystals possessing deformations in their liquid crystalline phase [128] and they have been frequently observed in optical micrographs of aligned aromatic polyester films [129] and high-modulus polyaromatic fibers [130] (Kevlar 49). For the field-oriented HBC-PhC_{12} films, the visualization of parallel stripes of alternate brightness (**Figure 65 a**) can be explained by molecules arranged in a normal or edge-on fashion with respect to the glass surface, creating columns with the columnar axis on average parallel to either the polarizer or the analyzer. According to Livolant and Bouligand [131], the alternation of bright and dark stripes that interchange when rotating the sample (**Figure 65 d**) originates from a quasi-periodic undulation of the director (bend deformation) around a fixed axis, where, by definition, the liquid-crystal director is the average direction of the liquid crystalline molecules.[132] A schematic representation of the HBC-PhC_{12} specimen, bearing bend deformations, is reported in **Figure 66 d**.

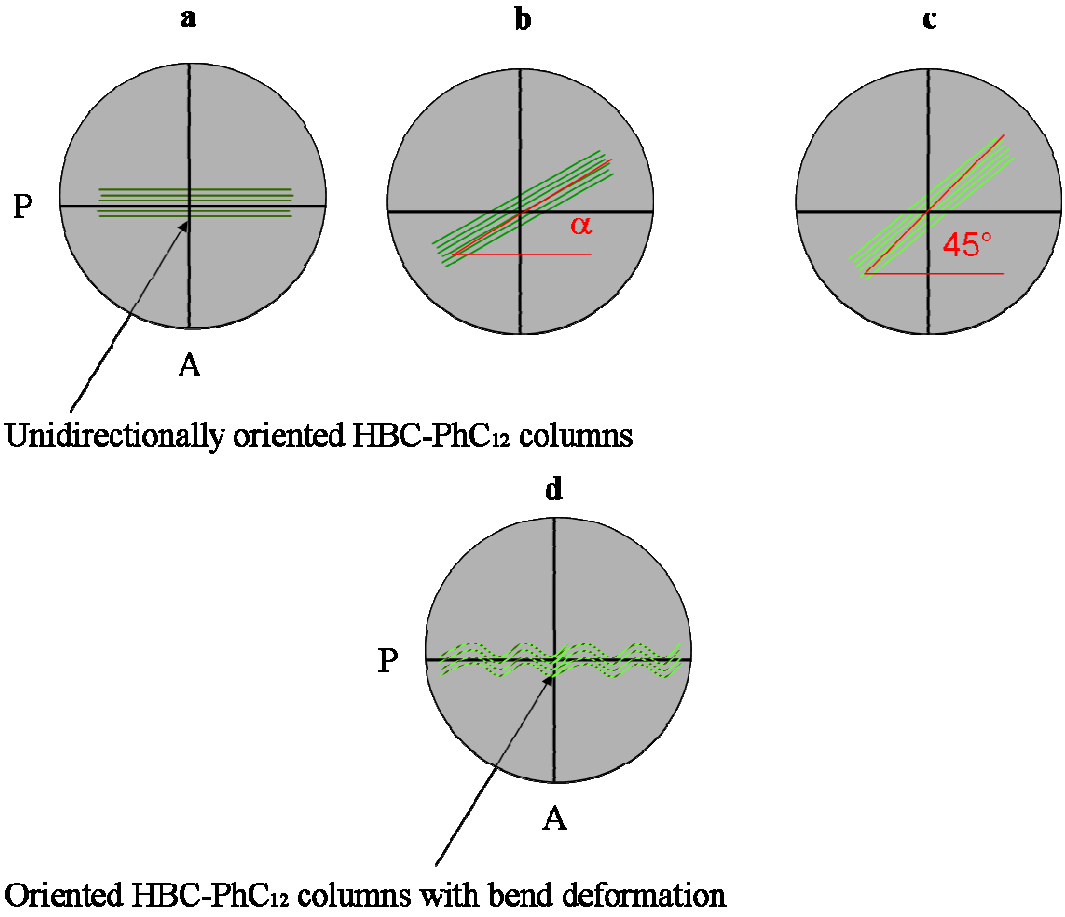

Figure 66. a,b,c) Schematic representation of anisotropic birefringent HBC-PhC$_{12}$ specimen with the long (optical) axis oriented in the direction of the columnar axis and parallel to the direction of the polarizer. d) Schematic representation of anisotropic birefringent HBC-PhC$_{12}$ specimen presenting bend deformation.

The bend deformation is one of the three possible distortions for a liquid crystal. Among the three deformations possible for liquid crystals (splay, bend and twist), which are schematically reported in **Figure 67**, the bend of the columnar director is the most frequent. It requires the least consumption of elastic energy and this justifies the frequency of its presence on the field oriented HBC-PhC$_{12}$ film.

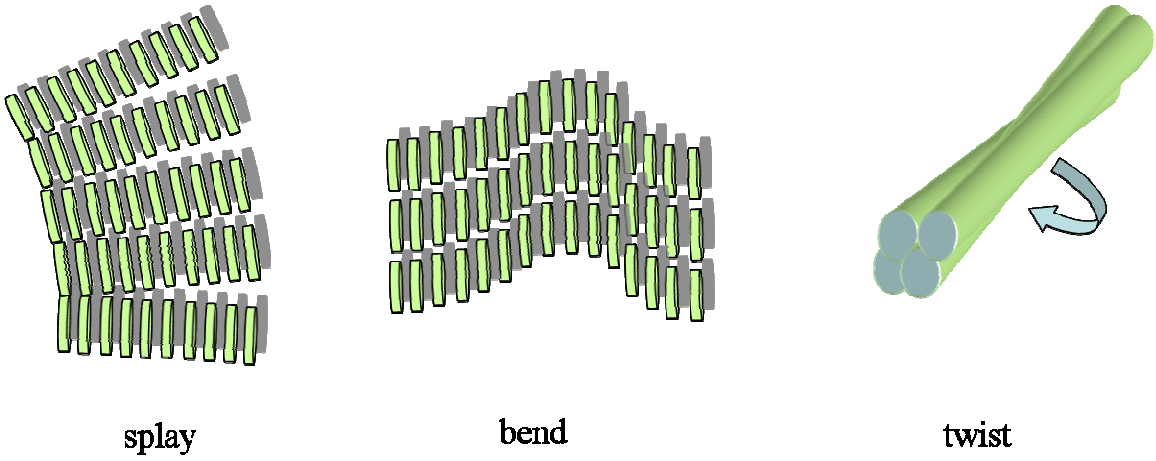

Figure 67. Deformations in columnar liquid crystals.

Within the uniaxially oriented HBC-PhC_{12} films displaying undulating features under crossed polarizers, triangular defects were found (**Figure 68**) [133]. This phenomenon is related to space filling problems in areas of pronounced bend of the columnar director [134].

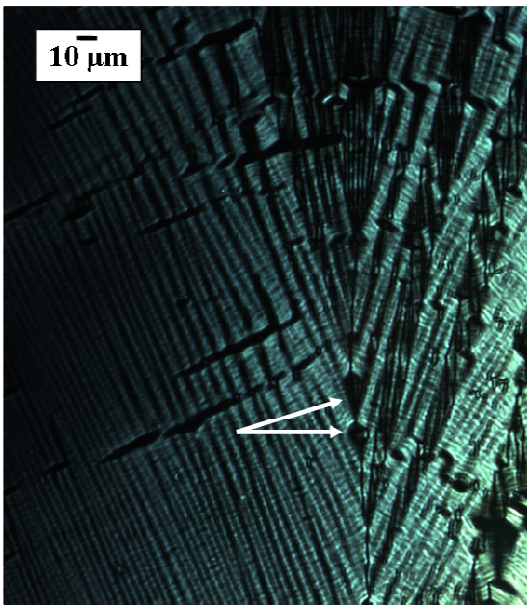

Figure 68. Optical micrograph of an oriented HBC-PhC_{12} film displaying triangular defects.

For comparison, a drop-cast film of HBC-PhC_{12}, which was prepared in the absence of an electric field, was studied by polarizing microscopy. The micrograph in **Figure 65 f** suggests no extended uniaxial orientation of the HBC-PhC_{12} molecules. Only in small regions, where the molecules self-assemble with a higher degree of

order, one recognizes the presence of undulating textures due to columnar domains of HBC-PhC_{12} molecules directed in the same direction. It is reasonable to assume that these small oriented domains are probably due to solute migration during solvent evaporation.

On the contrary, the optical micrograph of a field oriented film reported in **Figure 65 e** provides evidence of the larger extension of uniaxially oriented domains represented by black and white stripes directed in the same direction of the field. When the field-force oriented films are observed in the microscope with one polarizer, evidence of a slight dichroism is found. For unoriented films, the dichroism phenomenon is not observed at all. The dichroism of the film is due to the absorbing property of the discs in the direction of their transition dipole moment. In the case of an HBC chromophore, the transition dipole is oriented along the plane of the aromatic core; therefore, the intensity of the light absorbed by unidirectionally oriented molecules normal to the surface changes twice when rotating the sample stage by 360°. In field-force oriented films, the dichroism effect is unexpectedly small. This suggests that it is probably averaged either by the varying orientation of the substituent phenyl groups tilted out from the aromatic plane or by the thickness inhomogeneity of the drop-cast films [135-136-137].

7.4.3 Film Morphology

7.4.3.1 Scanning Electron Microscopy (SEM)

Whereas the polarizing microscopy offered optical expressions of the periodical structures in the material, the morphology of the periodical structure was elucidated by SEM. The SEM micrograph in **Figure 69 a** reveals a zig-zag structure made of HBC-PhC_{12} columns that on average are perpendicularly oriented with respect to the direction of the applied electric field, represented in the micrograph by the red arrow.

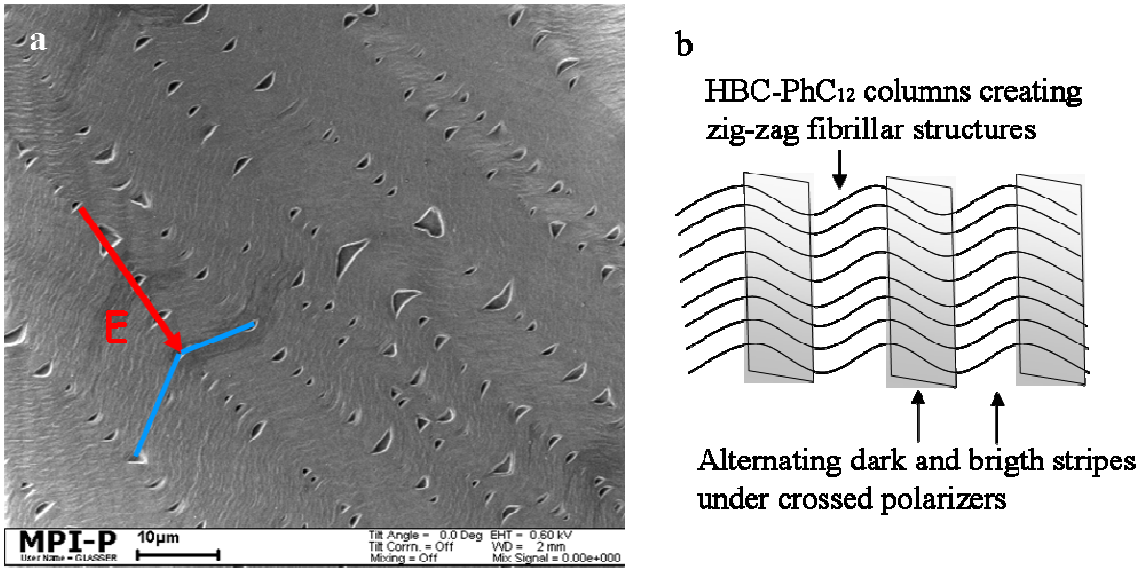

Figure 69. a) Scanning electron micrograph of an oriented film of HBC-PhC$_{12}$ molecules displaying a zig-zag structure. b) Model of the undulated structure created by the HBC-PhC$_{12}$ columns.

The half-periodicity of zig-zag structures has a length of about 10 µm, corresponding to the width of a stripe in the optical micrograph of **Figure 65 d**. The segments of the zig-zag structure deviate from the direction perpendicular to the electric field alternately by an angle of about 13°. The wavelike or zig-zag structures of the field-force oriented HBC-PhC$_{12}$ molecules (**Figure 69 b**) correspond to the stripes, which have been observed in the polarizing microscope. In addition, the SEM micrograph shows numerous triangular defects equally displayed in the optical micrograph of **Figure 68**.

The apex of the triangles is always directed away from the curvature center of the undulating columns. This evidence leads to relate the presence of triangular defects to that of undulating textures.

7.4.3.2 Atomic Force Microscopy (AFM)

Morphological micrographs at higher resolutions were acquired with an atomic force microscope operating in tapping mode. AFM micrographs of a field-force oriented film of HBC-PhC$_{12}$ molecules on glass substrate with different scan sizes are displayed in **Figure 70 a, c**.

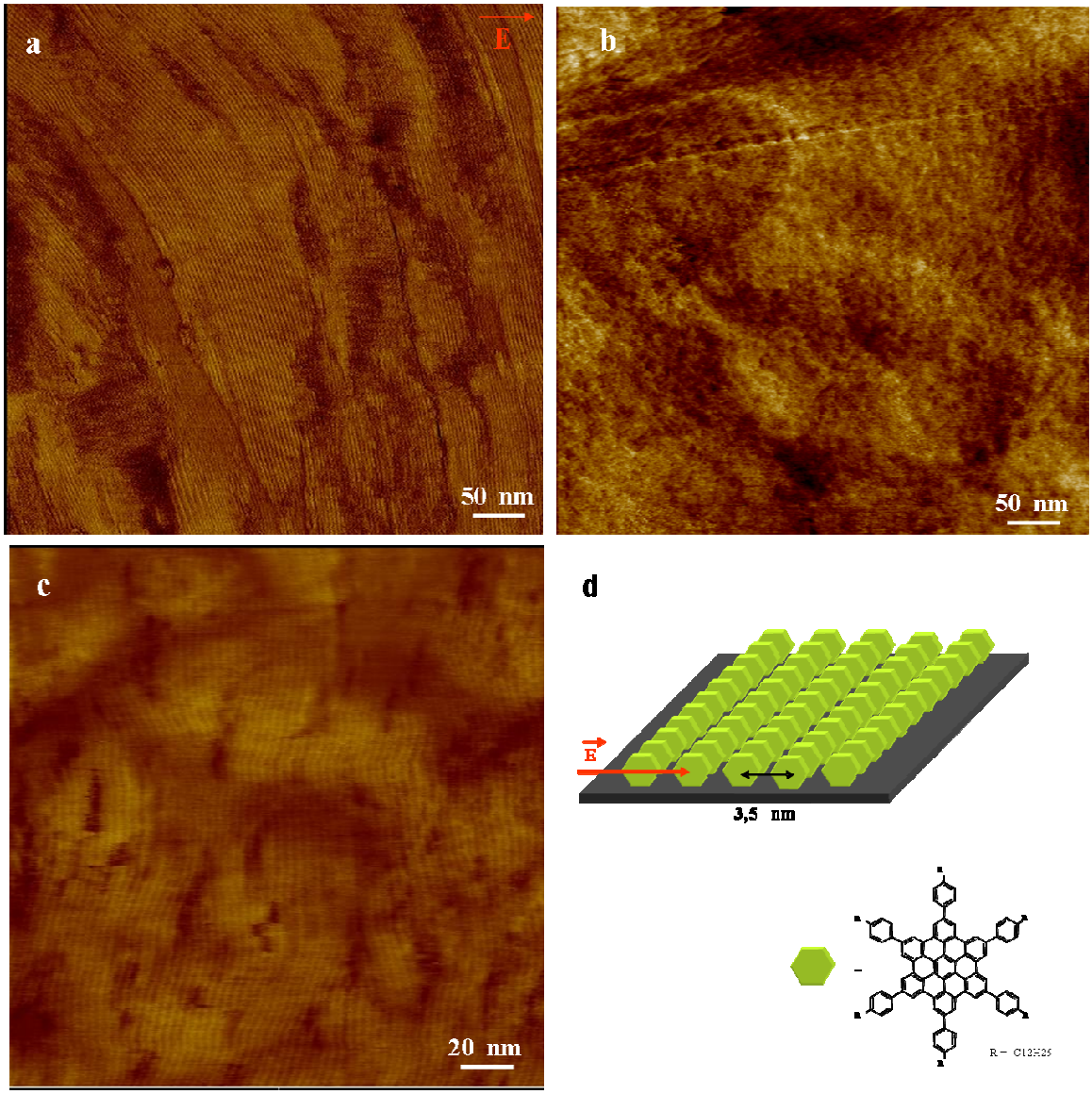

Figure 70. a), c) AFM phase images of field-force oriented HBC-PhC$_{12}$ films on a glass substrate with different scan sizes. b) AFM phase image of a nonoriented HBC-PhC$_{12}$ film on glass. d) Schematic representation of HBC-PhC$_{12}$ molecules creating lamellar structures.

Parallel striations separated by 3.56 ± 0.25 nm from each other that on average are perpendicularly oriented with respect to the direction of the applied electric field (red arrow in **Figure 70 a**) are detected. This value is in good agreement with the calculated distance between HBC-PhC$_{12}$ columns for molecules with completely extended alkyl chains (3.46 nm). This evidence further suggests that the HBC-PhC$_{12}$ molecules are arranged with their conjugated molecular planes along the field direction as schematically depicted in **Figure 70 d**. The formation of columnar structures is due to the strong tendency of HBC-PhC$_{12}$ molecules to aggregate in

stacks, resulting in the formation of columnar superstructures perpendicular to the field direction [138].

Figure 70 b shows an AFM micrograph of a drop-cast film of HBC-PhC_{12} molecules prepared in absence of an electric field. As opposed to the field-oriented samples, no parallel striations can be observed. This may be attributed to the random orientation of the columnar stacks of HBC-PhC_{12} molecules in absence of an electrical field.

7.4.3.3 Transmission Electron Microscopy (TEM)

Additional information about the morphological structure of the field-force oriented HBC-PhC_{12} specimen was obtained by transmission electron microscopy. A typical transmission electron micrograph of a surface replica of an oriented sample is reported in **Figure 71 a** and displays parallel striations, similar to that observed in the AFM micrograph with typical pile width of about 3.30 ± 0.22 nm. It has to be considered that the evaluation of the width of the striations, present in the TEM and in the AFM micrographs, possesses a relatively large experimental error. The stripe width (d) can be measured via a section analysis, which depends on the projection, from which the lamellae are observed. Thus, as reported in **Figure 71 b** the two values, d_1 and d_2, will slightly differ.

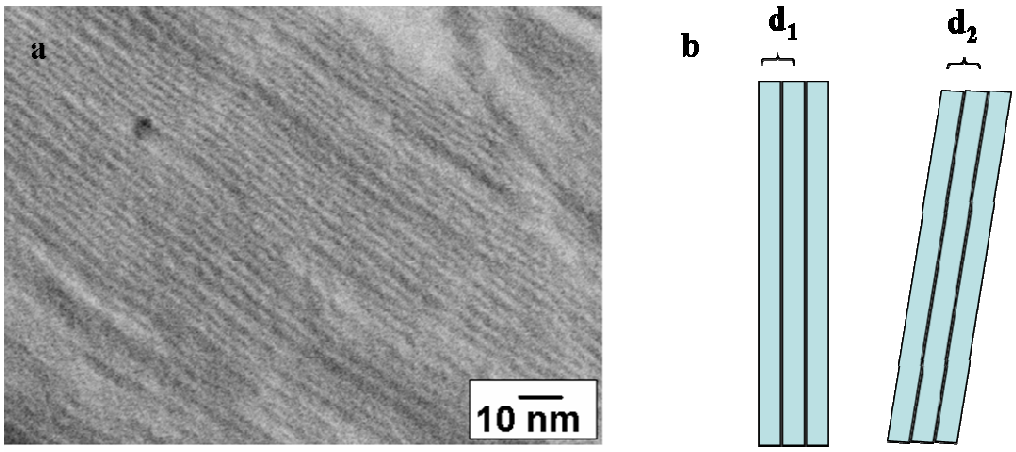

Figure 71. a) Transmission electron micrograph of an oriented HBC-PhC_{12} film replica. b) Sketch of striations with slight difference in orientation.

However, both values obtained via TEM and AFM agree well within their experimental error with the intercolumnar space between two conjugated HBC-PhC_{12} ideal stacks.

7.4.4 Diffraction Analyses

In order to elucidate the packing within HBC-PhC_{12} molecules stacks, electron and X-ray diffraction analyses were performed. The electron diffraction pattern of a field-force oriented HBC-PhC_{12} film at a beam incidence perpendicular to the surface is shown in **Figure 72 a**.

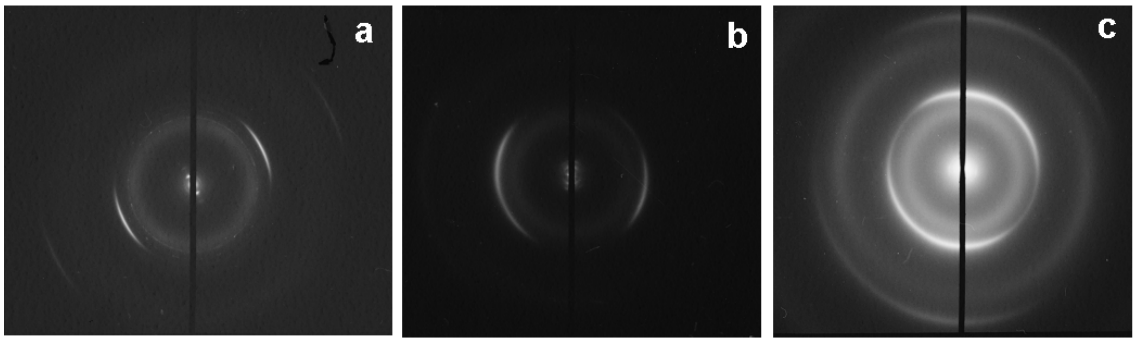

Figure 72. a) Electron diffraction pattern of HBC-PhC_{12} field-force oriented film, implying a small degree of columnar misalignment. The diameter of the selected area of the diffraction pattern is 1.55 mm. b) Electron diffraction pattern of HBC-PhC_{12} field-force oriented film with a diameter of the selected area of 12.4 µm. c) Electron diffraction micrograph of a HBC-PhC_{12} drop-cast film with a diameter of the selected area of 12.4 mm.

Two sets of reflections are present perpendicular to each other. The innermost reflection on the equator with a d-value of 3.09 nm is in agreement with the calculated intercolumnar distance between adjacent HBC-PhC_{12} columns. The meridional reflection with a d-value of 0.34 nm, seen in two orders, fits to the calculated thickness of an HBC-PhC_{12} molecule and this can be attributed to the intermolecular distance of the molecules within a column. In addition, the diffraction pattern shows that the aromatic planes are perpendicular to the glass surface (edge-on arrangement) and normal to the columnar axis. It is worth noting that the reflection is an arc and never a streak, indicating that the molecules of adjacent columns show no axial shift. Around the center, a halo is observed as a full circle caused by the disordered

aliphatic side chains. The azimuthal width of the arcs correlates with the diameter of the illuminated area and is a qualitative measure of the orientational distribution of arrays of adjacent columns.

The electron diffraction pattern of field-force oriented HBC-PhC_{12} films is similar to the diffraction micrograph of a fiber. This finding definitely confirms the presence of columns of HBC-PhC_{12} molecules in an edge-on arrangement on the glass surface. Electron diffraction analyses were additionally performed on drop-cast films of HBC-PhC_{12} molecules solidified in the absence of electric fields (**Figure 72 c**). The diffraction pattern of HBC-PhC_{12} columns in a drop-cast film shows closed rings of the meridional reflections with some sampling on the meridian, whereas up to a diameter of 12.5 μm, closed reflection rings were never observed in field-force oriented samples (**Figure 72 b**). This partial orientation can be attributed to the natural tendency of the HBC-PhC_{12} columns to create oriented aggregates, owing to the radial solvent flow towards the boundary of the droplet, as already discussed for the optical micrograph of **Figure 65 f**.

As electron diffraction is often regarded as a qualitative technique suitable for symmetry determination but too inaccurate for determination of intensity, lattice parameters, and molecular packing, also X-ray analyses were performed on field oriented films of HBC-PhC_{12} molecules (**Figure 73 a**).

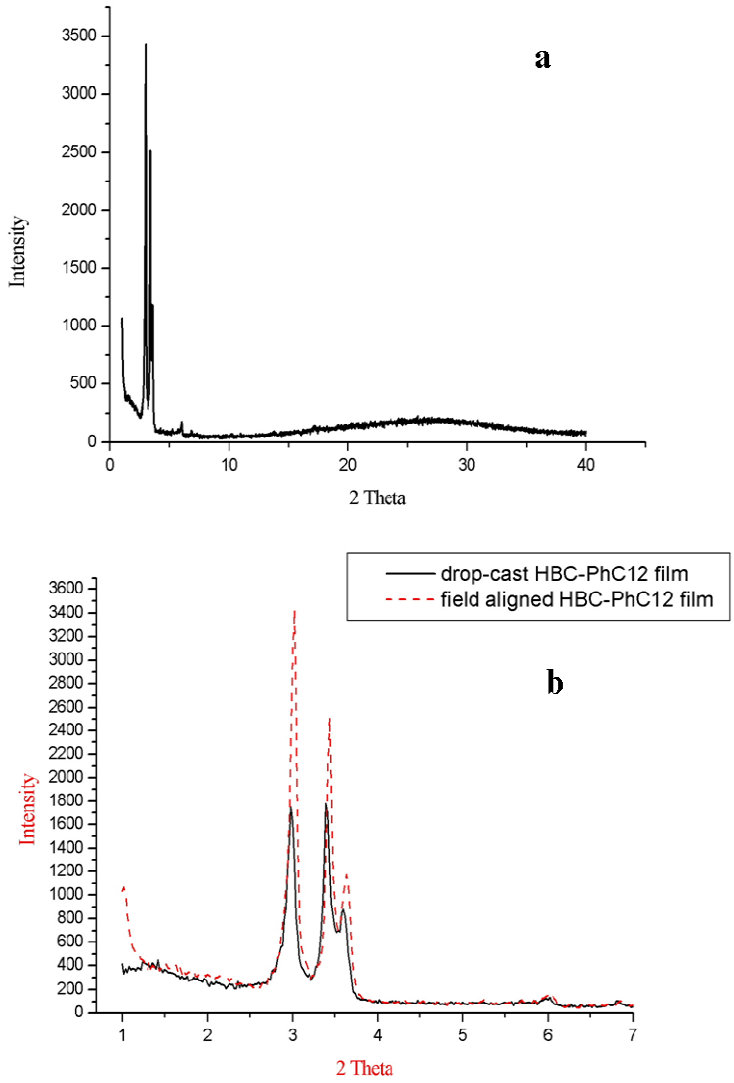

Figure 73. a) X-ray diffractogram of HBC-PhC$_{12}$ field-oriented film and b) enlarged innermost angular region for an HBC-PhC$_{12}$ field aligned film (dashed line) and for a drop-cast film (continuous line).

The diagram exhibits a set of distinct reflections superimposed on a broad halo. The latter originates partially from disordered side groups of the HBC-PhC$_{12}$ molecules but mainly from the amorphous glass substrate. It may be noted that the reflection corresponding to an intermolecular distance of 3.4 Å (001 reflection), expected at 2θ ~25.68, is missing in the X-ray diffractogram. This absence confirms the high degree of fiber axis orientation in the film parallel to the substrate. In fact, the reflections of type 00l do not fulfill Braggs' condition for the current texture and reflection geometry. The sharp and well-defined peaks indicate clearly the highly ordered structure created by the molecular columns (**Table 5**).

Table 5. X-ray diffraction data.

2 θ / °	d /Å	Intensity /a.u
2.97	29.75	very strong
3.43	25.76	very strong
3.61	24.47	strong
5.99	14.75	weak
6.8	13.00	very weak

The more or less cylindrically-shaped columns, however, do not occupy the knots of a hexagonal net as inferred from the absence of the sequence 1, √3, 2, √7,… for the positions of the equatorial reflections. For comparison, the X-ray diffraction diagram of a drop-cast film is reported (**Figure 73 b**, continuous line). The lower and varying peak intensity of the drop-cast film originates from the smaller number of ordered areas, contributing to the reflections in the used recording technique. This observation is therefore a proof of the more extended uniaxial orientation of field-force aligned HBC-PhC_{12} films.

7.5 Field-orientation of HBC-PhC_{12} molecules on gold substrate

In order to study the substrate influence on the electrical field orientation of HBC-PhC_{12} molecules, alignment experiments were conducted on a gold surface.
The film morphology was characterized via atomic force microscopy, whereas the molecular arrangement on the gold surface was clarified via FTIR absorption-reflection spectroscopy.

7.5.1 Atomic force microscopy

Field aligned HBC-PhC_{12} films were prepared on a polycrystalline gold layer, which was previously evaporated on a mica surface and successively annealed at 350°C for 1 hour. A 5 µm x 5 µm AFM micrograph of the sample is reported in **Figure 74 a**. The HBC-PhC_{12} molecules cover homogeneously the gold surface and assemble into a lamellar structure as evidenced by the magnified image in **Figure 74**

b. From section analysis (**Figure 74 c**) of the micrograph it is observed that the lamellae are on average perpendicularly oriented with respect to the applied electrical field and have a width of 3.470 nm. This value matches well with the van der Waals dimension of HBC-PhC$_{12}$ with completely extended alkyl chains (3.46 nm), which suggests that the observed lamellar packing is due to HBC-PhC$_{12}$ molecules assembled in the form of columns with their long axes perpendicular to the electrical field direction.

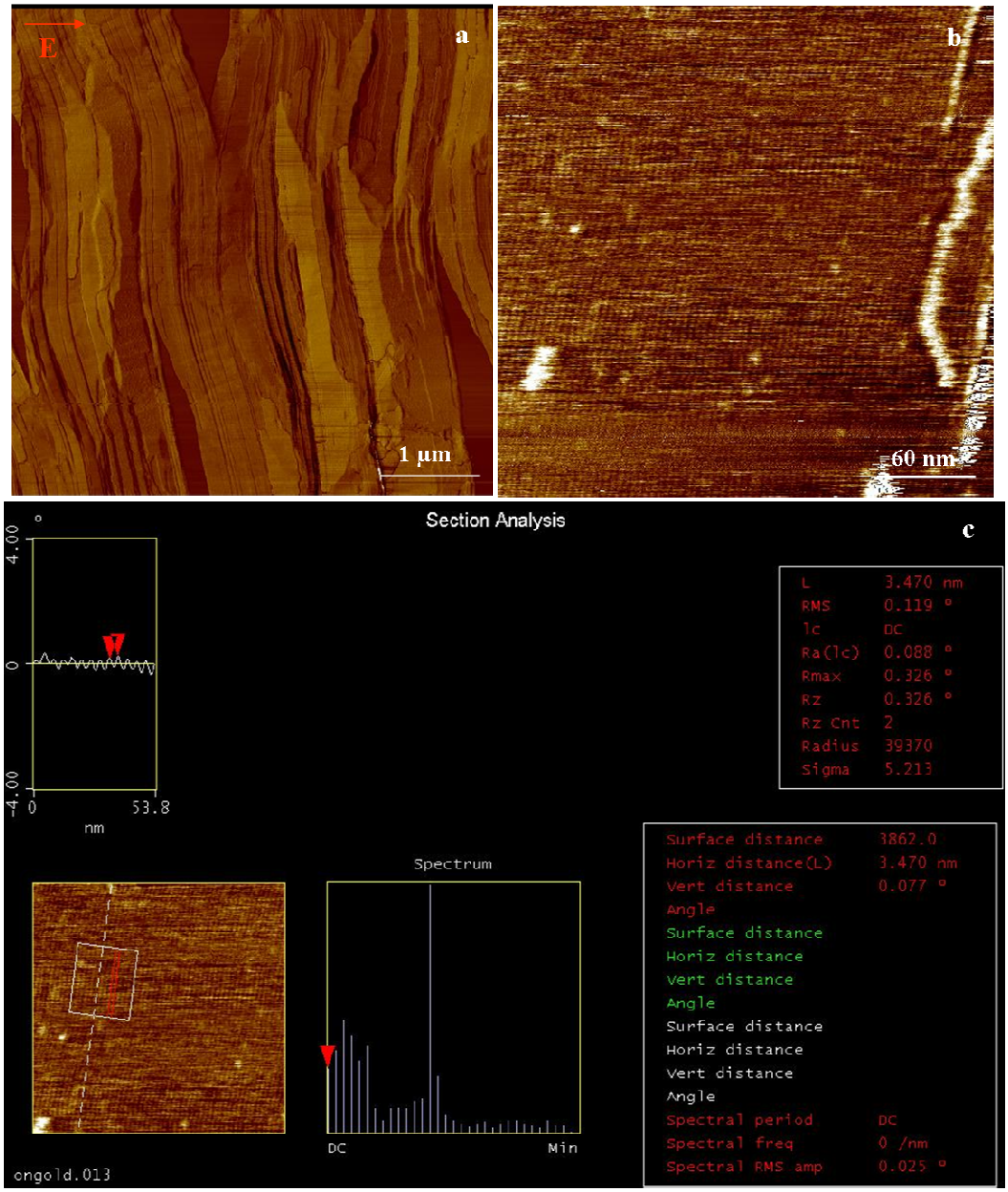

Figure 74. a) Tapping mode AFM micrograph of a field aligned HBC-PhC$_{12}$ film on gold surface. The red arrow indicates the electrical field direction. b) Magnified AFM micrograph. c) Section analyses of the film surface.

7.5.2 FT-IR reflection-absorption spectroscopy

In order to investigate the arrangement of the molecules on the gold surface, FT-IR reflection-absorption spectra of the field aligned HBC-PhC_{12} films were recorded.

The basis of this technique involves measurement of the reflected energy from a sample surface at a given angle of incidence and it is schematized in **Figure 75**. The incident FT-IR beam represented by I_0 illuminates the thin film of a given refractive index, n_2 and at an angle of incidence, θ_1. Some of the incident beam is reflected from the sample surface, represented by I_R at the incident angle, θ_1 and is also known as the specular component. Some of the incident beam is transmitted into the sample represented by I_T at an angle of θ_2 calculated from Snell's Law (**Equation 10**).

$$n_1 \sin\theta_1 = n_2 \sin\theta_2 \qquad \textbf{Equation 10}$$

At the reflective substrate, the beam reflects back to the surface of the thin film. Infrared energy is absorbed at characteristic wavelengths as this beam passes through the thin film and its spectrum is recorded.

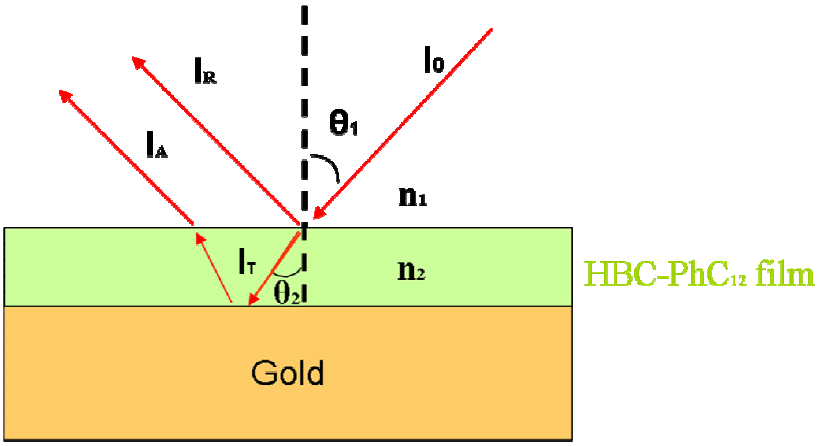

Figure 75. Beam path for Reflection-Absorption of a relatively thin film measured by specular reflectance

Reflection-absorption FT-IR spectroscopy provides useful information on molecular orientation on a reflective surface (gold) based on the selection rule that only vibrational modes having a transition dipole normal along the surface will get

excited[139]. It is therefore possible to distinguish between edge-on or face-on packing of the HBC-PhC_{12} discs on the gold substrate.

Suitable films for FT-IR measurements were prepared via casting a drop of HBC-PhC_{12} solution in p-xylene (15 mg/ml) in the presence of an electrical field on a glass surface which was previously covered with a 60 nm thin gold layer via thermal evaporation. **Figure 76** reports a FT-IR absorption-reflection spectrum of a field aligned HBC-PhC_{12} films (green trace); whereas, the red trace represents the FT-IR transmission spectrum of the bulk sample, for which every vibrational transition is allowed.

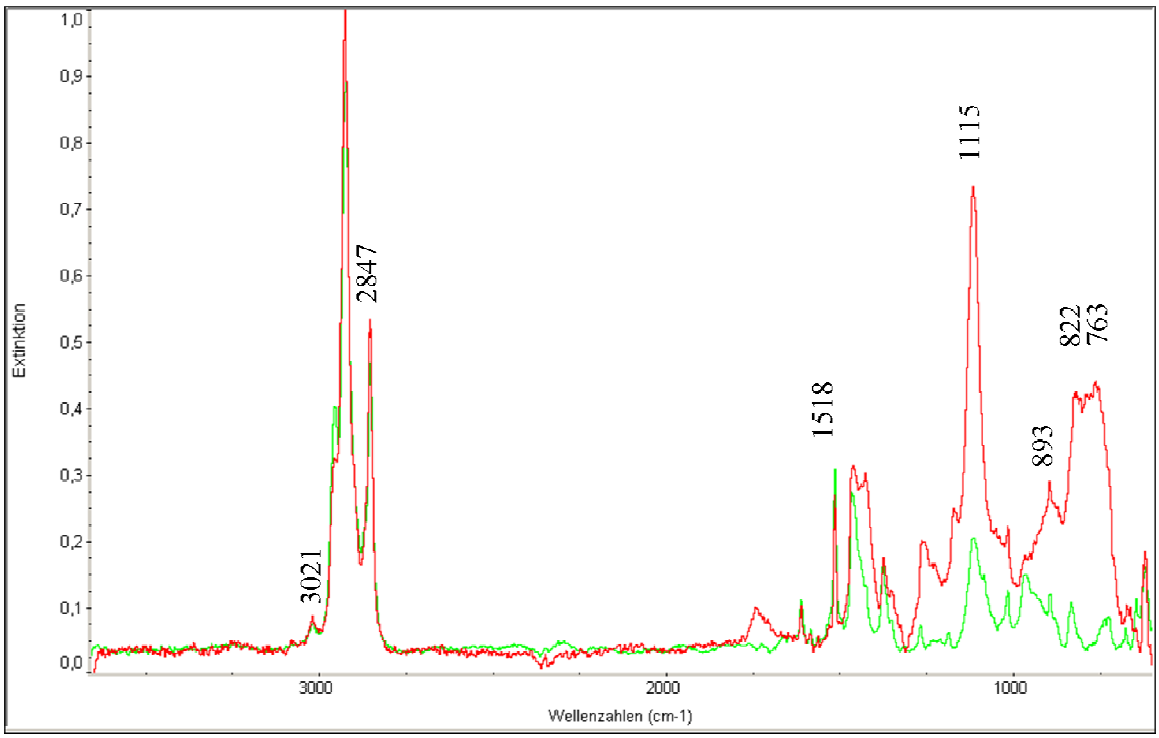

Figure 76. Normalized FT-IR absorption-reflection spectrum of field oriented HBC-PhC_{12} molecules (green trace). Normalized FT-IR spectrum of HBC-PhC_{12} molecules in bulk (red trace).

In the transmission FT-IR spectrum of the bulk sample, strong absorptions are recorded in the range between 750 and 900 cm^{-1}. They are assigned to the out-of the plane bending vibrations of the aromatic ring C-H´s and are extremely weak in the FT-IR absorption-reflection spectrum of the electrical field aligned HBC-PhC_{12} film.

Moreover, in both FT-IR spectra, together with the most prominent absorption bands in the range below 3000 cm^{-1}, which are assigned to the C-H stretch vibrations

of the aliphatic chains, a small absorption peak at 3021 cm^{-1} is visible. This is due to ring C-H stretch vibrations. Furthermore, both spectra present differently intense bands at 1518 and 1115 cm^{-1}. They are related to the ring stretch modes and to the ring C-H bending in the plane, respectively. All these vibration modes (**Table 6**) have their transition dipoles aligned normal or parallel to the ring plane. Their presence or absence in the FT-IR reflection-absorption spectrum of the field-oriented films allows to establish the fashion (face-on versus edge-on) of the HBC-PhC_{12} molecules on the gold substrate, as schematically reported in **Figure 16** [140].

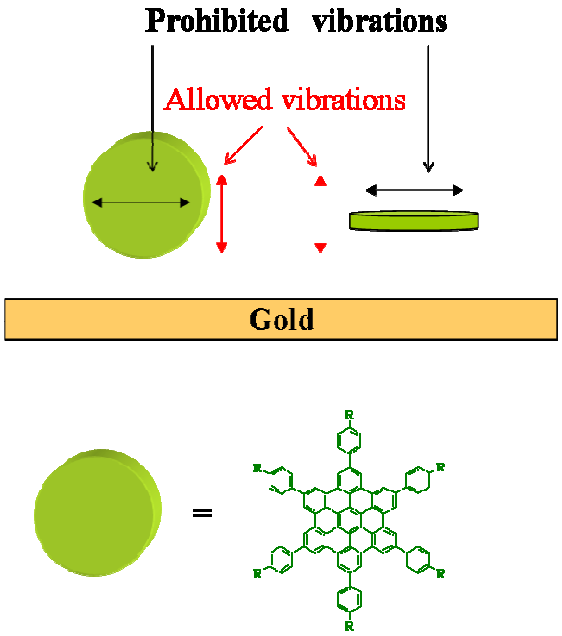

Figure 77. Schematic representation of allowed and prohibited vibration modes for face-on and edge-on HBC-PhC_{12} molecules.

The absence of the vibration bends between 750 and 900 nm (**Table 6**) in the FT-IR reflection-absorption spectrum of the oriented HBC-PhC_{12} film is the main reason to conclude that the molecules are edge-on arranged on the gold substrate. In fact, for edge-on arranged HBC-PhC_{12}, the transition dipole moment of the out-of-the plane bending is parallel to the substrate and therefore prohibited.

Table 6. Allowed and prohibited vibrational transitions for edge-on and face-on HBC-PhC$_{12}$ molecules

Transitions / cm^{-1}	Transition type	Edge-on molecules	face-on molecules
3021	ring C-H stretch	+	-
3000	Aliphatic C-H stretch	+	+
1518	ring C-H stretch	+	-
1115	ring C-H bending in plane	+	-
750-900	ring C-H bending out of plane	-	+

+ = allowed transition

- = prohibited transition

7.6 Electrical field-induced alignment of substituted hexabenzocoronene molecules into columnar structures on highly oriented pyrolitic graphite investigated by STM and AFM

As morphology, crystal structure and molecular ordering of the first organic layers adjacent to a substrate are essential determinants of charge carrier transport phenomena [141], this investigation is dedicated to the study of the electrical field influence on HBC-PhC_{12} thin films.

The morphology of the HBC-PhC_{12} films prepared via drop-casting and subsequent solvent evaporation in the presence of an electrical field was investigated via scanning tunneling microscopy (STM) and atomic force microscopy (AFM) on highly oriented pyrolitic graphite (HOPG) to obtain submolecular resolution. At solid-liquid interfaces, STM studies have shown for symmetrically substituted as well as unsubstituted HBC molecules a face-on arrangement on the HOPG substrate[142-62-143], defined as the arrangement of the molecules with their aromatic disc lying flat on the graphitic surface. So far, only non-substituted HBC molecules deposited from the gas phase on HOPG via soft-landing mass spectrometry showed a different behavior [9-34]. In this case, the molecules adopt an edge-on arrangement where the aromatic discs are oriented nearly perpendicularly to the surface plane. During a soft-landing deposition, HBC ions are formed by a matrix assisted laser desorption ionization (MALDI) source, accelerated, separated and then decelerated and focused on a conducting surface by means of electrical fields. Most likely dipole moments are induced into the molecules which orient their planar cores along the electrical field lines. Hypothesizing that this mechanism allows the molecules to adopt an edge-on arrangement on the HOPG surface, electrical fields should also be able to increase the order and control the arrangement of the molecules on the surface. Thus, the field influence on the assembly of HBC-PhC_{12} molecules is investigated. Additionally, a comparative STM study on HBC-PhC_{12} films drop-cast in absence of an electrical field at the solid-liquid interface and at the solid-air interface is conducted.

7.6.1 STM imaging of HBC-PhC_{12} molecules at the solid-liquid interface

The assembly of HBC-PhC_{12} molecules at the interface of a solution in 1,2,4-trichlorobenzene with HOPG was investigated by in-situ STM. HBC-PhC_{12} molecules

were physisorbed at the interface between the HOPG and a solution in 1,2,4-trichlorobenzene. The resulting STM images are reported in **Figure 78**.

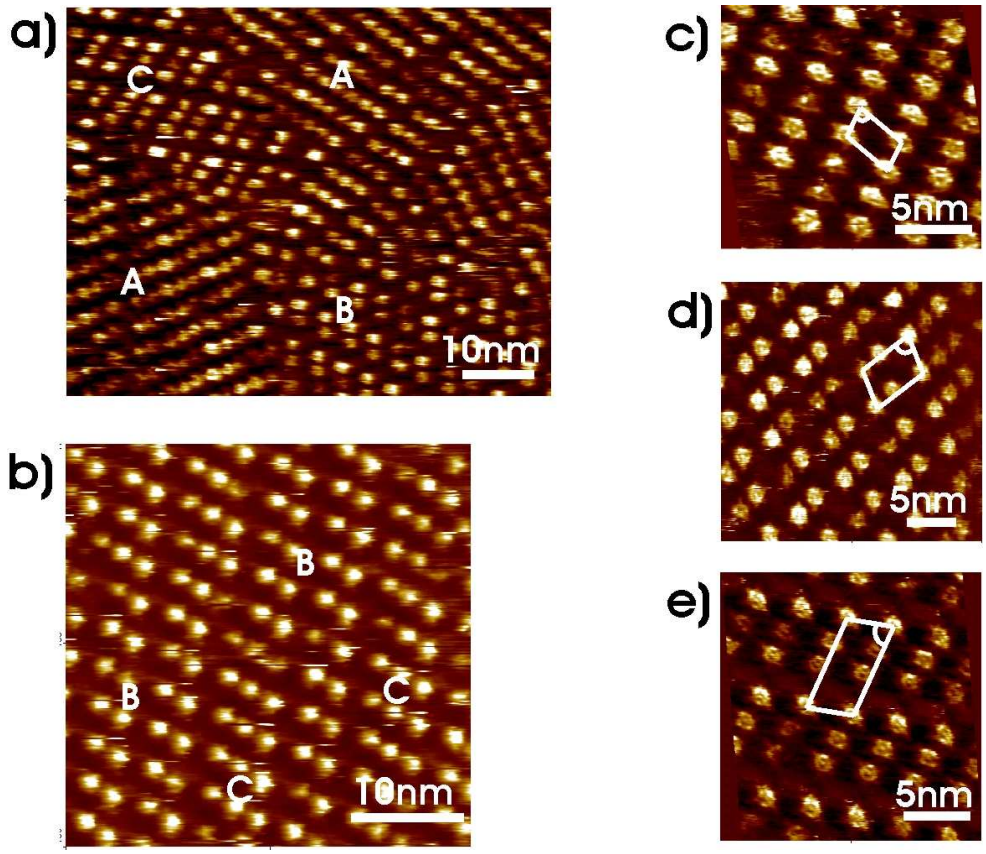

Figure 78. STM current images of HBC-PhC$_{12}$ at the HOPG-solution interface. Sample bias U_s= 1 V; average tunneling current I_t = 0.1 nA. a), b) Large scale images with three patterns marked by A, B and C patterns. c) Oblique structure, ascribed to pattern A. d) Dimer structure B. e) Trimer structure C.

In the STM current images (**Figure 78**), the bright features (corresponding to high tunneling probability) can be attributed to π-conjugated aromatic rings, because the energy difference between their frontier orbitals and the Fermi level of HOPG is rather small [144]. The aliphatic side chains, which are attributed to the dark parts of the images, could not be resolved, probably due to their high conformational mobility on a time scale faster than the STM imaging or larger energy difference between its frontier orbital and the Fermi level of HOPG.

Three different types of the 2D unit cells are presented in **Figure 78**, marked with A, B and C. The two-dimensional lattice A (**Figure 78 c**) is an oblique structure described by a unit cell with parameters a = (2.01 ± 0.11) nm, b = (3.30 ± 0.17) nm

and α = (76 ± 4) °. In case B (**Figure 78 d**), the 2D unit cell is a dimeric structure (a = (3.41 ± 0.05) nm, b = (5.54 ± 0.19) nm and α = (74 ± 1) °). The lattice constant of the trimer C, containing three molecules in a unit cell, is a = (3.48 ± 0.04) nm, b = (7.50 ± 0.34) nm and α = (75 ± 2) °. Most frequent is the oblique pattern constituted by single HBC-PhC_{12} molecules, while the trimer structure is rarest.

Interestingly, a random distribution of two dissimilar contrasts of the aromatic core in all of the three domains at the HOPG-liquid interface is recorded [145]. It could possibly be attributed to a conformational change of the HBC core with the lateral phenyls from planar to nonplanar, which causes a change in the electronic properties of the HBC cores, resulting in different contrasts in the STM images. Another interpretation would be different positions of the HBC-cores with respect to the STM-tip and the substrate [144]. In fact, the asymmetric position of the molecules between tip and substrate influences the contrast in STM current images, in accord with tunneling spectroscopy. Also both factors may contribute to the different contrast observed in the STM images.

7.6.2 STM characterization of field oriented HBC-PhC_{12} films

In order to study the electrical field influence on the arrangement of the HBC-PhC_{12} molecules on HOPG, dry HBC-PhC_{12} films were prepared. Electrical fields in the range of 4-5 x 10^5 V/m were applied during absorption of the HBC-PhC_{12} molecules from a solution in 1,2,4 trichlorobenzene onto the solid surface and maintained until solvent evaporation. Then, the films were characterized by STM at the solid-air interface.

Figure 79 a displays an STM image exhibiting characteristic stripes of ~ 3.6 nm width, oriented predominantly perpendicularly to the direction of the applied electric field.

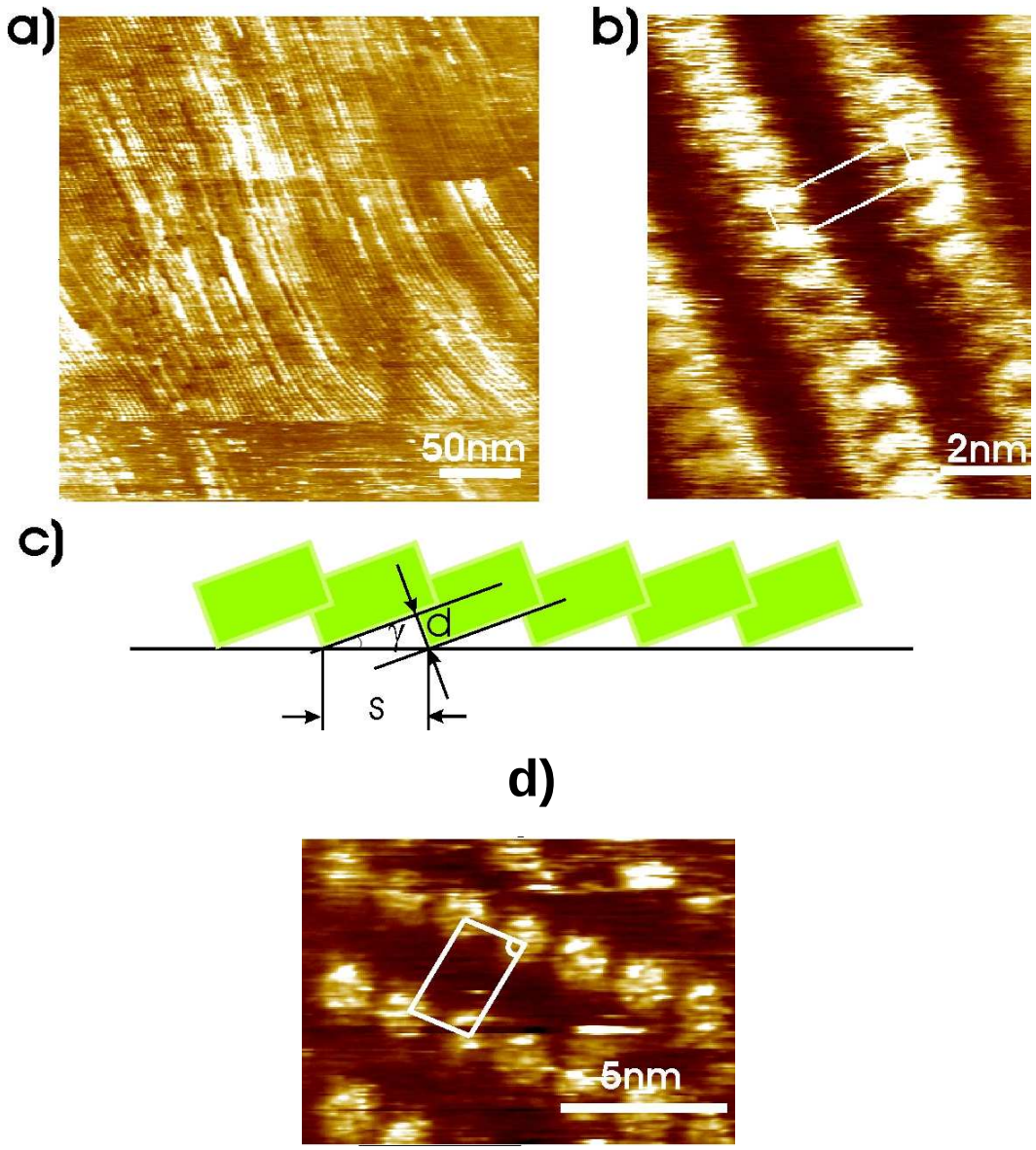

Figure 79. a) and b) STM current images of the surface of an electric field-oriented HBC-PhC$_{12}$ film. Sample bias U_s= 3 V; average tunneling current I_t = 0.1 nA, unit cell parameters: a = (1.03 ± 0.11) nm, b = (3.60 ± 0.16) nm and α = (79 ± 4) °. c) Schematic representation of the HBC disc arrangement with respect to the surface. d) STM current image of a dry film adsorbed without electric field, sample bias U_s= 1 V; average tunneling current I_t = 0.1 nA, unit cell parameters: a = (2.01 ± 0.11) nm, b = (3.30 ± 0.17) nm and α = (76 ± 4) °

The stripes can be attributed to HBC-PhC$_{12}$ columns within one domain as large as 300 nm across. No epitaxial growth was recognized [146], indicating that the structure of the deposited film was not dominated by the lattice structure of the HOPG substrate. The film displayed unidirectionally aligned stripes oriented perpendicularly

to the direction of the previously applied electrical field. From the highly resolved STM image (**Figure 79 b**) the spacings within the stripes and perpendicular to them are (1.03 ± 0.11) nm (s) and (3.6 ± 0.16) nm, respectively. The stripes are attributed to π-π stacked HBC-PhC_{12} cores, assembled in a tilted edge-on arrangement on the graphitic surface (**Figure 79 c**) with an angle γ, which can be estimated from d/s = sin γ = 0.33 to be ~ 19° [147]. The HBC-PhC_{12} molecules could be visualized at an average tunneling impedance (Z) of 30 GΩ.

The tunneling impedance is calculated according to the following equation (**Equation 11**):

$$Z = V / I \qquad \textbf{Equation 11}$$

Where V is the bias / Volts applied during the STM analysis and I is the current/ Ampere. Therefore, for a constant I value, changing the voltage corresponds to a change in tip-surface separation.

Upon reducing the tip-sample separation (average impedance of 10 GΩ), no layer with face-on HBC-PhC_{12} molecules was found. At even smaller impedance of ~0.1 GΩ, the graphitic substrate itself was visualized[148]. Even though an additional layer of face-on molecules was not recordable, its presence cannot be excluded, considering the high impedance value needed for the visualization of the columnar structures.

The packing of the HBC-PhC_{12} molecules, unidirectionally aligned by means of an electrical field, differed substantially from the arrangement, which the molecules adopt in dry films prepared in the absence of an electrical field (**Figure 79 d**). The image in **Figure 79 d** displays HBC-PhC_{12} discs face-on, arranged in a unit cell with parameters a = (2.11 ± 0.10) nm, b = (3.12 ± 0.15) nm and α = (70 ± 2) ° in an oblique structure which is indistinguishable from the oblique structure in the molecular monolayer obtained from the solid-liquid STM measurement within experimental error. The face-on HBC-PhC_{12} molecules could be visualized by using an average impedance of 10 GΩ. By increasing the impedance up to 30 GΩ, no edge-on HBC-PhC_{12} molecules were observed. At even smaller impedance of ~0.1 GΩ, the graphitic substrate itself was visualized [149]. This leads to conclude that no upper layers made of edge-on HBC-PhC_{12} molecules are present. In fact, the HBC-PhC_{12} molecules, deposited on a graphitic surface in absence of any external force, can

overlap their aromatic orbitals with the ones of the HOPG. Thus, the face-on arrangement results as the most energetically stable molecular assembly.

The observed tilted edge-on packing of the HBC-PhC_{12} molecules on the HOPG surface can be explained considering that, in the presence of an electrical field, the molecules are subjected not only to the strong π–π interactions between nanographene and graphene, but also to an external electrical force. The electrical field influence on the HBC-PhC_{12} molecules strongly competes with the graphene-nanographene affinity, forces the molecules to assume an edge-on arrangement and orients them in his direction avoiding epitaxial growth phenomena.

7.6.3 Atomic force microscopy

The morphology of the field-oriented HBC-PhC_{12} films on HOPG surface was additionally investigated by AFM (**Figure 80 a** and **73 b**).

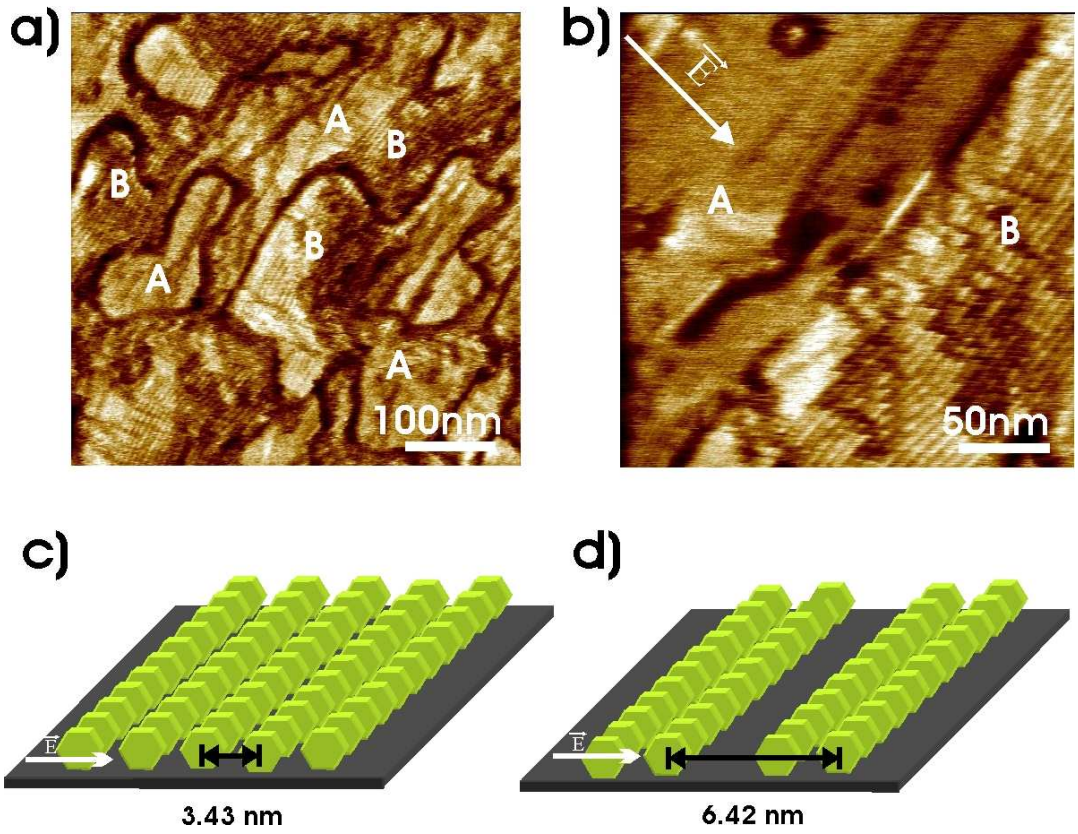

Figure 80. a) and b) Tapping mode AFM phase image of HBC-PhC12 films on HOPG, prepared within electric fields. c) Sketch of single HBC-PhC_{12} columns. d) Sketch of the stripes formed by two HBC-PhC_{12} molecules.

Two kinds of domains can be recognized in the film, indicated by A and B. In the zoomed image (**Figure 80 b**) the domain A exhibits narrow parallel stripes with a distance of (3.43 ± 0.12) nm. In the domain B, wide stripes (6.42 ± 0.09) nm are visible. Both stripes are on average oriented towards the perpendicular direction of the formerly applied electric field (marked by the white arrow and Ē). The width of the narrow stripes in domain A is in agreement with the width of the columns observed or single HBC-PhC_{12} with totally stretched alkyl chains (3.46 nm). In domain B, the width of the wide stripes is about twice that in domain A. As for field-oriented HBC-PhC_{12} molecules on a glass surface[74], the stripes of 3.4 nm width can be attributed to HBC-PhC_{12} molecules, oriented in the field direction and assembled in unidirectionally aligned columns (**Figure 80**). The 6.4 nm bright stripes may be formed by ordered dimers of HBC-PhC_{12}, which are schematized in **Figure 80 d**.

The formation of the wide stripes can be attributed to the high tendency of the HBC-PhC_{12} molecules to assemble into dimeric structures in 1,2,4-trichlorobenzene solvent, as the STM images of the molecules at the solid-liquid interface already proved (**Figure 78**).

However, dimers of HBC-PhC_{12} molecules assembled into a columnar structure were not visualized in the STM images of the field-oriented films (**Figure 79**). This evidence could be explained by a lower formation probability of the dimeric pattern.

7.7 Electrical field alignment of HBC molecules bearing dipoles

7.7.1 2-Cyano-5,8,11,14,17-penta(3,7-dimethyloctanyl)-hexa-peri-hexabenzocoronene as a model system

To investigate the electrical field influence on HBC molecules bearing dipoles attached to the core, alignment experiments were carried out on 2-cyano-5,8,11,14,17-penta(3,7-dimethyloctanyl)-hexa-peri-hexabenzocoronene (HBC-CN) molecules. The molecular structure is reported in **Figure 81.**

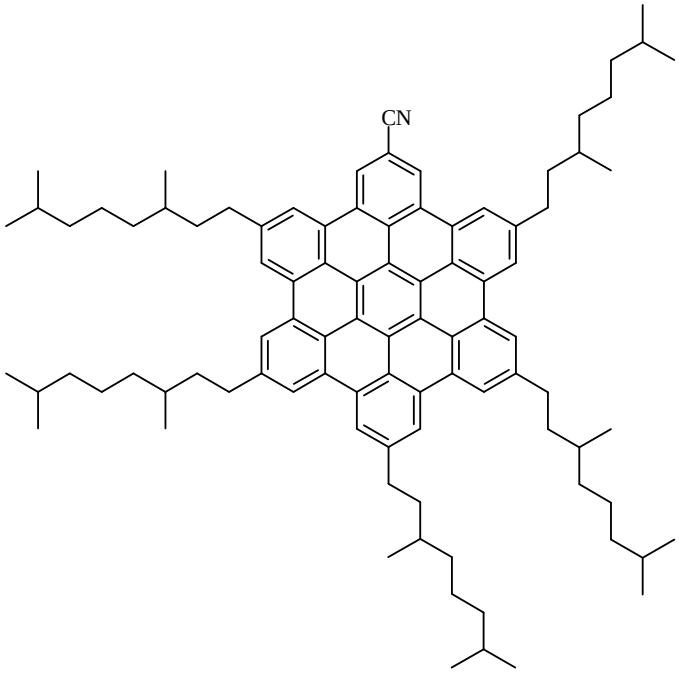

Figure 81. a) Molecular structure of the HBC-CN molecule.

The choice of selecting HBC molecules carring an electron-witdrawing (-CN) group instead of an electron-donating one was made considering that the former have greater propensity of forming columnar phase as compared to the latter that are essentially nonmesogenic [150]. Moreover, due to the electron withdrawing effect of the cyano group attached to the aromatic core, HBC-CN molecules possess a permanent electric dipole as large as $\mu \sim 4.55$ Debye [151-152].

Furthermore, HBC-CN molecules were selected as a model system as their liquid crystalline properties have been well clarified by a previous investigation. From that work, it is interesting to report that the presence of a strong dipole on the HBC core has the effect to destabilize the crystalline phase (Cr) of the HBC molecules. In the case of HBC-CN molecules, the Cr phase is completely unstable and the molecules possess only a hexagonal liquid crystalline phase (Col_h) at a temperature of 234 K. Thus, at room temperature the aromatic discs are free to rotate in plane. Moreover, according to Elmahdy et al. [152], the disc dynamics is characterized by large out of the plane excursion of $\sigma = 38°$.

7.7.2 Optical microscopy analyses

To study the influence of the electrical field on the supramolecular order of the HBC-CN molecules, optical microscopy analyses were performed on the field-oriented HBC-CN films. These films were prepared via casting a drop of HBC-CN solution in p-xylene (10 mg/mL) on a glass surface and letting evaporate in presence of an electrical field (5 kV/cm). The corresponding optical micrograph is reported in **Figure 82**.

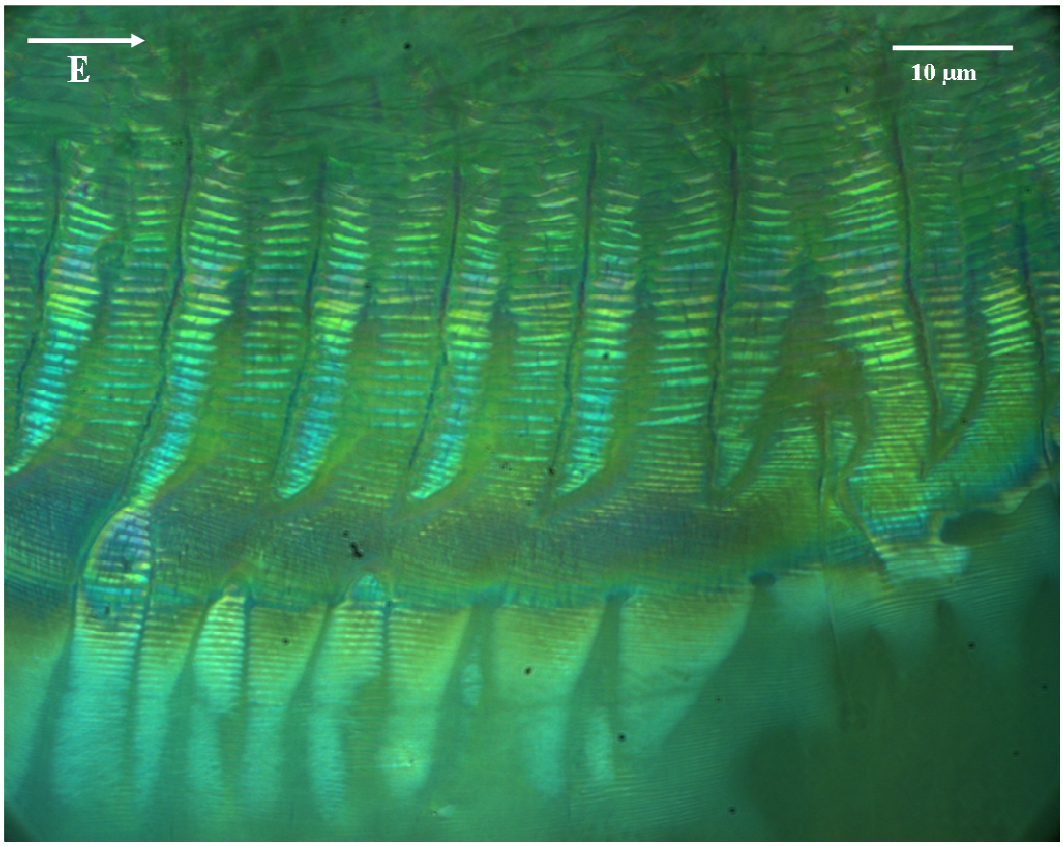

Figure 82. Optical micrograph of a field-oriented HBC-CN film between crossed polarizers. The electrical field direction is indicated by the white arrow.

An alternation of bright and dark stripes, directed in the same direction of the previously applied electrical field, can be observed in the optical microscope equipped with crossed polarizers. These features, already observed for field-oriented films of HBC-PhC_{12} molecules, can be related to the edge-on fashion of the HBC-CN molecules with respect to the glass surface. It can be in fact justified by HBC-CN molecules assembled into columnar structures with the axis parallel to either the

polarizer or the analyzer. The presence of stripe patterns is due to the bend deformation of the columnar director, which is related to the liquid crystalline nature of the HBC-CN molecules. The width of a stripe in the optical micrograph of **Figure 82** is 1.5 µm in average. This value is circa seven times smaller than the ones (10 mm) observed in the optical micrograph of the field-oriented film of non-polar HBC-PhC_{12} molecules (**Figure 65**). We conclude therefore that the columnar director of the HBC-CN molecules is more affected by bend deformations than that of HBC-PhC_{12} molecules. This phenomenon can be related to the high dipole moment value associated to the HBC-CN molecules. Polar molecules, in fact, can be subjected in the LC state to flexoelectric polarization [153]. Flexoelectricity denotes curvature-induced electric polarization in liquid crystals, subjected to orientational deformations of the director field. The flexoelectric effect is reversible and materials exhibiting the direct piezoelectric effect (the production of polarization when deformation is applied) also exhibit the converse piezoelectric effect (the production of deformation when an electric field is applied). Thus, through application of external electrical fields, flexoelectric polarization comports the appearance of torques and orientational deformations in the director field $E(r)$.

An additional justification for the pronounced bend deformation of the liquid crystalline phase of HBC-CN molecules could be the already mentioned out of the plane excursion of $\sigma = 38°$ of the aromatic cores of the HBC-CN. This motion of the aromatic core at a temperature higher than the glass transition for HBC-CN could disturb the unidirectional orientation action of the external electrical field and thus produce pronounced bend deformations.

7.7.3 AFM visualization

The morphology of the field aligned HBC-CN films was investigated via AFM. **Figure 83** reports the corresponding AFM micrograph.

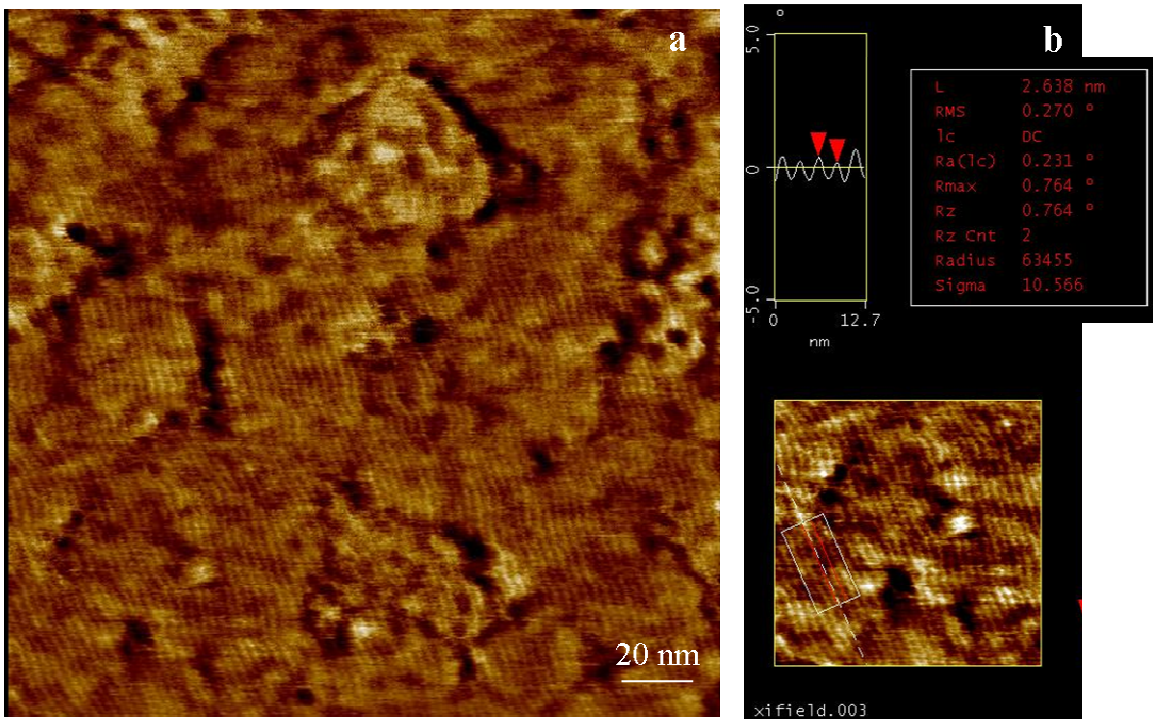

Figure 83. a) AFM micrograph of an electrical field aligned HBC-CN film. b) Section analysis of an electrical field aligned HBC-CN film.

HBC-CN molecules cover homogeneously the glass surface and self assemble into a lamellar structure. The lamella width was obtained via the section analysis of the AFM micrograph, as reported in **Figure 83 b**, and has a value of 2.638 nm. This value is in perfect agreement with the calculated size of HBC-CN molecules with stretched alkyl chains. Therefore, it is reasonable to assume that the stripes observed in **Figure 83** are due to the assembly of the HBC-CN molecules into columnar structures, which have their long axes normal to the direction of the previously applied electrical field. Thus, we concluded that ordered columnar arrays of HBC-CN molecules can be obtained via drop-casting and subsequent solvent evaporation in presence of an electrical field. The unidirectional orientation of the columns at a macroscopic level is however disturbed by the strong destabilization of the HBC-CN crystal phase caused by the presence of the strong dipole directly attached to the aromatic HBC core. As a result, the oriented HBC-CN columns are more affected by bend deformations than those constituted by unpolar HBC-PhC_{12} molecules.

7.8 Conclusions

Within this chapter the influence of an external electrical field on the packing and on the orientation of non polar discotic molecules, such as HBC-PhC_{12}, has been studied on different substrates: glass, gold and highly oriented pyrolitc graphite (HOPG) [75]. Under field action, the large aromatic discs are found to assemble into columnar structures, which are unidirectionally oriented on a range as large as several millimeters. The electrical field-aligned HBC molecules maintain their upright standing arrangement even on HOPG. Whereas, the aromatic core of the HBC-PhC_{12} molecules in absence of any external electrical force lays face to face on the graphitic substrate. Furthermore, the electrical field action on the orientation of disc-like molecules bearing a strong dipole moment, such as HBC-CN, has been tested. In this case, the field action leads to orientation of the molecules, which are arranged into columnar structures. However, pronounced bend deformations are observed in the field aligned HBC-CN films. This observation could be explained considering the likely occurrence of flexoelectric phenomena or considering the extremely high mobility (in plane rotation and out of plane excursion) of the aromatic cores of the HBC-CN molecules.

7.9 References

[103] H. Sirringhaus, R.J. Wilson, R.H. Friend, M. Inbasesekaran, W. Wu, E.P. Woo, M. Grell, D.D.C. Bradley, *Appl. Phys. Lett.*, **2000**, 77, 406.

[104] C.-Y. Liu, A.J. Bard, *Nature*, **2002**, 418, 162.

[105] M. Paulsson, S. Stafström, *J. Phys.: Condens. Matter*, **2000**, 12, 9433.

[106] P. Smolenyak, R. Peterson, K. Nebesny, M. Toerker, D.F. O'Brien, N.R. Armstrong, *J. Amer. Chem. Soc.* **1999**,121, 8628.

[107] K. Yase, S. Schwiegk, G. Lieser, G. Wegner, *Thin solid film*, **1992**, 210-211, 22.

[108] M. L. Swiggers, G. Xia, J.D. Slinker, A.A. Gorodetsky, G.G. Malliaras, R.L. Headrick, T. Brian, R.N. Shashidhar, C.S. Dulcey, *Appl. Phys. Lett.*, **2001**, 79, 1300.

[109] M. Brinkmann, S. Graff, C. Straupe`, J.-C.Wittman, C. Chaumont, F. Nuesch, A. Aziz, M. Schaer, L. Zuppiroli, *J. Phys. Chem. B*, **2003**, 107,10531.

[110] S. D. Wang, X. Dong, C.S. Lee, S.T. Lee, *J. Phys. Chem. B*, **2005**, 109, 9892.

[111] A. Tracz, J. K. Jeszka, M.D. Watson, W. Pisula, K. Müllen, T. Pakula, *J. Amer. Chem. Soc.*, **2003**, 125, 1682.

[112] S. Kubowicz, U. Pietsch, M.D. Watson, N. Tchebotareva, K. Müllen, A.F. Thünemann, *Langmuir*, **2003**, 19, 5036.

[113] J. Piris, M.G. Debije, N. Stutzmann, A.M. van de Craats, M.D. Watson, K. Müllen, J.M. Warman, *Adv. Mat.*, **2003**, 15, 1736.

[114] I. O. Shklyarevskiy, P. Jonkheijm, N. Stutzmann, D. Wasserberg, H.J. Wondergern, P. C. M. Christianen, A.P.H.J. Schenning, D.M. De Leeuw, Z. Tomovic, J. Wu, K. Müllen, J. C. Maan, *J. Amer. Chem. Soc.*, **2005**, 127, 16233.

[115] D. C. Martin, *Polymer*, **2002**, 43, 4421.

[116] M. Mas-Torrent, D. den Boer, M. Durkut, P. Hadley, A.P.H.J. Scenning, *Nanotechnology*, **2004**, 15, S265.

[117] K. Amundson, E. Helfand, X. Quan, *Macromolecules*, **1993**, 26, 2698.

[118] U. Zimmermann, N. Karl *Surface Science*, **1992**, 268, 296.

[119] R. Forker, T. Dienel, T. Fritz, K. Mullen, *Physical Review B: Condensed Matter and Materials Physics*, **2006**, 74, 165410/1.

[120] T. Schmitz-Hubsch, F. Sellam, R. Staub, M. Torker, T. Fritz, C. Kubel, K. Müllen, K. Leo, *Surface Science*, **2000**, 445, 358.

[121] A. M. van de Craats, N. Stutzmann, O. Bunk, M. M. Nielsen, M. Watson, K. Müllen, H. D. Chanzy, H. Sirringhaus, R. H. Friend, *Advanced Materials* **2003**, 15, 495.

[122] A. J. Fleming, J. N. Coleman, A. B. Dalton, A. Fechtenkoetter, M. D. Watson, K. Müllen, H. J. Byrne, W. J. Blau, *Journal of Physical Chemistry B*, **2003**, 107, 37.

[123] V. J . Docherty, D. Pugh, J. 0. Morley, *J. Chem.* SOC., *Furuday Trans.* 2, **1985**, 81, 1179.

[124] N. Matsuzawa, D. A. Dixon, *J. Phys. Chem.* **1992**, 96, 6241.

[125] I. O. Shklyarevskiy, P. Jonkheijm, N. Stutzmann, D. Wasserberg, H. J. Wondergern, P. C. M. Christianen, A. P. H. J. Schenning, D. M. De Leeuw, Z. Tomovic, J. Wu, K. Müllen, J. C. Maan, *J. Am. Chem. Soc.* **2005**, 127, 16233.

[126] K. Schmidt, H.G. Schoberth, F. Schubert, H. Haensel, F. Fischer, T. M. Weiss, G. J. A. Sevink, A. V. Zvelindovsky, A. Boeker, G. Krausch, *Soft Matter*, **2007**, 3, 448.

[127] Polarized Light in Optics and Spectroscopy, David S. Kliger; James W. Lewis; Cora Einterz Randall **1990** Academic press

[128] J. Hou, W. Wu, D. Shen, M. Xu, Z. Li, *Polymer* **1994**, 35, 699.

[129] S. Chen, J. Yongze, S. Hu, M. Xu, *Polym. Commun.* **1987**, 28, 208.

[130] M. G. Dobb, D. J. Johnson, B. P. Saville, *J. Polym. Sci.* **1977**, 15, 2201.

[131] F. Livolant, Y. Bouligand, *J. Phys.* **1986**, 47, 1813.

[132] J. V. Selinger, R. F. Bruinsma, *Phys. Rev. A* **1991**, 43, 2910.

[133] R. Ries, G. Lieser, S. Schwiegk, G. Wegner, *Acta Polym.* **1997**, 48, 536.

[134] P. Oswald, M. Kleman, *J. Phys.* **1981**, 42, 1461.

[135] I. Fischbach, T. Pakula, P. Minkin, A. Fechtenkötter, K. Müllen, H. W. Spiess, K. Saalwächter, *J. Phys. Chem. B* **2002**, 106, 6408.

[136] W. Pisula, Z. Tomovic, M. Stepputat, U. Kolb, T. Pakula, K. Müllen, *Chem. Mater*. **2005**, 17, 2641.

[137] W. Pisula, Z. Tomovic, M. D. Watson, K. Müllen, J. Kussmann, C. Ochsenfeld, T. Metzroth, J. Gauss, *J. Phys. Chem. B* **2007**, 111, 7481.

[138] J. Wu, A. Fechtenkötter, J. Gauss, M. D. Watson, M. Kastler, C. Fechtenkötter, M. Wagner, K. Müllen, *J. Am. Chem. Soc.* **2004**, 126, 11311.

[139] A. N. Parikh, D. L. Allara, *J. Chem. Phys.* **1992**, 96, 927.

[140] W. S. Hu, Y. T. Tao, Y. J. Hsu, D. H. Wei, Y. S. Wu, *Langmui*r **2005**, 21, 2260.

[141] C. D. Sheraw, T. N. Jackson, D. L. Eaton, J. E. Anthony, *Adv. Mater*. **2003**, 15, 2009.

[34] A. Stabel, P. Herwig, K. Müllen, J.P. Rabe, *Angew. Chemie* **1995**, 34, 1609.

[143] F. Jäckel, M. D. Watson, K. Müllen, J. P. Rabe, *Phys. Rev. B*, **2006**, 73, 045423/1.

[144] R. Lazzaroni, A. Calderone, J. L. Bredas, J. P. Rabe, *J. Chem. Phys.* **1997**, 107, 99.

[145] P. Samori, A. Fechtenkötter, F. Jäckel, T. Böhme, K. Müllen, J. P. Rabe, *J. Am. Chem. Soc.* **2001**, 123, 11462.

[146] Z. H. Cheng, L. Gao, Z. T. Deng, Q. Liu, N. Jiang, X. Lin, X. B. He, S. X. Du, H.-J. Gao, *J. Physic. Chem. C*, **2007**, 111, 2656.

[147] P. Samori, H. Engelkamp, P. de Witte, A. E. Rowan, Roeland J. M. Nolte, J. Rabe, *Angew. Chemie, Int. Ed.* **2001**, 40, 2348.

[148] M. L. Piot, Doctor thesis, Paris, **2006**, 51

[149] F. Jäckel, M. Ai, J. Wu, K. Müllen, J.P. Rabe, *J. Am. Chem. Soc.* **2005**, 127, 14580.

[150] E: J. Foster , R. B. Jones, C. Lavigueur, E. W. Williams, *J. Am. Chem. Soc*, **2006**, 128, 495.

[151] Xi, Dou, K. Müllen, M.M. Elmahdy, G. Floudas, not published results

[152] M. M. Elmahdy, X. Dou, M. Mondeshki, G. Floudas, H-J. Butt, H. W. Spiess, K. Müllen, *J. Am. Chem. Soc*, **2008**, 130, 5311.

[153] A. Derzhanski, A. G. Petrov, M. D. Mitov, *J. Phys.* (Fr.), **1978**, 39, 273.

8 Electrical field controlled assembly of rigid π-systems for improved organic electronics

8.1 Introduction

As discussed in the previous Chapter, an electrical field applyied during evaporation of a concentrated solution of substituted HBC molecules is able to induce unidirectional orientation in the resulting film. Here, this field capability is used to control the orientation of rod-like molecules, which are prospective candidates for novel organic electronic devices with improved performances. In this work, attention is focused on the field-induced orientation of a cyclopentadithiophene-alt-benzothiadiazole copolymer, as an example for rigid-rod semiconducting polymers, and on the alignment of pentacene molecules. The latter has been achieved by retro-Diels Alder reaction on 13,6-Sulfinylacetamidopentacene molecules in the presence of an electrical field. The degree of anisotropy achieved by employing electrical fields is monitored via optical, morphological and diffraction analyses. Finally, organic field effect transistor (OFET) characteristics of the oriented films have been evaluated using a facility developed in house.

7.2 Electrical field orientation of rigid rod polymers.

8.1.1 Cyclopentadithiophene-alt-benzothiadiazole copolymer as a model compound.

Simple processing of novel organic field-effect transistors (OFETs) is of key importance for the fabrication of flexible large-area device [154-155-156]. Therefore, solution-processible polymers have recently attracted phenomenal interest as a low cost alternative to silicon-based thin film transistors. The fabrication of polymers, which exhibit good transistor performances remains, however, the main obstacle to all-polymer optoelectronic circuits. Up to now, only a few polymers have been able to approach charge carrier mobilities of 0.1 cm^2/Vs or higher [157-158-159].

Great efforts have been made in developing novel synthetic routes to synthesize conjugated polymers composed of a rigorous alternation of electron donor and electron acceptor units[160], since it has been recognized that this construction may be responsible for a higher rate of intermolecular hopping and hence for higher charge

carrier mobilities [161-162]. By careful selection and design of the donor (p-type) and acceptor (n-type) building blocks, the intermolecular charge transfer interaction can be enhanced, allowing such D-A copolymer semiconductors to exhibit small band gaps, high electron affinity and low ionization potential, and thereby facilitating hole injection and transport in thin film field-effect transistors. As an example, benzothiadiazole (**BTZ**) and cyclopentadithiophene (**CDT**) copolymers (**Figure 84**) have attracted considerable attention recently for their semiconducting properties [163]. This kind of fused ring thiophene derivatives lowers the reorganization energy, which has been shown to strongly affect the rate of intermolecular hopping and hence the charge carrier mobility in organic semiconductors.

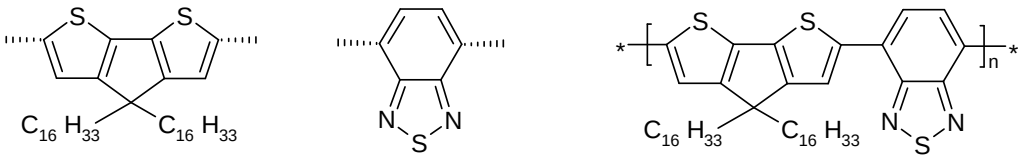

CTD **BTZ** **CTD-alt- BTZ**

Figure 84. Structures of CDT, BTZ and alternating CTD-alt-BTZ copolymer.

CTD-alt-BTZ copolymers with high molecular weigth have been found to possess the highest charge carrier mobility up to now reported for soluble polymers. Elevated saturated mobility values of μ_{sat} = 1.4 cm^2/Vs and an on/off ratio of 10^5 have been recorded for OFETs with CTD-alt-BTZ copolymers as semiconductor material.

Within this investigation, CTD-alt-BTZ oligomers (Mn = 10.000 Da) have been used for the alignment experiments. For this lower molecular weigth sample the highest value of saturated mobility has be reported to be 0.17 cm^2/Vs. However, thin films of this CTD-alt-BTZ copolymer, obtained by solution processing, did not show any long-range organization, neither did they exhibit any birefringence in polarized optical microscopy, nor discrete reflections in X-ray powder diffraction experiments. The high device performance was, therefore, attributed to the small π-stacking distance between the macromolecules.

Since long-range order is believed to enhance the device property of the resulting polymer film, the present investigation is dedicated to improve the packing of the CTD-alt-BTZ copolymer chains on the surface by means of electrical fields.

8.1.2 Film preparation

From a drop of 1 mg/ml BTZ-alt-CDT copolymer solution, the solvent 1,2,4 trichlorobenzene was allowed to evaporate in presence of an electrical field as strong as 400-500 kV/m on a clean glass surface maintained at a temperature of 70°C. The films produced in this way were subsequently characterized by polarized optical microscopy (POM), atomic force microscopy (AFM), X-ray and electron diffraction.

8.1.3 Optical microscopy

Figure 85 shows the optical micrograph of a thin film of BTZ-alt-CDT between crossed polarizers, which was prepared via casting a drop of polymer solution in the presence of an electrical field. Alternation of dark and bright parallel stripes can be recognized.

Brighter areas are visible as well and may originate from thickness fluctuations of the BTZ-alt-CDT copolymer film.

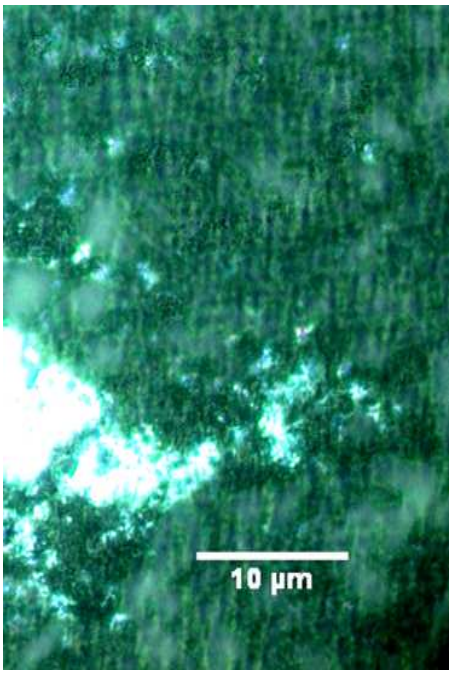

Figure 85. Optical micrograph of a field-oriented BTZ-alt-CDT copolymer film between crossed polarizers.

Stripes textures have been reported in literature by Wang et al.[164] in the study of the assembly behavior of soluble polydiacetylene. The optical micrographs of that work, exhibited nearly parallel stripes, when solvent evaporation from a "lyotropic" liquid crystal took place under the influence of a weak gravity force field. Conventionally, a material is called lyotropic if it forms liquid crystal phases due to the addition of a solvent and most likely BTZ-alt-CDT copolymer behaves in a similar fashion in a trichlorobenzene solution. It fulfills in fact the necessary requirements for the formation of a lyotropic liquid crystalline phase developed by Onsager [165], Flory [166], Di Marzio [167] and Frenkel [168]. These requirements can be summarized as following:

1. a rod-like conformation of the main chain;
2. a minimum molecular length, which can be expressed in terms of the axial ratio (the ratio (*A*/*B*) of the length (*A*) and diameter (*B*) of the molecule);
3. a solvent that is capable to dissolve the polymer beyond a critical concentration at which the solution becomes anisotropic and the lyotropic phase will appear.

The backbone of the BTZ-alt-CDT polymer chains is linear and rigid. The long aliphatic side chains make the rod-like copolymer soluble in trichlorobenzene and do not affect the rigidity significantly. Therefore, as the concentration of the elongated molecule is increased, a point will be reached beyond which randomness of orientation is not longer possible. Above this concentration, theory predicts that the solution will separate into two phases: a dilute phase, isotropic in the arrangement of the solute particles, and a more concentrated phase, which is anisotropic [169].

To find additional evidence of the lyotropic liquid crystalline nature of BTZ-alt-CDT copolymer, its assembly in a trichlorobenzene solution in absence of any external force (e.g. an external electrical field) was monitored by means of optical microscopy. A drop of concentrated solution of BTZ-alt-CDT copolymer in trichlorobenzene was cast on a glass substrate and allowed to anneal under a controlled atmosphere of trichlorobenzene/air at a temperature of 70 °C. The changes in the optical micrograph of the sample were observed in the optical microscope until total solvent evaporation. The sample was therefore intermittently taken out during different stages of drying and studied under an optical microscope.

The optical micrograph of the BTZ-alt-CDT copolymer in trichlorobenzene, displayed in **Figure 86 a**, shows star-like features. At this point, the solvent is not completely evaporated, but the solution is no more isotropic. We will define the time, in which an anisotropic solution is formed, as critical time (t_c).

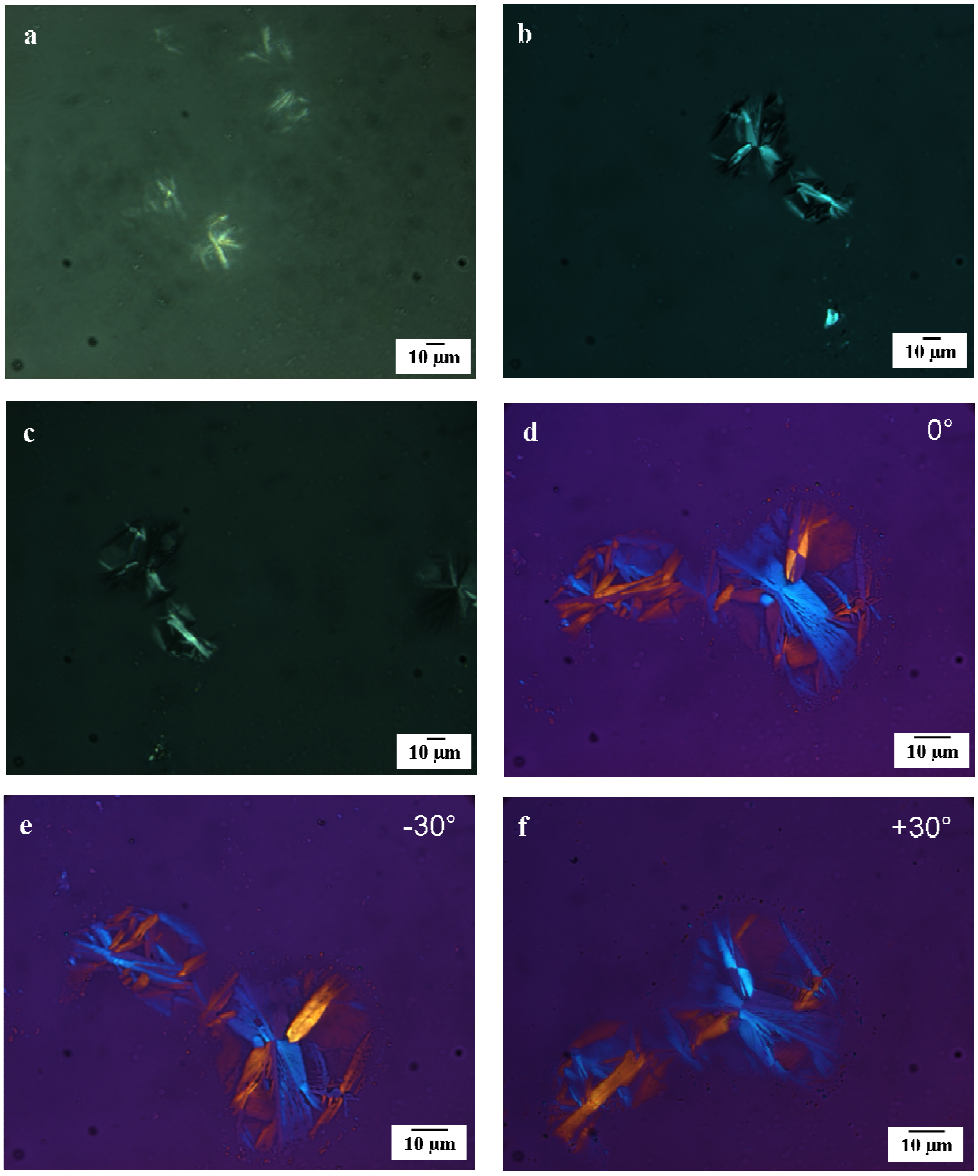

Figure 86. Optical micrographs of a drop of BTZ-alt-CDT copolymer solution in trichlorobenezene between crossed polarizers: a) Critical time t_c, b) 20 min after t_c, c) 25 min after t_c, d), e), f) completely dry film (evaporation time 14 days) with different orientations with respect to the crossed polarizers.

With increasing evaporation time (**Figure 86 b and c**), the stripe texture within the arms of the stars became visible. Upon complete solvent evaporation, a lamellar structure could be clearly identified in the micrographs of **Figure 86 e**, in

which the contrast is emphasized by a λ plate. [20] Very likely the organization of the BTZ-alt-CDT copolymer chains in lamellar structures starts when the BTZ-alt-CDT copolymer reaches the conditions for generating a lyotropic liquid crystalline phase in 1,2,4 trichlorobenzene. This structure is then “frozen” via evaporation of the solvent and remains visible in the dried film.

As reported by Toyoshima et al.[170], the order of rod-like polymers in their lyotropic liquid crystalline phase can be influenced by electrical fields in the range of less than 500 V/cm. Below a critical concentration, in which the polymer solution becomes anisotropic, Toyoshima showed that poly(γ-benzyl-L-glutamate) chains can be forced in the direction of an external electrical field. A similar mechanism for the alignment of the BTZ-alt-CDT copolymer chains (see optical micrograph of **Figure 85**) is suggested. Thus, ordered dry films are obtained.

8.1.4 Morphology study

The morphology of the field oriented BTZ-alt-CDT copolymer films was studied by tapping mode AFM. The images with different scan sizes are shown in **Figure 87 a-c**.

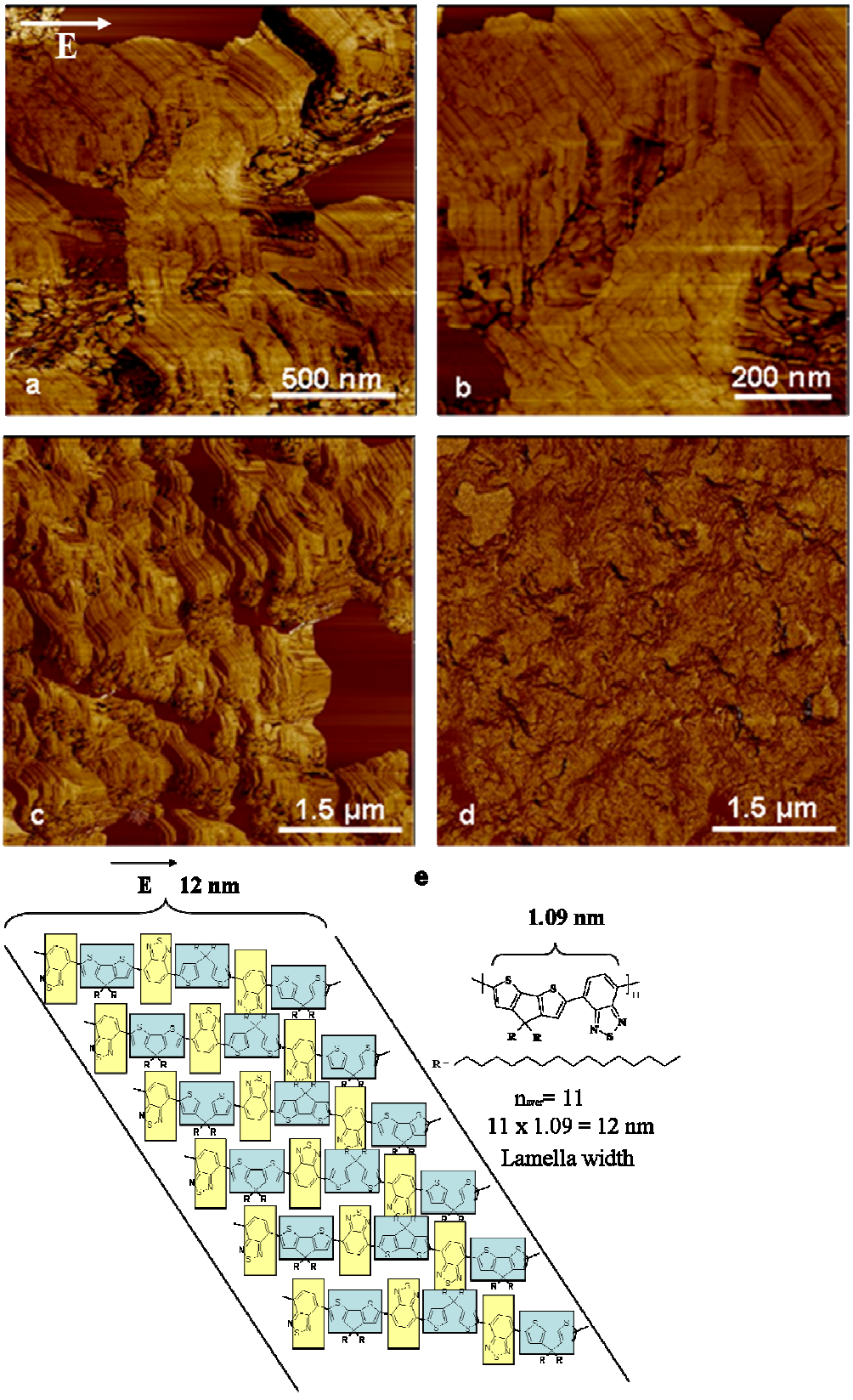

Figure 87 a), b), c) AFM phase images of BTZ-alt-CDT films obtained in electrical field presence with different scan size. The white arrow represents the applied field direction. d) AFM phase image of a drop-cast BTZ-alt-CDT film without application of electrical field for comparison. e) Schematic representation of the molecular packing within the lamellae.

The AFM images of the field-aligned polymer films shows the presence of stripes, which could be justified by the assembly of the polymer chains into a lamellar structure. The thickness of the lamellae is not constant and fluctuates around an average lamellar width of 11 nm. Furthermore, the presence of lamellae pointed at the extremities (wedge-shaped) is seen as well. The mechanism of the formation of lamellar structures has been already theoretically described for rod-like polymer chains of uniform length by de Gennes [171] and Frenkel [172]. Experiments with polydisperse systems were performed by Wang et al. [7,173] and Albrecht et al.[174] They showed the predicted behavior of lyotropic liquid crystals that the lamella thickness is a function of the molecular length as the rigid polymer chains cannot fold. The distribution of the chain length has its effect on ordering phenomena of the polymers. The molecules segregate with respect to their length. This process results in the formation of thinner and thicker lamellae or pointed ones. In both cases, short chains are expelled from the interior of an aggregation of long chains. In the first case, the formation of thinner and thicker lamellae, the transport process is dominated by longitudinal motion of short chains. The shortest chains accumulate in the region between the lamellae of longer chains, forming there a thin lamella. In contrast to the longitudinal motion, the transport process leading to the pointed lamellae works by a transversal migration of short chains. As a final result, the lamellar width is correlated to the molecular chain length. The segregation of the chains with respect to their length is characteristic for liquid crystalline systems and can be used as additional evidence of the liquid crystalline nature of the BTZ-alt-CDT copolymer. The BTZ-alt-CDT copolymer has an average number molecular weight of M_n ~ 10.000 g/mol. For an average number of repeating units of 11, the size of a chain was calculated to be ~ 12 nm (**Figure 87 e**). This value agrees well with the average lamellar width in **Figure 87 b**.

For comparison, an AFM micrograph of a reference BTZ-alt-CDT copolymer film, prepared via drop-casting in absence of the electrical field, is shown in **Figure 87 d**. No formation of stripes can be recognized; therefore, the higher anisotropic character of the BTZ-alt-CDT copolymer film in **Figure 87 a, b, c** can be unambiguously related to the influence of the electrical field and its capability to improve the molecular packing of the polymer chains.

8.1.5 Diffraction analyses

To get an insight into the molecular packing of the BTZ-alt-CDT copolymer chains, both X-ray and electron diffraction analyses were carried out. The combination of both diffraction techniques has the advantage to probe the sample under two different directions of incidence of the used irradiation, therefore to see in an oriented sample various features of the molecular packing. In an X-ray powder diffractometer the reflections of lattice planes parallel to the substrate are predominantly recorded. Electron diffraction sees indeed lattice planes perpendicular to the substrate. A schematic representation of the different directions of the irradiation beams in electron and X-ray diffraction are shown in **Figure 88 a** and **b**, respectively.

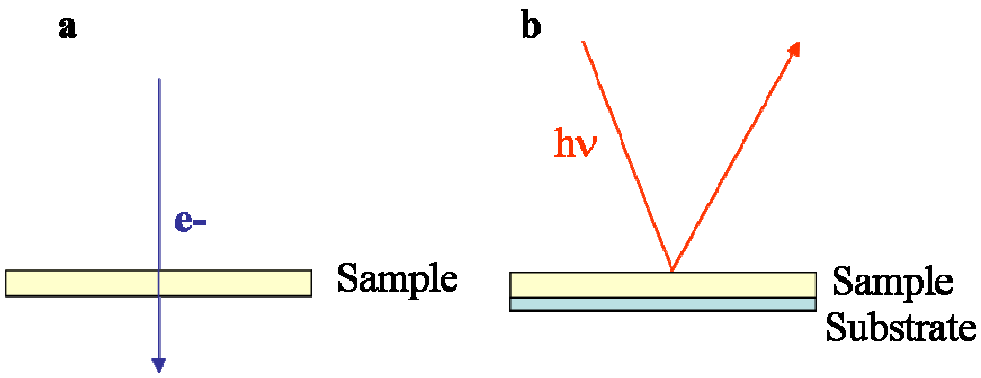

Figure 88. a) Incidence of the electron beam with the sample in transmission electron microscopy. b) Incidence of the X-ray beam with the sample in X-ray diffraction.

8.1.5.1 X-ray diffraction

Figure 89 a displays an X-ray diagram of a BTZ-alt-CDT copolymer film on a glass surface.

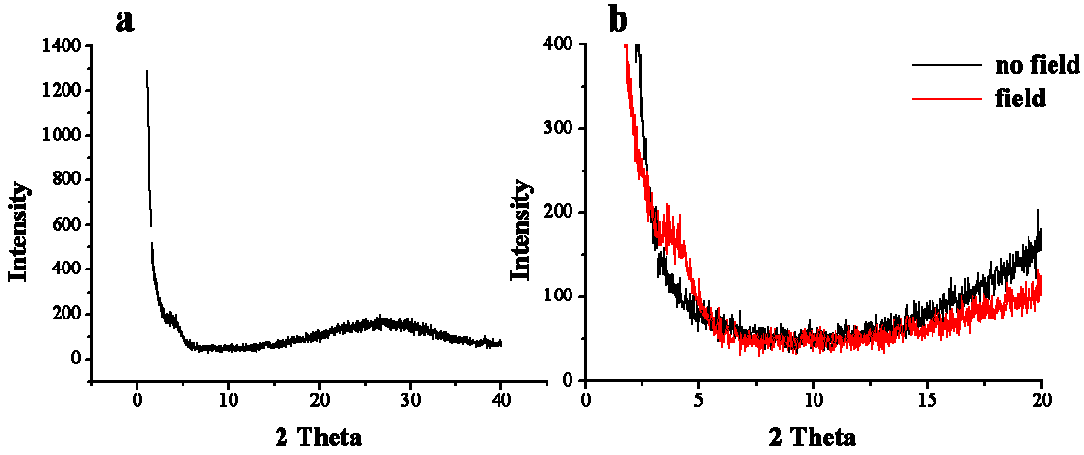

Figure 89. a) X-ray diagram of field oriented BTZ-alt-CDT film on glass surface b) enlarged innermost angular region of a (red trace). X-ray diagram of drop-cast BTZ-alt-CDT film on glass surface (black trace).

The diagram of the oriented sample exhibits a shoulder at 2θ ~ 3.8° superimposing a continuous trace with a halo centered round ~ 27°. The latter could have originated partially from disordered alkyl chains of the BTZ-alt-CDT copolymer, but mainly from the amorphous glass substrate. The reflection at 2θ = 3.8° corresponds to a d-value of ~ 2.5 nm, which is related to the distance of the lattice planes containing the polymer chains. These lattice planes are oriented parallel to the substrate. They contain the aromatic rigid backbone and are held apart by a distance of ~ 2.5 nm by disordered aliphatic side chains. This d-value is in agreement with the one of 2.66 nm observed as an equatorial reflection on a wide-angle X-ray fiber diagram, which occurred on an extruded sample of the BTZ-alt-CDT copolymer [163].

The X-ray diagram of the reference sample, prepared without the presence of an electrical field, did not show any reflection (**Figure 89 b**). This evidences the electrical field influence on the arrangement of the BTZ-alt-CDT copolymer chains.

8.1.5.2 Electron diffraction

Electron diffractograms by normal beam incidence to BTZ-alt-CDT films are shown in **Figure 90**. A diffractogram of a film, prepared in the presence of an electrical field is pictured in **Figure 90 a**. **Figure 90 b** shows, as a reference, the electron diffractogram of a drop cast film prepared analogously in absence of an electrical field. Both micrographs have been recorded by cooling the sample down to a temperature of -125 °C to avoid significant irradiation damages.

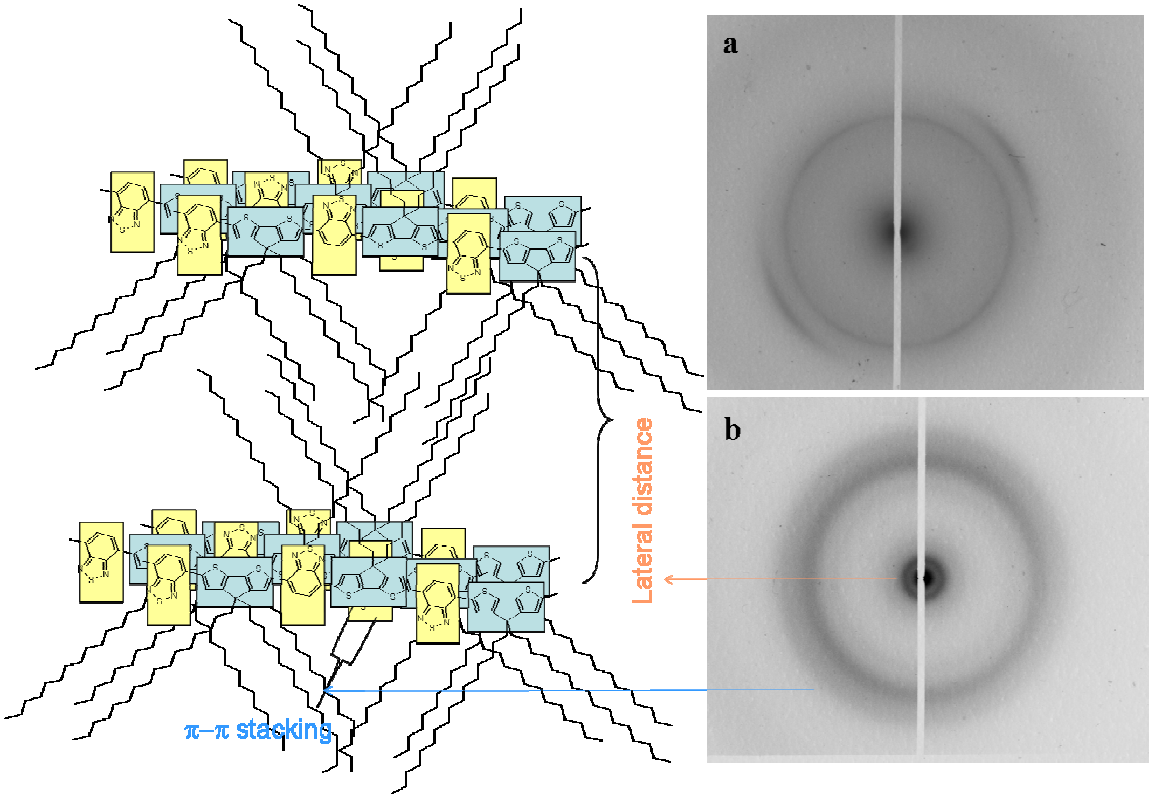

Figure 90. a) Electron diffraction micrograph of a field aligned BTZ-alt-CDT copolymer film at T= -125°C. b) Electron diffraction micrograph of a drop-cast BTZ-alt-CDT copolymer at T= -125°C for comparison. A sketch of the molecular packing is inserted.

The diffractogram of the film prepared under the influence of an electrical field (**Figure 90 a**) shows two distinct reflections. The outermost of them is arced, thus pointing to orientation in a preferential direction. It has a d-value of 0.336 nm and can be attributed to the exceptionally small π–π stacking distance of the flat aromatic constituents of the polymer chains. The d-value of the reflection ring is

0.414 nm. It is due to the packing of the side alkyl chains anchored at the BTZ-alt-CDT copolymer. Very likely, the observed reflection is due to the crystallization of the tips of the side chains. Investigations on a number of comb-like polymers have shown that the first 8-10 units in long alkyl chains cannot crystallize and adopt a liquid–like disordered packing. They act as spacers for the subsequent units, which are packed temporarily in a more regular way [175]. Over the time the same side chain can belong to various adjacent crystallites.

Surprisingly, no reflection, corresponding to the X-ray reflection at 3.8°, occurs which can be attributed to the packing of the main chains. This reflection is, however, seen on the electron diffractogram of the drop-cast polymer film deposited without field (**Figure 90 b**). It appears as an innermost ring with a d value of 2.7 nm. The second and third rings are much more diffuse than both the ring and the arc in **Figure 90 a**. We assume they represent the correlation between the side chains and the π–π stacking of the aromatic units, respectively. The data obtained from X-ray and electron diffraction are complementary (see **Figure 88**) and lead to the conclusion that the packing in non-oriented and field-oriented polymer films is different as shown in **Figure 91 a** and **b**, respectively. The suggested molecular packing, presented in **Figure 90,** is justified by the following observation: i) the lattice distance of 2.7 nm gives a ring reflection when crystallites are isotropically distributed round the polymer chain direction. On the contrary, the orientation of the corresponding lattice planes cannot fulfill Braggs´ condition in the used technique of X-ray diffraction. The BTZ-alt-CDT chains cannot fold, but their length is short enough to build lamellae with the chains normal to the substrate. ii) In the arrangement of **Figure 91 b** the main chain axes are parallel to the substrate. Within this assembly, the lattice planes with a distance of 2.7 nm are in reflection for the X-ray geometry, but they are normal to the incoming electron beam and thus do not fulfill Braggs' conditions.

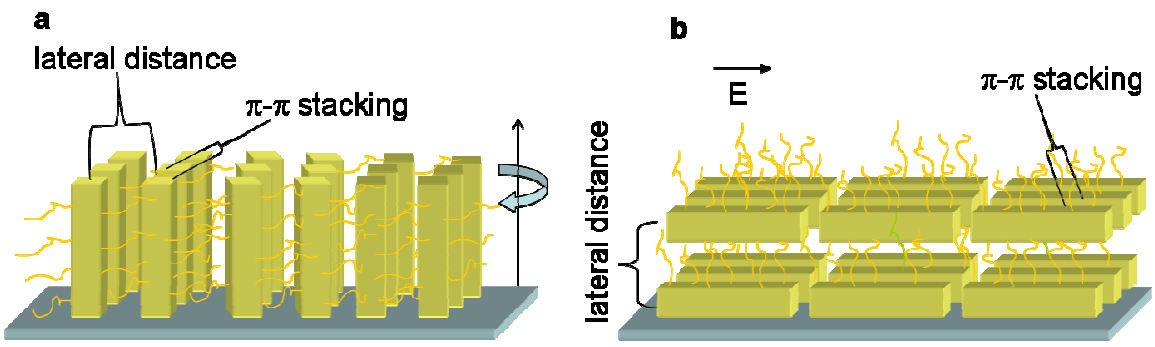

Figure 91. a) Schematic representation of the BTZ-alt-CDT copolymer chains on the glass surface in a polymer film prepared by drop-casting in absence of an electrical field. b) Assembly of the BTZ-alt-CDT copolymer chains in presence of an external electrical field parallel to the surface.

8.1.6 Electronic performances of organic field effect transistors based on electrical field aligned BTZ-alt-CDT copolymer films

As controlling the orientation of organic semiconducting molecules for organic field effect transistors is of key importance for obtaining improved device performance[176-177], electrical field oriented BTZ-alt-CDT polymer films were tested as semiconducting layers for OFET.

Organic field-effect transistors (OFET) were fabricated by Hoy Nok Tsao using a bottom-gate, bottom-contact structure consisting of a highly n-doped silicon wafer with a 150 nm thermally grown silicon dioxide layer treated with hexamethyldisilazane (HMDS). On top of this, gold source and drain electrodes with a channel length of 10 µm and width of 5 mm were evaporated after photolithographic steps. A solution of BTZ-CDT copolymer in 1,2,4-trichlorobenzene (5 mg/ml) was drop cast on those transistor substrates and the sample was kept at a temperature of 70°C. Then, an electrical field was applied parallel to the source and drain contacts during solvent evaporation and maintained for a period of three days (**Set 1**). A schematic representation of the device structures and of the deposition procedure is reported in **Figure 92 a**. The same procedure (**Set 2**) was additionally repeated, but the electrical field was maintained normal to the contact electrodes, as schematized in **Figure 92 b**. These two sets of experiments were performed to clarify the transport mechanism acting in a BTZ-CDT copolymer film which will be described later in details.

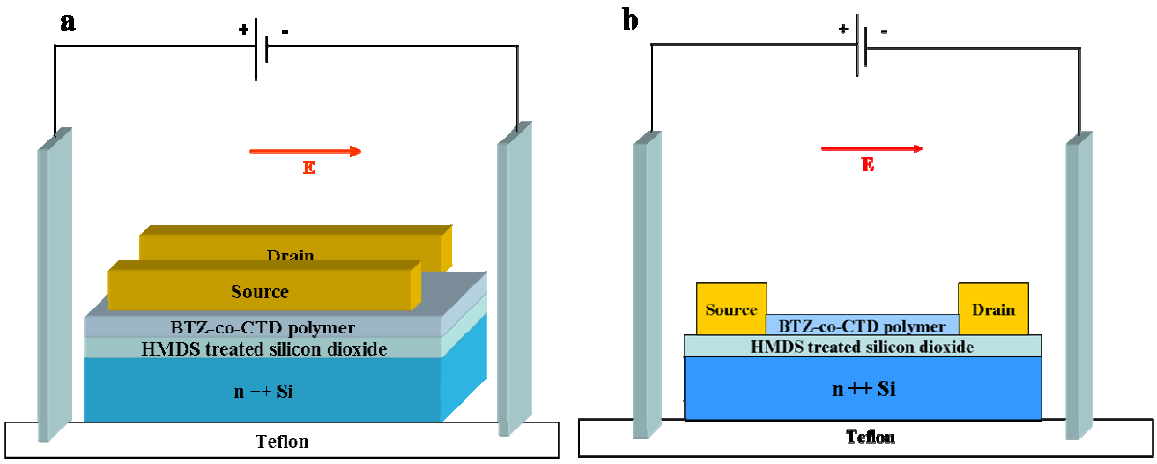

Figure 92. Schematic view of bottom contact, bottom gate OFET based on field oriented BTZ-alt-CDT copolymer film: a) the source and drain electrodes are parallel to the applied field, b) the source and drain electrodes are perpendicular to the external electrical field.

Within the device geometry reported in **Figure 92**, when the gate electrode is biased negatively with respect to the grounded source electrode, a conducting channel is generated in the semiconducting BTZ-alt-CDT film and charges (in our case holes) are accumulated. In these conditions, the OFET works in accumulation mode.

Figure 93 a (left) shows the plot of drain current (I_{SD}) versus drain voltage (V_{SD}) at various gate voltages (V_G) for the device described in **Figure 92 a** (electrical field parallel to the electrodes). It is possible to evaluate that at low V_{SD}, I_{SD} increases linearly with V_{SD} (linear regime) and it is approximately determined from the following equation:

$$I_{SD} = \frac{WC_i}{L}\mu(V_G - V_T - V_{SD}/2)V_{SD} \qquad \textbf{Equation 13}$$

where L is the channel length, W is the channel width, C_i is the capacitance per unit area of the insulating layer, V_T is the threshold voltage (the necessary voltage to switch the transistor on), and μ is the field-effect mobility.

The latter indicates how fast the holes move from one electrode to the other and can be calculated in the linear regime from the transconductance g_m,

$$g_m = \left(\frac{\partial I_{SD}}{\partial V_G}\right)_{VD=const} = \frac{WC_i}{L}\mu V_{SD} \qquad \textbf{Equation 2}$$

by plotting I_{SD} versus V_G at a constant low V_{SD} and equating the value of the slope of this plot to $g_{m.}$ The calculated value for the BTZ-alt-CDT field-effect transistors was 0.07 $cm^2V^{-1}s^{-1}$.

When the gate electrode is biased positively, the channel region is depleted of carriers and the BTZ-alt-CDT field-effect transistors operated in the depletion mode. The value of the current in the depletion mode is necessary to calculate the current modulation, also referred as I_{on}/I_{off}, expressed as the ratio of the current in the accumulation mode over the current in the depletion mode. The calculated value for a BTZ-alt-CDT field-effect transistor was 10^5.

For V_{SD} more negative than V_G, I_{SD} tends to saturate (saturation regime) owing to the pinch-off of the accumulation layer, and is modeled by the equation:

$$I_{SD} = \frac{WC_i}{2L}\mu(V_G - V_T)^2 \qquad \textbf{Equation 3}$$

In the saturation regime, μ can be calculated from the slope of the plot of $|I_{SD}|^{1/2}$ versus V_G (**Figure 93 a**, right). For the device based on the BTZ-co-CDT copolymer, the highest mobility calculated in the saturated regime has a maximum value of 0.14 $cm^2V^{-1}s^{-1}$. After short annealing at a temperature of 200° C of the field oriented BTZ-co-CDT film, the saturated mobility reached a value of 0.2 $cm^2V^{-1}s^{-1}$.

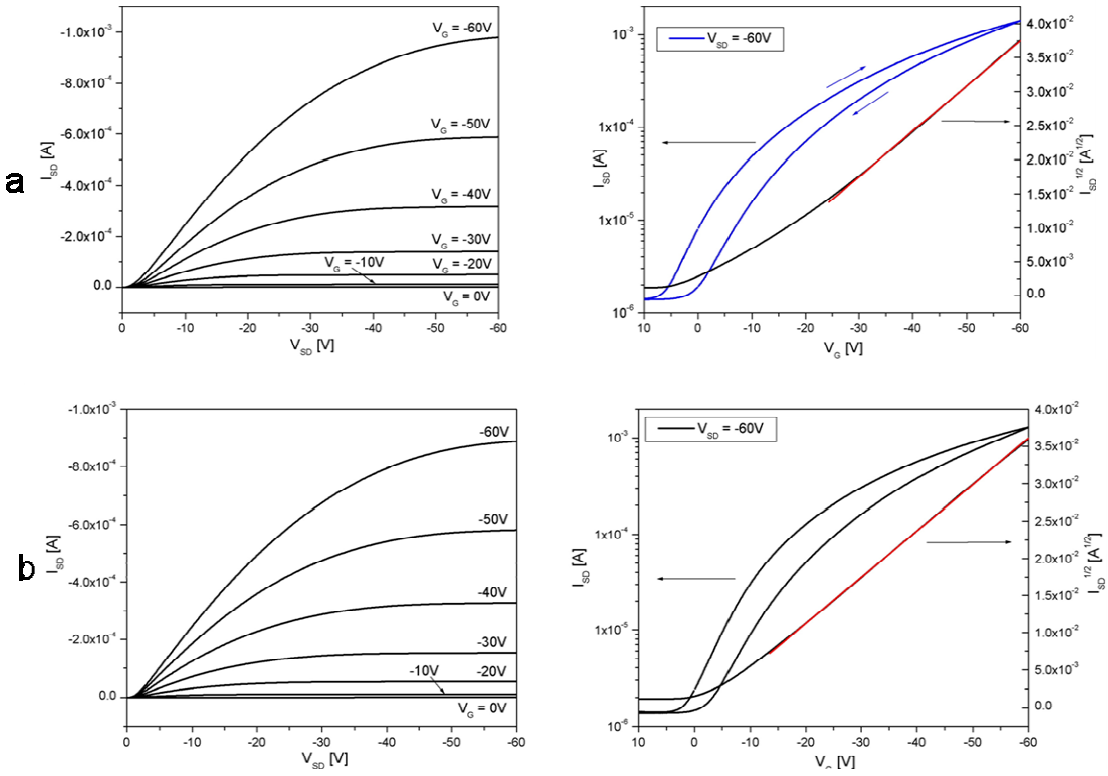

Figure 93. a) OFET performances of a BTZ-alt-CDT copolymer film prepared in presence of an electrical field. Output curves taken at different gate voltages (left); transfer curves displaying the saturation regime for V_{SD} = -60V (right). b) The same sample after three month aging.

Moreover, the film obtained in presence of an external field showed comparable charge carrier mobility values after repeating the mobility measurements after a period of time of three months as shown in **Figure 93 a** and **b**, thereby indicating that the device characteristics of the sample remain intact even after several months of aging.

The highest mobility μ_{sat} (0.2 cm^2/Vs), recorded for the field oriented films is higher (17.6%) than that reported in the literature for the BTZ-alt-CDT oligomers used in this investigation. Moreover, there was considerable improvement in the linear mobility μ_{lin} of the electrical field oriented polymer film. The obtained value of 0.07 cm^2/Vs is two orders of magnitude higher than that in unoriented drop-cast films (0.001 cm^2/Vs).

According to Zhang et al., the low linear mobility value of the BTZ-alt-CDT copolymer film, presented in that work, was due to the high molecular disorder of the polymer chains at the electrodes. In that investigation, high polymer concentration (10 mg/ml) was necessary to achieve satisfactory performances with the drawback of

disordered aggregation of the polymer chains in the first layers and worsening of the μ_{lin} value. In the presented experiments, the better packing of the BTZ-alt-CDT copolymer chains, caused by their self-assembly in presence of an electrical field, improved the electronic performances in the linear regime. In this regime, the drain to source voltage V_{SD} is much less than the gate to source voltage V_G and drain current I_{SD} is proportional to drain voltage. If drain to source voltage is increased, the shape of the conducting channel is altered significantly and asymmetrically due to the gradient of potential from source to drain. The shape of the channel becomes "pinched-off" near the drain-end of the channel. When drain-to-source voltage is increased further, the pinch-off point of the channel begins to move away from the drain towards the source and the saturated regime is reached. The channel length in the transistor in saturation mode is therefore shorter than that in the linear regime. This could justify the major influence of the improved long-range order on μ_{lin} in the field oriented BTZ-alt-CDT copolymer film compared to the more modest improvement in the μ_{sat} value. Furthermore, the linear mobility can be affected by contact problems. The improved order of the field-oriented BTZ-alt-CDT copolymer film in presence of an electrical field can additionally be responsible for an improvement in the contact between polymer chains and gold electrodes and thus for an improvement of the μ_{lin} value.

Moreover, to examine the change in transistor performance when no external field was applied, the whole device was prepared in the same way as described before except for the absence of an electric field. In this case, the hole mobility decreased to $1x10^{-5}$ cm^2/Vs. It is worth noting that the two values differ by five orders of magnitude. We attribute this notable difference to the observed disorder of the drop-cast film prepared in absence of the influence of an external field.

8.1.7 Charge transport in BTZ-alt-CDT copolymer film

For a deeper understanding of the charge transfer mechanism acting in a BTZ-alt-CDT copolymer film, the device performance of a film, prepared by applying an electrical field perpendicular to the source and drain contacts during solvent evaporation (see **Figure 92**), were tested too.

For a conjugated system three different types of charge transport are possible:

1. Band conductivity (along the polymer backbone)
2. Hopping between separated molecules
3. Tunneling

Higher charge mobility along the polymer backbone indicates the band conductivity model as the most probable mechanism of charge transport. On the contrary, higher charge mobility perpendicular to the polymer chains suggests hopping between separated molecules as the most likely process.

For the device prepared by evaporating the BTZ-alt-CDT copolymer film in presence of an electrical field, perpendicular to the direction of the electrodes, a μ_{sat} value of 0.08 cm^2/Vs was calculated from the curves shown in **Figure 94**. These graphs show the I_{SD}/V_{SD} characteristic of the devices (left) and the transfer curve displaying the saturation regime for a V_{SD} of -60 V (right), respectively.

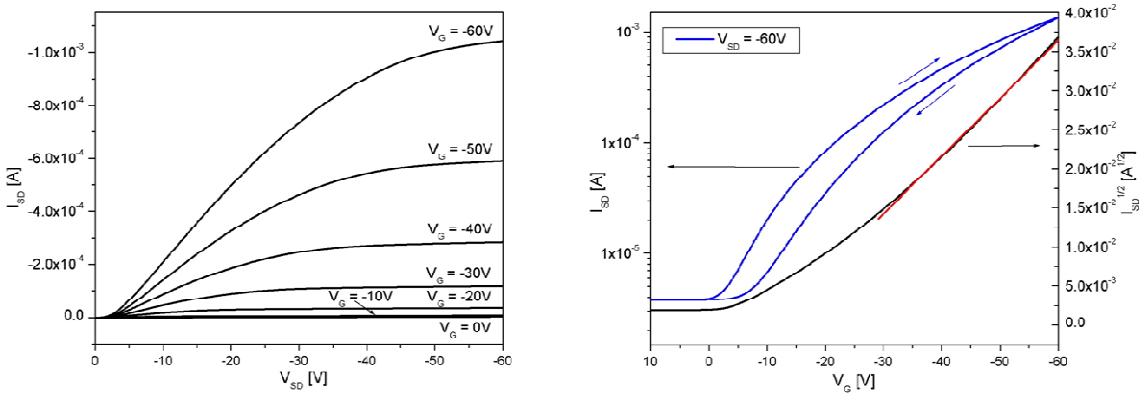

Figure 94. OFET performances of a BTZ-alt-CDT copolymer film prepared in presence of an electrical field perpendicular to the source drain contacts. Output curves taken at different gate voltages (left); transfer curves displaying the saturation regime for V_{SD} = -60V (right).

It is interesting to point out that within this geometry the backbone of the polymer chains is oriented perpendicular to the electrodes as the polymer chains are aligned in the field direction; Whereas, in the device, described before, the polymer backbone was oriented parallel to the electrode direction. By comparison of the two charge transport values related to the two device geometries, it is possible to conclude that the charge carrier mobility among separated polymer chains (hopping process) is slightly higher than the carrier speed along the polymer backbone (band conductivity).

Thus, the hopping process dominates the transport mechanism in the BTZ-alt-CDT copolymer film.

8.2 Retro-Diels Alder reaction of 13,6-Sulfinylacetamidopentacene in the presence of an electrical field

Among all the electroactive organic molecules pentacene (PEN) has recently emerged as promising molecular system to design OFET with charge carrier mobility as large as 0.7 cm^2/Vs on SiO_2/Si substrates [178], 1.5 cm^2/Vs on chemically modified SiO_2/Si substrates [179] and 3 cm^2/Vs on polymer gate dielectrics [180]. Unfortunately, the low solubility of pentacene in common organic solvents limits its processability to the vapor phase deposition or molecular beam deposition. It has already been shown that the presence of polar groups on pentacene enhances its solubility in common organic solvents. 13,6-Sulfinylacetamidopentacene [181,182], as an example, is a commercially available modified pentacene precursor soluble in chlorinated solvent. Heated at a temperature higher than 120° C, it louses sulfinylacetamide in a retro-Diels Alder reaction to produce the non-substituted and insoluble pentacene (**Figure 95**). Solution processing of the pentacene precursor speeds up the film preparation process and leads to pentacene layers with excellent charge carrier mobility (0.89 cm^2/Vs) [181]. In this work, we explore the possibility to increase the molecular order in the pentacene film by performing the retro Diels Alder reaction on 13,6-Sulfinylacetamidopentacene in presence of an electrical field.

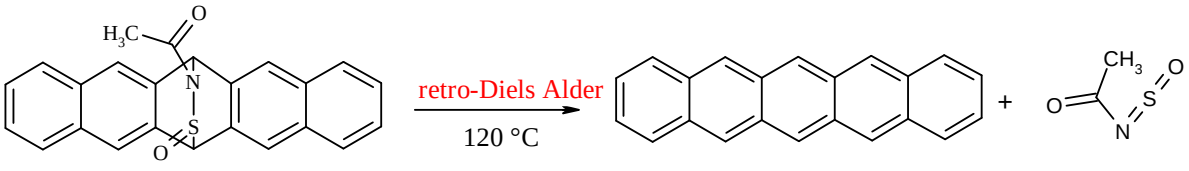

Figure 95. Retro Diels-Alder reaction of 13,6-Sulfinylacetamidopentacene

8.2.1 Alignment experiments and optical analysis

A solution of 13,6-Sulfinylacetamidopentacene in chloroform with a concentration of 2% by weight was cast on a glass surface and treated at a

temperature of 135°C under nitrogen atmosphere for 30 minutes in the presence of an electrical field (500 kV/m).

A visible change in the film color from light yellow to dark blue was observed and indicated the formation of a thin pentacene film on the glass surface.

Information regarding the supramolecular organization of the pentacene molecules in the films prepared in electrical field presence was obtained via optical microscopy. **Figure 96 a** shows an optical micrograph of a field aligned pentacene film between crossed polarizers; the yellow arrow indicates the electrical field direction.

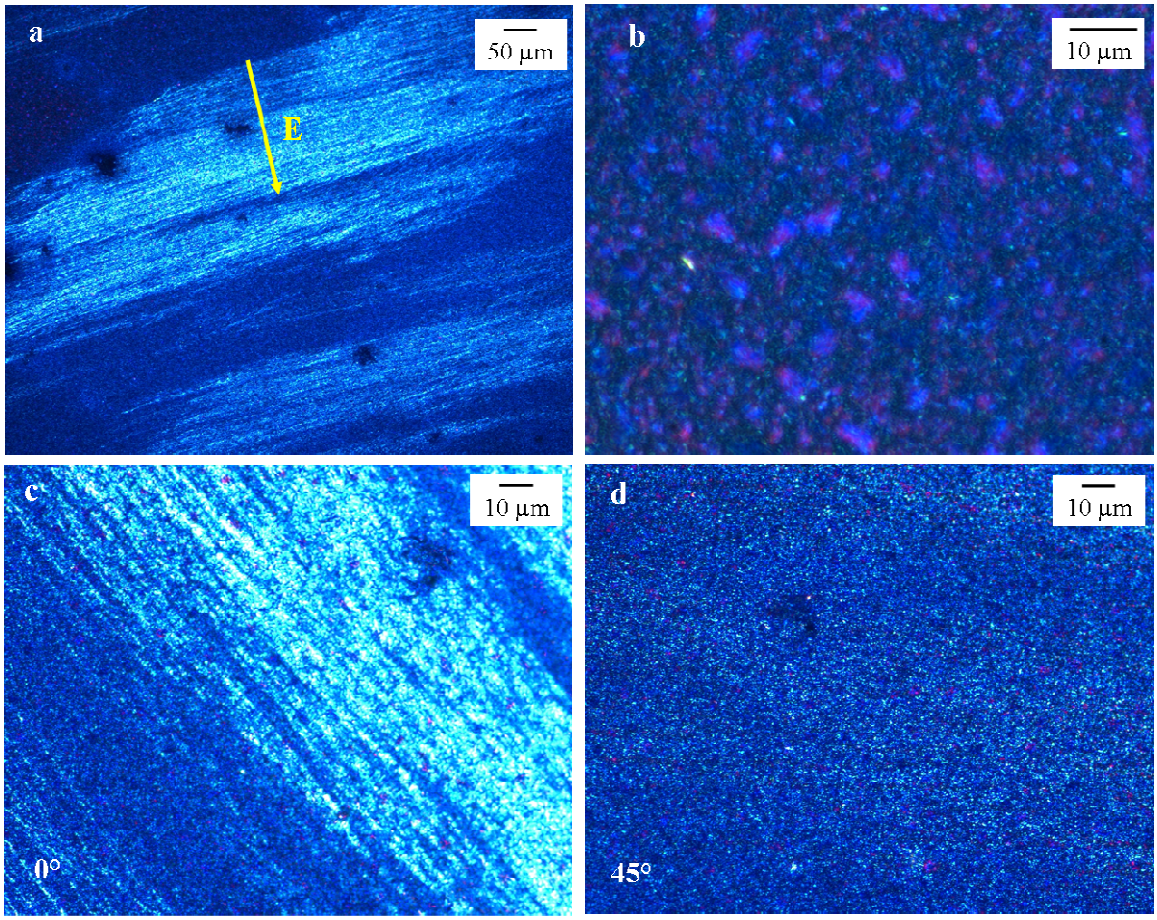

Figure 96. a) Optical micrograph of a field oriented PEN film under crossed polarizers. b) Optical micrograph of a reference PEN film prepared in absence of electrical field. c), d) Optical micrographs at higher magnification of a field oriented PEN film under crossed polarizers at 0° and upon rotation of the sample holder at 45°.

As shown in the magnified POM image of **Figure 96 c**, a bright micrograph is observed, which is extinguished upon rotation of the sample stage at an angle of 45°

under crossed polarizers (**Figure 96 d**). This is due to the fact that the PEN film, obtained by solution-processing of 13,6-Sulfinylacetamidopentacene in presence of an electrical field, is constituted by crystals oriented in a preferential direction.

For comparison, an optical micrograph of a PEN film solution processed in absence of electrical field is reported. No uniaxial orientation was recognized and only at higher magnification a polycrystalline structure made of randomly oriented crystals was observed (**Figure 96 b**).

8.2.2 X-ray analysis

In order to clarify the arrangement of the field aligned pentacene molecules on the glass surface, X-ray experiments were carried out.

According to literature [109], pentacene has three different polymorphs (α, ß, γ) when crystallized on a plane substrate, which can be distinguished via X-ray characterization. They are characterized by d_{001}= 1.41 nm for the γ-pentacene, by a d_{001} value of 1.45 nm for the ß-pentacene and the α-pentacene, so called "thin film phase", by a d_{001} value of 1.55 nm.

Figure 97 reports the X-ray diagrams of the field oriented pentacene (black trace) and its precursor in the retro-Diels Alder reaction (red trace).

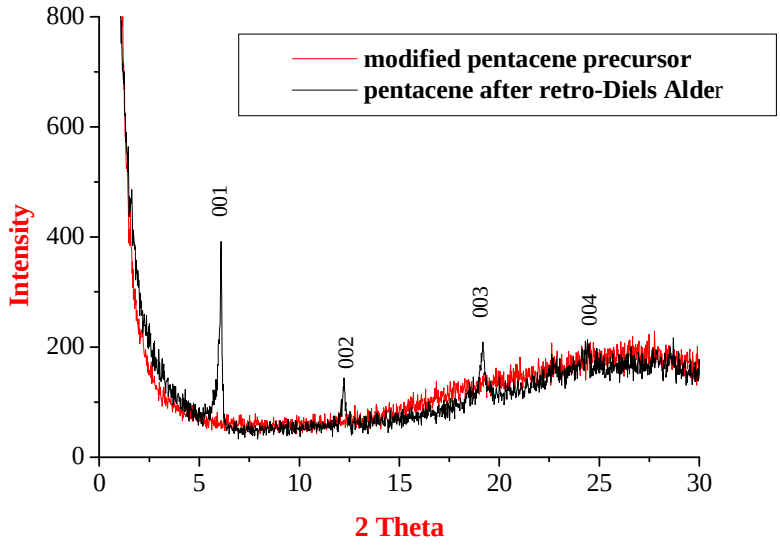

Figure 97. X-ray diagram of field aligned pentacene molecules on glass (black trace) and X-ray of pentacene precursor molecules on glass (red trace).

Field oriented PEN films exhibit a sequence of diffraction peaks with maxima at 1.45, 0.727, 0.461, 0.3653 nm; whereas, no reflections can be observed in the X-ray diagram of the pentacene precursor. These peaks correspond to (00l) reflections ($1 \leq l \geq 4$) of a bulk structure of pentacene, defined as β pentacene, and indicate a preferential orientation of the crystalline domains. Reflections related to α-pentacene and γ-pentacene are not present. The relative stability of the α in comparison to the β polymorphs relates to the size and thickness of the crystals. Small crystals grow in a α structure and large ones in a β structure. The absence of the α structure, therefore, indicates the presence of large crystals on the surface. In this work, the preferential formation of β-pentacene crystals can be related to two factors: the electrical field improves the PEN crystallization and allows the formation of larger pentacene crystals. The high temperature used for the retro Diels-Alder reaction increases the crystal size. The presence of symmetric reflections only of the type 00l indicates that PEN is aligned with its long axis almost parallel to the substrate surface[183]. The long axis of pentacene has a calculated size of 1.61 nm; whereas, the interplanar d spacing in the X-ray diagram in **Figure 97** has a value of 1.45 nm. This evidence suggests that the long pentacene axis aligns at an angle of about 25 ° from the surface normal as schematized in **Figure 98**.

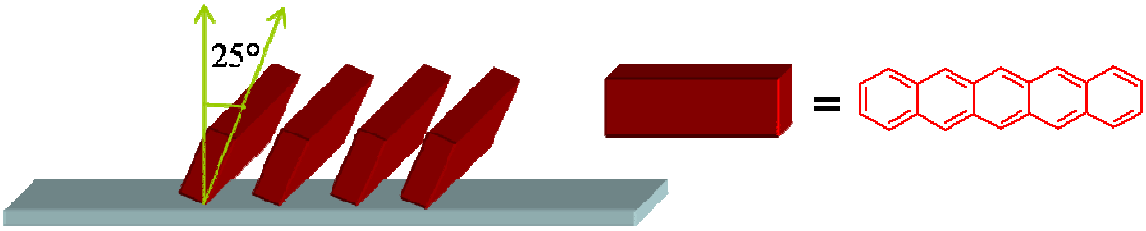

Figure 98. Schematic view of the PEN arrangement on the glass surface.

8.2.3 OFET performance

The field effect transistor measurements of thin pentacene films prepared by field alignment were carried out on a bottom-gate template with bottom contact, schematic represented in **Figure 99 a**. A drop of a 2% solution of 13,6-Sulfinylacetamidopentacene in $CHCl_3$ was cast on the template. Then the substrate

was heated, after solvent evaporation, at a temperature of 130°C for 30 minutes in presence of an electrical field. The resulting thin pentacene film exhibits p-type characteristic as the plot of drain current I_{SD} versus drain voltage V_{SD} at various gate voltages V_G in **Figure 99 b** shows.

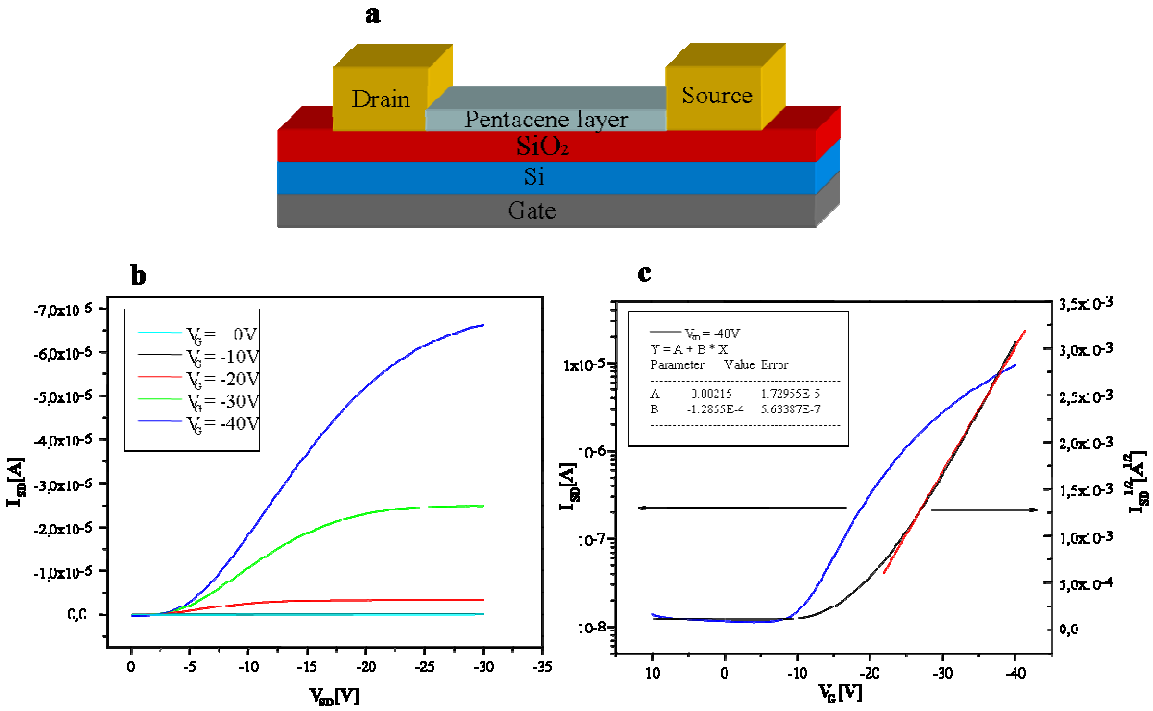

Figure 99. a) Schematic representation of a bottom contact, bottom gate OFET. b) Drain current I_{SD} versus drain voltage V_{SD}, as a function of gate voltage, V_G. Channel length 10 µm. c) plot of I_{SD} and $I_{SD}^{1/2}$ versus V_G at constant V_D = -40 V for the device in (a).

The charge carrier mobility μ_{sat} was calculated in the saturated regime from the transconductance to be 0.002 $cm^2V^{-1}s^{-1}$ as already described in the previous chapter. The obtained value was however much less as compared to that reported in literature for pentacene. Therefore, alignment experiments were now carried out at higher temperature (200° C). It was observed that μ_{sat} value (0.02 $cm^2V^{-1}s^{-1}$) of the sample prepared at 200° C is an order of magnitude higher than that obtained for samples prepared at 130° C. For comparison, the electronic performances of PEN film, prepared by annealing at 200°C in absence of electrical fields were tested. The charge carrier mobility drops to a value of 0.004 $cm^2V^{-1}s^{-1}$ and it leads evidence that the presence of an electrical field improved the packing of PEN molecules.

The μ_{sat} values obtained in this work are however still lower than that published for PEN. This can be due to the high PEN sensitivity to oxidation and to the non-

oxygen-free preparation conditions, which may have an extreme influence on the device performance of PEN.

8.3 Conclusions

Within this work, the long-range order of conjugated polymers has been improved by means of an electrical field. The cyclopentadithiophene-alt-benzothiadiazole copolymer has been chosen as a model system for this investigation as it is a promising candidate for novel organic electronics. An electrical field, applied parallel to the deposition surface, has been found to align the CTD-alt-BTZ copolymer chains during crystallization from solution. The field influence on the assembly of CTD-alt-BTZ copolymer chains can be related to its lyotropic liquid crystalline nature in trichlorobenzene. Beyond a critical concentration, the rod-like CTD-alt-BTZ copolymer chains create a liquid crystalline phase and can be directed in the field direction. Via solvent evaporation, the uniaxial order of the polymer chains is "frozen" to obtain well-oriented films in the solid state. Their anisotropy is characterized via optical microscopy, atomic force microscopy and diffraction analyses. On the contrary, the CTD-alt-BTZ copolymer chains of a reference film, prepared via drop-casting in absence of an electrical field, are arranged in a different manner with a preferential orientation of their backbone perpendicular to the deposition surface. The strongly enhanced order of the CTD-alt-BTZ copolymer film and the alignment parallel to the surface are responsible for the improved performance of an organic field effect transistor made thereof. Linear and saturated mobilities as high as 0.07 and 0.14 cm^2/Vs could be achieved, respectively.

Furthermore, electrical field alignment experiments have been conducted on the soluble pentacene precursor: 13,6-Sulfinylacetamidopentacene. Well oriented ß-pentacene films, have been obtained via performing the retro-Diels Alder reaction on the 13,6-Sulfinylacetamidopentacene molecules in presence of an electrical field. The charge mobility of the field effect transistors made thereof increases by one order of magnitude in comparison to the electronic performance of a reference film prepared in absence of external electrical forces.

8.4 References

[154] G. Yu, J. Gao, J. C. Hummelen, F. Wudl, A. J. Heeger, *Science* **1995**, 270, 1789.

[155] J. Y. Kim, K. Lee, N. E. Coates, D. Moses, T.-Q. Nguyen, M. Dante, A. J. Heeger, *Science*, **2007**, 317, 222.

[156] K. M. Coakley, M. D. McGehee, *Chem. Mater.* **2004**, 16, 4533.

[157] H. Sirringhaus, N. Tessler, R. H. Friend, *Science,* **1998**, 280, 1741.

[158] B. S. Ong, Y. Wu, P. Liu, S. Gardner, *J. Am. Chem. Soc.* **2004**, 126, 3378.

[159] I. McCulloch, M. Heeney, C. Bailey, K.Genevicius, I. MacDonald, M. Shkunov, D. Sparrowe, S. Tierney, R. Wagner, W. Zhang, M. L. Chabinyc, R. J. Kline, M. D. McGehee, M. F. Toney, *Nat. Mat.*, **2006**, 5, 328.

[160] Y. Zhu, R. D. Champion, S. A. Jenekhe, *Macromolecules*, **2006**, 39, 8712.

[161] L. Yang, J.-K. Feng, A.-M. Ren, *Theochem*, **2007**, 816, 161.

[162] A. Babel, J. D. Wind, S. A. Jenekhe, *Adv. Funct. Mater*, **2004**, 14, 891.

[163] M. Zhang, H. N. Tsao, W. Pisula, A. K. Mishra, K. Müllen, *J. Am. Chem. Soc.* **2007**, 129, 3472.

[164] W. Wang, G. Lieser, G. Wegner, *Makromolekulare Chemie* **1993**, 194, 1289.

[165] L. Onsager, *Ann. N. Y. Acad. Sci*, 1949, 51, 627.

[166] P. J. Flory, G. Ronca, *Molec. Crystals liq. Crystals*, **1979**, 54, 289.

[167] E. A. Di Marzio, *J. Chem Phys.* **1961**, 35, 658.

[168] D. Frenkel, *Journal of Physical Chemistry*, **1988**, 92, 5314.

[169] S. P. Papkov, *Advances in Polymer Science*, **1984**, 59, 75.

[170] Y. Toyoshima, N. Minami, M. Sukigara, *Mol. Cryst. Liq. Cryst.* **1976**, 35, 325.

[171] P. G. De Gennes, *The Physic of Liquid Crystals*, **1974**, (Clarendon Press)

[172] D. Frenkel, *J. Phys. Chem.* **1998**, 92, 3280.

[173] W. Wang, G. Lieser, G. Wegner, *Liquid Crystals*, **1993** 15, 1.

[174] C. Albrecht, G. Lieser, G. Wegner, *Progress in Colloid & Polymer Science* **1993**, 92, 111.

[175] N. Platé, V. P. Shibae, *Comb-shaped polymers and liquid crystals*, Plenum, New York, 1987.

[176] C. D. Sheraw, T. N. Jackson, D. L. Eaton, J. E. Anthony, *Adv. Mater*. **2003**, 15, 2009.

[177] M. Paulsson, S. Stafström, *J. Phys.: Condens. Matter*, **2000**, 12, 9433.

[178] D. J. Gundlach, J., J. Lin, T., N. Jackson, S., F. Nelson, D. G. Schlom, *IEEE Electron Device Lett*. **1997**, 18, 87.

[179] J. J. Li., D. J. Gundlach, S. F. Nelson, T. N. Jackson, *IEEE Electron Device Lett.* **1997**, 18, 606.

[180] H. Klauk., M. Halik, U. Zschieschang, G. Schmid, W. Radlik, W**.** Weber, *J. Appl. Phys,*. **2002**, 92, 5259.

[181] A. Afzali, C. D. Dimitrakopoulos, T.L. Breen, *J. Am. Chem. Soc*. **2002**, 124, 8812.

[182] A. R. Brown, R. A. Pomp, D. M. de Leew, D. B. M. Klaassen, E. E. Havinga, P. T. Herwing, K. Müllen, *J. Appl. Phys.* **1996**, 79, 2136.

[183] T. Minakata, Y. Natsume, *Synthetic Metals* **2005**, 153, 1.

9 Summary

The reported investigation is focused on the study of the desorption/ionization characteristics of polycyclic aromatic hydrocarbons (PAHs) in MALDI-TOF-MS and takes advantage of the use of the novel solvent-free procedure for the sample preparation for the mass characterization of slightly soluble or totally insoluble analytes.

The aim of this investigation is to understand the relationships between physico-chemical properties of PAHs and their ionization and desorption efficiencies which is here recognized as the most important requirement for extracting reliable qualitative and quantitative information from a MALDI spectrum.

The investigation starts with the analysis of model systems composed of equimolar hexabenzocoronene mixtures (HBC) chosen as reference compounds among the PAH family. The HBCs composing the blends differ only by the different length of the alkyl substituents anchored to their periphery. Thus, bearing the same aromatic core, they possess a comparable absorption coefficient at the laser light wavelength and consequently are photo-ionized with comparable probability. The analysis of these mixtures allows discovering the influences of the intermolecular π–π interactions on the desorption step.

The influence of the size of the aromatic system on their desorption/photionization process is instead investigated via analysis of mixtures composed of a substituted HBC (HBC-C_{12}) and its dendritic precursor in the cyclodehydrogenation reaction. Their substantially different absorption at 337 nm (N_2 laser light) causes a remarkable difference in photoionization probability, with as a result the underestimation of the weakest absorbing species. The presence in the gas plume of an analyte amount, which is not representative of the solid mixture prepared for the MALDI, is the problem related to straightforward quantitative analysis via MALDI-TOF-MS. The way to overcome this drawback, proposed here, rests upon the application of the standard addition method to the MALDI analysis of PAH blends.

The method of standard addition is used in instrumental analysis to determine the concentration of a substance (analyte) in an unknown sample by comparison to a set of samples of known concentration, similar to using a calibration curve.

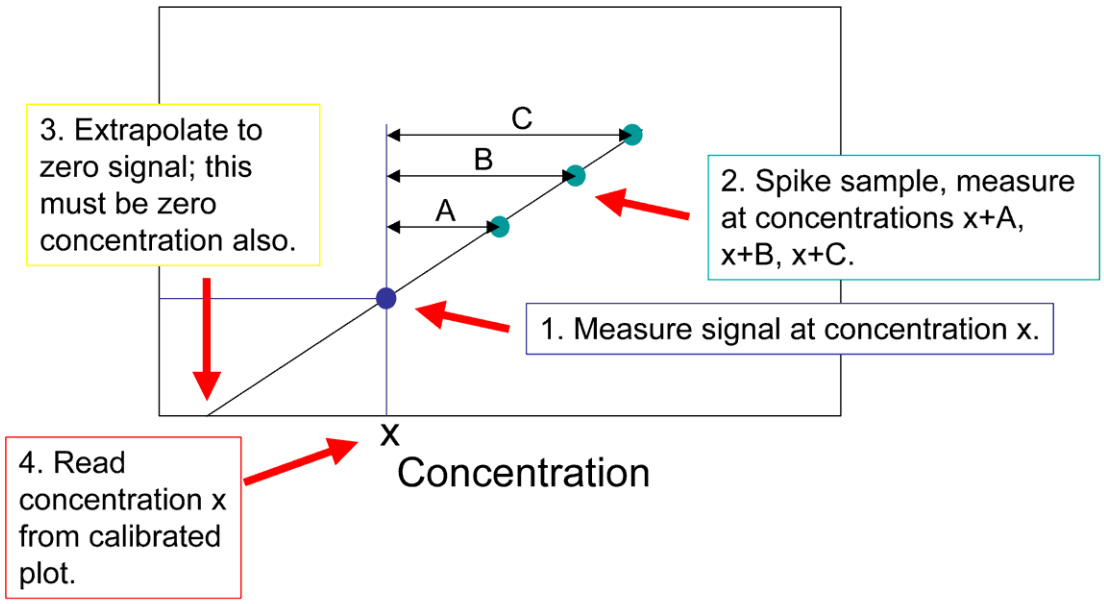

Figure 100. Example of a standard addition plot.

Standard addition (see **Figure 100**) can be applied to most analytical techniques and is used instead of a calibration curve to solve the "matrix effect" problem. Here the expression "matrix effect" is referred to the different desorption/photionization of the analytes.

Within this work, this procedure is used for the quantitative analysis of the binary mixture, composed of HBC-C_{12} and its precursor, with the aim to develop a straightforward procedure for the quantitative characterization of slightly soluble or insoluble binary blends, when just one of the two analytes is available as a pure sample (e.g. incomplete cyclodehydrogenation reaction).

The informations collected via analyses of model mixtures of synthetic PAHs are then employed for the quantitative characterization of natural PAHs, such as pitches.

Petroleum pitches are produced by the thermal polymerization of aromatic decant oil, a by-product of the fluid catalytic cracking (FCC) of the heavy gas oil fraction of crude oil, and are generally regarded to consist of alkylated polycyclic aromatic hydrocarbons (PAHs) with a molecular weight ranging from approximately 200 to 2000 [184-49].

To quantify the amount of monomers, dimers, trimers and tetramers, present in mesophasic pitch samples, this study relies on the following strategy:

1) The oligomeric fractions belonging to the pitch samples are separated via dense-gas extraction (DGE), a multistage separation technique, followed by the application of both new and conventional analytical techniques for identifying the specific molecular structures that exist in petroleum pitches.

2) The isolated fractions are then used as standards for building calibration plots which allow a reliable quantitative characterization of crude pitch samples.

Moreover, this study discovers a completely novel use of the mass spectrometer, employed not only for the resolution of complex analytical problems, but also as a novel tool for growing ultrapure, crystalline thin films of organic molecules.

Ions of the analytes are obtained by using a conventional ion source (secondary ion mass spectrometry SIMS), separated by an analyzer (double focusing sector field analyzer) depending on their different mass to charge ratios, decelerated via employing suitable decelerating potentials and landed on a conducting surface with retention of their structure, in a process defined as “soft-landing”.
For the landing experiments two systems are chosen:

1) A polyethylenoxide oligomer (PEO) with the aim to demonstrate the unique purification conditions offered in a soft-landing deposition, such as selection of mass-defined chains from the PEO molecular distribution, and to study the morphology of the films made thereof. The corresponding mass spectra before and after soft-landing are reported in **Figure 101**.

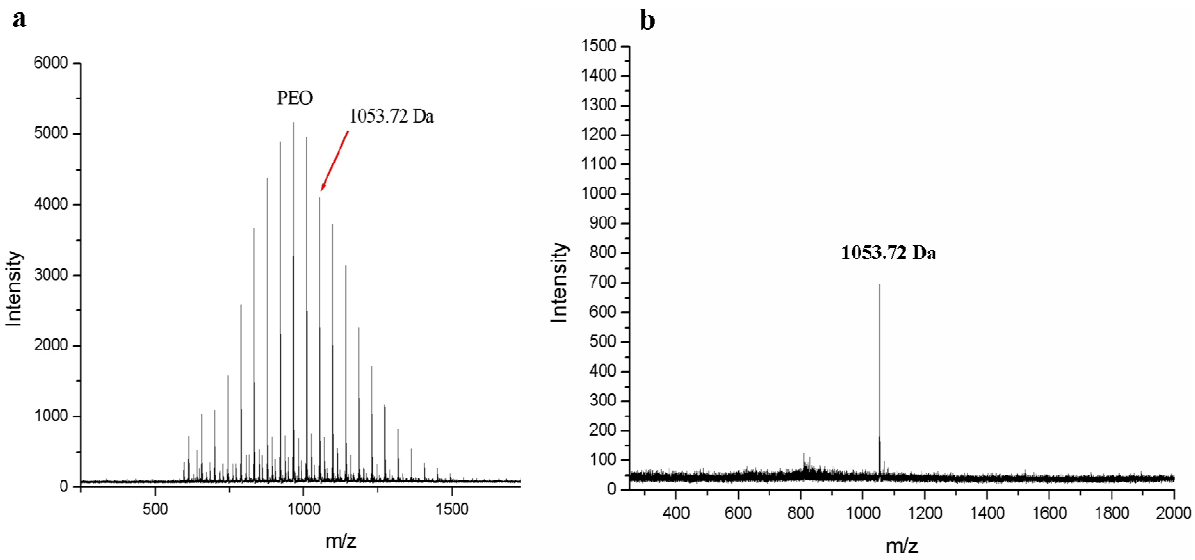

Figure 101. MALDI spectra of a PEO oligomer before (a) and after (b) soft-landing.

2) A rod-like molecules, such as dibenzo[b,b']thieno[2,3-f:5,4-f']-carbazole, for growing ultrapure (single isotopes, see **Figure 102 b**) thin films and for studying the packing of the molecules in soft-landed films.

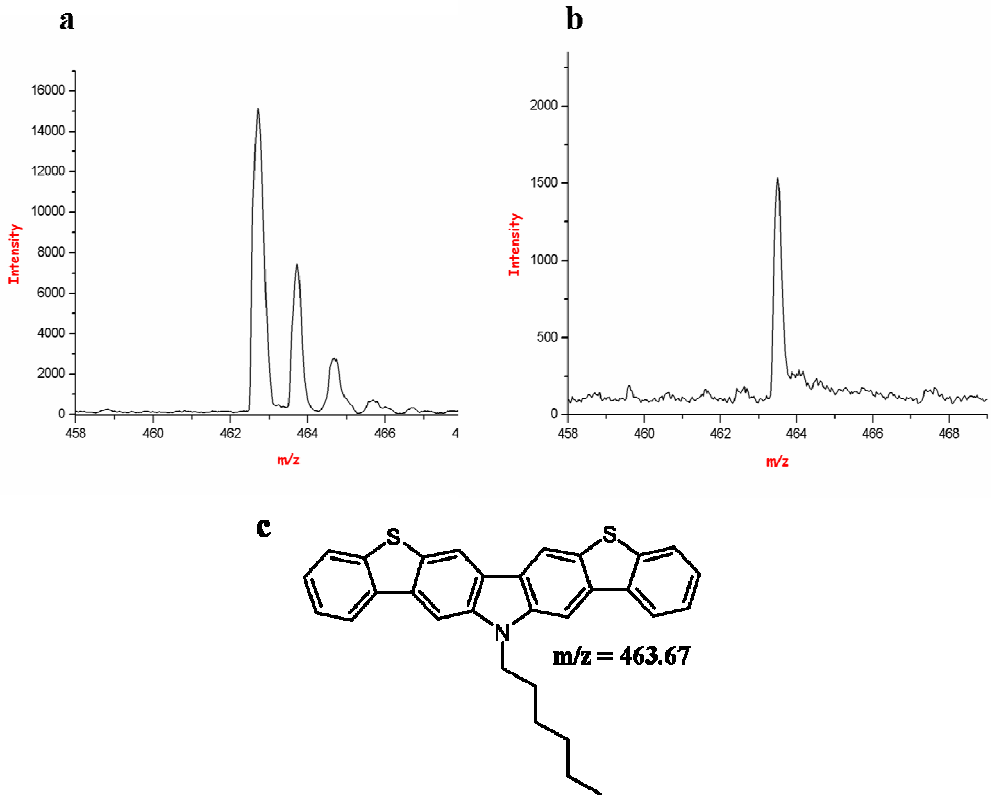

Figure 102. MALDI spectra of Dibenzo[b,b']thieno[2,3-f:5,4-f']-carbazole before (a) and after (b) soft-landing. c) Molecular structure is inserted.

From the work of Räder et al. [34], dedicated to the soft-landing of HBC molecules, it is in fact known that soft-landing is able to grow ordered films of HBC molecules with an unusual edge-on arrangement on a graphitic surface. Whereas a preferential face-on growth is observed for HBC molecules sublimed or drop-cast on HOPG. In the deposition of rod-like and polar molecules, performed here, the comparison of the assembly of the molecules in soft-landed films with that in drop-cast film reveals also a substantial difference, which can be related either to the ionic nature of the analyte or to the use of decelerating potential as strong as 8 kV for avoiding crash-landing of the analytes.

The influence of an electrical field of a strength comparable to that used during soft-landing on aromatic molecules bearing an extended π-system, such as HBCs, is moreover investigated via performing soft-landing-independent experiments.

The assembly of symmetrically (apolar) and asymmetrically (polar) substituted HBC molecules is studied in films obtained by casting concentrated solutions of HBC molecules and evaporation of the solvent in the presence of an electrical field. The alignment experiments are performed on different surfaces such as glass, gold and HOPG to discover the substrate influence on the molecular packing of substituted HBC molecules.

Under field action, the large aromatic discs are found to assemble into columnar structures that are unidirectionally oriented on a range as large as several millimeters (see **Figure 103**).

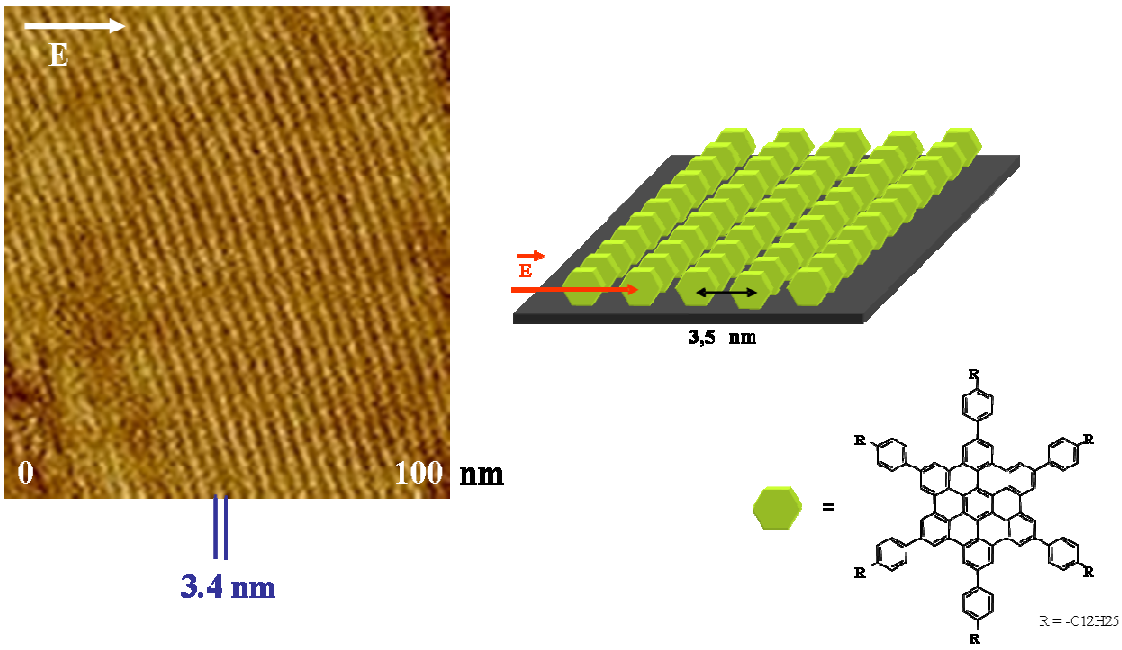

Figure 103. AFM micrograph of a field-oriented HBC-PhC_{12} film (left) on a glass surface. Sketch of the molecular arrangement. Molecular structure is inserted.

The electrical field-aligned HBC molecules maintain their upright standing arrangement even on HOPG (**Figure 104 a** and **94 b**, enlarged vision). Whereas, the aromatic core of the HBC-PhC_{12} molecules in absence of any external electrical force is face to face on the graphitic substrate (**Figure 104 d**). A schematic representation of the molecular assembly on HOPG is reported in **Figure 104 c**.

Note that the HOPG affinity to the nanographene molecules leads to a slightly tilted edge-on arrangement of the HBC molecules oriented in presence of an electrical field, whereas, the HBC molecules in field-oriented films, cast on glass, stack with their planes orthogonal to the columnar axis.

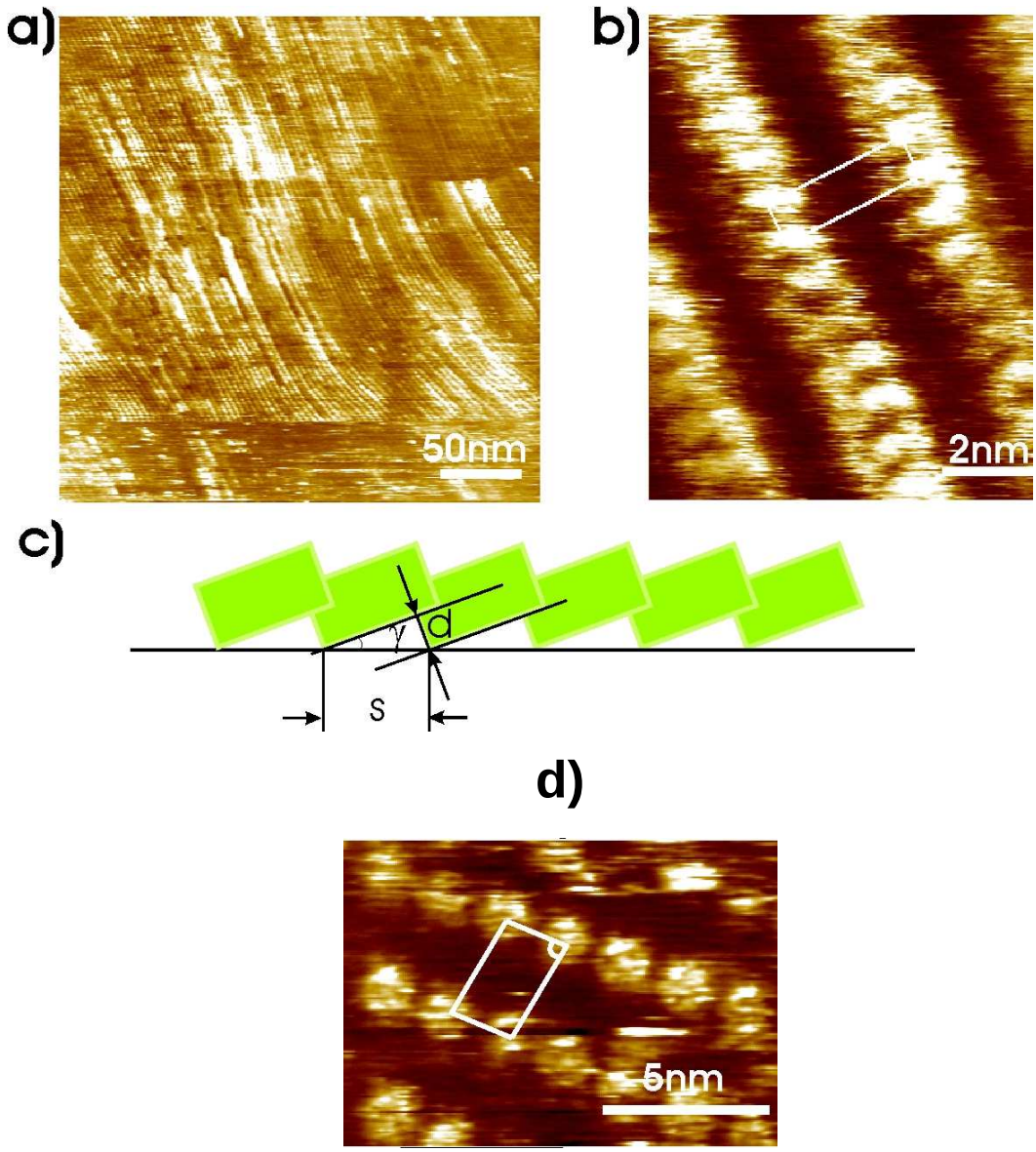

Figure 104. a) and b) STM current images of the surface of an electric field-oriented HBC-PhC$_{12}$ film. c) Schematic representation of the HBC disc arrangement with respect to the surface. d) STM current image of a dry film adsorbed without electric field.

Moreover, the field capability to control the orientation of anisotropic molecules is then used to produce ordered films of solution-processible rod-like molecules, such as cyclopentadithiophene-alt-benzothiadiazole copolymer (CTD-alt-BTZ copolymer, molecular structure in **Figure 105 a**), as an example for rigid-rod semiconducting polymers, and pentacene molecules. The latter is achieved performing a retro-Diels Alder reaction on 13,6-Sulfinylacetamidopentacene molecules in presence of an electrical field (**Figure 105 b**).

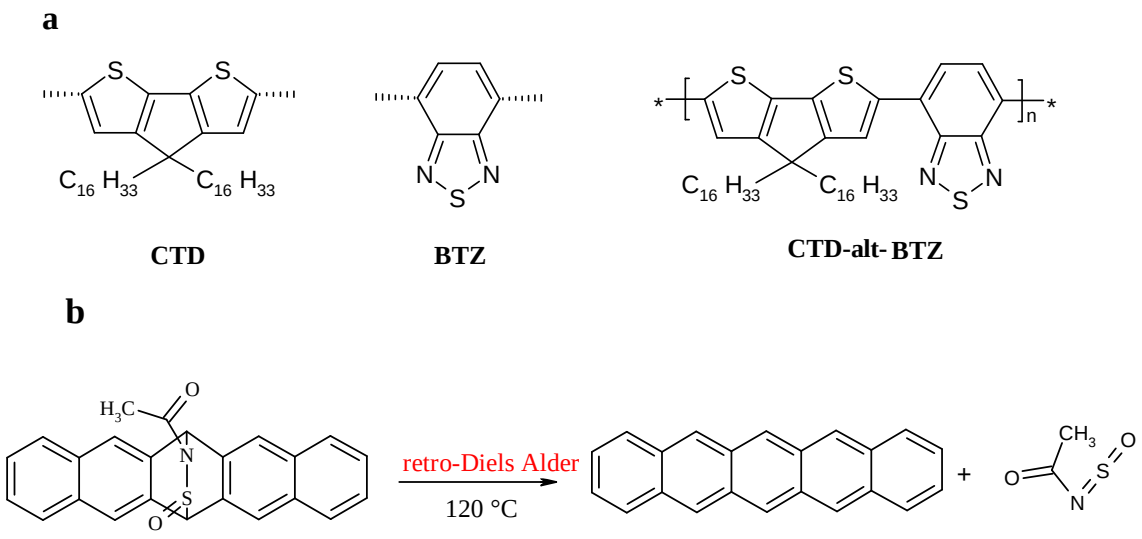

Figure 105. a) Structures of CDT, BTZ and alternating CTD-alt-BTZ copolymer. b) Retro Diels-Alder reaction of 13,6-Sulfinylacetamidopentacene.

The alignment experiments on the rod-like polymer are conducted on a glass substrate via casting a drop of CTD-alt-BTZ copolymer solution in trichlobenzene and dried in field presence. Optical microscopy, morphology (AFM) and diffraction studies reveal that the polymer chains can be directed in the field direction and are aligned parallel to the deposition substrate. The related AFM micrographs are reported in **Figure 106 a-c**.

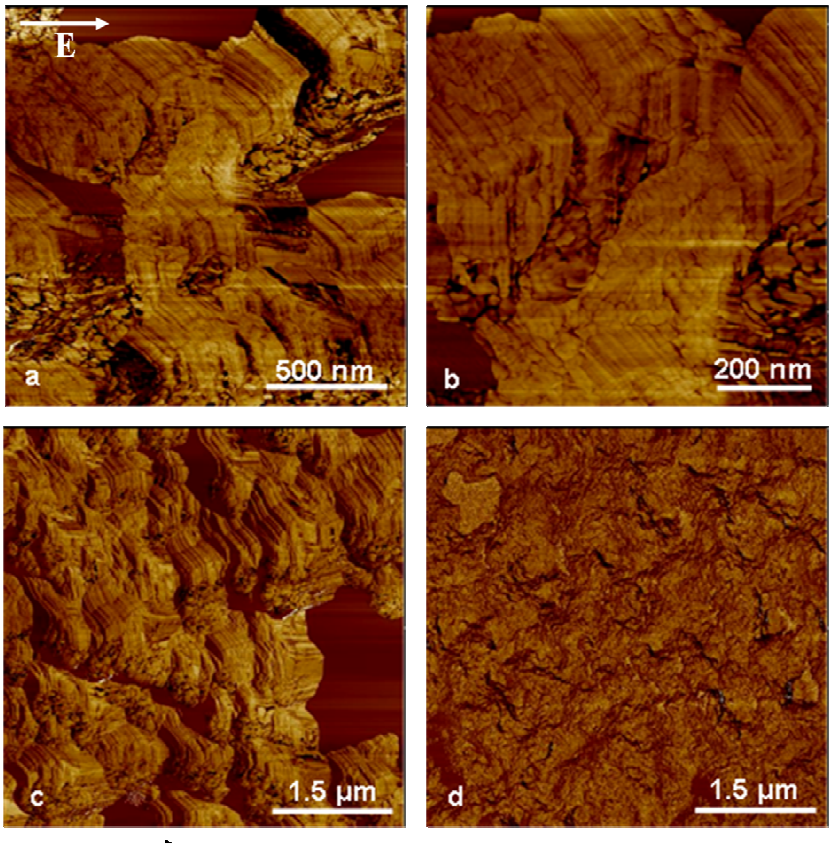

Figure 106. AFM micrograph of CTD-alt-BTZ copolymer films prepared in presence of an electrical field (a-c, with different magnification) and in absence of an electrical field (d).

On the contrary, the polymer chains of a reference sample, drop-cast in absence of an external field, are arranged in a different manner with a preferential orientation of their backbone perpendicular to the deposition surface (**Figure 107**).

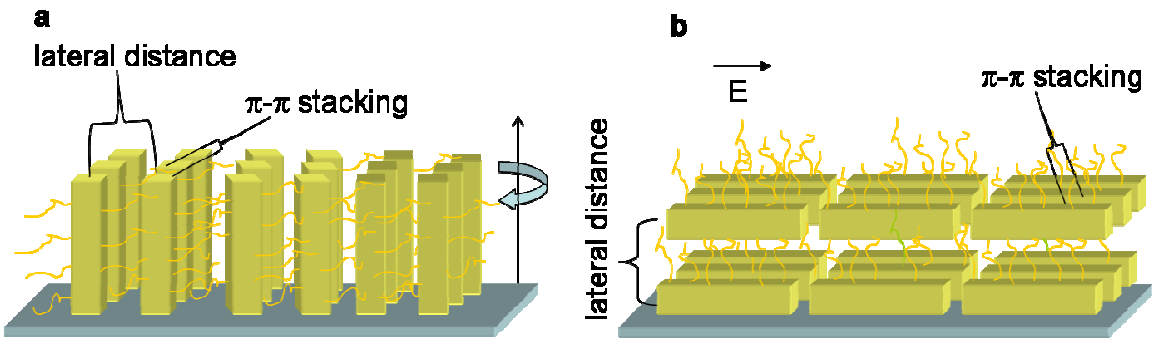

Figure 107. a) Schematic representation of the BTZ-alt-CDT copolymer chains on the glass surface in a polymer film prepared by drop-casting in absence of an electrical field. b) Assembly of the BTZ-alt-CDT copolymer chains in presence of an external electrical field parallel to the surface.

The strong field influence on the assembly of CTD-alt-BTZ copolymer chains can be related to its lyotropic liquid crystalline nature in trichlorobenzene. Beyond a critical concentration, the rod-like CTD-alt-BTZ copolymer chains create a liquid crystalline phase and can be directed in the field direction. Via solvent evaporation, the uniaxial order of the polymer chains is frozen to obtain well-oriented films in the solid state.

Electrical field-aligned films of CTD-alt-BTZ copolymer are then used as semiconducting layers for building organic field effect transistor. A saturated mobility as high as 0.2 cm^2/Vs and a linear one of 0.01 cm^2/Vs are measured for the oriented films. These values are five orders of magnitude higher when compared to the electronic performances of non-oriented reference films.

In summary, this investigation has:

1) explored the the desorption/photoionization characteristics of giant PAHs to extract qualitative and quantitative information from their MALDI spectra;
2) used the mass spectrometry principles to growth ultrapure thin films of organic molecules and clarified the processes which in a soft-landing deposition influence the packing of the molecules reaching the deposition substrate;
3) employed the capability of electrical fields of orienting in their direction anisotropic molecules to grow oriented films of semiconducting molecules for the fabrication of OFETs possessing improved electronic performances.

9.1 References

[184] R. A. Greinke, *Carbon*, **1986**, 24, 677.

10 Experimental part

10.1 Clustering behavior of PAHs in MALDI-TOF-MS

10.1.1 Materials

10.1.1.1 Synthesis of symmetrically substituted HBC molecules:

1) HBC-C_6 molecules
2) HBC-C_8 molecules

The HBC-C_6 and HBC-C_8 moleculs were synthetized according to the synthesis route for symmetric HBCs [62] which is reported below.

HBC-C_6 molecules

At first, a two-step synthetic approach was employed to prepare alkyl substituted 4,4´-diphenylacetylenes which represent the crucial building block for the hexafold-substituted HBC derivatives (**Scheme 3**):

1) Hydroboration of alkene
2) Suzuki reaction

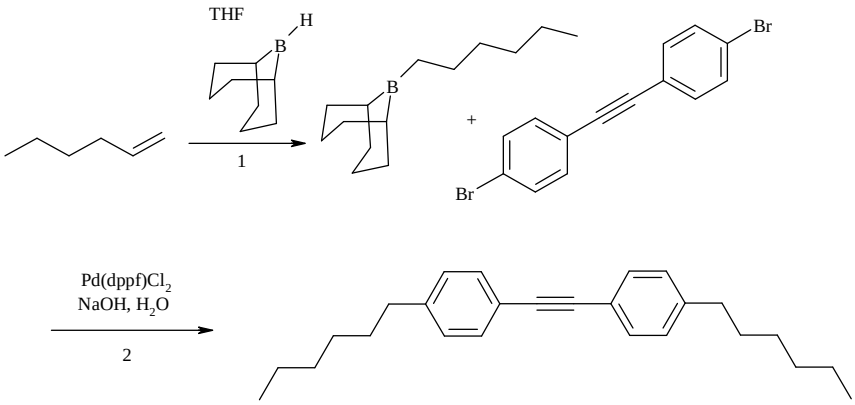

Scheme 3. 1) Hydroboration, 2) Suzuki reaction

In a subsequent cyclotrimerization under catalytic conditions, the 4,4´-bis(alkyl)diphenylacetylenes were reacted to the hexaphenylbenzene derivatives **1a** (**Scheme 4**).

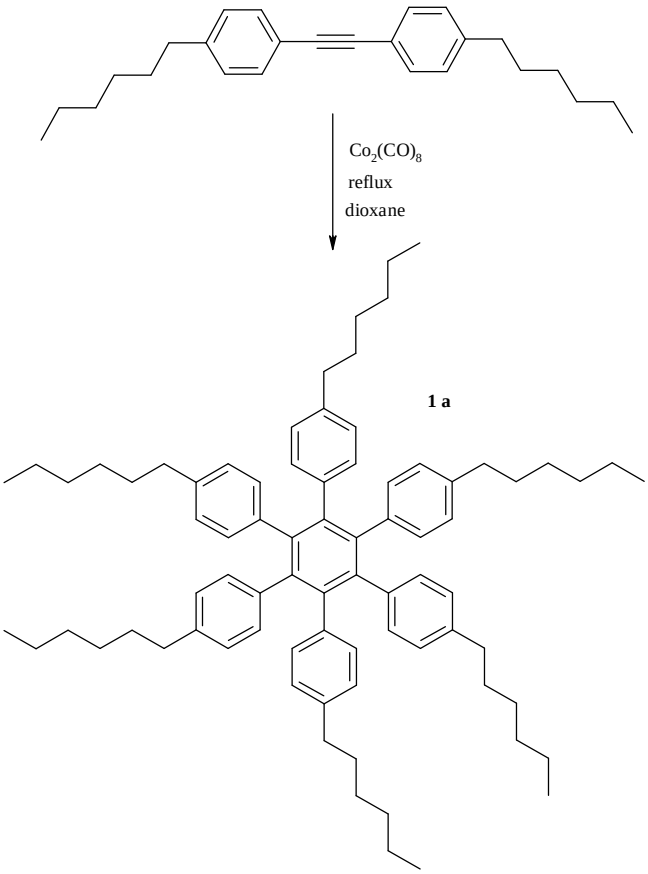

Scheme 4. Cyclotrimerization reaction

Unfortunately, the FD mass showed HPB derivatives with one missing alkyl chain. This undesired effect is probably due to a debromination during the Suzuki reaction. For this reason, a one-step synthesis for the desired diphenylacethylene was considered, starting from 1-(4-bromophenyl)hexane under Sonogashira palladium-catalyzed cross-coupling conditions (**Scheme 5**).

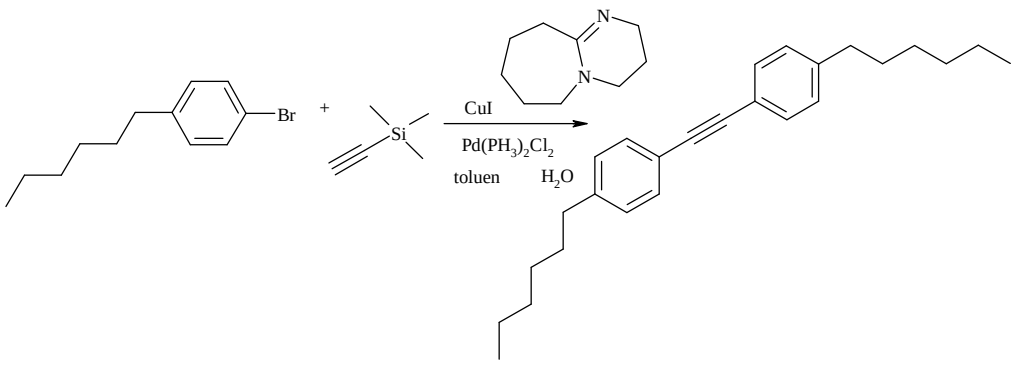

Scheme 5. Elevated temperature Sonogashira palladium-catalyzed cross-coupling reaction.

By using this approach, the subsequent cyclotrimerization reaction did not afford HPB derivatives with missing alkyl chains and the crude product could be easily purified. In the following step, (oxidative planarization) using $FeCl_3$, hexa(4-hexylphenyl)benzene was reacted to hexa-(hexyl)-hexabenzocoronene (**Scheme 6**).

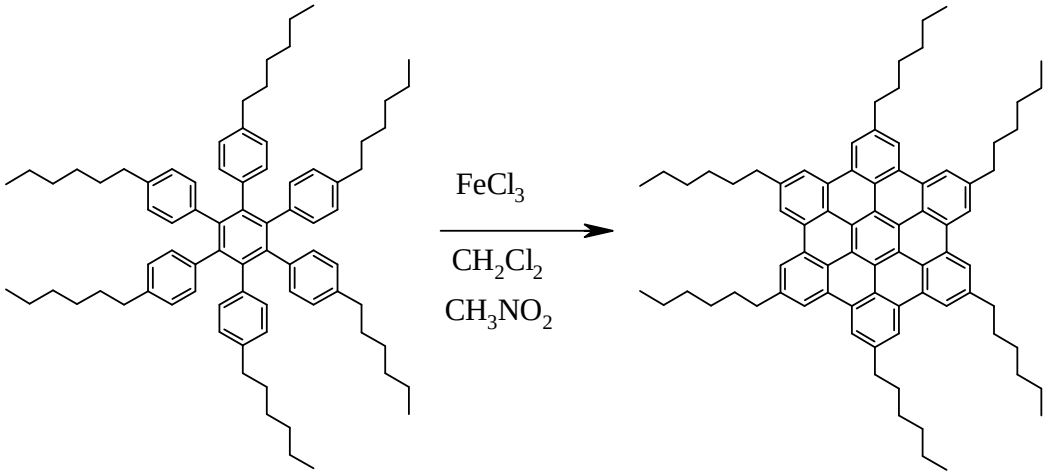

Scheme 6. Cyclodehydrogenation reaction of hexa(4-hexylphenyl)benzene.

The same synthetic procedure was followed for synthesizing hexa(octyl)hexabenzocoronene.

10.1.1.2 Other materials

The syntheses of hexabenzocoronene (HBC), hexa(methyl)hexa-*peri*-hexabenzocoronene, hexa(propyl)hexa-*peri*-benzocoronene, hexa(dodecyl)hexa-*peri*-hexabenzocorone (HBC-C_{12}) and its precursor hexa(4n-dodecyldiphenyl)benzene as have already been reported. [51-52]

The synthesis of $C_{222}H_{42}$ and its dendritic precursor have been described elsewhere [185].

7,7,8,8 tetracyanoquinodimethane (TCNQ, 98%) and *trans*-2-[3-(4-*tert*-butylphenyl)-2-methyl-2-propenylidene]malononitrile (DCTB) were purchased from Acros Organics (Belgium) and used without further purification. Fullerite was purchased from Sigma Aldrich (Munich, Germany).

10.1.2 MALDI instrument and calibration: general requirement

MALDI and LD analyses were performed using a Bruker Reflex II mass spectrometer (Bremen, Germany) operating in reflectron mode. The instrument was equipped with a nitrogen laser (wavelength 337 nm) and the MALDI spectra were recorded with a pulse rate of 3 Hz. The ions were accelerated by a voltage of 20 kV and detected by using a micro channel plate detector. Calibration was carried out before each measurement by using a fullerite mixture.

10.1.3 Sample preparation

Solvent-free method

A four component equimolar mixture of HBC, HBC-C_1, HBC-C_3, HBC-C_{12} was prepared with TCNQ (**set 1**) and with DCTB (**set 2**) as the matrices in a molar ratio of 1/850 by using an MM 2000 ball mill from F. Kurt Retsch GmbH & Co. KG (Haan, Germany). The powder was then spread on three different places of a polished stainless steel sample holder with a flat spatula. For each sample a composite MALDI spectrum was acquired by summing 500 single shots.

By using the same experimental conditions, the equimolar binary mixtures HBC/HBC-C_1, HBC/HBC-C_{12}, HBC/HBC-C_8, $C_{222}H_{42}/C_{222}H_{150}$ were prepared and measured.

Laser desorption analyses were conducted via spreading the analyte powder on a sample holder with a flat spatula. Laser desorption spectra were then recorded by summing 200 single shots.

For the sake of simplicity the signal intensities of the peaks were evaluated instead of their relative areas, once the non-variance of the results was established.

10.1.4 Preparation of TCNQ/HBC-C_{12} films

Hexa(dodecyl)hexa-*peri*-hexabenzocoronene and 7,7,8,8 tetracyanoquinodimethane molecules were dissolved in THF with a concentration of 0.25 mg/mL and 0.6 mg/mL, respectively. Solutions with a donor-acceptor molar ratio of 1/1 were then prepared. TCNQ-HBC-C_{12} films were obtained via drop-casting on a glass substrate and slowly evaporating in an atmosphere saturated with solvent vapour.

10.2 Quantitative MALDI analyses of PAHs and fullerenes

10.2.1 Materials

The syntheses of hexa(dodecyl)hexa-*peri*-hexabenzocorone (HBC-C_{12}) and its precursor hexa (4n-dodecyldiphenyl)benzene (Set 1) have been reported elsewhere [185]. C60 and C70 fullerene (Set 2) were obtained from Sigma Aldrich (Munich, Germany) and used without further purification.

10.2.2 MALDI sample preparations

10.2.2.1 Solvent-free method (general procedure)

The analytes were milled together with the TCNQ matrix by using a MM 2000 ball mill from F. Kurt Retsch and Co. KG (Haan, Germany). The powder was then spread on a polished stainless steel sample holder with a flat spatula while moving the sample position. For each sample, a composite MALDI spectrum was acquired by summing 500 single shots. All the MALDI spectra were recorded with the same laser power (88% laser attenuator). The best conditions for the quantitative characterization were found by adjusting the laser power well above the desorption-ionization threshold of the analytes.

SET 1: Quantitative MALDI analysis for the system HPB-C_{12}/HBC-C_{12}

In order to perform quantitative MALDI analyses on the binary mixture HPB-C_{12}/HBC-C_{12}, the amount of HPB-C_{12} was varied whereas the amount of HBC-C_{12} and TCNQ was kept constant. HPB-C_{12} and HBC-C_{12} were mixed in ratios as listed in **Table 7**

Table 7. Composition of the mixtures for the system HPB-C_{12} / HBC-C_{12} prepared via solvent-free sample preparation.

Mixture	HBC-C_{12}/mg	HPB-C_{12}/mg	TCNQ/mg	analyte:matrix molar ratio
1	0.27	0.27	230.15	1/3211
2	0.25	0.61	230.14	1/2020
3	0.30	0.87	230.02	1/1484
4	0.26	1.21	232.95	1/1197
5	0.28	1.82	229.71	1/827
6	0.25	2.19	230.15	1/807
7	0.28	3.32	233.40	1/528

MALDI spectra were measured and the intensity ratios were calculated and expressed as Int. (HPB-C_{12})/Int.(HBC-C_{12}) as listed in **Table 8**.

Table 8. Measured intensity ratios of the system Int.(HPB-C_{12})/Int. (HBC-C_{12}) for different mass ratios HPB-C_{12} / HBC-C_{12}.

Mixture	Int.(HPB-C_{12})/ Int.(HBC-C_{12})	Standard deviation	Mass ratio HPB-C_{12}/HBC-C_{12}	mg. of added HPB-C_{12}
1	0.110	0.017	1.0	0
2	0.228	0.022	2.2	0.34
3	0.357	0.081	2.9	0.57
4	0.460	0.090	4.6	0.95
5	0.612	0.110	6.4	1.55
6	0.701	0.069	8.7	1.92
7	0.738	0.064	11.8	3.05

For the sake of simplicity, during quantitative analyses, the signal intensities of the peaks were evaluated instead of their relative areas, once the non-variance of the results has been established.

10.2.2.2 Solvent-based method

In order to reach the best crystallization conditions, THF was selected as a common solvent for samples and matrix to perform quantitative MALDI analyses on the mixture HPB-C_{12}/HBC-C_{12}. Both components were dissolved in THF with a concentration of 0.061 mg/mL ($4.00x10^{-5}$ M) and 0.070 mg/mL ($4.5x10^{-5}$ M) respectively, while TCNQ was dissolved in THF at a concentration of 2.5 mg/mL ($1.2x10^{-2}$ M). Seven mixtures of the two components were prepared with different molar ratios as listed in **Table 9**. The quantities of HPB-C_{12} were varied whereas the concentration of HBC-C_{12} in the mixtures was kept constant.

Table 9. Composition of the mixtures for the system HPB-C_{12}/HBC-C_{12} prepared via solvent based sample preparation.

SET 1	TCNQ/µL	HBC-C_{12}/µL	HPB-C_{12}/µL	analyte:matrix molar ratio
1	20	4	4	1/706
2	20	4	5	1/523
3	20	4	6	1/558
4	20	4	7	1/505
5	20	4	8	1/ 461
6	20	4	9	1/425
7	20	4	10	1/393

The responses for the different molar ratios, obtained from the MALDI measurements and expressed as Int. (HPB-C_{12})/Int. (HBC-C_{12}) are reported in **Table 10**.

Table 10. Measured intensity ratios of system HPB-C_{12}/HBC-C_{12} for different molar ratios.

Mixture	Int. (HPB-C_{12}) / Int. (HBC-C_{12})	Standard deviation	Molar ratio HPB-C_{12}/HBC-C_{12}	µL of HPB-C_{12} solution
1	0.254	0.048	1.12	0
2	0.370	0.116	1.41	1
3	0.422	0.086	1.7	2
4	0.473	0.080	2.0	3
5	0.483	0.086	2.25	4
6	0.621	0.093	2.53	5
7	0.665	0.199	2.81	6

SET 2: Quantitative MALDI analysis for the system C70/C60

Solvent-free method

To quantitatively characterize binary mixtures of C70/C60 fullerenes via MALDI-TOF MS, the amount of C70 was varied whereas the amount of C60 and TCNQ was kept constant analogous to the procedure in Set 1. **Table 11** reports the composition of the different mixtures. The fullerite powder with unknown composition was mixed with the TCNQ matrix in a mass ratio of 1/407.

Table 11. Composition of the mixtures for the system C60/C70 prepared via solvent-free sample preparation.

Mixture	C60/mg	C70/mg	TCNQ/mg	analyte:matrix molar ratio
1	0.40	0.17	200.29	1/1294
2	0.38	0.40	199.31	1/973
3	0.37	0.77	202.65	1/693
fullerite	0.50		203.55	Mass ratio: 1/407

The responses for the different molar ratios, obtained from the MALDI measurements and expressed as Int. C70/Int. C60, are reported in **Table 12**.

Table 12. Measured intensity ratios of system C70/C60 for different molar ratios.

Mixture	Molar ratio C70/C60	Int. C70/ Int. C60	Standard deviation
1	0.36	0.680	0.037
2	0.90	1.625	0.084
3	1.78	2.432	0.067
fullerite	x	0.203	0.010

10.2.3 HPLC characterization of C70/C60 mixtures

High pressure liquid chromatography analyses of the C70/C60 mixtures were performed by using a C18 reversed phase column coupled with a diode array detector working at a fixed wavelength of 330.2 nm which was selected by considering the strong absorption of the analytes at this wavelength. A solvent mixture composed of

toluene and acetonitrile (CHROMASOLV® Plus, for HPLC, ≥ 99.9%) was chosen as eluent for the chromatographic analyses.

Solutions of C60 and C70 were prepared by dissolving C60 and C70, respectively, in a 4:1 solvent mixture of 1,2,4 trichlorobenzene and toluene (0.20 mg/mL). To establish the calibration curve for the system C70/C60, solutions of C70/C60 mixtures were prepared with the molar ratios reported in **Table 13**.

Table 13. Concentration of C70/C60 solutions for HPLC analyses.

Mixture	Molar ratio C70/C60	Concentration (mg/mL)
1	1/1.0	0.20
2	1/1.5	0.20
3	1/ 2.0	0.20
fullerite	x	0.20

Three injections were performed for each sample, then the resulting data expressed as C70/C60 peak area ratios were averaged and plotted against the respective C70/C60 molar ratios (**Table 14**).

Table 14. Measured signal area ratios of system C70/C60 for different molar ratios.

mixture	Molar ratio C70/C60	Area ratio C70/C60	Standard deviation
1	1	0.951	0.054
2	0.66	0.742	0.044
3	0.5	0.632	0.065

The commercially available fullerene mixture, known as fullerite, was dissolved in a 4:1 solvent mixture of 1,2,4 trichlorobenzene and toluene (0.20 mg/mL) and analyzed by HPLC.

10.3 MALDI analyses of mesophasic pitch

10.3.1 Materials

The feed pitch to the DGE process was an isotropic pitch, M-50, which was obtained from Marathon Petroleum Company LLC. Four fractions of M-50 pitch were isolated by DGE and then subjected to analysis: Fractions containing 79 and 98% monomer,

and fractions consisting of 89 and 97% dimmer. Both toluene (HPLC grade, 99.8% purity, CAS 108-88-3) and methanol (HPLC grade, 99.9% purity, CAS 67-56-1) were obtained from Fisher Scientific and were used as dense-gas solvents without further purification.

10.3.2 Dense-gas extraction apparatus and procedure

Because DGE is reported in detail elsewhere [186], only a brief description is given here. The two monomer-rich fractions were produced by continuous DGE; the two dimer-rich fractions by semi-batch DGE.

The continuous DGE unit consists of a packed column with a height of 1.5 m of packing and an inner diameter of 1.8 cm. For a typical experiment, molten M-50 pitch is fed to the top of the column at ~120 g/h via a single-screw extruder, and a liquid chromatography pump is used to deliver the dense-gas solvent at ~600 g/h to the bottom of the column. The dense-gas solvent flows up the column, the pitch feed flows down the column, and selected fractions of the feed pitch are extracted into the solvent phase. As would be expected, higher operating pressures increase the density of the solvent and increase the average mol wt of the overhead extract. However, the column operating temperature has been found to exhibit more complex behavior, with the establishment of a positive temperature gradient from the bottom to the top of the column yielding the best product purities. [187] A liquid-level detector at the bottom of the column operates based on the difference in electrical resistivity between the top and bottom phases and ensures complete separation between the solvent-rich top phase and pitch-rich bottom phase. Steady-state operation is typically reached within an hour, and an experimental run takes 6-12 h, depending on how much pitch product is to be produced.

For a semi-batch run ~15 g of the M-50 feed pitch is charged to a still pot in the bottom of a packed column. Continuous flow of the dense-gas solvent is then initiated. The solvent flows through the pitch charge, extracts a portion of the pitch depending on the operating (column) temperature and pressure, flows up the column, and removes the extracted pitch fraction out as top product. As with continuous DGE, a positive temperature gradient is established along the length of the column to enhance product purity. Liquid reflux of a portion of the product back down the

column, which is created by use of a heated reflux finger, is also used to enhance overhead product purity.

10.3.3 Analytical characterization of pitch fractions isolated by DGE

Pitch fractions isolated by the DGE experiments described above were subjected to a wide range of analytical characterization techniques as described below. Field desorption–mass spectrometry (FD-MS) analyses were performed using a Fisons Instruments VG ZAB2_SE_FPD Sectorfield mass spectrometer. CH_2Cl_2 (Fisher Scientific, HPLC grade) was used as the solvent for all analyzed pitch fractions, and a drop of the resulting solution was placed on the emitter of the mass spectrometer. Ions were produced by field desorption of the analytes by employing an extraction potential of 8 kV. Calibration was carried out before each measurement by using acetone (Fluka, 99.5%).

^{1}H-NMR analyses were performed with a Bruker 700 MHz NMR Spectrometer Avance instrument. Five mg of a given pitch fraction were dissolved in deuterated 1,2-dichlorobenzene-d_4 (Deutero GmbH, 99%) and measurements were carried out at 80°C. This above-ambient temperature was used to improve resolution and to ensure that all fractions were completely soluble in the NMR solvent.

UV-Vis analyses were carried out with a Perkin Elmer Lambda 9 instrument, with all pitch fractions being dissolved in 1,2,4 trichlorobenzene (Sigma-Aldrich, 99%). FT-IR analyses of the monomer-rich fraction were performed on the bulk analyte with a Nicolet 730 spectrometer. Elemental analysis was performed with a PerkinElmer CHNS/O Model 2400 Series II elemental analyzer.

10.3.4 MALDI and post-source decay

For MALDI analysis, samples were analyzed using a Bruker Daltonics Autoflex MALDI-TOF mass spectrometer equipped with 337 nm nitrogen laser. The reflectron mode was used for this study. The target plate was positively charged and set to 19.0 kV; the secondary ion source to 16.5 kV, the lens to 9.40 kV, and the reflector to 20 kV. Ions generated after laser bombardment were accelerated using pulsed-ion extraction after a time delay of 90 ns. Other important parameters used during the

analysis included a detector gain of 4.0, resolution of 2.0, and mol wt suppression up to 210. MALDI calibration was carried out using a fullerite mixture (Sigma-Aldrich) before the analysis. Laser powers ranging from 20 to 26% of maximum were used for the MALDI analysis of M-50 petroleum pitch and its fractions, with 200 laser shots being used to generate the spectra shown herein. MALDI m/z values were accurate to within ±0.1 Da.

Both solid-state and solvent-based sample preparation methods were used to prepare samples for MALDI analysis. Based on previous studies [49, 20], 7,7,8,8-tetracyanoquinodimethane (TCNQ; 98% min. from TCI America) was used as the matrix. For the solid-state analysis of M-50 pitch, the pitch and TCNQ were mixed using a grinding mill (Thermo Electron Corp., model Wig-L-Bug). The sample was then transferred to the MALDI target-plate cell using our water-spotting method [188]. For the solvent-based sample preparation of monomer-rich and dimer-rich fractions, a fine powder of TCNQ was prepared using a grinding mill. A thin film of this matrix powder was then transferred to the MALDI target via water-spotting. Each pitch fraction was then dissolved in carbon disulfide (Fisher Scientific; 99.9% min purity) at a concentration of 0.02 w/v %, and a drop of the prepared solution was placed on the film of TCNQ and allowed to dry before analysis.

Post-source decay (PSD) analyses were performed with the MALDI instrument described above, operating in the reflectron mode and with the Bradbury-Nielsen ion gate activated. The ion gate was programmed to pass parent species ions of specified mol wt to within ±5 Da, as well as all fragment ions associated with the parent species. The target plate was positively charged and set to 19.0 kV, the secondary ion source to 16.8 kV, and the lens to 7.6 kV. Reflector voltage was initially set to 20 kV and then progressively reduced to analyze fragment ions of decreasing mol wt. The pulsed ion extraction delay was set to 90 ns, the resolution to 1.0, and 300 laser shots were used to generate all spectra. The laser power ranged from 26 to 33%, with higher laser power than that employed in conventional MALDI being required to fragment a given pitch species, and further increases in laser power being required to produce fragment ions of decreasing mol wt. The detector gain employed ranged from 6 to 16, with higher gains required to achieve an adequate detector response for smaller ion fragments. Fragmentation spectra via PSD are less accurate than conventional MALDI, that is, to within ±0.25 Da.

Solvent-based sample preparation was used as described above, with 1,2,4 trichlorobenzene (VWR, GPC grade; 99% min. purity) being used to dissolve the samples at a w/v % of 0.1.

10.4 Soft-landing experiments

10.4.1 Soft-landing apparatus

Soft-landing deposition was performed by using a tandem mass spectrometer modified for deposition experiments. The deposition apparatus was assembled as following:

1. Liquid secondary ionization mass spectrometry ion source;
2. A double focusing sector field analyzer
3. A deceleration unit
4. A deposition unit.

10.4.2 Deposition of mass-selected PEO chains

Positive LSIMS was in this work used to ionize the PEO chains. A solution of PEO in THF (1mg/mL) was mixed with a volume ratio of 1/3 with 3-nitrobenzyl acid. The matrix presence allowed the formation of a continuous flow of intact PEO ions.
PEO single chains were deposited on stainless steal substrate, which was previously covered with TCNQ, for a soft-landing time of 7 hours.

10.4.3 Deposition of single isotope Dibenzo[b,b']thieno[2,3-f:5,4-f']-carbazole molecules

3-nitrobenzyl alcohol (3-NBA matrix) was mixed with a solution of Dibenzo[b,b']thieno[2,3-f:5,4-f']-carbazole molecules in THF (10 mg/mL) in 4-1 volume ratio. The analyte molecules were ionized using Liquid secondary mass spectrometry (LSIMS) and soft-landed on a stainless steal-TCNQ surface, by using a

deceleration potential of 80 V and a focusing potential of 2.25 V. The deceleration potential for the deposition of Dibenzo[b,b']thieno[2,3-f:5,4-f']-carbazole molecules on carbon-covered aluminum foil and copper surfaces was found to be 65 V, by keeping constant the focusing potential. After a deposition time of two hours, Dibenzo[b,b']thieno[2,3-f:5,4-f']-carbazole crystals were observable on the deposition surface.

For the TEM analyses of the soft-landed films, the landing experiments were carried out on carbon-covered copper grids.

10.5 Electrical field alignment experiments of HBC molecules

10.5.1 Orientation experiments of HBC-PhC_{12} molecules on glass surface

10.5.1.1 Film Preparation

The synthesis for HBC-PhC_{12} is described in ref. 185. Films of HBC-PhC_{12} were obtained by drop-casting solutions (1.5–15 $mgmL^{-1}$) in p-xylene (Acros Organics 99%) on a glass surface at ambient temperature. Before the application of the drop to the surface, the HBC-PhC_{12} solutions were sonificated for 20 min. Electric fields in the range of 4–5 $kVcm^{-1}$ (DC) were applied parallel to the glass surface and maintained until the complete evaporation of the solvent (1 hour). To ensure the uniaxial orientation of the molecules, the highest field strength was selected. At higher voltages (> 5 $kVcm^{-1}$), a flashover between the electrode plates was observed. The preparation of the reference sample was done with exactly the same experimental conditions except for the application of the electrical field.

10.5.1.2 Experimental set-up

The experiments to increase the degree of supramolecular order in films of HBC-PhC_{12} molecules were carried out in a home-built apparatus. According to **Figure 108**, two stainless-steel electrodes (area= 3 x 3 cm^2, thickness = 0.5 mm) were fixed parallel to each other on a Teflon support. This geometry was selected to create a

uniform electric field (0–24 $kVcm^{-1}$) by charging one electrode and grounding the other one with a high-voltage power supply (Fug Electronic HCN GmbH 0–24 kV).

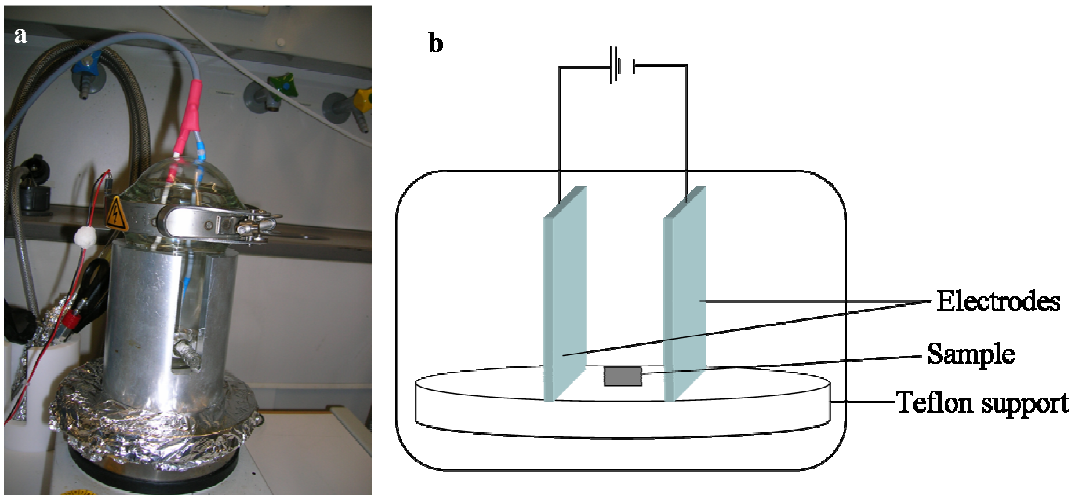

Figure 108. a) Experimental set-up for alignment experiments with an electrical field. b) Schematic representation of the apparatus elements.

The sample plate was placed between the electrodes on the Teflon support. To reduce the field inhomogeneity near the rim of the electrodes, the electrodes were three times larger than the sample plate. A drop of dissolved HBC-PhC_{12} molecules was cast on a glass substrate. Then, the electric field was applied parallel to the glass surface and maintained until the solvent was totally evaporated. The experiments were performed in a small glass box to control the evaporation rate of the solvent. Crystallization in an atmosphere saturated with vapor of the organic solvent was employed to improve the alignment of HBC-PhC_{12} molecules under electric field influence.

10.5.1.3 Optical Microscopy

The anisotropy of field-force oriented $HBCPhC_{12}$ films was investigated with a polarizing microscope (Zeiss Axiophot microscope with AxioCam Camera) with one polarizer or crossed polarizers parallel to the micrograph edge, taking advantage of the dichroism or the birefringence of the samples, respectively. The microscope was equipped with a rotating sample stage. The drop-cast films on glass were analyzed in transmitted light.

10.5.1.4 Electron Microscopy

For morphological analyses, replicas of the field-force oriented HBC-PhC_{12} films were prepared by covering the film surfaces with platinum from carbon electrodes. A carbon supporting film was then evaporated onto the sample. After floating off the films onto a water surface and transferring them to copper grids, the samples were exposed to chloroform to dissolve the organic film. Morphological features were observed with a Zeiss EM 902 transmission microscope (TEM with Henry-Casting Energy Filter) at high voltage (80 kV). Electron diffraction analyses were performed on the thin films prior to dissolving the samples.

For these analyses, a Zeiss 912 transmission microscope (with integrated Omega Energy Filter) was used at a high voltage of 120 kV. The instrument was equipped with a rotating sample holder and a goniometer stage. The apparent diffraction length was calibrated with a film of evaporated thallium chloride. Scanning electron microscopy analyses were performed by using a LEO 1530 low-voltage, high-resolution scanning electron microscope with an accelerating voltage of 0.60 kV for the field-force oriented films deposited on glass.

10.5.1.5 X-ray Analyses

The X-ray diffraction (XRD) experiments for oriented and drop-cast HBC-PhC_{12} films on glass substrates were performed using a Philips powder diffractometer with graphite monochromatized copper irradiation operating in reflection mode. The scattered intensity was measured in the range of the scattering angle 2θ between 18 and 40°.

10.5.1.6 Atomic Force Microscopy

The morphology of the films on glass substrates was studied using a scanning force microscope in tapping mode (Multimode Nanoscope 5.12r5). The film surface was explored by using an E scanner (12 x 12 μm^2, molecular resolution) at room temperature with a scan rate of 1 Hz and a resolution of 512 x 512 pixels. All of the images were reprocessed by using the Nanoscope 5.12r5 software.

10.5.2 Experiment on polycrystalline gold

10.5.2.1 Film preparation

In order to investigate the surface influence on the electrical field induced alignment of HBC-PhC_{12} molecules, alignment experiments were performed on a glass surface previously covered by a thin gold layer.
A 50 nm thin gold film was thermally evaporated on the glass surface. To improve the adhesion to the glass surface, the glass substrate was previously covered with a 1.5 nm thin Chromium film. A solution of HBC-PhC_{12} molecules in p-xylene (15 mg/ml) was cast on the glass surface and let evaporate in presence of an electrical field as strong as 4-5 kV/cm.

10.5.2.2 Film Characterization via FT-IR

The ordered HBC-PhC_{12} films were characterized via FT-IR absorption-reflection analyses with an instrument operating in reflection mode.
On the contrary a FT-IR instrument was used to analyze to record the IR absorption spectrum of the sample in bulk.

10.5.3 Orientation experiments of HBC-PhC_{12} molecules on HOPG

10.5.3.1 Film Preparation

Dry films were prepared by drop-casting a solution of HBC-PhC_{12} molecules in 1,2,4-trichlorobenzene (15 mg/ml) at room temperature onto freshly cleaved HOPG, while an electrical field in the range of 4-5 $x10^5$ V/m was applied parallel to the surface. The experiments were performed in a small glass box to control the evaporation rate of the solvent.

10.5.3.2 STM and AFM analyses

STM and AFM analyses were performed subsequently on the dry films at the solid-air interface. For comparison, films were also prepared without the presence of an electrical field, and then characterized by STM. Moreover, HBC-PhC_{12} molecules in 1,2,4-trichlorobenzene (15 mg/ml) were drop-cast on freshly cleaved HOPG without the presence of an external electrical field. STM was then performed at the solid-liquid interface.

STM measurements were performed using a home-built beetle-type STM interfaced to a commercial control unit (Omicron Nanotechnology GmbH). STM tips were prepared by mechanically cutting a 0.25 mm thick Pt/Ir (80%/20%) wire. SFM experiments were carried out with a Nanoscope III (Digital Instruments, Inc., Santa Barbara) in the tapping mode with an E-type scanner (12 x 12 μm^2) in air at room temperature. Commercial silicon tips (Digital instruments) on cantilevers with spring constants between 17 and 64 Nm^{-1}, were used at typical resonance frequencies in the range between 280 and 320 kHz.

10.6 Alignment experiments of rod-like molecules

10.6.1 Preparation of cyclopentadithiophene-alt-benzothiadiazole film

Dry films were prepared by drop-casting a solution of CTD-alt-BTZ copolymer in 1,2,4-trichlorobenzene (5 mg/mL) at 70° C onto a glass substrate, while an electrical field in the range of 4-5 kV/cm was applied parallel to the surface by using a home-built apparatus that was previously described. The reference sample was prepared under exactly the same experimental conditions except for the application of the electrical field.

10.6.1.1 OFET measurement of cyclopentadithiophene-alt-benzothiadiazole films

Bottom contact FET substrates consist of highly n-doped silicon wafers with 150nm thermally grown SiO_2. Photolithography followed by evaporation of 60nm gold on 4

nm chrome was used to define source and drain electrodes of 10μm channel lengths and 5mm channel widths. To prevent interfacial charge carrier trapping, the SiO_2 layer was treated with hexamethyldisilazane (HMDS) vapor at 120°C for 2 hours.
The polymer film was grown by drop-casting from 5 mg/ml cyclopentadithiophene-alt-benzothiadiazole solution in 1,2,4-trichlorobenzene on substrates heated at 70 °C. During solvent evaporation an electrical field as strong as 4-5 KV/cm was applied until total solvent evaporation. Organic FET's were measured using a Keithley 4200 Semiconductor Characterization System. The devices were prepared and measured in dry nitrogen atmosphere.

10.6.2 Retro-Diels Alder reaction of 13,6-Sulfinylacetamidopentacene in presence of an electrical field

10.6.2.1 Materials

13,6-Sulphinilacetamidopentacene was obtained by Sigma-Aldrich and used without further purification. Chloroform was purchased by ACROS and used as received.

10.6.2.2 Film preparation

A solution of 13,6-sulphinilacetamidopentacene in chloroform (1-2 % in weight) was cast on a glass surface. After solvent evaporation, the film was placed in a glass box between two stainless steal electrodes on a Teflon support. Electrical fields in the order of 4-5 kV/cm were applied parallel to the glass substrate. During the field-alignment experiment, the temperature was increased from 25 °C to 130°C and from 25°C to 200°C in a Nitrogen atmosphere. The temperature was kept at 130°C and at 200° C for 30 minutes, respectively, and then the film was cooled down always under electrical field influence. The reference sample was prepared exactly in the same conditions except for the electrical field presence.

10.6.2.3 OFET film preparation

A drop of solution of modified pentacene was drop-cast on a bottom-contact OFET. After solvent evaporation, electrical fields of 4-5 KV/cm were applied in Nitrogen atmosphere during annealing at 130° C and at 200°C, respectively. The reference sample was prepared exactly in the same conditions but in absence of electrical fields.

10.7 Referenzen

[185] C. D. Simpson, J. D. Brand, A. J. Berresheim, L. Przybilla, H. J. Räder, K. Müllen *Chem.*s *Eur. J.* **2002**, 8, 1424.

[186] W. F. Edwards, M. C. Thies. *Carbon*, **2006**, 44, 243.

[187] E.G. Cervo, M.C. Thies, B. Fathollahi. *J Am Ceram Soc* **2008**, 91, 1416.

[188] W. F. Edwards, M.C. Thies, *Fluid Phase Equilib.* **2005**, 228-229, 421.